博士学位論文
Doctoral Thesis

論文題目

Thesis Title

Quantifying the Contributions of Atmospheric-Oceanic Indices and Hydro-Meteorological Elements on Wildfires

林野火災における大気・海洋変動指標と水文気象要因の定量的分析

東北大学大学院工学研究科

Graduate School of Engineering,

TOHOKU UNIVERSITY

専攻/Department:　土木工学専攻

学籍番号/ ID No:　C0TD6005

氏名/Name:　Ke Shi

QUANTIFYING THE CONTRIBUTIONS OF ATMOSPHERIC-OCEANIC INDICES AND HYDRO-METEOROLOGICAL ELEMENTS ON WILDFIRES

ABSTRACT : Wildfire has become one of the major natural hazards worldwide due to its strong suddenness, great destructiveness, frequent occurrences, and difficulty during the rescue. To reduce the losses caused by wildfires, exploring the spatiotemporal characteristics of wildfires and their causes is crucial. In particular, the frequency and severity of wildfires are strongly related to atmospheric-oceanic indices and hydro-meteorological elements. However, the impacts of atmospheric-oceanic indices on global wildfire homogeneous zones have not been explored, and no studies have systematically discussed how different hydro-meteorological elements cause different types of wildfires in any region or globally.

Therefore, this dissertation first explored the impacts of atmospheric-oceanic indices on the homogeneous drought zones, taking Japan as an example, and compared the homogeneous drought zones with wildfire statistics. Then, similar methods were further applied at the global scale. This dissertation identified the global homogeneous wildfire zones for the first time. It quantified the controlling effect of atmospheric-oceanic indices on the spatiotemporal pattern of the global burned area. Next, this dissertation proposed a new probability-based framework to describe the wildfire bivariate characteristics comprehensively. On this basis, the mechanism of how different hydro-meteorological elements cause different types of wildfires was discussed at the continental United States and global scales. And through the wildfire bivariate simulation of the artificial neural network, the quantitative evaluation of the relationship between hydrometeorology and wildfire was carried out.

Consequently, according to different drought characteristics, Japan can be divided into nine homogeneous drought zones with more than 60% explained variance. Also, these nine zones are dominated by different large-scale climate signals: the Arctic Oscillation has the strongest impact on zones 1, 7, and 8; the influence of the North Atlantic Oscillation on zones 3, 4, and 6 is significant; zones 2 and 9 are both dominated by the Pacific decadal oscillation; and El Ni˜no–Southern Oscillation dominates zone 5. The results will be valuable for drought management and drought prevention.

Similarly, eight global homogeneous wildfire zones and their dominant atmospheric-oceanic indices were identified. The most effective combinations of hotspots and atmospheric-oceanic indices were the Atlantic Multidecadal Oscillation + East Pacific/North Pacific Oscillation + Pacific North American Pattern (PNA) with the wildfire pattern around Ukraine and Kazakhstan, the El Niño/Southern Oscillation + Arctic Oscillation (AO) + East Atlantic/Western Russia Pattern (EA/WR) with the wildfire pattern in Australia, and PNA + AO + Polar/Eurasia Pattern + EA/WR with the wildfire pattern in Brazil. These results provide a reference for predicting wildfire and understanding wildfire homogeneity.

Additionally, compared to the direct joint probability, the wildfire priority index based on the probability framework proposed in this dissertation is more sensitive in capturing extreme wildfire events. And wildfire risk exhibits an increasing trend in California, Texas, and Arkansas, while most of the southeastern United States exhibits decreasing wildfire risk trends. Overall, this analysis can provide a reference to understand the spatiotemporal characteristics of wildfire statistics better and contribute to wildfire management.

Based on the framework of the wildfire priority index, wildfires could be classified into five types: WT-1 (mega-wildfire), WT-2 (joint wildfire-1), WT-3 (joint extremes), WT-4 (joint wildfire-2), and WT-5 (super frequent wildfires). Furthermore, according to the control effect of hydro-meteorological elements on different types of wildfires, the continental United States could be further divided into four cluster zones. In the four new cluster zones, intensifying droughts are a concern in clusters 1 and 4, while there are multiple concerns in cluster 3, namely, stronger winds, higher temperatures, and more drought. The hydrometeorology-wildfire relationship analysis based on the wildfire bivariate probabilistic framework proposed in this study provides new information on the causes of wildfires and other compound disasters.

Finally, back propagation artificial neural network (BPNN) was applied to simulate the wildfire priority index, and this model has achieved excellent performance. In the wildfire bivariate characteristics simulation results of the BPNN model, there were five sub-regions where the model achieved high simulation accuracy, with the R^2 reaching more than 0.90. In addition, eleven sub-regions also achieved good simulation results, and their R^2 was between 0.8 and 0.9. Only two sub-regions had poor simulation accuracy with R^2 below 0.5. When the observed time series had significant periodicity and the hydro-meteorological element-wildfire relationship was highly correlated, the model accuracy of BPNN would be very high. For example, the R^2 in the Alaska/N.W. Canada and Southern Africa sub-regions were as high as 0.89 and 0.95, respectively. On the other hand, when the correlation between hydrometeorology and wildfire was weak, BPNN was insufficient to simulate time series accurately. Still, its ability to follow the original observation time series was not inferior. The reliability of the hydrometeorology-wildfire relationship is also demonstrated by the good performance of the wildfire priority index in the simulation.

Overall, this paper carried out a comprehensive analysis of wildfire causes from two aspects of factors, including atmospheric-oceanic indices on a global scale and hydro-meteorological elements on a local scale. The main five innovations of this doctoral dissertation are as follows: (1) nine homogeneous drought zones with different characteristics were identified across Japan, and leading atmospheric-oceanic indices were quantified for each homogeneous drought zones; (2) global homogeneous wildfire zones were identified and the role of atmospheric-oceanic indices controlling different global wildfire patterns was quantified; (3) a new wildfire priority index was proposed, which can comprehensively consider the wildfire bivariate characteristics. ; (4) based on the fire priority index, the control effect of hydro-meteorological elements on different wildfire types can be analyzed; (5) based on the relationship between hydro-meteorological elements and wildfires, the wildfire priority index was simulated on a global scale and achieved good results. The above results provide new ideas for understanding the causes of wildfires and are helpful for future wildfire management and prevention around the world.

Acknowledgments

Whether you are pursuing a master's degree or a Ph.D., you will graduate one day. But there is no end to the academic pursuit. During my three years at Tohoku University, I have learned a lot, and at the same time, I have become increasingly aware of my ignorance in the academic world. I constantly want to touch the end of my research, but I can never touch the boundaries that seem so close. The ancient Chinese philosopher Zhuangzi once said that ‘吾生也有涯，而知也無涯.’ This sentence means, ‘Our life has a limit, but knowledge has none.’ So my graduation is not the end for me, but a new beginning. I am very grateful to the professors and friends here, who have become the beacon and torches on my way up.

First of all, I would like to thank Prof. So Kazama for giving me the opportunity to come to Hydro-Environmental System Laboratory at Tohoku University. Prof. So Kazama has created a good and relaxed learning and working environment in the laboratory, which makes me enjoy my study and life here. Secondly, I am very grateful to Asst. Prof. Yoshiya Touge. Asst. Prof. Yoshiya Touge carried out the direction of wildfire research in the field of hydrology from nothing in our laboratory, making our team grow gradually. He always brings me new ideas academically and works with me to achieve our goals. Equally, I would like to thank Prof. Shunichi Koshimura and Prof. Keiko Udo for serving on my committee and for their insightful comments and suggestions about my dissertation. Particularly, I would like to thank the China Scholarship Council for the financial support during my studies.

I have unforgettable memories in Japan, and I will always remember those days when we drank together and talked about everything. So I want to thank Dr. Chang, Dr. Jacque, Mr. Sartsin, Mr. Yamamoto, Mr. Xiao, Mr. Lawson, Mr. Yanagihara, Ms. Wang, Mr. Dong, Ms. Sun, Ms. Huang, Mr. Chai, and all my other friends and colleagues in Japan for the wonderful time I spent with them.

Finally, I would like to thank my parents, who have supported me greatly. No matter what life road I choose, they will always not hesitate to support me, love me, and give me advice. I am so sorry that I cannot go back to visit my parents for three years for various reasons. Words cannot express how much I miss my parents and my hometown. I cannot wait to go home with Japanese sake to drink with my father and eat my mother's cooking.

Ke SHI

Tohoku University

October 2022

Contents

List of Figure

List of Table

List of symbols

Akaike information criterion	AIC
Ali-Mikhail-Haq	AMH
Antarctic Oscillation	AAO
Arctic Oscillation	AO
Arctic Oscillation Index	AOI
Artificial Neural Networks	ANNs
Atlantic multidecadal Oscillation	AMO
Atlantic Multi-decadal Oscillation	AMO
Bayesian information criterion	BIC
Clayton	CLA
The coefficient of skewness	CS
The coefficient of variation	CV
The cone of influence	COI
Cross wavelet transform	XWT
Dipole Mode	DM
Distinct empirical orthogonal function	DEOF
Distinct principal components	DPCs
Dynamical Regional Downscaling Japanese 55-year Reanalysis	DSJRA-55
East Atlantic Pattern	EA
East Atlantic/Western Russia Pattern	EA/WR
East Pacific/North Pacific Oscillation	EP/NP
El Niño-Southern Oscillation	ENSO
Exponential distribution	EXP
Forest Service Fire Program Analysis-Fire Occurrence Database	FPA-FOD
Frank	FRA
Gaussian	GAU
Generalized extreme-value distribution	GEV

Generalized logistic distribution	GLO
Gumbel	GUM
Gumbel (extreme-value type I) distribution	GUN
Independence	IND
Keetch-Byram drought index	KBDI
Log-burned-area (log m^2)	LBA
Log-transformed burned area anomalies	logBAA
Log-wildfire-activity (log times)	LFA
Markov Chain Monte Carlo	MCMC
Monthly moisture anomalies	MMA
Multivariate ENSO Index	MEI
National Oceanic and Atmospheric Administration	NOAA
Normal distribution	NOR
North Atlantic Oscillation	NAO
North Atlantic Oscillation Index	NAOI
Oceanic Niño Index	ONI
Pacific Decadal Oscillation	PDO
Pacific Decadal Oscillation Index	PDOI
Pacific/North American Pattern	PNA
Pearson type III distribution	P-III
Percent area of significant coherence	PASC
Polar/Eurasia Pattern	POL
Potential evapotranspiration (mm)	PET
Potential loss (mm)	PL
Potential recharge (mm)	PR
Potential runoff (mm)	PRO
Precipitation (mm)	PRE
Probability plot correlation coefficient	PPCC
Return period (month)	RP

Root mean square error	RMSE
Simple Biosphere including Urban Canopy	SiBUC
Southern Oscillation index	SOI
Standardized Precipitation-Evapotranspiration Index	SPEI
Surface soil moisture (percentage)	SSM
Temperature (Celsius, °C)	TEM
Trend-free Prewhitening Mann-Kendall	TFPW-MK
Tropical Northern Atlantic Pattern	TNA
Tropical Southern Atlantic Pattern	TSA
Wavelet coherence	WCO
Weibull distribution	WEI
Western Pacific Pattern	WP
Wildfire extent vector	WEV
Wildfire increase vector	WIV
Wildfire priority index (probability)	WP
Wildfire type-1	WT1
Wildfire type-2	WT2
Wildfire type-3	WT3
Wildfire type-4	WT4
Wildfire type-5	WT5
Wind speed (m/s)	WS

Chapter 1 Introduction

1.1 Overall background

The wildfire is caused by an initial high-temperature heat source, which may be produced by lightning, volcanic activity, or caused by people, either intentionally or by negligence. Wildfires can produce a lot of smoke pollution and damage forest ecosystems. But wildfires are also a natural part of ecosystems, allowing vital nutrients to return to the soil and giving plants and animals a new beginning, which plays an important role in the reproduction of some plants (Supriya, 2017). Generally, when the wildfire intensity is low, it is conducive to exchanging energy and materials in the forest ecosystem. It also maintains a steady state of the ecosystem at the same time. On the other hand, controlled burning can reduce litter that cannot be naturally decomposed and promote the natural renewal of forest vegetation, thereby reducing the risk of extreme wildfires. However, in recent years, under the influence of anthropogenic climate change and human activities (expansion of the wildland-urban interface, deforestation, etc.), wildfires have become more extreme (more frequent and larger burned areas) around the world. Frequent wildfires have led to large consumption of forest biomass. The carbon-containing gas emitted after the combustion also poses a serious threat to the atmosphere, becoming a major driving force of global climate change.

Wildfires have become one of the major global natural hazards due to their strong suddenness, great destructiveness, frequent occurrences, and difficulty during the rescue (Doerr et al., 2016; McCaffrey, 2004). In particular, some very large, high-impact wildfires are also called mega-wildfires. The term "mega wildfire" became common in 2002 when five states in the western United States experienced the worst wildfires on record, with prominent scale and impact even in the regions where wildfires were frequent (Williams, 2013). For example, Table 1.1 shows five representative wildfire events (mega-wildfires) in the world. From August to November 2020, a wildfire broke out in California, United States, causing the burned area of 418,000 hectares, destroying 935 structures, and damaging five structures. August Complex was the largest wildfire event in recorded California history (Keeley et al., 2021). During

September 2019 and March 2020, wildfires burned 12,600,000 hectares in many forested regions of Australia, and smoke affected large numbers of people. Due to this unprecedented wildfire, more than 3,000 houses were destroyed, and 33 people passed away (Arriagada et al., 2020). A destructive wildfire swept through Canada from July to September 2017. A total of 1,216,053 hectares of areas were burned, and 444 buildings were destroyed, causing more than 39,000 people to be evacuated from their homes (Kirchmeier-Young et al., 2019). In April 2015, wildfires in Russia burned 1,100,000 hectares and damaged about 1,300 buildings, leaving roughly 6,000 people homeless (Liesowska, 2015). The substantial social, ecological, and economic effects of wildfires, especially mega-wildfires, have made wildfire-related research (how the wildfire occurred, how it spread, and how to control it) a hotspot in recent years.

Table 1.1 Representative extreme wildfire events (mega-wildfires) around the world in recent years

Date	Name	Location	Burned area (hectares)	Note	References
08/2020~ 11/2020	August Complex	United States	418,000	One firefighter fatality, 935 structures were destroyed, and 5 structures were damaged.	Keeley et al. (2021)
09/2019~ 03/2020	Black Summer	Australia	12,600,000	More than 3,000 houses were destroyed, and 33 people passed away	Arriagada et al. (2020)
07/2017~ 09/2017	2017 British Columbia wildfires	Canada	1,216,053	More than 39,000 people were evacuated from their homes, and 444 buildings were destroyed	Kirchmeier-Young et al. (2019)
04/2015	2015 Russian wildfires	Russia	1,100,000	Approximately 1,300 homes were damaged, leaving roughly 6,000 people homeless	Liesowska (2015)

Specifically, the intensity and frequency of wildfires are strongly related to atmospheric-oceanic indices and hydrometeorology. For example, as for atmospheric-oceanic indices, the historical study of wildfires in the western United States found that precipitation was the main factor affecting the occurrence of wildfires in this region (Sibold et al., 2006). Furthermore, the distribution of precipitation had significant synchronization with the Pacific Decadal Oscillation (PDO) and the Atlantic Multi-decadal Oscillation (AMO), indicating that the precipitation/drought in the western United States was influenced by atmospheric-oceanic indices (Sibold et al., 2006). Analogously, some scholars have analyzed spatiotemporal wildfire patterns. For example, the wildfires in southern Canada were affected by atmospheric-oceanic indices (McCabe et al., 2004). Notably, relevant scholars generally believe that the impacts of atmospheric-oceanic indices on the distribution of wildfires should be analyzed from two aspects. On the one hand, on an inter-decadal scale, the change in the coupled atmospheric-hydrological system affected the distribution of vegetation, which further affected the type of forest and the combustible loading in the forest. On the other hand, unusual climate patterns could lead to widespread droughts or high temperatures, and such extreme events could trigger wildfires (Flannigan et al., 2000; Stephens et al., 2003).

Simultaneously, hydrometeorology is a comprehensive manifestation of various hydro-meteorological elements in a region over a period of time. Hydrometeorology is the fluctuation of the climate system. Compared with atmospheric-oceanic indices, hydrometeorology has a more direct impact on wildfires. A hydrometeorology system accompanied by drought, high temperatures, and strong winds can easily induce wildfires. The occurrence of large-scale wildfires, especially mega-wildfires, is by no means accidental but contains a complex process under the influence of various hydro-meteorological elements. Also, wildfires often have obvious regional and seasonal characteristics and vary with the hydro-meteorological elements. There are also vibrations in wildfire-prone and infrequent years with the changes in average and extreme weather conditions in the same region.

1.2 Literature view

1.2.1 Current status of research on climate-wildfire teleconnections

The discussion on the teleconnections between atmospheric-oceanic indices and wildfires began in the 1990s. Swetnam et al. (1990) have found a significant correlation between wildfires in the western United States and El Niño-Southern Oscillation (ENSO) for the first time. They have analyzed the teleconnections between the wildfire and the Southern Oscillation Index (SOI) in regions affected less by human disturbance. They also discussed whether there was a difference between the ENSO index in severe wildfire years and the ENSO index in wildfire-free years through resampling and superposed epoch analysis (Swetnam et al., 1990). These two methods determine the robustness of this teleconnection not only on time series but also on spatial scales. Since then, similar studies of teleconnections between atmospheric-oceanic indices and wildfires have sprung up. ENSO-fire dynamic in insular Southeast Asia (Murphy, 2006) and the impact of the Arctic Oscillation pattern (AO) on inter-annual wildfire variability in Central Siberia (Balzter et al., 2005) have been well-known to wildfire-related scholars in recent years.

On the one hand, many scholars used statistical methods to quantify this teleconnection by directly analyzing and discussing the relationship between atmospheric-oceanic indices and regional wildfire statistics. For example, Urrutia-Jalabert et al. (2018) found that ENSO significantly correlated with wildfires in central Chile. And the AO during winter through summer was positively correlated with wildfires across central Chile due to drier/warmer conditions associated with the positive phase of this oscillation. Shabbar et al. (2011) used the multivariate singular value decomposition to explore the relationship between atmospheric-oceanic indices and wildfires in Canada. Their results indicated that the ENSO and the Pacific Decadal Oscillation (PDO) played a significant role in Canadian wildfires. Simultaneously, at the decadal scale, wildfires in the British Columbia coastal temperate rainforest were more likely to follow the positive ENSO and PDO phases (Hoffman et al., 2016). Through wavelet analysis, Mariani et al. (2016) determined that ENSO exerts a persistent and significant influence on southeast Australian wildfires.

On the other hand, some scholars analyzed the relationship between drought and wildfire and then indirectly explored the relationship between climate and wildfire through the driving effect of atmospheric-oceanic indices on drought. Because there may be spatial heterogeneity in wildfire characteristics due to differences in spatial characteristics of drought. For example, as for the wildfires in the western United States, wildfires in Oregon generally occurred in El Niño years, while wildfires in New Mexico, Arizona, and southern Utah generally occurred in La Niña years (Kitzberger et al., 2001; McCabe et al., 2004). Schoennagel et al. (2005) also indicated that the positive phase superposition of El Niño and PDO would cause drought, promoting wildfires in the northern Rocky Mountains. While the negative phase superposition of La Niña and PDO may cause drought in the southern Rocky Mountains and large-scale wildfires. Also, Alencar et al. (2006) found that drought in the Amazon triggered by ENSO has greatly increased the risk of severe wildfire events. In central and eastern Washington State, the United States, the connections between atmospheric-oceanic indices-drought-wildfire were explored through wavelet analysis (Hessl et al., 2004). Their results showed that wildfires tended to occur during dry summers and the positive phase of the PDO in this region (Hessl et al., 2004).

Although the research on the impacts of atmospheric-oceanic indices on wildfire has been widely carried out, it has mainly focused on regional studies. Since atmospheric-oceanic indices have a wide range of influences and are often not confined to a particular region, it is still unclear how to understand the driving mechanism of atmospheric-oceanic indices on wildfires from a global perspective. Additionally, most studies only focus on point-to-point analysis (the relationship analysis between the atmospheric-oceanic indices and wildfire statistics of specific grid cells or the summation of wildfire statistics in a certain region). As a result, there still is a lack of holistic understanding, nor has it fully explored the differences in the driving mechanisms of atmospheric-oceanic indices on wildfires in different regions. Therefore, in this dissertation, the first key research objective is to explore the driving mechanism of atmospheric-oceanic indices on global wildfire patterns. A detailed description of this research gap and the research objective of the study is given in chapter 1.3.

1.2.2 Current status of research on hydrometeorology-wildfire relationships

Research exploring the relationship between hydrometeorology and wildfires has a long history. Richardson (1919) analyzed the hydro-meteorological conditions (also called weather) of the wildfires in northeastern Minnesota, United States, as early as 1919. Then in 1928, Van Wagner (1974) began to study hydro-meteorological elements as a predictor for wildfires and found that wildfire could occur when the humidity was less than 50%. Then, Calvert (1934) proposed wildfire warnings based on hydro-meteorological conditions. A few years later, Gisborne and Hesterov proposed the theory of wildfire forecasting based on integrated hydro-meteorological elements in 1936 and 1944, respectively. Then, Jackson (1968) suggested using the drought index for wildfire-related forecasting. Since the 21st century, related studies on the relationship between hydrometeorology and wildfire have emerged in an endless stream, including regional scales, global scales, single hydro-meteorological elements, and multiple hydro-meteorological elements based on statistical or physical models. In the studies of hydrometeorology-wildfire relationships so far, the three most well-known and proven systems are the Canadian Forest Service Fire Weather Index Rating System, the Australian McArthur Mark 5 Rating System, and the U.S. Forest Service National Fire-Danger Rating System.

The Canadian Forest Service Fire Weather Index Rating System, also known as the Fire Weather Index System, contains six components that describe the effects of hydro-meteorological elements on wildfire and fuel conditions before the wildfire (Van Wagner, 1974; Van Wagner et al., 1987; Van Wagner et al., 1985). In this system, the hydro-meteorological elements entered into the calculations are temperature, relative humidity, wind speed, and precipitation on a daily scale. Then these four hydro-meteorological elements are used to calculate a total of six wildfire-related indicators, including fine fuel moisture code, duff moisture code, drought code, initial spread index, buildup index, and fire weather index. The hydrometeorology-wildfire relationships based on the Canadian Forest Service Fire Weather Index Rating System have been widely used for wildfire warning and forecasting in Portugal (Carvalho et al., 2008), China (Tian et al., 2011), France (Fox et al., 2018) and elsewhere.

The Australian McArthur Mark 5 Rating System, also known as McArthur Forest Fire Danger Index System, comprises three components: Keetch-Byram Drought Index (KBDI), drought factor, and fire danger index. Temperature, wind speed, relative humidity, and precipitation are the essential hydro-meteorological elements in the calculation of this system (Cruz et al., 2015; Keetch et al., 1968; McArthur, 1967; Moore, 1986). In addition, the system uses the results of more than 800 experimental fire and wildfire observations to determine an empirical formula between hydro-meteorological elements and wildfire to determine wildfire risk in Australian forest areas. This Australian McArthur Mark 5 Rating System is considered to have good performance for wildfire warning and forecasting in Australia. It is also used in other countries, such as New Zealand (Anderson, 2009), South Africa (Kraaij et al., 2018), Indonesia (Hadisuwito et al., 2021), etc.

The U.S. Forest Service National Fire-Danger Rating System has four components based on the relationship between hydrometeorology and wildfire, including ignition component, spread component, energy release component, and burning index. In addition to the same four hydro-meteorological elements as in the Canadian Forest Service Fire Weather Index Rating System and Australian McArthur Mark 5 Rating System, this system also requires solar radiation, vapor pressure deficit, and day length for calculations. In addition, this system explicitly calculates the moisture of dead and living vegetation. Dead fuels are divided into categories based on their rapid or slow response to changes in air temperature and relative humidity. Live fuels are divided into herbaceous and woody shrubs (Mees et al., 1991; Schlobohm et al., 2002). The spread and energy release components are largely controlled by fuel structure, weather, and antecedent drought. These two components control the burning index (Schoenberg et al., 2007). Similar to the other two hydrometeorology-wildfire relationship systems, except where the U.S. Forest Service National Fire-Danger Rating System is developed, this system is also used in other regions such as Turkey (Yamak, 2006).

Although the research on the hydrometeorology-wildfire relationships has been widely carried out, and even though the above three proven systems for describing hydrometeorology-wildfire relationships have been developed, some gaps still have not been filled. First, previous studies have only focused on the univariate wildfire characteristics independently, targeting the occurrence of wildfire or the final total burned area. Second, previous studies have only discussed the spatial heterogeneity of the impact of hydrometeorology on wildfires without considering the temporal heterogeneity, even within the same region. The mechanism of how different hydro-meteorological elements cause different types of wildfires has not been explored. Therefore, the second key research objective is to explore the influence of hydro-meteorological elements on wildfire bivariate characteristics (a comprehensive consideration of burned area and wildfire activity). A detailed description of this research gap and the research objective of the study is given in chapter 1.3.

1.3 A detailed description of research gaps and research objectives

Altogether, this study aims to fill the two gaps that the previous studies did not fully explore the effects of climatic factors and hydro-meteorological elements on wildfire. These two main research objectives can be further subdivided into five directions, as shown in Figure 1.1.

To achieve final goal 1, the methods that need to be used include cluster analysis, space-time decomposition, and wavelet analysis. First, there are few studies on the overall spatiotemporal characteristics of drought and wildfire conditions in Japan. Only Lee et al. (2012b) used the effective drought index to describe the characteristics of drought in Japan. Still, they did not consider the control effect of atmospheric-oceanic indices on drought and drought-wildfire relationships. To fill this gap, this study first identified the homogeneous drought zones in Japan and selected the atmospheric-oceanic indices that may impact the drought in Japan. Then the effect of atmospheric-oceanic indices on different homogeneous drought zones was quantified in Japan. And by comparing the homogeneous drought zone with the wildfire statistics in Japan, the drought-wildfire relationship can be discussed qualitatively.

Second, similar homogeneous zone explorations are applied globally. Regarding global wildfire patterns, Page et al. (2008) discussed the spatiotemporal wildfire patterns. However, only wildfire activity was analyzed in their study, and only the impacts of ENSO on wildfire were discussed. Another key factor for measuring wildfire is the burned area, which has been linked to paleo records (Bowman et al., 2009) and is used to calculate fluxes of carbon from the biosphere to the atmosphere (Van der Werf et al., 2010), reflecting the extent of wildfire severity (Keeley, 2009). Therefore, this study takes the global burned area as the target object. The influence of more than a dozen climatic factors on the global burned area patterns was analyzed, which provides a new important reference for global wildfire characteristics.

To achieve final goal 2, the first thing to solve is how to consider wildfire bivariate characteristics comprehensively. There are many studies on extreme wildfires, but they are often analyzed independently from the wildfire univariate characteristics. Therefore, the third direction is to explore a new method or index to comprehensively describe the wildfire bivariate characteristics (burned area and wildfire activity). Finally, wildfire activity and burned area are integrated into a new wildfire priority index using a probabilistic model based on copula theory.

Based on the five wildfire types classified by the wildfire priority index, the relationship between hydrometeorology and wildfire types can be fully discussed. Therefore, the fourth direction is to quantify the control effects of hydro-meteorological elements on different wildfire types in different ecological regions in the continental United States.

Finally, the hydrometeorology-wildfire relationship is determined on a global scale based on the wildfire priority index. On this basis, through back propagation neural network, a model for simulating the wildfire priority index is constructed, and the model achieves great performance.

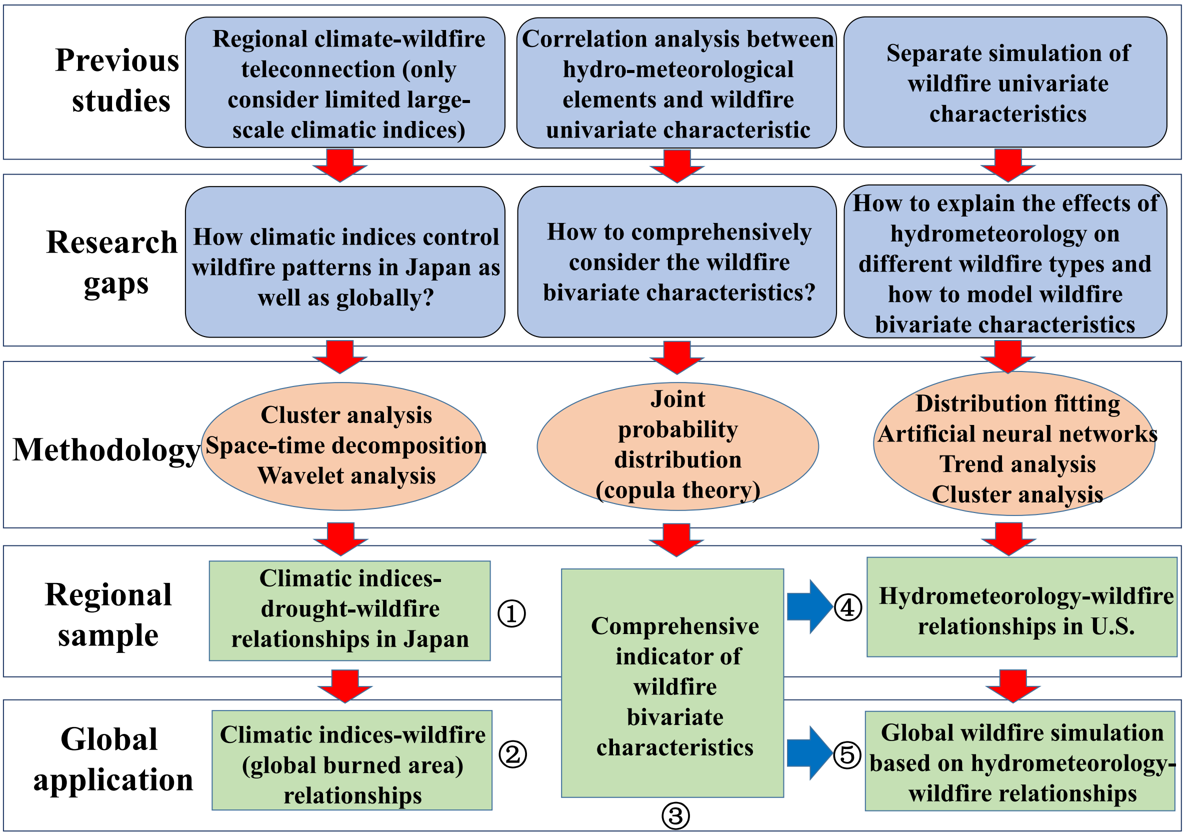

Figure 1.1 The conceptual representation of research gaps, methodology, regional sample, and global application.

1.4 Organization of dissertation

The organizational structure and research chart of this dissertation are shown in Figure 1.2. Chapter 1 describes the overall background of this dissertation and is therefore not shown in the organizational chart. Chapter 2 describes all the basic data sources and their preprocessing required for subsequent computations. And the physical model for drought, the theory and equations of drought index, and various statistical models are also explained in detail in this chapter.

Chapters 3 and 4 aim to explore the teleconnection between atmospheric-oceanic indices and wildfires. Chapter 3, with Japan as the target region, explores how atmospheric-oceanic indices affect drought and how drought affects wildfire characteristics based on homogeneous drought zones. In addition, chapter 3 lays the technical support for the subsequent calculations in chapter 4.

In chapter 4, the impact of atmospheric-oceanic indices on global wildfire patterns (burned area) is quantified with global targeting. The hotspots in the global wildfire patterns are discussed in detail, which provides a new idea for exploring the atmospheric-oceanic indices-wildfire teleconnections. These results can also provide a new reference for predicting wildfires based on atmospheric-oceanic indices in hotspot regions.

Chapters 5, 6, and 7 aim to explore the relationships between hydro-meteorological elements and wildfires. Chapter 5 is the theoretical basis for chapters 6 and 7. In addition, chapter 5 proposed a new wildfire priority index to comprehensively describe wildfire activity and burned areas.

Chapter 6 takes the continental United States as the target area, divides wildfires into different types according to the wildfire priority index, and quantifies the control effects of hydro-meteorological elements on different wildfire types.

Chapter 7 is a further extension of chapters 5 and 6, aiming at the global target region and quantifying the control effects of hydro-meteorological elements on wildfire bivariate characteristics in each climate sub-region worldwide. And the results are applied to wildfire simulation.

Chapter 8 is also not shown in the organizational chart. Chapter 8 summarizes the important results in the previous chapter and the main conclusions of this doctoral dissertation. Additionally, the limitations of this dissertation and prospects for future work are also discussed in this chapter.

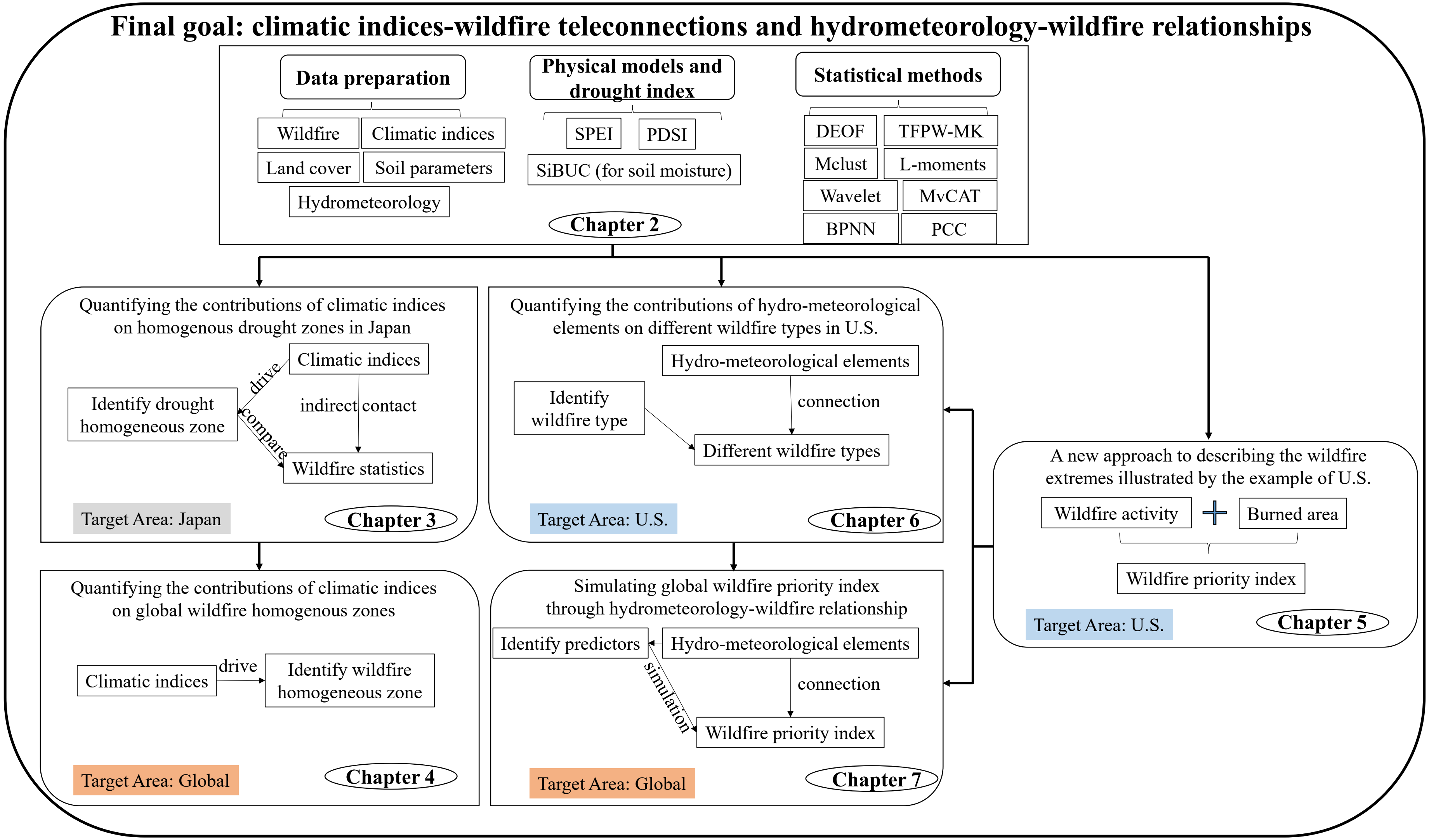

Figure 1.2 The organizational structure and research flow chart of the dissertation.

Chapter 2 Data and Methodology

2.1 Data sources and processing

2.1.1 Wildfire data for Japan, the continental United States, and the world

The wildfire statistics data sources are divided into three parts: Japan, the continental United States, and the world. As for Japan, the burned area and wildfire activity data come from fire reports provided by the Fire and Disaster Management Agency of Japan (https://www.fdma.go.jp/). The original data contains information on the time of wildfire occurrence (Unit: times) and the final burned area (Unit: m^2) from 1995 to 2017. The information is accurate to the specific city or village. However, to comply with the data privacy policy, only wildfire statistics information on the prefecture scale is shown in the results of this dissertation.

As for the continental United States, the wildfire statistics data were obtained from the 5th edition of the Forest Service Fire Program Analysis-Fire Occurrence Database (FPA-FOD) (Short, 2021) (https://www.fs.usda.gov/rds/archive/catalog/RDS-2013-0009.5). There were 2.17×10^6 million wildfire events during 1992~2018 with a total burned area of 667.7×10^9 m^2 in this dataset, which was obtained from the reporting systems of federal, state, and local fire organizations. This dataset is the fourth update of a publication originally generated to support the National Fire Program Analysis System. For records to be included in this dataset, the basic data elements were mainly included: discovery date, final fire size, and a point location at least as exact as a Public Land Survey System (PLSS) section (1-square mile grid). The data were modified to comply with the National Wildfire Coordinating Group's data standards, including an updated wildfire-cause standard. And this dissertation integrates event-based primary data into gridded data (incorporate wildfire events into the nearest grid based on ignition). In particular, the obtained wildfire data was transformed into 0.25° × 0.25° spatially in the continental United States in Chapter 5. Monthly time series are constructed for each wildfire event in each grid cell by assigning it to a specific month based on the discovery and end date of the wildfire event. Any grid cells with fewer than 100 wildfire records during the 27 years were removed to ensure accurate estimation of univariate and bivariate distributions. The spatial distribution of the reserved grid cells and representative samples across the conterminous United States are shown in Figure 2.1. The units of burned area and wildfire activity are m^2 and times, respectively. Additionally, log transformation was performed to process the obtained wildfire statistics into log-burned-area (LBA) and log-wildfire-activity (LFA) data. Log transformation is commonly employed in statistical analysis of wildfires and can better consider rarely affected wildfire-sensitive ecosystems with a lower vegetation restoration capability than other wildfire-dependent ecosystems (Bistinas et al., 2013; Collins et al., 2006; Lei et al., 2019).

(a) Spatial distribution of meshes for frequency analysis

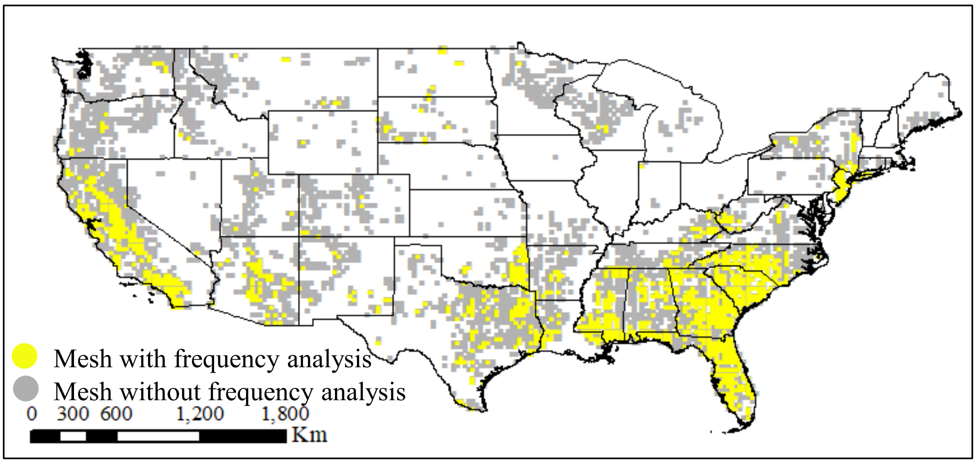

(b)Representative sample for frequency analysis

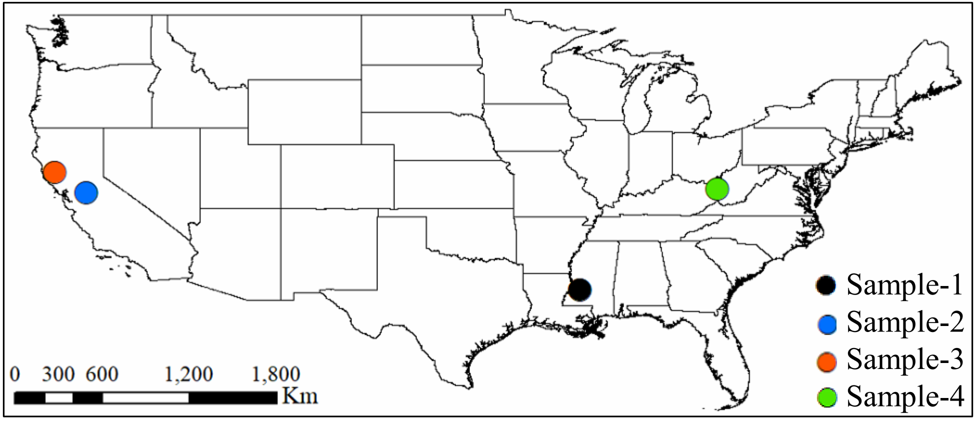

Figure 2.1 Spatial distribution of meshes for frequency analysis and representative samples for frequency analysis in chapter 5.

Notably, as for chapter 6, to be consistent with the spatial resolution of hydro-meteorological elements, wildfire statistics data was converted to 0.5°×0.5° grid cells across the contiguous United States spatially.

When the target is global wildfire statistics, the existing burned area datasets have advantages and limitations. There are four widely used global wildfire datasets (Table 2.1). Chuvieco et al. (2018) developed the Fire CCI v5.1 dataset for 2001 to 2019 based on a hybrid approach combining the highest resolution (250 m) near-infrared band of MODIS with active wildfire information. The Fire CCI dataset has been found to be very useful for describing and better understanding distributions of burned areas and wildfire activity at regional and global scales (Chuvieco et al., 2018). Also, Fire CCI v5.1 was considered a better performer than NASA MCD64A1 v006, particularly regarding small wildfire detection capabilities (Lizundia-Loiola et al., 2020). As for the GFED 4.1s and GABAM datasets, the available times of these two datasets are unsatisfactory for this study. Spatiotemporal trends in BA from the Fire CCI dataset were confirmed to be consistent with those contained in GFED dataset, and the regional differences provide new insights into potential problems or strengths of existing wildfire databases. For example, during the extreme wildfires in Eastern Europe in the spring of 2006, Fire CCI data captured burned areas more realistically than GFED data (Chuvieco et al., 2018). Ultimately, the Fire CCI v5.1 dataset was used. It is important to note that this dataset is treated at different spatial resolutions in different sections for different purposes. A coarser resolution of 1°×1° was chosen in chapter 4 to reduce localized interference in identifying homogeneous wildfire zones. This dataset was processed to the same resolution of 0.5°×0.5° as the hydro-meteorological elements when exploring hydrometeorology-wildfire relationships. The unit of burned area in the Fire CCI dataset is m^2.

Table 2.1 Information for the candidate global burned area datasets

Global burned area datasets	Resolution	Available times
GFED 4.1s	0.25°	1997/1~2016/12
GABAM	30 m	2000, 2005, 2010, 2015, 2018

Global burned area datasets	Resolution	Available times
Fire CCI v5.1	250 m	2001/11~2019/12
NASA MCD64A1 v006	500 m	2000/11~2020/6

In addition, if the original global burned area time series were used directly, homogeneous burned area zones would be occupied by regions with large burned areas, such as the United States or Canada. Therefore, explaining the climatic causes of homogeneous burned area zones would be difficult under the original time series. To avoid this problem, log transformation was performed for the original burned area data.

Log transformation can increase the focus on wildfire-sensitive ecosystems that are rarely affected by wildfire and have a lower capacity for vegetation recovery than other wildfire-dependent ecosystems (Bistinas et al., 2013; Collins et al., 2006; Lei et al., 2019). Then, the monthly log-transformed burned area anomalies (logBAA) in chapter 3 can be calculated by the following equation:

$$\log BAA_{i,n} = \log BA_{i,n} - \frac{\sum_{n=1}^{m} \log BA_{i,n}}{m} \tag{2.1}$$

Where $\log BA_{i,n}$ is the monthly log-transformed wildfire burned area in the month i of year n in a given mesh; m is the number of years in the study period; and $\log BAA_{i,n}$ is the monthly log-transformed wildfire burned area anomaly in the month i of year n in a given mesh.

2.1.2 Hydro-meteorological data for Japan, the continental United States, and the world

For Simple Biosphere including Urban Canopy (SiBUC) forcing data in Japan, the forcing data other than precipitation with high resolution (5 km × 5 km) during 1958-2012 come from the Dynamical Regional Downscaling Japanese 55-year Reanalysis (DSJRA-55) dataset (Kayaba et al., 2016), including temperature (Unit: K), radiation (Unit: W/m^2), barometric pressure (Unit: Pa), etc. (https://jra.kishou.go.jp/DSJRA-55/index_ja.html). The precipitation

(Unit: mm) data from 1958 to 2012 were taken from the Asian Precipitation Highly Resolved Observational Data_Japan (APHRO_JP) gridded dataset (Kamiguchi et al., 2011; Kamiguchi et al., 2010; Yatagai et al., 2012) (http://aphrodite.st.hirosaki-u.ac.jp/). In the statistical analysis, precipitation from APHRO_JP shows good performance for both mean and extreme values (Kamiguchi et al., 2011; Kamiguchi et al., 2010).

For SiBUC forcing data in the continental United States and globally, the underlying meteorological data for this study were obtained from ERA5 hourly data at a 0.5°×0.5° resolution from 1992 to 2019 (Hersbach et al., 2018). The global and continental United States simulation timeframes are 2001~2019 and 1992~2018, respectively. Temperature (TEM, Unit: K), wind speed (WS, Unit: m/s), and precipitation (PRE, Unit: mm) were directly used to analyze the relationship between hydro-meteorological elements and wildfires. Hourly TEM and WS data were calculated as monthly averages, and hourly PRE data were calculated as monthly totals. In addition, other hydro-meteorological data (barometric pressure, shortwave radiation, longwave radiation, etc.) were used to calculate the soil moisture and drought index in Chapter 2.2.

2.1.3 Global atmospheric-oceanic indices data

The relationship between atmospheric-oceanic indices and extreme weather has been widely discussed worldwide, including in the United States (Meehl et al., 2007), China (Gu et al., 2017), and Turkish (Baltacı et al., 2018). The selection of targeted atmospheric-oceanic indices for different study areas is an important step in this type of research. In chapter 3, when considering Japan as a target area, four atmospheric-oceanic indices (AO, NAO, ENSO, and PDO) were used to analyze the teleconnections between the atmospheric-oceanic indices and drought in Japan. These four indices have been shown to influence the hydro-meteorological characteristics of Japan. For example, a warm winter in East Asia may be caused by a positive winter AO (He et al., 2017). Aizen et al. (2001) noted that NAO could significantly affect rainfall conditions in western Japan. Similarly, Hu et al. (2005) found an important role for ENSO in the variability of summer rainfall in East Asia. Lee et al. (2012b) pointed out that negative PDO years could increase rainfall as tropical cyclones approached Japan. Specifically, chapter 3 quantifies the impact of these atmospheric-oceanic indices through the Arctic Oscillation Index (AOI) (Jianping et al., 2003), North Atlantic Oscillation Index (NAOI) (Jianping et al., 2003), Pacific Decadal Oscillation Index (PDOI) (Mantua et al., 2002), and Oceanic Niño Index (ONI) (Bamston et al., 1997).

For the teleconnections between atmospheric-oceanic indices and wildfires in chapter 4, sixteen atmospheric-oceanic indices that may impact wildfires were selected (Table 2.2). Chapter 4 selects as many atmospheric-oceanic indices as possible to assess the influence of climate on the spatiotemporal characteristics of wildfire. All atmospheric-oceanic indices are from the National Oceanic and Atmospheric Administration (https://www.noaa.gov/, last access: 18 October 2022). All atmospheric-oceanic indices used in this dissertation are dimensionless.

Table 2.2 Description and key references of sixteen atmospheric-oceanic indices

Climate pattern	Abbreviation	Primitive elements	Key references
Polar/Eurasia Pattern	POL	geopotential height field	Barnston et al. (1987)
Dipole Mode	DM	sea surface temperature	Saji et al. (1999)
Arctic Oscillation	AO	sea level pressure	Thompson et al. (1998)
Antarctic Oscillation	AAO	geopotential height field	Gong et al. (1998) (1999)
Western Pacific Pattern	WP	geopotential height field	Barnston et al. (1987) Wallace et al. (1981)
East Atlantic/Western Russia Pattern	EA/WR	geopotential height field	Barnston et al. (1987)
Pacific/North American Pattern	PNA	geopotential height field	Blackmon et al. (1984)

Climate pattern	Abbreviation	Primitive elements	Key references
Pacific Decadal Oscillation	PDO	sea surface temperature	Newman et al. (2016)
East Pacific/North Pacific Oscillation	EP/NP	geopotential height field	Bell et al. (1995)
Multivariate ENSO Index	MEI	sea level pressure, sea surface temperature, surface zonal winds, surface meridional winds, and outgoing longwave radiation	Wolter et al. (1993) (1998) (2011)
Oceanic Niño Index	ONI	sea surface temperature	Huang et al. (2017)
Atlantic multidecadal Oscillation	AMO	sea surface temperature	Enfield et al. (2001)
North Atlantic Oscillation	NAO	sea level pressure	Barnston et al. (1987) Hurrell (1995) Wallace et al. (1981)
East Atlantic Pattern	EA	geopotential height	Barnston et al. (1987) Wallace et al. (1981)
Tropical Northern Atlantic Pattern	TNA	sea surface temperature	Enfield et al. (1999)
Tropical Southern Atlantic Pattern	TSA	sea surface temperature	Enfield et al. (1999)

2.1.4 Land cover and soil parameters for Japan, the continental United States, and the world

For the calculation of SiBUC in Japan, the land-use and land-type data come from the Global Land Cover Characterization (Loveland et al., 2000) and Ministry of Land, Infrastructure, Transport and Tourism, Japan (https://nlftp.mlit.go.jp/ksj/index.html, last accessed 30 September 2022). Soil and vegetation parameters, such as the leaf area index, come from ECOCLIMAP (Champeaux et al., 2005). For the calculation of SiBUC in the continental United States and globally, the land cover and soil parameters are also from the Global Land Cover Characterization and ECOCLIMAP, respectively (Champeaux et al., 2005).

2.1.5 Ecoregions in the continental United States and climate zones in the world

Chapter 6 divides the United States into 17 ecoregions based on Environmental Protection Agency regional offices (McMahon et al., 2001; Omernik, 1987, 2004; Omernik et al., 2014) (https://www.epa.gov/eco-research/ecoregions), as shown in Figure 2.2. Ecoregions are geographical areas with broadly comparable ecosystems and types, qualities, and quantities of natural resources. This ecoregion framework is based on mapping done in cooperation with EPA regional offices, other Federal agencies, state resource management agencies, and bordering North American nations, as well as the work of Omernik (1987). Ecoregions identify areas of similarity in the mosaic of biotic, abiotic, terrestrial, and aquatic ecosystem components, with humans being considered part of the biota. They are designed to serve as a spatial framework for the research, assessment, and monitoring of ecosystems. These areas are crucial for organizing and putting into practice ecosystem management strategies among federal agencies, state agencies, and nonprofit groups that are in charge of various resource categories within the same geographical areas.

Similarly, in chapter 7, AR5 (IPCC 5th Assessment Report) Reference Regions (IPCC, 2014) (https://www.ipcc-data.org/guidelines/pages/ar5_regions.html) are used when exploring the relationships between hydro-meteorological elements and different types of wildfire around the globe, as shown in Figure 2.3.

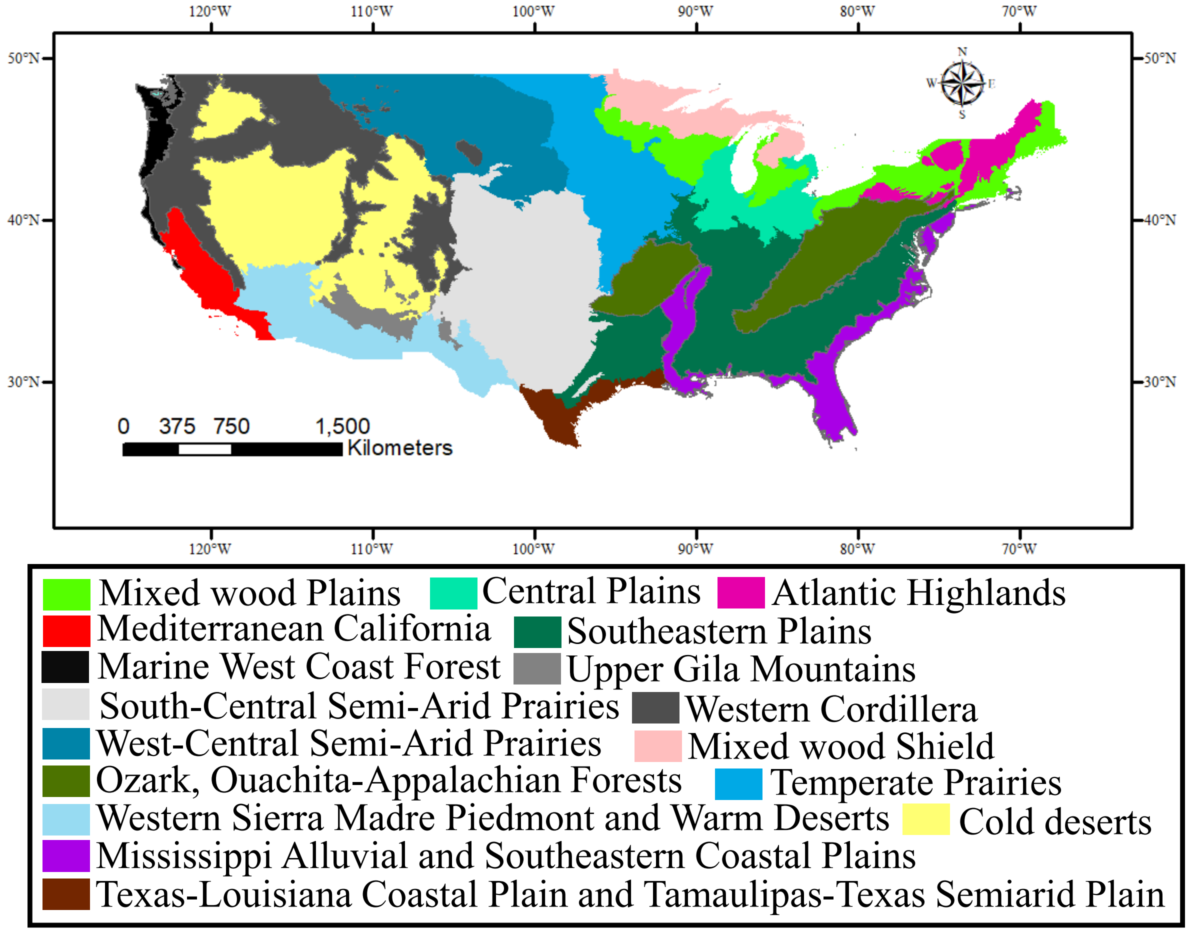

Figure 2.2 Ecoregions of the contiguous United States.

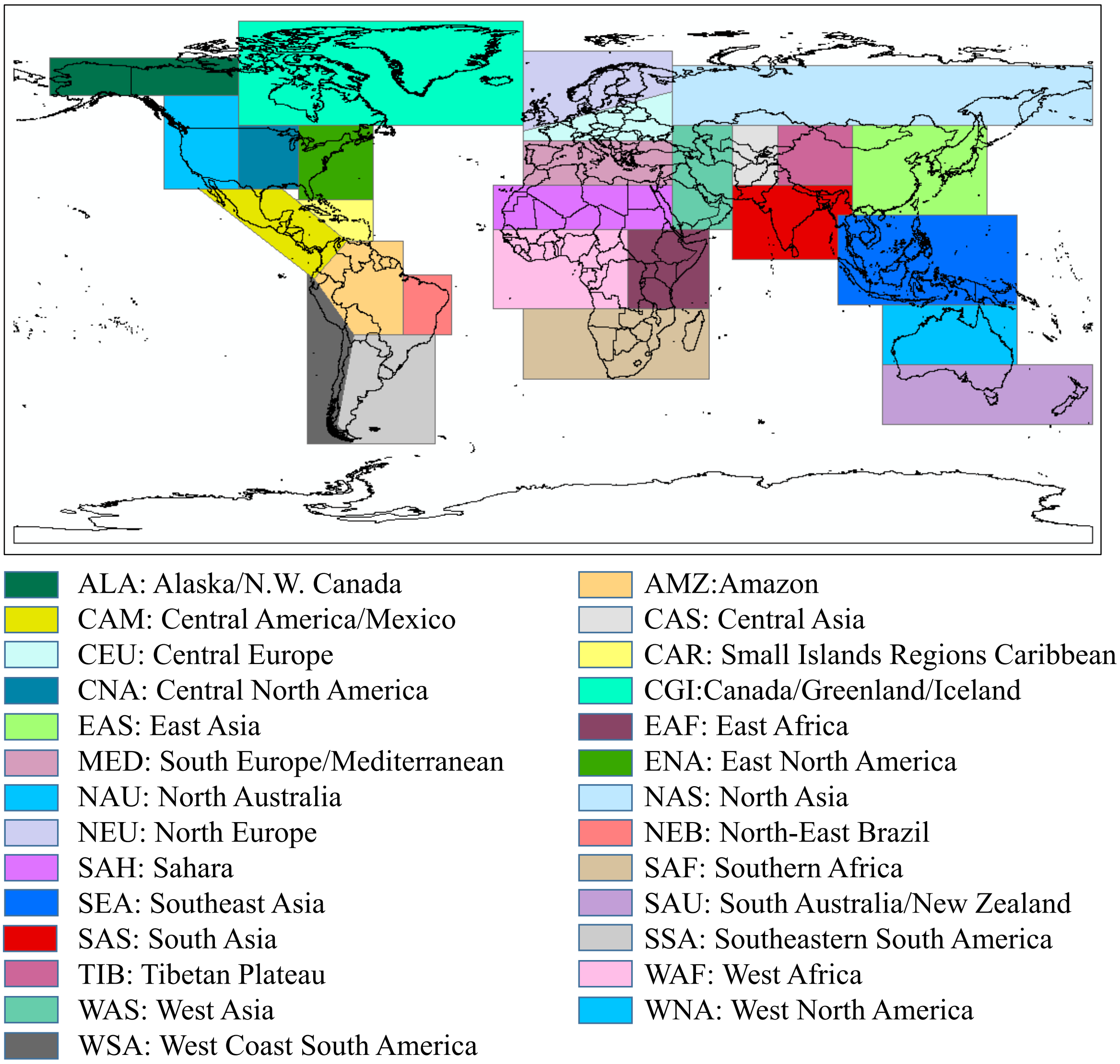

Figure 2.3 The spatial boundaries of the geographical regions used in the IPCC 5th Assessment Report.

2.2 Physical models and drought index

2.2.1 Simple Biosphere including Urban Canopy (for soil moisture)

Soil moisture acts as a good drought index, reflecting recent precipitation and preceding conditions, indicating vegetation potential and available water storage (Keyantash et al., 2002). The soil moisture used in this dissertation is derived from simulations using the Simple

Biosphere Model including Urban Canopy (SiBUC), which was developed by Tanaka (2004). The schematic diagram of the SiBUC is shown in Figure 2.4. In the physical processes in SiBUC, water and heat are transferred between state quantities called forecast variables, and the values of forecast variables are determined for each land cover. The forecast variables are the following 4 types and 16 variables: (1) surface temperature (Unit: K): surface temperature in the canopy (T_c), surface temperature in the ground (T_g), surface temperature in the water body (T_{wb}), surface temperature in the bulk roof (T_{br}), surface temperature in the bulk wall (T_{bw}), surface temperature in the urban ground (T_{ug}); (2) underground temperature (Unit: K): underwater temperature (T_{dw}), the underground temperature in vegetation area (T_{dg}), underground urban temperature (T_{du}); (3) intercepted moisture (Unit: m/s): intercepted moisture in the canopy (M_c), intercepted moisture in ground (M_g), intercepted moisture in the bulk roof (M_{br}), intercepted moisture in urban ground (M_{ug}); (4) soil moisture (Unit: %): soil moisture in the surface layer (W_1), soil moisture in the root zone (W_2), soil moisture in recharge zone (W_3). The soil moisture in the surface layer (W_1) was used in this dissertation.

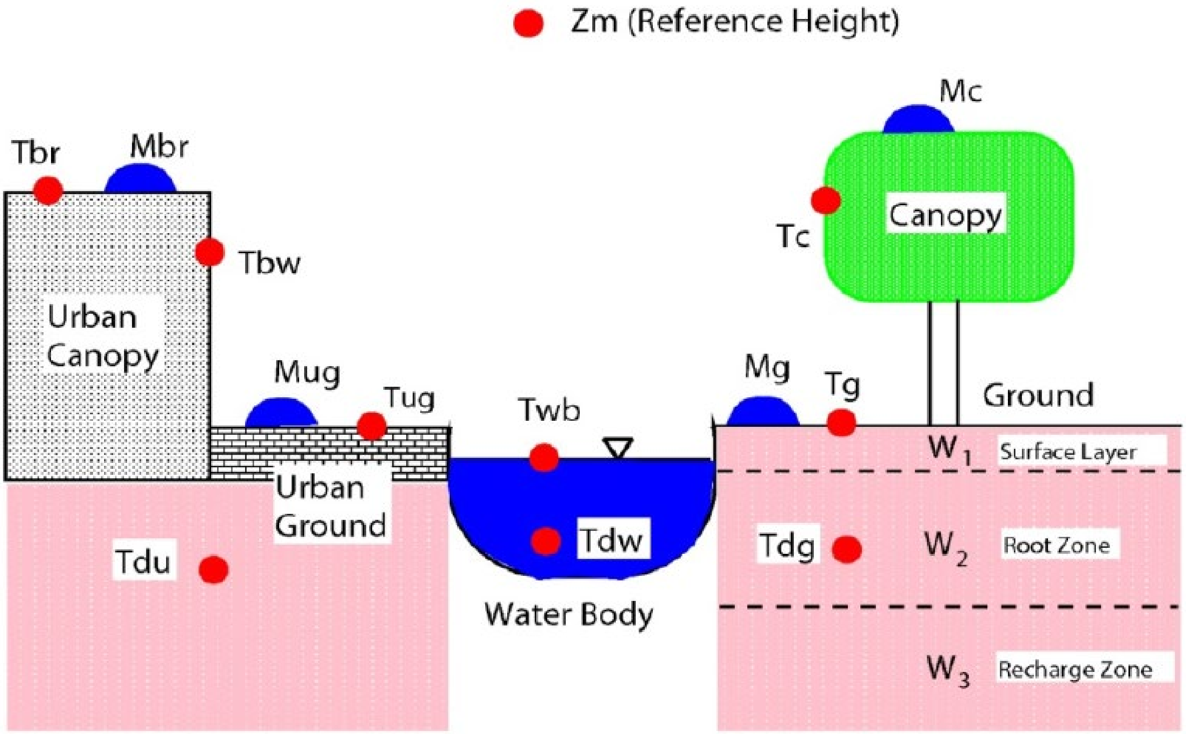

Figure 2.4 The structure of the SiBUC (Tanaka, 2004).

The program of the SiBUC is based on FORTRAN. Additionally, a single-layer snow model is also considered in the SiBUC, providing an opportunity to consider spring water supply based on snowmelt processes. The model has been used in Turkey (Fujihara et al., 2008), Japan (Kotsuki et al., 2015), and Southeast Asia (Kotsuki et al., 2013) with great performances. And the impact of human activity is eliminated in the SiBUC calculations by removing irrigation. Using river discharge, SiBUC was nicely validated. The SiBUC is a model based on physical processes, which is more credible than the empirical model. To further ensure the accuracy of the soil moisture results from SiBUC, we have validated the model results in chapter 3. Notably, the soil moisture simulated by SiBUC in this study is the saturation ratio in the first layer. After obtaining the daily soil moisture, the monthly minimum soil moisture was extracted to show the driest situation every month.

2.2.2 Standardized Precipitation-Evapotranspiration Index

The Standardized Precipitation-Evapotranspiration Index (SPEI) is based on the monthly difference between precipitation and potential evapotranspiration. Different time scales of SPEI can represent different climatic water balances. The potential evapotranspiration was calculated through the Penman-Monteith equation rather than the Thorntwhaite equation because the former can more realistically estimate potential evapotranspiration. The specific formula is listed as follows:

$$PET = \frac{0.408\Delta\ (R_n - G) + \gamma \frac{900}{TEM + 273} WS_2\ (e_s - e_a)}{\Delta + \gamma\ (1 + 0.34 WS_2)} \tag{2.2}$$

Where PET is potential evapotranspiration (Unit: mm/day), R_n is the net radiation (Unit: MJ/m^2/day), G is the soil heat flux density (Unit: MJ/m^2/day), TEM is the air temperature at a 2 m height (Unit: °C), WS_2 is the wind speed at a 2 m height (Unit: m/s), e_s is the vapor pressure of the air at saturation (Unit: kPa), e_a is the actual vapor pressure (Unit: kPa), Δ is the slope of the vapor pressure curve (Unit: kPa/°C), and γ is the psychrometric constant (Unit: kPa/°C) (Allen et al., 1998). The calculated initial PET is the daily scale, and then the daily scale PET is summed to become the PET at a monthly scale (Unit: mm/month).

With a value for potential evapotranspiration, the difference between the precipitation (Unit: mm/month) and potential evapotranspiration (Unit: mm/month) for the month *i* can be calculated as follows:

$$D_i = PRE_i - PET_i \tag{2.3}$$

The calculated D_i values are aggregated at different time scales. The difference in a given month *j* and year *i* depends on the chosen timescale *k*. For example, the accumulated difference for one month in a particular year *i* with a 12-month timescale can be calculated as follows (Vicente-Serrano et al., 2010):

$$X_{i,j}^{k} = \begin{cases} \sum_{l=13-k+j}^{12} D_{i-1,l} + \sum_{l=1}^{j} D_{i,l}, \ j < k \\ \sum_{l=j-k}^{j} D_{i,l}, \qquad j \geq k \end{cases} \tag{2.4}$$

Based on the behavior of the most extreme values, the log-logistic distribution is very suitable for normalizing the D-series to obtain the SPEI (Vicente-Serrano et al., 2010). The probability density function of a three-parameter log-logistic distributed variable is expressed as:

$$f(x) = \frac{\beta}{\alpha}\left(\frac{x-\gamma}{\alpha}\right)^{\beta-1}\left[1+\left(\frac{x-\gamma}{\alpha}\right)^{\beta}\right]^{-2} \tag{2.5}$$

Where α, β, and γ are scale, shape, and origin parameters, respectively, for *D* values in the range ($\gamma > D < \infty$).

The probability distribution function of the *D* series, according to the log-logistic distribution, can be given by

$$F(x) = \left[1+\left(\frac{\alpha}{x-\gamma}\right)^{\beta}\right]^{-1} \tag{2.6}$$

Then, the SPEI can be easily obtained as the standardized values of *F*(*x*) (Abramowitz et al., 1964).

$$SPEI = W - \frac{C_0 + C_1W + C_2W^2}{1 + d_1W + d_2W^2 + d_3W^3} \tag{2.7}$$

Where

$$W = \sqrt{-2\ln(P)} \quad , \quad P \le 0.5 \tag{2.8}$$

And P is the probability of exceeding a determined D value, $P = 1 - F(x)$. If $P > 0.5$, then P is replaced by $1-P$, and the sign of the resultant SPEI is reversed. The constants are: C_0=2.515517, C_1=0.802853, C_2=0.010328, d_1=1.432788, d_2=0.189269, and d_3=0.001308.

The SPEI1 usually represents a meteorological drought, while SPEI3 is often used as an agricultural drought index. SPEI at longer scales, such as SPEI5 and SPEI12, can indicate hydrological drought and monitor surface water resources (Beguería et al., 2014; Hayes et al., 2011). It should be noted that the SPEI used in this study is the mean of SPEI1, SPEI3, SPEI6, SPEI9, and SPEI12. The SPEI calculation program in this dissertation is written by MATLAB. And the SPEI class is shown in Table 2.3. The SPEI is dimensionless.

Table 2.3 Categories of dryness/wetness degree according to the SPEI values

Categories	SPEI values
Extremely wet	[2.0, +∞)
Severely wet	[1.5, 2.0)
Moderately wet	[1.0, 1.5)
Slightly wet	[0.5, 1.0)
Near normal	(-0.5, 0.5)
Slightly dry	(-1.0, -0.5]
Moderately dry	(-1.5, -1.0]
Severely dry	(-2.0, -1.5]

Categories	SPEI values
Extremely dry	(-∞, -2.0]

2.2.3 Palmer Drought Severity Index

The Palmer Drought Severity Index (PDSI) was presented by Palmer Palmer (1965). The PDSI is calculated from the monthly moisture anomalies (MMA) determined by estimating the difference between the actual precipitation and the precipitation required for the climate to be suitable for existing conditions (Zhai et al., 2010). The PDSI is dimensionless. The PDSI calculation program in this dissertation is written by MATLAB. The PDSI incorporates antecedent precipitation, water supply, and water demand into a hydrological system (Dai et al., 2004). Specifically, the equation used to calculate the MMA is shown as follows:

$$MMA_i = K(PRE - (\alpha_i PET + \beta_i PR + \varphi_i PRO - \delta_i PL)) \tag{2.9}$$

The *MMA* can show dryness/wetness in the month *i*. *K* is a climatic characteristic value that varies over time and space to account for climate changes. α_i, β_i, φ_i, and δ_i are the weighted values according to the climate of the area. *PRE*, *PET*, *PR*, *PRO,* and *PL* represent precipitation (Unit: mm/month), potential evapotranspiration (Unit: mm/month), potential recharge (Unit: mm/month), potential runoff (Unit: mm/month), and potential loss (Unit: mm/month), respectively. Through the *MMA*, the PDSI value can be calculated for a given month using the following equation:

$$PDSI_i = PDS\mathrm{I}_{i-1} + \frac{MMA_i}{3} - 0.103PDSI_{i-1} \tag{2.10}$$

2.3 Statistical methods

2.3.1 Gaussian Mixture Modelling for Model-Based Clustering for chapter 3 and chapter 6

The Gaussian Mixture Modelling (Mclust toolkit) based on R was used for cluster analysis in this dissertation, containing three parts: (1) initialization by model-based hierarchical clustering approach; (2) maximum likelihood estimation based on an expectation-maximization algorithm (Bradley et al., 1998; Dempster et al., 1977); (3) selection of the number of clusters and the Bayesian model via Bayesian Information Criterion approximation (Fraley et al., 2002; Fraley et al., 2012; Scrucca et al., 2016). Specifically, the Gaussian Mixture Modelling is divided into the following four steps: (1) determine a maximum number of clusters (It is set to 15 for the maximum number of clusters in this dissertation, and the optimal clustering numbers of the results in this dissertation are all less than 15) and a set of hybrid models to consider; (2) perform hierarchical clustering to maximize the classification likelihood for each model, and obtain the corresponding classifications for up to the maximum number of clusters; (3) apply the expectation-maximization algorithm for each model and each number of clusters; (4) compute Bayesian Information Criterion approximation for the single-cluster case for each model and the hybrid model with the optimal parameters (Fraley et al., 2002; Fraley et al., 2012; Scrucca et al., 2016). In addition, noise and outliers can be dealt with by iterative sampling, where points with low probability are removed from the clusters. The clustering/removal process is repeated until all remaining observations have a relatively high density (Fraley et al., 2002; Fraley et al., 2012; Scrucca et al., 2016). It is important to note that all input data were normalized before clustering. For more detailed information about the Gaussian Mixture Modelling for Model-Based Clustering, please refer to the Mclust toolkit (https://cran.r-project.org/web/packages/mclust/index.html).

For a sample $X=\{x_1,x_2,\cdots,x_i,\cdots,x_n\}$ of n independent and identically distributed observations, through the use of a finite mixture model with G components, a probability density function that describes the distribution of each observation can be provided:

$$f(x_i;\Psi)=\sum_{k=1}^{G}\pi_k f_k(x_i;\theta_k) \tag{2.11}$$

Where $\Psi=\{\pi_1,\cdots,\pi_{G-1},\theta_1,\cdots,\theta_G\}$ are the parameters of the mixture model, $f_k(x_i;\theta_k)$ is the kth component density for observation x_i with parameter vector θ_k, (π_1, ..., π_{G-1}) are the mixing weights or probabilities (such that $\pi_k > 0$, $\sum_{i=1}^{n} \pi_k = 1$), and G is the number of mixture components (Fraley et al., 2002; Fraley et al., 2012; Scrucca et al., 2016). Typically, the parameters Ψ must be estimated because they are unknown. In this Gaussian Mixture Modelling, the Expectation–Maximization (EM) algorithm is used to calculate the maximum likelihood estimation of parameters (Dempster et al., 1977).

For the input data used for clustering in chapter 3, the drought probability distribution characteristics, duration of drought, seasonality of drought, and distance between regions were assembled, as shown in Table 2.4. The mean soil moisture indicates the average state of soil moisture over the entire study period and influences the overall position of the probability distribution curve of soil moisture. The coefficient of variation (CV) represents the ratio of the standard deviation to the average value. It shows the degree of variability of the data relative to the average value, which determines whether the soil moisture probability distribution curve is steep or gentle. Also, the coefficient of skewness (CS) indicates the tail of the probability distribution curve. For example, a positive CS value indicates a probability curve with the right tail, while a negative CS value indicates a probability curve with the left tail. The specific equation for calculating CS is shown below:

$$CS = \frac{\sum_{i=1}^{N} \left(X_i - \bar{X} \right)^3}{\sigma^3 \cdot N} \tag{2.12}$$

Where N is the number of samples, which is the number of months in this study; X is the sample; $\bar{X}$ is the average of samples; σ is the standard deviation.

When discussing the drought duration, the drought event must first be defined. In this dissertation, drought is defined as occurring when the soil moisture of a month is lower than 90% of the other months during the entire study period. On this basis, the average length of the drought period was calculated by counting the number of continuous months of each drought. The number of months between two drought events is considered to be the reoccurring periods of drought.

As for the seasonality of drought, the average soil moisture for spring (March-May), summer (June-August), autumn (September-November), and winter (December-February) was calculated. In order not to disperse homogeneous drought sub-regions, the longitude and latitude of each grid were also used as variables for clustering analysis.

Table 2.4 Variables used in the clustering of homogeneous drought zones in Japan.

Category	Data type
Probability distribution-related variable	Average soil moisture
	Coefficient of variation (CV)
	Coefficient of skewness (CS)
Duration-related variable	Length of drought period
	Reoccurring periods of drought
Seasonality-related variable	Average soil moisture in spring
	Average soil moisture in summer
	Average soil moisture in autumn
	Average soil moisture in winter
Distance-related variable	Latitude
	Longitude

As for chapter 6, the median values of hydro-meteorological elements under each wildfire type were used as input (missing wildfire types were entered as 0). In this case, not only the presence or absence of wildfire types and hydrometeorology-wildfire can be used for clustering the continental United States.

2.3.2 Distinct empirical orthogonal function decomposition for chapters 3~4

The distinct empirical orthogonal function (DEOF) decomposition, proposed by Dommenget (2007), was used to identify homogeneous drought or wildfire zones. The DEOF method decomposes the spatiotemporal matrix into the distinct spatial function component (DEOF) and the temporal function component (distinct principal component, DPC). The DEOF calculation program in this dissertation is written by MATLAB. The detailed calculation process is shown below.

Assuming that a hydro-meteorological element X consists of m spatial points and n temporal points, then X can be expressed as:

$$X = \begin{bmatrix} x_{11} & x_{12} & \cdots & x_{1n} \\ x_{21} & x_{22} & \cdots & x_{2n} \\ \vdots & \vdots & \vdots & \vdots \\ x_{m1} & x_{m2} & \cdots & x_{mn} \end{bmatrix} \tag{2.13}$$

X can be decomposed into $V*T$, where $V=m*r$ is the space function part which does not change with time; $T=r*n$ is the time function part which only depends on time; r is the rank of the matrix X. Through the linear combination of time and space function, different principal components of X can be obtained. The map associated with an EOF represents a pattern that is statistically independent and spatially orthogonal to the others. The eigenvalue indicates the variance accounted for by the pattern (Kim et al., 2011).

The DEOF method, with the addition of an isotropic diffusion process, differs from the classical EOF technique (Lorenz, 1956), reducing the possibility of failing to identify spatial patterns with underlying physical mechanisms due to interference from spatial white noise (Dommenget, 2007). Similar to the EOF decomposition, a larger explained variance of the DPCs implies that more information about the original field is focused on the decomposed patterns.

The leading DEOF pattern is defined as the pattern that maximizes the differences in explained variance Δ_{var}:

$$\Delta var = Var_{obs}(DEOF) - Var_{null}(DEOF) \tag{2.14}$$

Where $Varb_{obs}$ is the variance that the DEOF pattern explains in the observer data, and Var_{null} is the variance that the DEOF pattern explains under the null hypothesis (Dommenget, 2007).

2.3.3 Wavelet analysis for chapters 3~4

Wavelet analysis is an effective tool for identifying teleconnections between hydro-meteorological elements and weather extremes. The calculation program of wavelet analysis is based on the Wavelet Toolbox from MATLAB. Specifically, the coherence between two time series can be calculated by the cross wavelet transform (XWT) (Torrence et al., 1998) and wavelet coherence (WCO) (Torrence et al., 1999). The first step for wavelet analysis is to perform a continuous wavelet transform (CWT) of the data. A wavelet is a zero-mean, frequency- and time-local function. A wavelet can be characterized by how localized it is in time (Δ_t) and frequency (Δ_ω, known as the bandwidth). The Morlet wavelet can be defined as:

$$\psi_0(\eta) = \pi^{-\frac{1}{4}} e^{i\omega_0 \eta} e^{-\frac{1}{2}\eta^2} \tag{2.15}$$

Where ω_0 is the dimensionless frequency and η is dimensionless time. And when $\omega_0=6$ in Morlet wavelet, it is considered to be a good balance of time and frequency localization (Grinsted et al., 2004). This is also the bandwidth used in the subsequent analysis of this dissertation.

After the process of CWT, the time series is stretched in time by varying its scale (s, $s=\ldots$, 4, 8, 16, 32, 64, 128, … , unit: months), and we can get $\eta=s*t$. The CWT of a time series (x_n, $n=1, \ldots, N$, N is the length of the time series) with uniform time steps δ_t (month is the time step for wavelet analysis of this dissertation), is defined as the convolution of x_n with the scaled and normalized wavelet:

$$W_n^X(s) = \sqrt{\frac{\delta t}{s}} \sum_{n'=1}^{N} x_{n'} \psi_0 \left[\frac{(n'-n)\delta t}{s} \right] \tag{2.16}$$

Where the range of *n'* is from *n* to *N*. Then the wavelet power can be defined as $|W_n^X(s)|^2$. The complex argument of $W_n^X(s)$ can be interpreted as the local phase.

Furthermore, the WCO between two time series can be calculated by normalizing and smoothing their XWT:

$$W_n^{XY}(s) = W_n^X(s) W_n^{Y*}(s) \tag{2.17}$$

Where $W_n^X(s)$ and $W_n^Y(s)$ represent the wavelet power spectrum of the time series x_n and y_n with n=1, 2… N, respectively; *s* is the wavelet scale; * denotes its complex conjugate; and *n* is the location of the wavelet in time.

The higher coherence indicates that the two time series are more similar in the time-frequency plane. However, it should be noted that the part outside the cone of influence (COI) should also be interpreted with caution (Torrence et al., 1998). The wavelet coherence coefficient ranges from 0 to 1, and higher values indicate greater coherence (Torrence et al., 1998). In addition, a significance level of $P<0.05$ was used to assess the statistical significance of the results.

To quantitatively compare the strength of the effects of different atmospheric-oceanic indices on drought or wildfire, the percent area of significant coherence (PASC) relative to the wavelet scale-location domain and global wavelet coherence coefficient were adopted (Hu et al., 2016). A large PASC value indicates a greater coherence between atmospheric-oceanic indices and weather extremes. And the global wavelet coherence coefficient (Partal et al., 2006) was defined to evaluate the coherence between two time series at different scales while neglecting the influence of time. The difference between PASC and global wavelet coherence coefficient is that they are used to identify the most significant coherent variable and quantitatively judge the level of coherence, respectively.

2.3.4 L-moment estimators for marginal distribution for chapters 5~7

The univariate distribution parameter estimation approach involves the L-moment theory, which Hosking Hosking (1990) developed based on order statistics. The first four L-moments are defined as:

$$\begin{aligned}\lambda_1 &= \beta_0, \\ \lambda_2 &= 2\beta_1 - \beta_0, \\ \lambda_3 &= 6\beta_2 - 6\beta_1 + \beta_0, \\ \lambda_4 &= 20\beta_3 - 30\beta_2 + 12\beta_1 - \beta_0\end{aligned} \tag{2.18}$$

Where β_i is defined based on probability-weighted moment methods (Greenwood et al., 1979):

$$\beta_i = \int_0^1 x(F)F^i dF \tag{2.19}$$

Where F is the non-exceedance probability, and $x\ (F)$ denotes the inverse or quantile function of x. Then, L-moment ratios are calculated as follows:

$$\begin{aligned}\tau_2 &= \frac{\lambda_2}{\lambda_1}, \\ \tau_3 &= \frac{\lambda_3}{\lambda_2}, \\ \tau_4 &= \frac{\lambda_4}{\lambda_2}\end{aligned} \tag{2.20}$$

Where τ_2, τ_3, and τ_4 are L-coefficients of the variance (L_{Cv}), L-skewness (L_{Cs}), and L-kurtosis (L_{Ck}), respectively (Hosking, 1990).

Through the above L-moment ratios, distribution parameters can be calculated. For more details, please refer to Hosking (Hosking, 1990; Hosking et al., 1997). A total of seven commonly considered marginal distributions was selected, and the specific expressions of these functions are provided in Table 2.5.

Table 2.5 Theoretical probability distributions of the alternative marginal distributions. Note that α, β, and γ are the location, scale, and shape parameters.

Distribution	Abbreviation	Probability density function (PDF) and Parameter estimates
Generalized extreme-value distribution	GEV	PDF: $f(x)=\frac{1}{\beta}\left(1+\gamma\frac{x-\alpha}{\beta}\right)^{-1/\gamma-1}\exp\left[-\left(1+\gamma\frac{x-\alpha}{\beta}\right)^{-1/r}\right]$ Parameter estimates: $\gamma\approx 7.8590c+2.9554c^{2}$ $c=\frac{2}{3+\tau_3}-\frac{\log 2}{\log 3}$ $\beta=\frac{\lambda_2\gamma}{(1-2^{-\gamma})\Gamma(1+\gamma)}$ $\alpha=\lambda_1-\frac{\beta\{1-\Gamma(1+\gamma)\}}{\gamma}$
Gumbel (extreme-value type I) distribution	GUM	PDF: $f(x)=\frac{1}{\beta}\left(1+\frac{x-\alpha}{\beta}\right)^{-2}\exp\left[-\left(1+\frac{x-\alpha}{\beta}\right)^{-1}\right]$ Parameter estimates: GUM is a special type of GEV distribution, and parameter estimates are the same as GEV distribution.
Generalized logistic distribution	GLO	PDF: $f(x)=\frac{\gamma\exp\left(-\frac{x-\alpha}{\beta}\right)}{\beta\left(1+\exp\left(-\frac{x-\alpha}{\beta}\right)\right)^{\gamma+1}}$ Parameter estimates:

Distribution	Abbreviation	Probability density function (PDF) and Parameter estimates
		$\gamma \approx -\tau_3$ $\beta = \frac{\lambda_2 \sin\gamma\pi}{\gamma\pi}$ $\alpha = \lambda_1 - \beta\left(\frac{1}{\gamma} - \frac{\pi}{\sin\gamma\pi}\right)$
Normal distribution	NOR	PDF: $f(x) = \frac{1}{\sqrt{2\pi}\,\beta}\exp\left(-\frac{(x-\alpha)^2}{2\beta^2}\right)$ Parameter estimates: $\alpha = \lambda_1$ $\beta = \pi^{1/2}\lambda_2$
Weibull distribution	WEI	PDF: $f(x) = \frac{\gamma}{\beta}\left(\frac{x-\alpha}{\beta}\right)^{\gamma-1}\exp\left[-\left(\frac{x-\alpha}{\beta}\right)^{\gamma}\right],\ x \geqslant 0$ Parameter estimates: WEI is a special type of GEV distribution, and parameter estimates are the same as GEV distribution.
Pearson type III distribution	P-III	PDF: $f(x) = \frac{1}{\beta\gamma\Gamma(\gamma)}(x-\alpha)^{\gamma-1}\exp\left(-\frac{x-\alpha}{\beta}\right)$ Parameter estimates:

Distribution	Abbreviation	Probability density function (PDF) and Parameter estimates
		$k \approx \begin{cases} \dfrac{1+0.2906z}{z+0.1882z^2+0.0442z^3}, & 0<\lvert\tau_3\rvert<\dfrac{1}{3},\ z=3\pi\tau_3^2 \\ \dfrac{0.36067z-0.59567z^2+0.25361z^3}{1-2.78861z+2.56096z^2-0.77045z^3}, & \dfrac{1}{3}\leqslant\lvert\tau_3\rvert<1,\ z=1-\lvert\tau_3\rvert \end{cases}$ $\gamma=2k^{-1/2}\mathrm{sign}(\tau_3)$ $\beta=\dfrac{\lambda_2\pi^{1/2}k^{1/2}\Gamma(k)}{\Gamma\left(k+\frac{1}{2}\right)}$ $\alpha=\lambda_1$
Exponential distribution	EXP	PDF: $f(x)=\begin{cases} \dfrac{x-\alpha}{\beta}\exp\left(-\dfrac{x-\alpha}{\beta}\right), & x\geqslant 0 \\ 0, & x<0 \end{cases}$ Parameter estimates: EXP is a special type of P-III distribution, and parameter estimates are the same as the P-III distribution.

The probability plot correlation coefficient (PPCC) and root mean square error (RMSE) are utilized for the goodness of fit. The specific calculation functions are expressed in Equations 2.18 and 2.19, respectively. The RMSE is one of the most widely employed indicators representing the goodness of fit (Yang et al., 2018). Moreover, the PPCC evaluates how well the simulated L-skewness and L-kurtosis of a fitted distribution match the average regional L-skewness and L-kurtosis values obtained from observation data. The PPCC statistic achieves a maximum value of 1. The PPCC has been verified as a powerful index to evaluate the goodness-of-fit of a wide range of alternative distribution hypotheses (Stedinger, 1993) and to perform hypothesis tests of various two-parameter distribution alternatives.

$$RMSE=\sqrt{\frac{\sum_{i=1}^{n}(P_e-P_t)^2}{n}} \tag{2.21}$$

Where P_e and P_t are empirical cumulative probability and theoretical cumulative probability, respectively.

$$PPCC = \frac{\sum_{i=1}^{n}\left(X_i - \bar{X}\right)\left(M_i - \bar{M}\right)}{\sqrt{\sum_{i=1}^{n}\left(X_i - \bar{X}\right)^2\left(M_i - \bar{M}\right)^2}} \tag{2.22}$$

Where X_i and M_i are the ordered observations and the order statistic medians, respectively; $\bar{X}$ and $\bar{M}$ are the average value of observations and statistic medians, respectively (Filliben, 1975).

2.3.5 Bayesian analysis and Markov Chain Monte Carlo algorithm for bivariate joint distribution for chapters 5~7

The joint frequency analysis method used in this study is based on Multivariate Copula Analysis Toolbox (MvCAT) in MATLAB (Sadegh et al., 2017). This approach for estimating the parameters of the univariate distribution includes Bayesian analysis and the Markov Chain Monte Carlo (MCMC) algorithm. In particular, Bayes' law conveniently attributes all modeling uncertainties to the parameters and estimates the posterior distribution of model parameters as follows:

$$p\left(\theta \middle| \tilde{Y}\right) = \frac{p(\theta)\, p\left(\tilde{Y} | \theta\right)}{p\left(\tilde{Y}\right)} \tag{2.23}$$

Where $P(\theta)$ and $P\left(\theta \middle| \tilde{Y}\right)$ denote the prior and posterior distributions, respectively, of the parameters. The prior distribution is a constant value in modeling practice based on the evidence. It can be omitted from analysis if the main goal is to estimate the posterior distribution of the parameters, and the posterior distribution of the parameters can be estimated as:

$$P\left(\theta \middle| \tilde{Y}\right) \propto P(\theta)\, P\left(\tilde{Y} | \theta\right) \tag{2.24}$$

Bayes' equation is usually difficult to solve analytically, and a numerical method, the MCMC algorithm, is adopted to sample the posterior distribution. MCMC algorithms comprise a class of statistical methods to sample high-dimensional complex distributions (Andrieu et al., 2008). The equilibrium state of the MCMC algorithm, if the transition kernel warrants ergodicity, represents the target distribution.

The RMSE, Akaike information criterion (AIC), and Bayesian information criterion (BIC) are employed in terms of the goodness of fit. The AIC considers both the model complexity and minimization of error residuals and provides a more robust measure of the quality of model predictions. Furthermore, the AIC avoids the problem of over-conditioning by adding a penalty term based on the number of parameters. The AIC is formulated as (Aho et al., 2014; Akaike, 1974):

$$AIC = 2D - 2l \tag{2.25}$$

Where D is the number of parameters of the statistical model, and *l* is the log-likelihood value of the best parameter set.

Similar to the AIC, the BIC is expressed as (Schwarz, 1978):

$$BIC = D \ln n - 2l \tag{2.26}$$

A total of 8 commonly considered joint distributions were selected, and the expressions of the specific functions are listed in Table 2.6.

Table 2.6 Theoretical probability distributions of the alternative joint distributions. The Φ denotes the standard Gaussian distribution. The θ is the joint distribution of the parameter.

Distribution	Abbreviation	Probability density function (PDF)
Gaussian copula	GAU	$\int_{-\infty}^{\Phi^{-1}(u)} \int_{-\infty}^{\Phi^{-1}(v)} \frac{1}{2\pi\sqrt{1-\theta^2}} \exp\left(\frac{2\theta xy - x^2 - y^2}{2(1-\theta^2)}\right) dxdy$

Distribution	Abbreviation	Probability density function (PDF)
Clayton copula	CLA	$\max\left(u^{-\theta}+v^{-\theta}-1,0\right)^{-1/\theta}$
Frank copula	FRA	$-\frac{1}{\theta}\ln\left(1+\frac{(\exp(-\theta u)-1)\,(e\exp(-\theta v)-1)}{(\exp(-\theta)-1)}\right)$
Gumbel copula	GUM	$\exp\left\{-\left[(-\ln(u))^{\theta}+(-\ln(v))^{\theta}\right]^{1/\theta}\right\}$
Independence copula	IND	uv
Ali-Mikhail-Haq copula	AMH	$\frac{uv}{1-\theta(1-u)\,(1-v)}$

2.3.6 Trend-free Prewhitening Mann-Kendall test for chapter 3 and chapters 5~6

The trend analysis method used in this study is the Trend-free Prewhitening Mann-Kendall (TFPW-MK) test, which was based on the Mann-Kendall (MK) test proposed by Mann (1945) and modified by Kendall (1948). Hydro-meteorological time series often exhibit serial correlation, increasing the probability of detecting a significant trend with the MK test, thus changing the magnitude of the estimated serial correlation (Yue et al., 2002). Therefore, the TFPW-MK test was recommended to efficiently eliminate the effect of serial correlation (Yue et al., 2002). The steps for the specific TFPW-MK test are shown as follows:

Step 1. Using the Theil-Sen method, the slope (b) of the time series trend is estimated. If the slope is almost equal to zero, then there is no need to continue with the trend analysis. If the slope is different from zero, then the time series is detrended using the following equation:

$$X_t^{'}=X_t-T_t=X_t-bt \tag{2.27}$$

Step 2. The lag-k serial correlation coefficient r_k of detrended series X_t' is computed with equation 2.24, and the auto-regression model (k) is then removed from X_t' according to the following equation:

$$r_k = \frac{\frac{1}{n-k}\sum_{(t=1)}^{(n-k)}[X_t - E(X_t)][X_{(t+k)} - E(X_t)]}{\frac{1}{n}\sum_{(t=1)}^{n}[X_t - E(X_t)]^2} \tag{2.28}$$

$$Y'_t = X'_t - r_1 X'_{(t-1)} \tag{2.29}$$

This prewhitening procedure after series detrending is referred to as the TFPW procedure. After applying the TFPW procedure, the resultant time series should be independent.

Step 3. The identified trend T_t and residual Y_t' are blended with the following equation:

$$Y_t = Y_t' + T_t \tag{2.30}$$

Step 4. The MK test is applied to the blended series to assess the significance of the trend. The statistic Z value can be obtained through the TFPW-MK test, thereby measuring the degree to which a given trend consistently decreases or increases (Table 2.7) (Wang et al., 2015).

Table 2.7 Trend categories according to the Z value

Categories	Z value
Significant increasing trend	[1.96, +∞)
Weak increasing trend	[1.64, 1.96)
No significant increasing trend	[0, 1.64)
No significant decreasing trend	(-1.64, 0)
Weak decreasing trend	(-1.96, -1.64]
Significant decreasing trend	(-∞, -1.96]

2.3.7 Wildfire priority index and return period for chapters 5~7

The direct application of bivariate probability distributions in wildfire frequency analysis can neglect single mega-wildfire events and numerous wildfire events with a normal-sized burned area. Accordingly, the weighted average method was adopted to determine the wildfire priority (WP) probability to balance bivariate and univariate probability. The return period can be calculated as the inverse of the probability. The specific equation for WP is as follows:

$$\begin{gathered} P_{WP} = \alpha P_{F(x,y)}(x_i \geqslant X, y_i \geqslant Y) + \beta P_{F(x)}(x_i \geqslant X) + \gamma P_{F(y)}(y_i \geqslant Y) \\ \alpha + \beta + \gamma = 1 \end{gathered} \tag{2.31}$$

Where *α, β,* and *γ* are weighting coefficients. To ensure sufficient weighting at the joint extremes, *α* is set to 1*α* to 1/3. Then we use the traversal algorithm to select the optimal *β* and *γ*. *β* is set to C*2/3, and *γ* is (1-C)*2/3. C is discrete from 0 to 1 in steps of 0.01. This study requires WP probability to perform better than bivariate joint probability in the case of super frequent wildfires and mega-wildfires. Therefore, the objective function (OF) is set to the sum of the proportion of WP probability that is better than the joint probability (when the probability of LBA is greater than 0.95 and when the probability of LFA is greater than 0.95). The specific objective equation is as follows:

$$\begin{gathered} OF1 = \frac{number\ of\ [P_{WP} - P_{F(x,y)}(x_i \geqslant X, y_i \geqslant Y)] > 0\ \ when\ P_{F(x)}(x_i \geqslant X) \geqslant 0.95}{number\ of\ P_{F(x)}(x_i \geqslant X) \geqslant 0.95} \\ OF2 = \frac{number\ of\ [P_{WP} - P_{F(x,y)}(x_i \geqslant X, y_i \geqslant Y)] > 0\ \ when\ P_{F(y)}(y_i \geqslant Y) \geqslant 0.95}{number\ of\ P_{F(y)}(y_i \geqslant Y) \geqslant 0.95} \\ OF = OF1 + OF2 \end{gathered} \tag{2.32}$$

2.3.8 Pearson correlation coefficient for chapter 7

The Pearson correlation coefficient was used to detect the correlation between hydro-meteorological elements and wildfire bivariate characteristics. The Pearson method assesses the correlation coefficient of two conditioning factors. The correlation value is calculated by their covariance divided by the product of their standard deviations, as follows:

$$r_{XY} = \sum_{i=1}^{n} \frac{X_i - \bar{X}}{\sqrt{\sum_{k=1}^{n} \left(X_i - \bar{X}\right)^2}} * \frac{Y_i - \bar{Y}}{\sqrt{\sum_{k=1}^{n} (Y_i - Y)^2}} \tag{2.33}$$

Where *X* and *Y* are two time series, and the $\bar{X}$ and $\bar{Y}$ are the average value of the time series.

Pearson correlations are represented in square tables called correlation matrices, which compute Pearson correlations for each column pair of a set of variables. Each matrix value represents the calculated correlation of the corresponding row and column variables (Tehrany et al., 2019).

2.3.9 Artificial Neural Networks for chapter 7

As for Artificial Neural Networks (ANNs). In particular, the BPNN model consists of three layers (Figure 2.4): the input layer, the hidden layer, and the output layer. BPNN has all the features and unique advantages of ANNs, and BPNN is a popular choice in the field of hydrology to deal with a variety of complex physical processes. Therefore, this study selects BPNN as the model to simulate the wildfire bivariate characteristics.

Specifically, in the study, the training function of BPNN is the Levenberg-Marquardt algorithm (Moré, 1978). The Levenberg-Marquardt algorithm can train the BPNN several times faster than the traditional algorithm, an iterative algorithm for locating the minimum of a function expressed as a sum of squares of nonlinear functions. Furthermore, the Levenberg-Marquardt algorithm obtains the smallest error associated with the weights through the damped least-squares Method (Duncan, 2014). Compared with other algorithms, the disadvantage of this algorithm is that it needs to occupy more memory during calculation. But it is widely recognized for its extremely fast training speed and for outperforming simple gradient and conjugate descent methods (Tabbussum et al., 2020). The performance equations are mean squared error (MSE) and coefficient of determination (R^2), as follows:

$$MSE = \frac{1}{n}\sum_{i=1}^{n}\left(Y_i - \hat{Y}_i\right)^2 \tag{2.34}$$

$$R^2 = \frac{\frac{1}{n}\sum_{i=1}^{n}\left(\hat{Y}_i - \overline{Y}\right)^2}{\frac{1}{n}\sum_{i=1}^{n}\left(Y_i - \overline{Y}\right)^2} \tag{2.35}$$

Where n is the sample length, Y is the observed value, $\overline{Y}$ is the mean of the observed data, and $\hat{Y}$ is the simulated value.

As for the input data, the data were randomly divided into the training group (75%), validation group (15%), and test group (15%) in this study. The training group is used to find an optimal set of parameters in a given hypothesis space. The purpose of the validation group is to find the optimal hyperparameters. The optimal set of hyper-parameters can be obtained by comparing the effects of the models trained with each set of hyper-parameters through the validation group. The test group is used to evaluate the final generalization ability of the model. In addition, the BPNN model will be trained fifty times, and the final simulation results will be taken as the average time series of the fifty simulations.

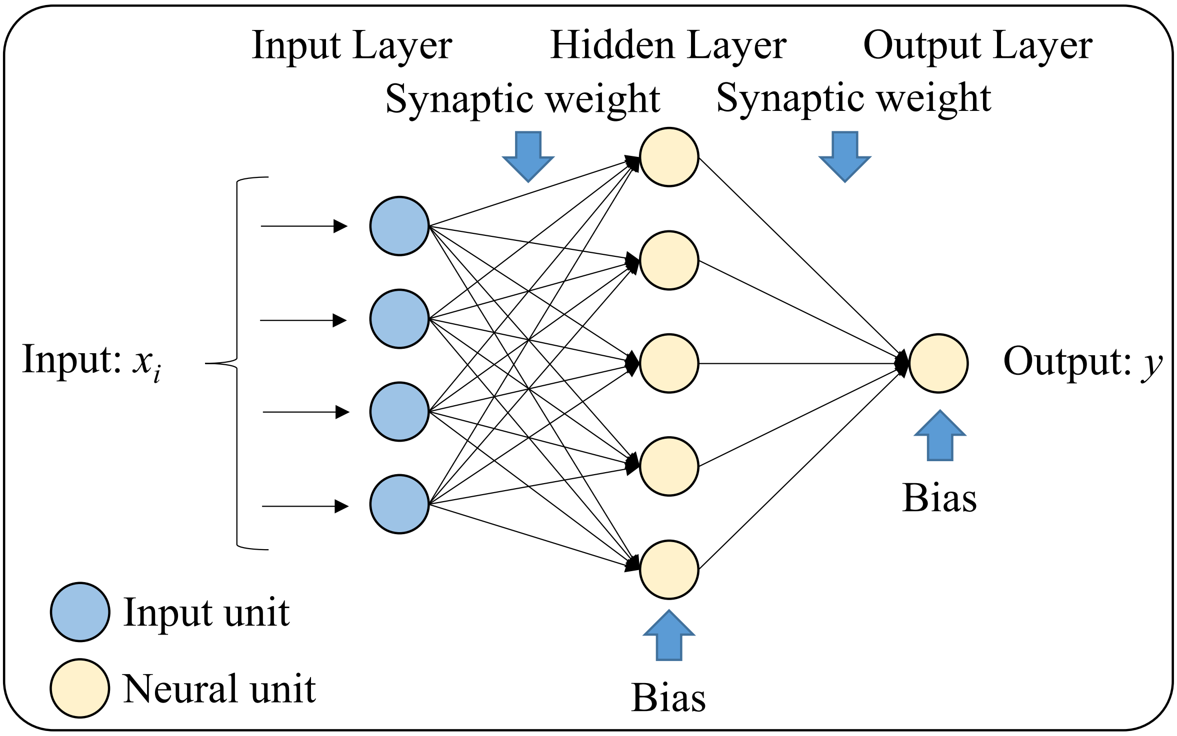

Figure 2.5 Structure of back-propagation neural network.

Chapter 3 Quantifying the Contributions of Atmospheric-Oceanic Indices on Homogenous Zones Illustrated by the Example of Japan

This chapter was published in the Journal of Applied Meteorology and Climatology in January 2022: Ke Shi, Yoshiya Touge, and So Kazama. "Defining Homogeneous Drought Zones Based on Soil Moisture across Japan and Teleconnections with Large-Scale Climate Signals." Journal of Applied Meteorology and Climatology 61.1 (2022b): 43-60.

3.1 Introduction

Drought is one of the most complex and insurmountable weather extremes (Dai, 2011; Hagman et al., 1984; Kogan et al., 2016). Compared to other weather extremes, severe droughts are more widespread and can last for a year or even several years (Asong et al., 2018). As an illustration, in 1934, an extreme drought swept through nearly the entire western North America, severely impacting agriculture and water resources (Cook et al., 2014). Southeastern Australia experienced one of the worst droughts observed in the world from 2001 to 2003 due to several years of lack of rainfall and record-high temperatures that almost completely dried up surface water resources (Leblanc et al., 2009). Strikingly, droughts and their impacts vary by region, with varying intensity, duration, and seasonality (Edwards et al., 2019; Herrera-Estrada et al., 2017; Mishra et al., 2010; Wilhite et al., 2007). Droughts in South America and Asia tend to spread more rapidly, while those in Africa and Australia spread relatively slowly (Herrera-Estrada et al., 2017). These spatial and temporal characteristics and the multiple causes of drought lead to heterogeneity of droughts in different climatic zones and even in the same geographical location. And whether the consequences of drought, such as wildfire, are also heterogeneous across regions has not been explored.

This chapter explores the causes and effects of homogeneous drought zones, using Japan as the target region, where heterogeneity of drought is evident. Mountains cover 70% of Japan, and the rapid flow of rain to the sea after it falls has led to unique drought characteristics in

Japan (Lee et al., 2012a). Historically, most of Japan has experienced varying droughts, such as in 1967, 1973, 1978, 1984, 1985, and 1994 (Okada, 2016). The 1994 drought was considered the worst in Japan, with almost the entire country experiencing exceptional drought (Lee et al., 2012a). In addition, anthropogenic climate change has increased the uncertainty in the spatial and temporal characteristics of drought in Japan, which poses additional challenges in defining homogeneous drought zones and analyzing the relationship between drought and wildfire.

Previous studies exploring the impact of atmospheric-oceanic indices on drought found a strong relationship between El Niño-Southern Oscillation (ENSO) and drought in the East African rainy season, quantified by correlation coefficients (Park et al., 2020). More than half of the multi-year drought frequency in the United States was caused by the Pacific Decadal Oscillation (PDO) and the Atlantic Multidecadal Oscillation (AMO) (McCabe et al., 2004). Based on the principal component analysis, the established relationship between North Atlantic Oscillation (NAO) phases and drought indices was also found suitable for predicting widespread drought in the Mediterranean basin (Vicente-Serrano et al., 2010). However, previous studies on the impacts of atmospheric-oceanic indices on drought have only focused on analyzing relationships at specific grid points or remote links between atmospheric-oceanic indices and principal components across the region, ignoring the possible heterogeneity of the same region. In other words, they do not fill the gap in exploring homogeneous drought zones and climate impacts, nor do they discuss the impact of drought (such as wildfire).

Meanwhile, similar studies on drought or wildfire have never been conducted in Japan. For other hydro-meteorological elements, the relationship between precipitation in western Japan and NAO has been shown to be significant (Aizen et al., 2001). Furthermore, the occurrence of ENSO can strengthen the link between the South Asian summer monsoon and East Asian summer precipitation, as highlighted in previous studies (Hu et al., 2005). In addition, it has been suggested that a positive winter AO may lead to a warmer winter in East Asia (He et al., 2017). Overall, the hydro-meteorological characteristic in Japan has been confirmed to be affected by these large-scale climate signals. However, considering the heterogeneity of Japan, gridpoint-specific relationship analysis is limited by the resolution of the data, and the teleconnections between large-scale climate signals and principal components of the entire region cannot distinguish the exact climatic causes between different homogeneous zones in the same geographical location.

When analyzing homogeneous drought zones, drought characteristics and other factors (such as the distance between meshes) should be considered because two homogeneous drought zones far apart are not conducive to uniform drought risk reduction. Therefore, variables related to probability distributions, drought duration and seasonality, and distances between regions are considered in this chapter. In fact, the homogeneous hydro-meteorological elements zones have attracted the attention of researchers in recent years. By identifying the latent spatial structure of seasonal variation and magnitude of precipitation, four uniform precipitation bands were obtained in Nepal, corresponding to four independent precipitation types (Kansakar et al., 2004). Classifying homogeneous wildfire zones based on unique biophysical and anthropogenic attributes affecting California wildfires was also explored (Syphard et al., 2020). Similar studies on identifying homogeneous regions emerge in an endless stream, including homogeneous aerosol zones (Omar et al., 2005). Such analyses can better identify regional features and establish teleconnections to atmospheric-oceanic indices. However, this definition of a homogeneous hydro-meteorological elements zones has not been applied to the analysis of the spatiotemporal characteristics and climatic causes of drought

Therefore, this study first attempts to provide a way to define homogeneous drought zones in Japan by dividing the regional space into natural clusters, and then discusses the causes of drought and its effects. This approach highlights the characteristics of homogeneous drought zones and produces clusters that consider the linkages between different homogeneous regions. Droughts can be significantly heterogeneous due to various factors and thus may be dominated by different atmospheric-oceanic indices even within the same geographic location. This approach could also improve drought predictions by accounting for the effects of large-scale climate signals. However, when comparing the homogeneous drought zones with the wildfire statistics, it can be found that only considering the drought still cannot fully explain the wildfire characteristics.

3.2 Results

3.2.1 Soil moisture validation

A total of 662 days of soil moisture data were collected in Kawasaki town of Japan (140.6° E, 38.2° N) from March 11, 2019, to December 31, 2020, to validate soil moisture simulation results. A time domain reflectometry (TDR) moisture sensor recorded the observed soil moisture hourly. Since high-resolution data from DSJRA-55 was unavailable after 2012, meteorological forcing data with a resolution of 0.25° were extracted from the ERA5 reanalysis dataset for validation (Hersbach et al., 2020). The other data, including land use and land type, soil parameters, and vegetation parameters, are the same as the original simulation data.

In addition, to accommodate the observational data, the soil moisture saturation ratio of the model simulation results was converted to volume-based soil moisture. The specific results are shown in Figure 3.1. The simulation results are highly consistent with the observed data. Especially SiBUC model can simulate the changing process of soil moisture after precipitation. This validation process of soil moisture can ensure subsequent analysis of the identification of homogeneous drought zones.

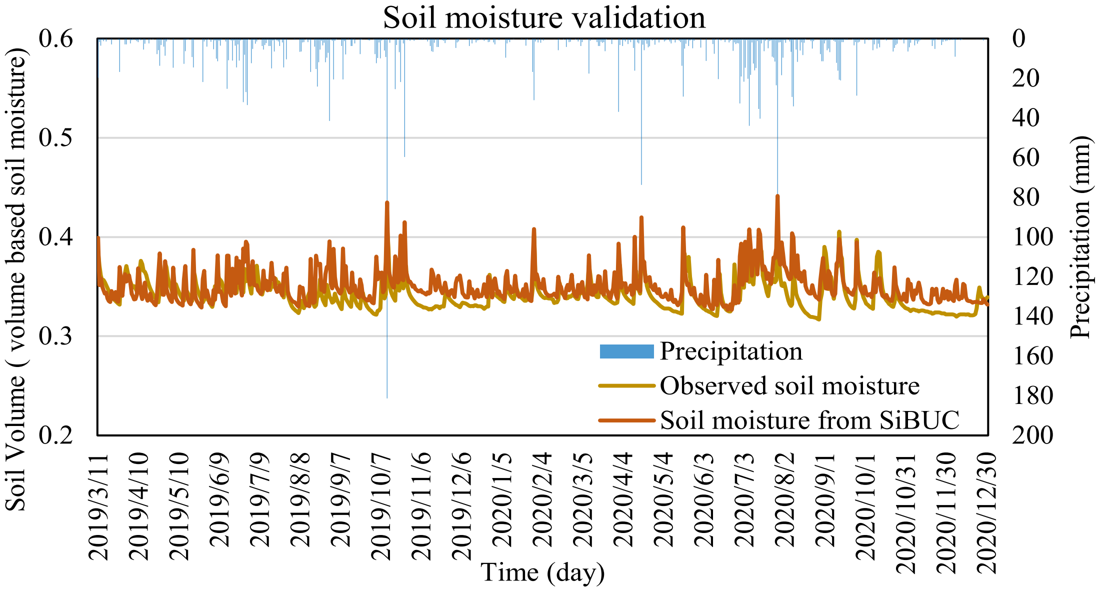

Figure 3.1 Comparison of model simulation soil moisture and observed soil moisture at Kawasaki Town (140.6° E, 38.2° N) during 2019/3/11-2020/12/31

3.2.2 Identifying homogeneous drought zones

Nine homogeneous drought zones with different characteristics were identified in Japan based on Gaussian Mixture Modelling for Model-Based Clustering, as shown in Figure 3.2. The specific characteristics of the nine homogeneous drought zones identified by clustering are shown in Table 3.1. This partitioning suggests significant heterogeneity across Japan. For example, Hokkaido, located at the northernmost tip of Japan, was dominated by zones-4 and -9, with a small part of zones-1 and -3. Furthermore, even though the topography was not considered in the clustering in this chapter, the Ou Mountains divide the Tohoku region into two main heterogeneous parts (zones-3 and -5). In particular, the Kanto Plain was the region with the most obvious drought heterogeneity, including four sub-zones: zones-1, -5, -6, and -7. Zone-8 was a homogeneous drought zone dominated by high mountains, spanning the Chubu, Kinki, Shikoku, and Kyushu regions of Japan. Zones-6 and -7 were located near the coastline or at the foot of mountains, where precipitation flows into the ocean. Zone-2 mainly dominated Chugoku and Kyushu. The appearance of zone-1 over a wide area from Hokkaido to Shikoku suggests that this zone may represent a unique drought situation with a high coefficient of variation, long drought recurrences, and long dry periods that can break through distance constraints.

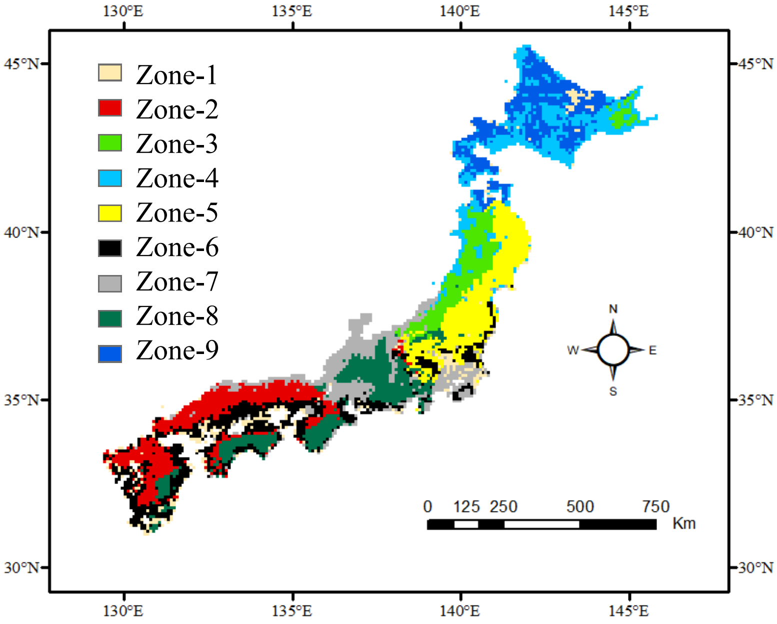

Figure 3.2 Spatial distribution of homogeneous drought zones across Japan.

Table 3.1 Characteristics of the nine homogeneous drought zones identified by clustering. The recorded data are the median, minimum, and maximum values of each drought characteristic (parentheses).

Characteristic	Zone-1	Zone-2	Zone-3	Zone-4	Zone-5	Zone-6	Zone-7	Zone-8	Zone-9
Average soil moisture, %	69.1 (19.8~86.7)	66.9 (57.8~81.2)	70.9 (67.6~76.0)	72.3 (60.7~89.3)	67.2 (54.5~78.3)	63.0 (39.8~78.4)	71.0 (60.7~89.8)	70.5 (62.8~75.3)	67.7 (49.3~80.1)
Coefficient of variation (CV)	0.12 (0~0.59)	0.09 (0~0.17)	0.07 (0.02~0.11)	0.06 (0.01~0.11)	0.09 (0.02~0.26)	0.14 (0.05~0.35)	0.06 (0~0.14)	0.04 (0.02~0.09)	0.11 (0.01~0.29)
Coefficient of skewness (CS)	-1.1 (-1.5~1.7)	-1.9 (-5.0~-0.2)	-1.8 (-3.4~-0.5)	-1.5 (-3.5~0.9)	-1.6 (-3.1~-0.4)	-1.2 (-3.1~1.2)	-2.2 (-7.9~0.6)	-0.9 (-2.2~1.1)	-1.9 (-3.3~-0.3)
Reoccurring periods of drought, months	19.3 (10.2~49.8)	17.3 (11.9~25.4)	19.3 (13.9~24.4)	19.8 (13.2~30.3)	18.8 (14.2~27)	17.1 (11.5~24.8)	16.3 (12.3~27.8)	15.6 (11.5~23)	21.8 (11.6~31.8)
Length of drought period, months	2.2 (1.1~6.3)	2.0 (1.2~3.2)	1.8 (1.2~2.5)	2.0 (1.2~3.1)	1.9 (1.2~3.6)	1.9 (1.1~3.3)	1.7 (1~3.3)	1.6 (1~2.6)	2.3 (1.2~4)
Average soil moisture in spring, %	69.5 (19.5~87.5)	65.0 (54.4~81.9)	68.9 (64.8~76.2)	71.3 (56.6~89.1)	63.5 (47.4~78.3)	60.9 (35.1~79.1)	70.1 (58.5~89.9)	69.8 (62.8~73.9)	67.0 (46.7~80.5)
Average soil moisture in summer, %	69.7 (17.0~86.0)	66.9 (56.6~82.1)	67.8 (61.8~74.3)	69.6 (56.8~88.5)	65.4 (44.9~77.3)	65.4 (43.5~82.6)	69.8 (55.5~85.8)	71.4 (63.4~77.5)	62.3 (39.8~79.6)

Characteristic	Zone-1	Zone-2	Zone-3	Zone-4	Zone-5	Zone-6	Zone-7	Zone-8	Zone-9
Average soil moisture in autumn, %	68.9 (18.9~85.6)	67.2 (57.8~80.1)	73.1 (70.3~77.3)	74.4 (62.1~90.2)	70.0 (59.3~80.5)	63.8 (41.1~80.4)	71.8 (59.9~90.3)	71.9 (63.7~76.4)	61.6 (54.3~80.3)
Average soil moisture in winter, %	45.8 (5.8~80.5)	45.9 (17.9~75.6)	70.4 (62.8~76.7)	69.8 (51.5~88.7)	57.2 (26.3~77.0)	32.5 (14.6~52.4)	66.5 (38.6~92.1)	61.6 (33.9~73.4)	55.6 (24.4~77.0)

3.2.3 Probability distribution-related variable of drought in homogeneous drought zones

The shape of the probability distribution curve of the soil moisture time series is determined by the coefficient of variation (CV), coefficient of skewness (CS), and average value. The average value of these three parameters in each grid in Japan from 1958 to 2012 is shown in Figure 3.3. High CV values are concentrated in the vicinity of the Seto Inland Sea and the northern side of the Kitami Mountains in Hokkaido, suggesting that the soil moisture in these areas varies greatly from month to month. These areas with high CV values belong to zones-1 and -6, respectively. Higher positive CS values occurred in zones-1, -6, and -8, indicating that more than half of the monthly soil moisture was below the long-term average. Zone-7 had the long left tail (small negative CS) in the probability distribution curve. Zone-7 also had the opposite drought characteristics to zones-1, -6, and -8, indicating that wetness was the norm and dryness was the norm in these two types of zones, respectively.

The probability distribution curves of monthly soil moisture and specific parameters for several representative homogeneous drought zone samples are shown in Figure 3.4 and Table 3.2. Differences in the average value will result in clear distinctions between zone-8 with zone-1 and zone-8 with zone-6, even though their curves were all right-skewed. In zone-6, the soil moisture changed greatly, which led to its high CV value. In addition, from the example of the probability distribution curve of zone-7, it can be directly seen that this zone belongs to the humid region of Japan.

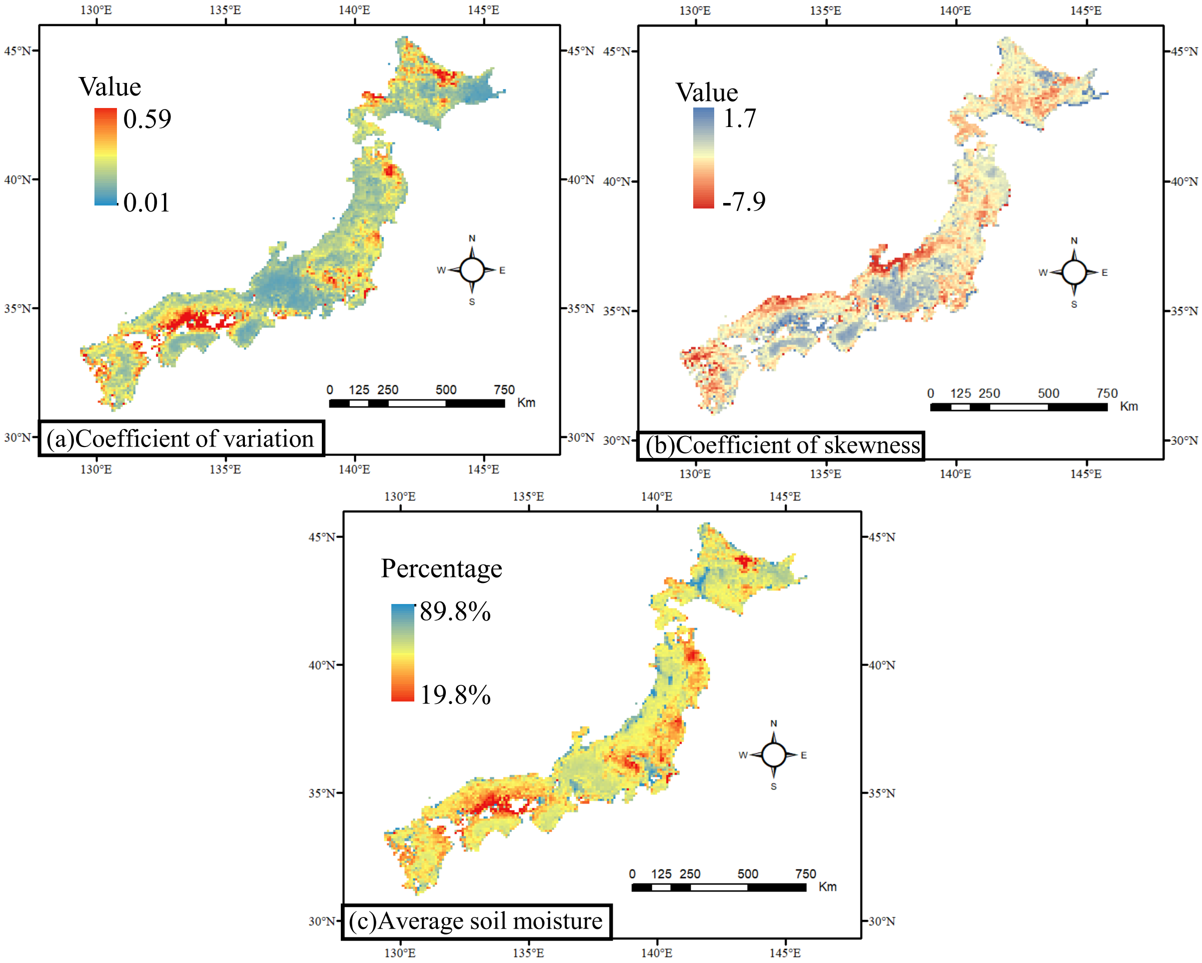

Figure 3.3 The spatial distribution of the average probability distribution parameter values in each mesh across Japan from 1958 to 2012. (a) Coefficient of variation; (b) Coefficient of skewness; (c) Average soil moisture.

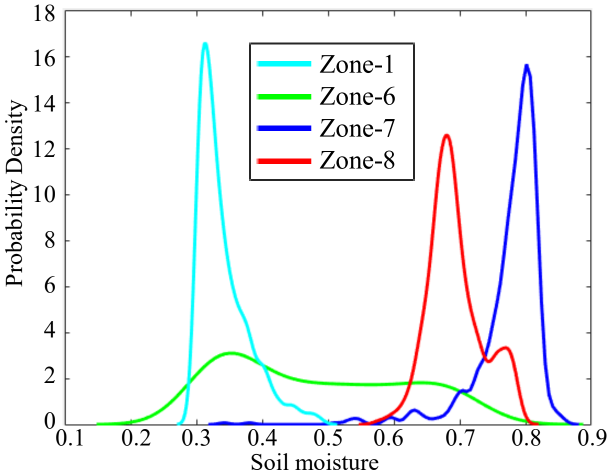

Figure 3.4 Examples of probability distribution curves in zone-1 (cyan), zone-6 (green), zone-7 (blue), and zone-8 (red).

Table 3.2 Examples of probability distribution parameter values in zone-1, zone-6, zone-7, and zone-8.

	Coefficient of variation (CV)	Coefficient of skewness (CS)	Average soil moisture (%)
Zone-1	0.18	1.0	34.0%
Zone-6	0.28	0.3	47.9%
Zone-7	0.07	-3.2	77.6%
Zone-8	0.06	0.4	69.3%

3.2.4 Duration and seasonality of drought in homogeneous drought zones

The spatial distribution of drought duration in each grid in Japan over the period 1958 to 2012 is presented in Figure 3.5. The long duration of the drought and the large reoccurring period were the distinguishing features of the northwestern Kanto Plain (identified as zone-1), an area known for being affected by the foehn wind (Nishi et al., 2019). And the relationship between drought characteristics is shown in Figure 3.6. In chronically wet or dry regions, drought duration and the reoccurring period were strongly limited. Regions frequently affected by extreme events, such as persistent lack of precipitation or extreme heat events, are vulnerable to prolonged extreme drought. But after soil moisture has dropped to insufficient levels due to extreme events, it often takes a long time to return to its normal level. For example, the soil moisture time series for representative zones-1 and -8 are shown in Figure 3.7. These two different types of time series showed that more extreme droughts were accompanied by longer durations of droughts, with longer reoccurrences. Unlike the severe drought in zone-1, the zone -8 example experienced more frequent but weaker drought events.

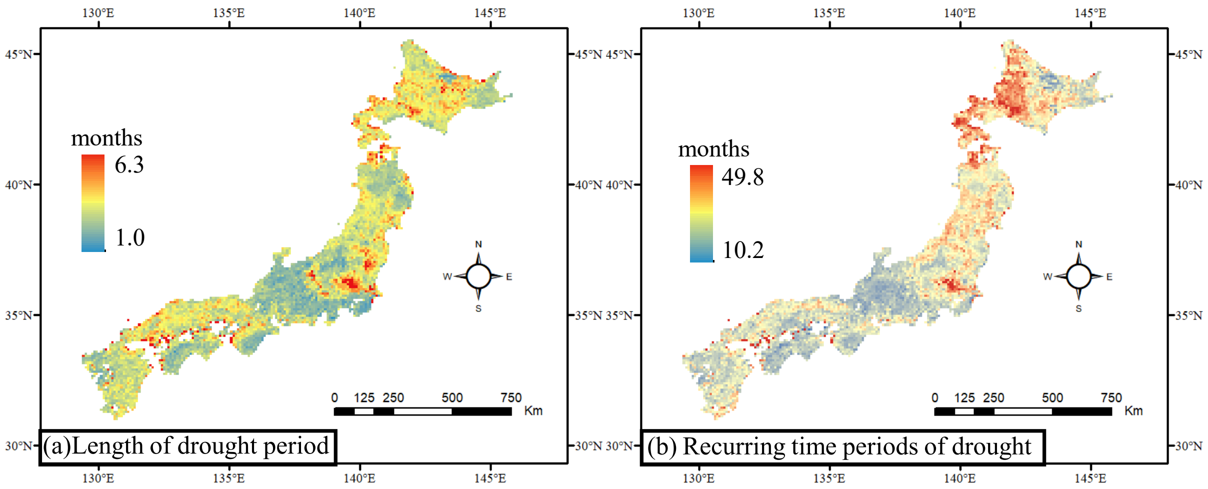

Figure 3.5 The spatial distribution of the drought duration in each mesh across Japan from 1958 to 2012. (a) Length of drought period; (b) Reoccurring periods of drought.

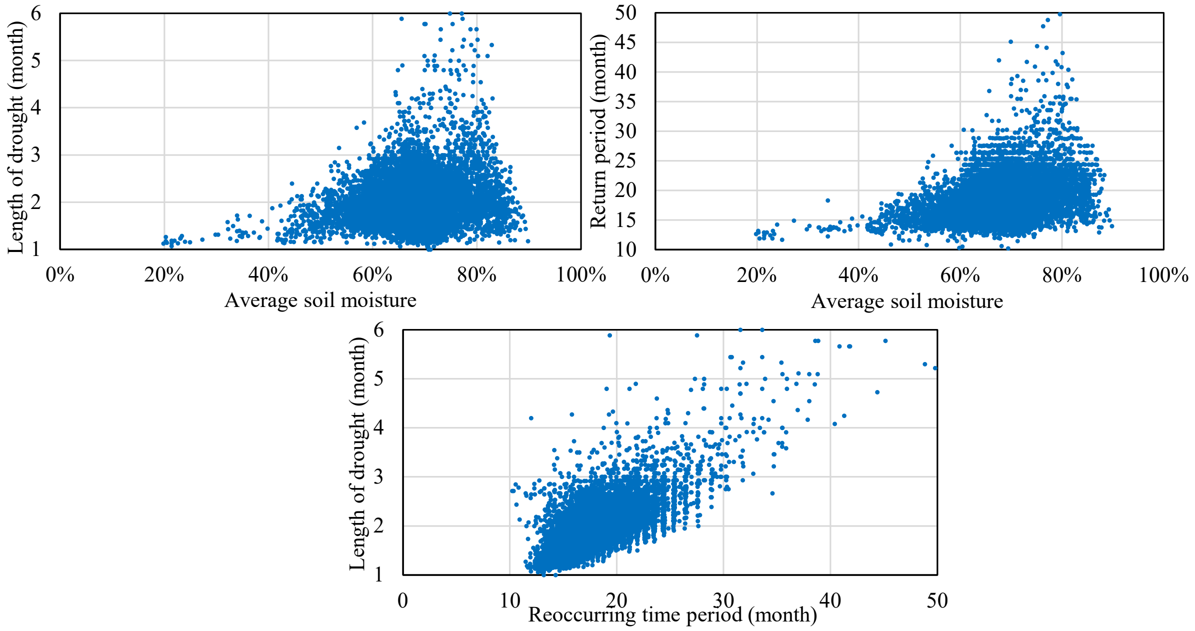

Figure 3.6 Scatter plots between the length of drought, reoccurring periods of drought, and average soil moisture across Japan from 1958 to 2012.

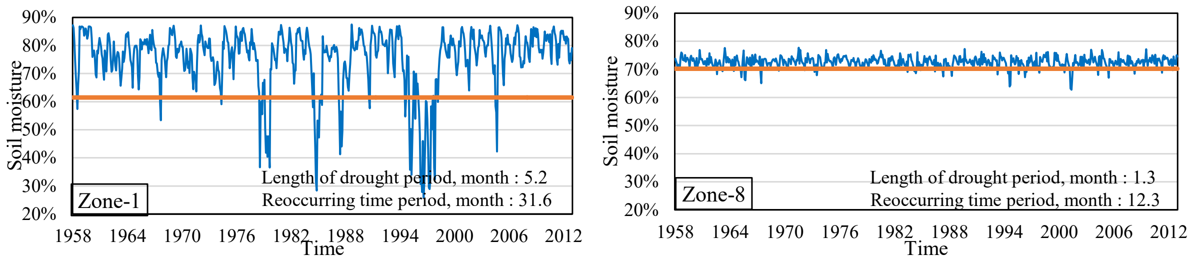

Figure 3.7 Examples of soil moisture time series in zone-1 and -8. The red line indicates the drought threshold, and values below the threshold indicate drought occurrence.

For seasonality, the average soil moisture for each season is shown in Figure 3.8. Notably, soil moisture in zones-1 (around the Seto Inland Sea) and -6 (on the north side of the Kitami Mountains in Hokkaido) was lower than in the rest of Japan in all seasons. While the northwestern Kanto Plain showed low soil moisture only in spring. Figure 3.9 shows the number of drought months in different seasons. And strong spatial homogeneity was found in drought seasonality. Spring drought mainly occurs in central and southern Japan, and summer drought mainly occurs in northern Japan. The spring drought was mainly distributed in zones-2, -5, -6, and 8, and the summer drought was mainly distributed in zones-3, -4, and -9. Zones-1, -6, and -8 were mainly occupied by autumn and winter droughts.

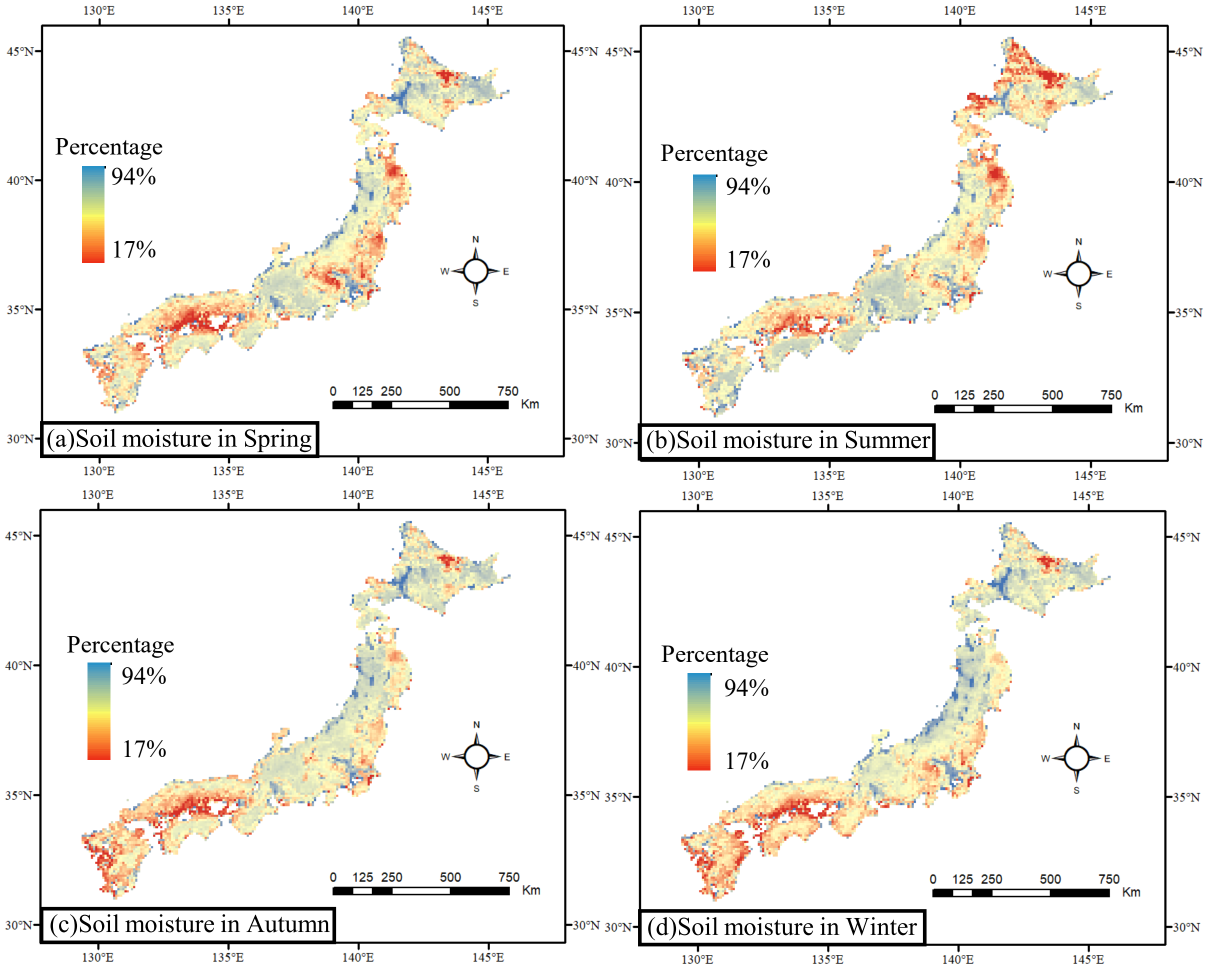
(a)Soil moisture in Spring

(b)Soil moisture in Summer

(c)Soil moisture in Autumn

(d)Soil moisture in Winter

Figure 3.8 Average soil moisture in different seasons across Japan from 1958 to 2012.

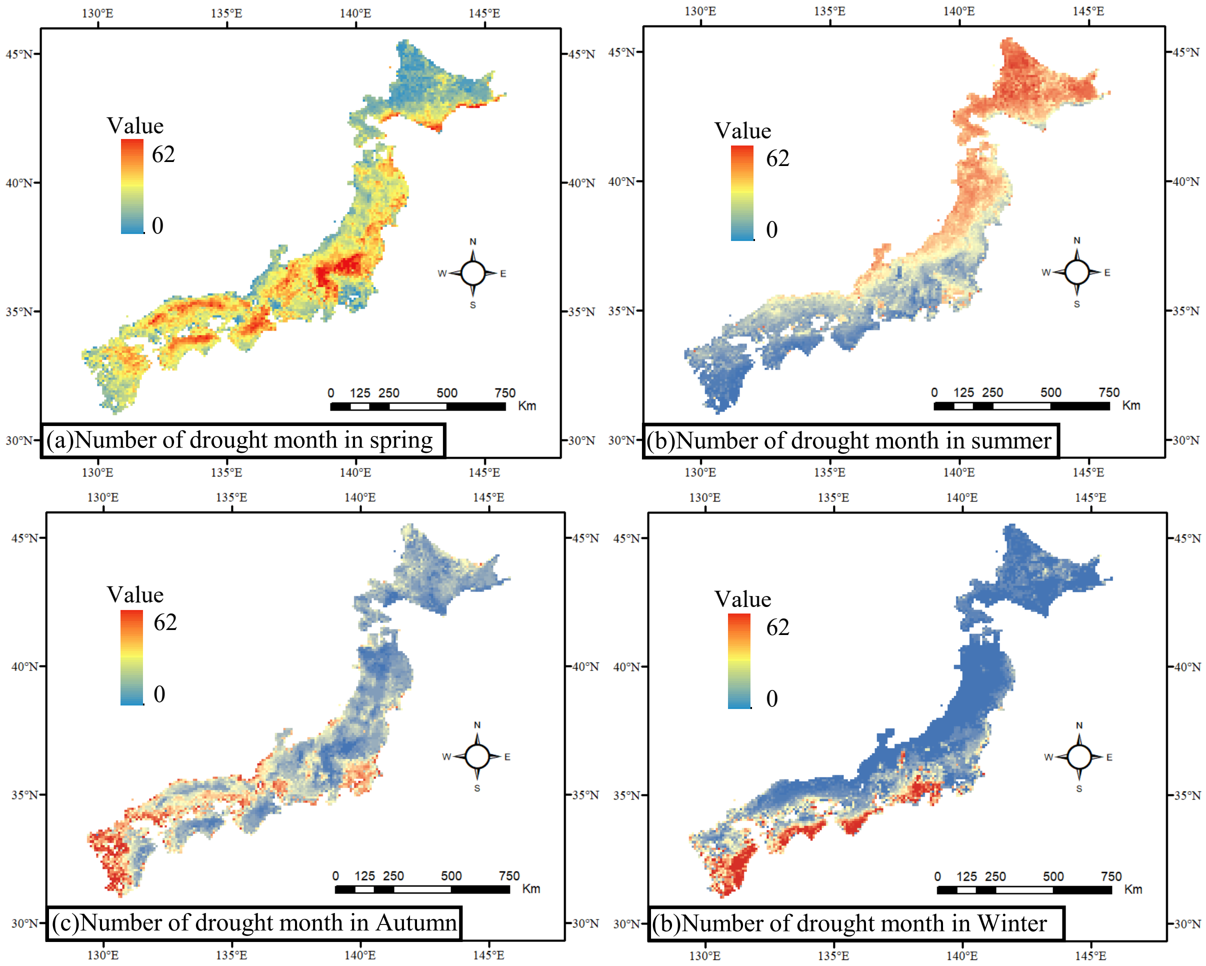

Figure 3.9 The number of drought months (months below the drought threshold) in different seasons across Japan from 1958 to 2012.

3.2.5 Teleconnections between homogeneous drought zones and atmospheric-oceanic indices

DEOF first simplified the multiple time series of each homogeneous arid area into one principal component to analyze the impact of atmospheric-oceanic indices on the nine homogeneous drought zones. Figure 3.10 shows the first DPC time series of the nine homogeneous drought zones. Higher explained variance indicates more significant homogeneity in homogeneous drought zones. Except for zone-1, the explained variance for all remaining homogeneous arid zones was above 60%. In particular, the explained variance of zones-3 and -8 even reached more than 80%. The reason for the low explained variance of zone-1 was that this zone was distributed throughout Japan, and this zone often experienced extreme drought and had a long recurrence period. Except for zone-4 and -9, the 1994 drought affected almost all of Japan. 1994 was considered the driest year since 1958, consistent with the study by Lee et al. (2012b).

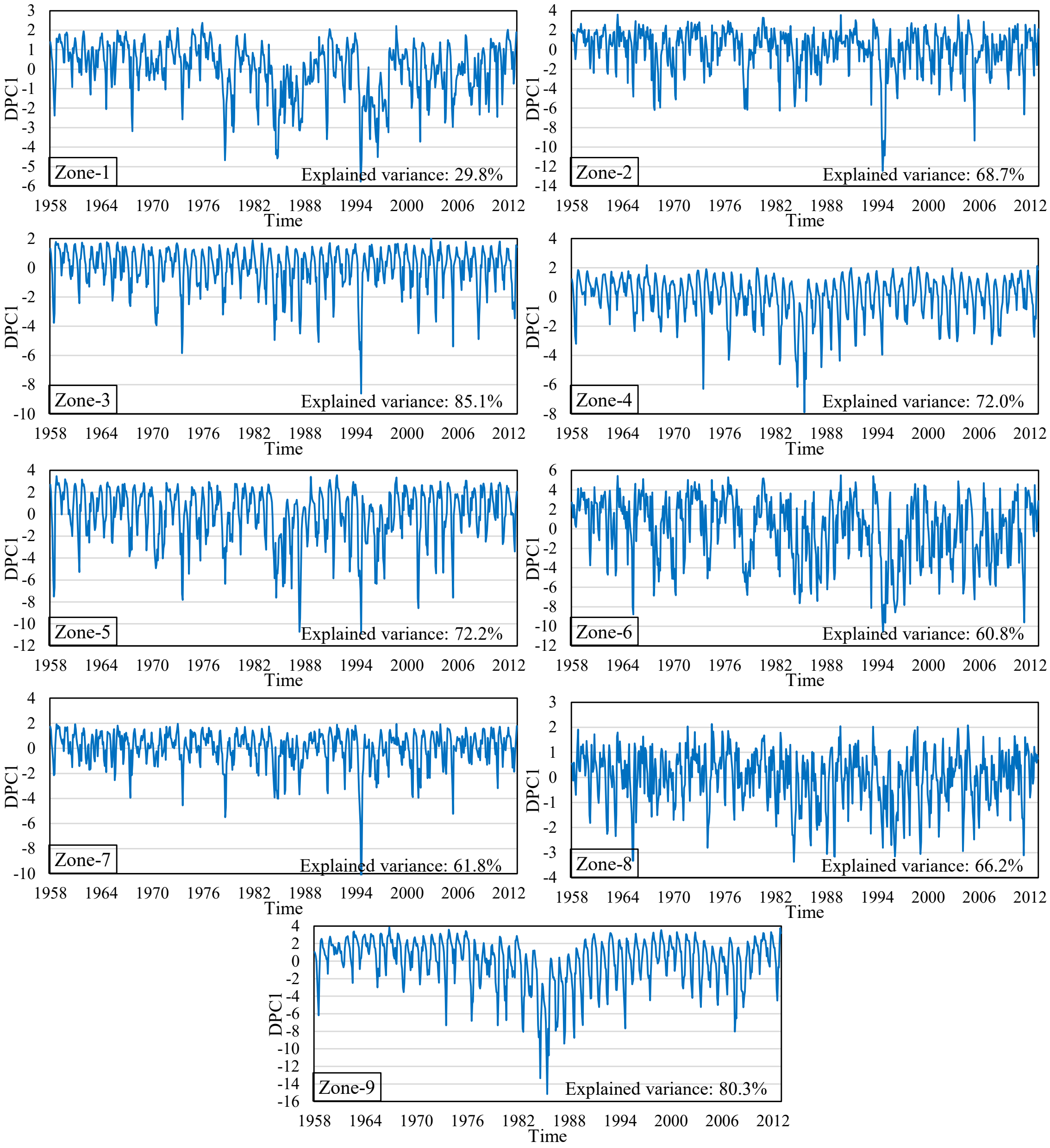

Figure 3.10 First distinct principal component (DPC) of nine homogeneous drought zones. The explained variance in distinct principal component-1 in homogeneous drought zones is at the bottom right of the figures.

Table 3.3 shows the effects of large-scale climate signals on homogeneous drought zones. The most significant atmospheric-oceanic indices (with the largest PASC) are shown in bold. From the PASC results, it can be seen that different atmospheric-oceanic indices have different contributions to homogeneous drought zones. For example, among the nine homogeneous drought zones, the coherence between zone-9 and the atmospheric-oceanic indices was the weakest (the largest PASC in zone-9 was only 11.4%). On the other hand, zone-1 had the strongest relationship with atmospheric-oceanic indices, with a PASC value of 16.7%. However, the teleconnection results need to be treated with caution given the lower explained variance of zone-1. Even though zones-4 and -9 were geographically concentrated in the Hokkaido region, their dominant large-scale climate signals differed. It also hints at the limitations of traditional geographic regions and the advantages of these homogeneous drought regions in identifying dominant atmospheric-oceanic indices.

Table 3.3 PASC between the distinct principal components of homogeneous drought zones and atmospheric-oceanic indices. The largest PASC of the four atmospheric-oceanic indices is bolded.

	PDO	ENSO	NAO	AO
Zone-1_DPC1	13.4%	6.6%	13.6%	**16.7%**
Zone-2_DPC1	**12.6%**	11.0%	12.5%	10.3%
Zone-3_DPC1	6.5%	8.7%	**14.4%**	9.0%
Zone-4_DPC1	7.5%	4.0%	**13.6%**	8.3%
Zone-5_DPC1	5.6%	**12.1%**	6.8%	7.6%
Zone-6_DPC1	11.9%	12.3%	**14.0%**	12.7%
Zone-7_DPC1	4.2%	3.9%	9.4%	**12.1%**
Zone-8_DPC1	10.2%	9.7%	10.0%	**14.8%**
Zone-9_DPC1	**11.4%**	3.7%	11.1%	6.4%

Then, Figure 3.11 shows the WTC results between dominant atmospheric-oceanic indices and DPCs of nine homogeneous drought zones. Only zones-8 and -9 were affected by atmospheric-oceanic indices throughout the study period. For the AO, which controlled zones-

1, -7, and 8, the coherence mainly occurred at ten years (128 months). At the same time, a temporally negative correlation between 20 and 32 months can also be found during 1992-2000. On the other hand, the effects of NAO on zones-3, -4, and -6 were concentrated on a scale of approximately eight years (96 months). The longest coherence period with NAO was with zone-6 from 1958 to 2010, while its coherence period with zone-4 was only from 1975 to 2000. Both zones-2 and -9 were strongly affected by PDO, even though the two regions were far apart. From 1970 to 2012, there was a negative correlation on a ten-year scale between PDO and zone-2. At the same time, the impact of PDO on zone-9 was mainly concentrated outside the cone of influence. ENSO was only detected to affect zone 5 on the 16-year (1958~2000) and 5-year (2000~2012) scales significantly.

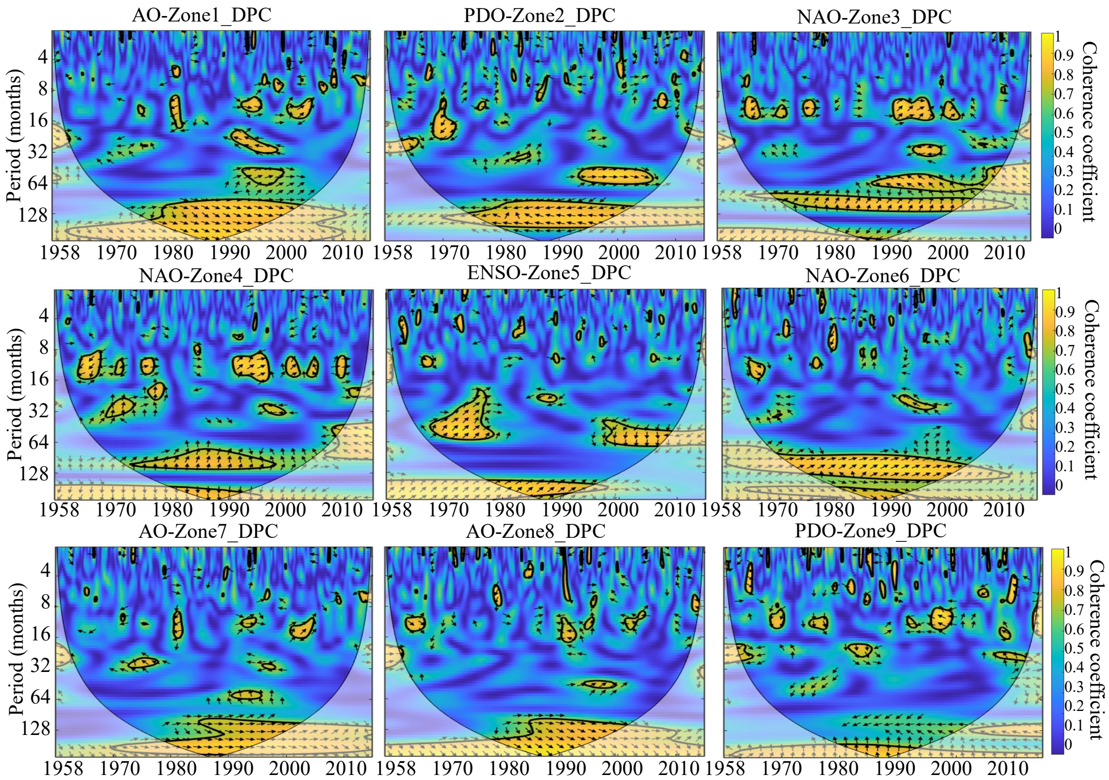

Figure 3.11 Squared wavelet coherence between large-scale climate signals and distinct principal components (DPCs) of nine homogeneous drought zones. The black contour designates the 95% confidence level against red noise, and the cone of influence (COI), where edge effects might distort the picture, is shown as a lighter, paler shade.

The global coherence coefficients evaluated average coherence between homogeneous drought zones and atmospheric-oceanic indices over different timescales (Figure 3.12). It can be found that all other regions have high global coherence coefficients with NAO on the ten-year scale except for zones-8 and -9. On the other hand, zones-1, -2, -5, and -6 were affected by ENSO on a fifteen-year scale. The global coherence coefficients between AO and zone-1, -3, -6, and -8 showed an increasing trend over several decades, while the coherence coefficients in other homogeneous zones have reached a maximum value at about a ten-year or fifteen-year scale. Similar to the AO, the global coherence coefficient between the PDO and zones-1, -2, and -6 has reached a maximum over the study period. However, the coherence coefficients between PDO and zones-3, -4, and -9 were still increasing on the scale of decades.

NAO was detected to impact hydrometeorology in the western region of Japan (Aizen et al., 2001). However, the effects of PDO and AO were also highlighted in zones-2 and -8 in western Japan by identifying homogeneous drought zones. This result suggests that even if precipitation heterogeneity is not apparent in the same geographical location, droughts may have significant heterogeneity due to various factors and thus be dominated by atmospheric-oceanic indices. In addition, identifying homogeneous drought zones minimizes the loss of information and allows the quantification of significant periods when the atmospheric-oceanic indices affect each homogeneous drought zone.

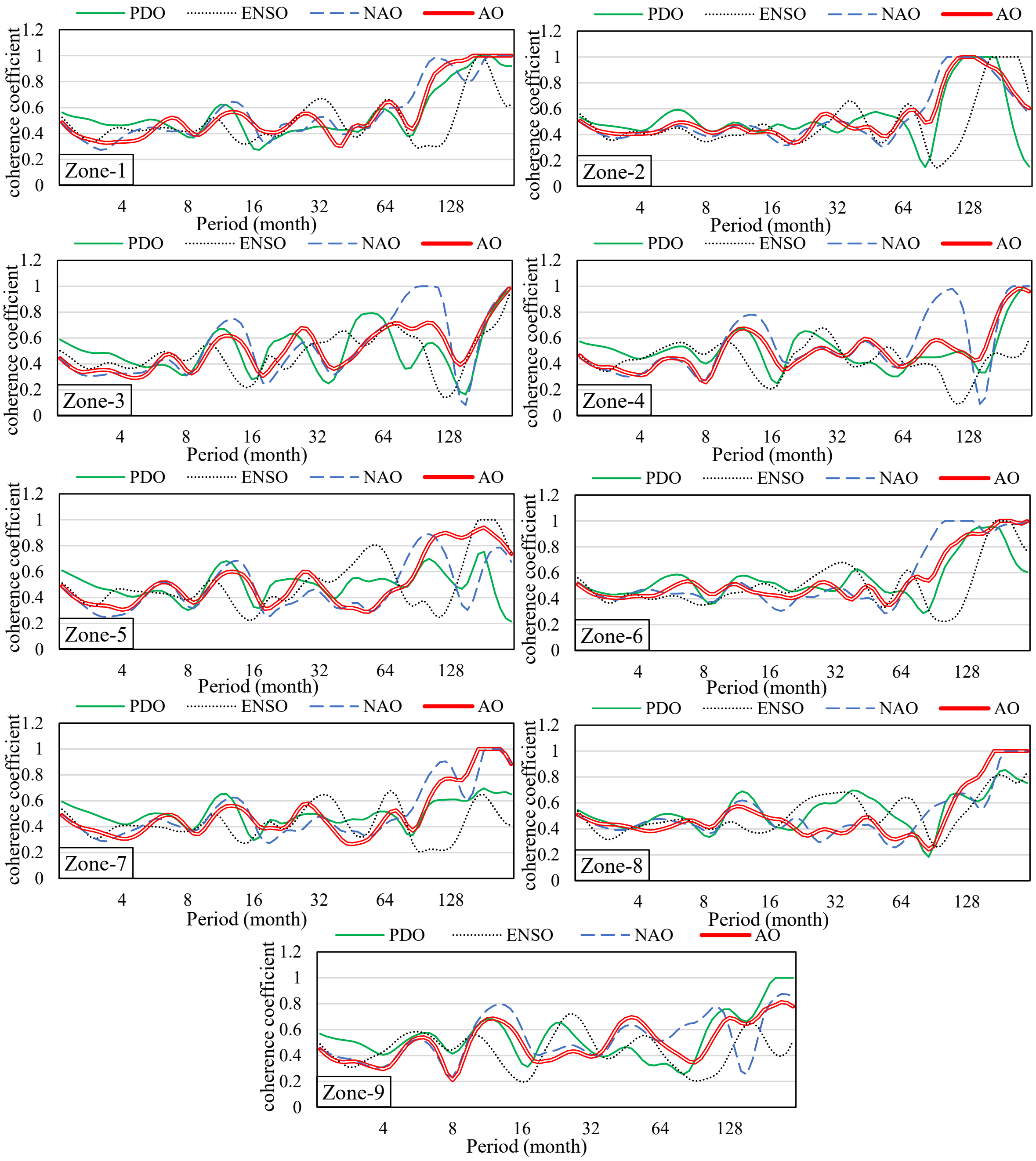

Figure 3.12 The global coherence coefficients between large-scale climate signals and distinct principal component-1 (DPC1) of nine homogeneous drought zones.

3.2.6 Comparison of homogenous drought zones and wildfire statistics

To discuss the effects of drought, Figure 3.313 illustrates the statistical characteristics of wildfires at the prefectural scale in Japan. As for the burned area, zone-6 has a large burning area, especially around the Seto Inland Sea. However, the Iwate Prefecture of Japan, which also has a large burning area, cannot be explained by the homogeneous drought zone-5. There was a much larger area in zone-5, but Miyagi Prefecture of zone-5 does not have as large burned areas as Iwate Prefecture. Similarly, the Fukushima Prefecture, which has many wildfire activities, was difficult to identify from the homogeneous drought zone. This result suggests that only the drought characteristics regions around the Seto Inland Sea were consistent with wildfire statistics. It also shows that it is not enough to consider only one factor (such as drought) when discussing wildfire characteristics.

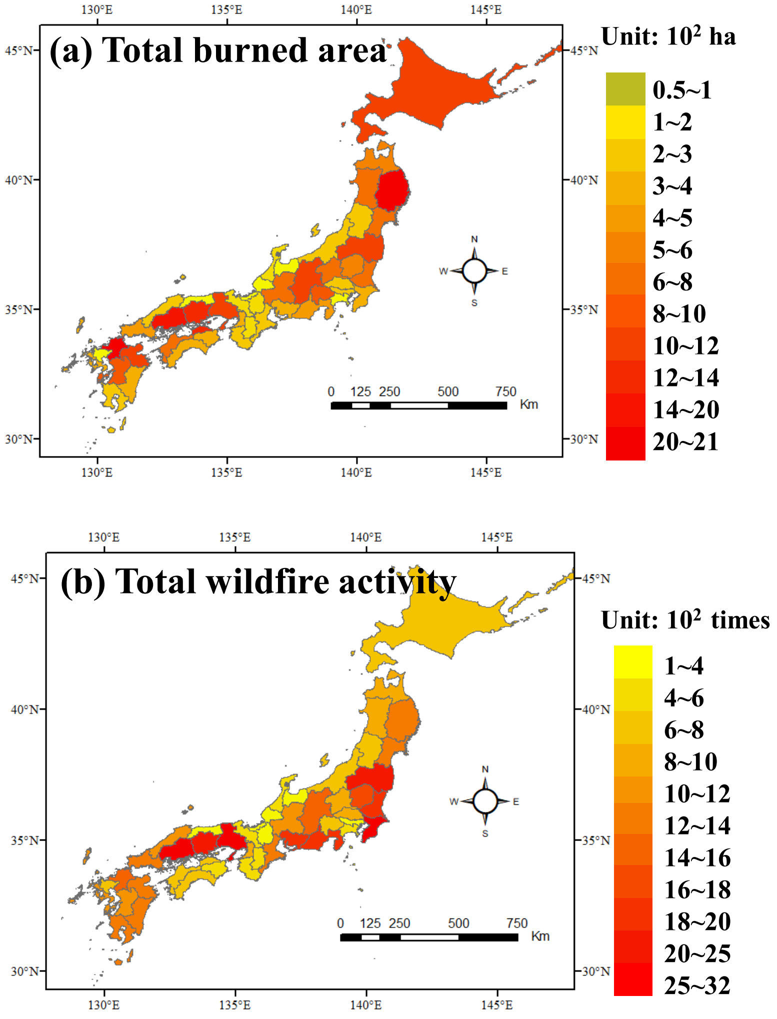

Figure 3.13 Total burned area and wildfire activity across Japan from 1995 to 2017.

3.3 Discussion

Previous studies have not fully explored the effects of atmospheric-oceanic indices on homogeneous drought zones and the relationship between homogeneous drought zones and wildfire characteristics. To fill this research gap, this chapter proposed a new framework for analyzing the teleconnections between drought and atmospheric-oceanic indices based on modeled soil moisture in Japan (the region with significant drought heterogeneity) from 1958 to 2012. First, nine homogeneous drought zones were delineated by considering the probability-related variables, drought duration, seasonality, and the distance between regions. Then, combining cluster analysis, DEOF, and WCO, the first principal components of the nine homogeneous drought zones with high explained variance were remotely correlated with atmospheric-oceanic indices to elucidate their qualitative relationships. And the shortcomings of the homogenous drought zone in its ability to analyze wildfire characteristics were also revealed. Overall, the results of this chapter can provide a reference for defining homogeneous drought zones in Japan, overcoming the shortcomings of classical drought analysis in identifying the causes of drought.

Zone-1 was dominated by extreme drought events and is the region with the longest drought periods, the longest reoccurring periods, and the largest coefficient of variation of the nine homogeneous drought zones. On the other hand, spring droughts were mainly found in homogeneous drought zones-2 and -6, and the lowest average soil moisture was found in zone-6. Furthermore, the Tohoku region of Japan was divided into two parts by Ōu Mountains: zones-3 and -5. Zones-4 and -9 were dominated by summer drought and were both located in the Hokkaido region. The degree of rightward bias in the probability distribution curve of soil moisture for zone-7 was the most significant of the nine zones, implying that the zone was wet most of the time. On the other hand, homogeneous drought zone-8 covered by high mountains was dominated by weak drought events with short dry periods and reoccurring periods. Furthermore, some of these nine zones were separated since soil moisture could show the same characteristics even in two areas distant from each other. As an illustration, zone-6 was characterized by marked variability and low soil moisture. Topographically, zone-6 was located on the coastal edge or at the foot of the mountains. On the one hand, during the rainy season, soil moisture increases greatly on rainy days and decreases rapidly after rain in this zone. On the other hand, in the non-rainy season, high temperatures and strong transpiration make it easy to keep soil moisture at a low level in zone-6.

Except for zone-1, the explained variances of the principal components in the other regions all exceeded 60%, reflecting the high homogeneity of these regions. Different atmospheric-oceanic indices dominated the nine homogeneous drought zones. AO had the strongest impacts on homogeneous drought zones-1, -7, and -8 on the ten-year scale. The effect of NAO on zones-3, -4, and -6 was mainly concentrated on a scale of around eight-year. Zones-2 and -9 were far apart, but they were both dominated by PDO. ENSO mainly controlled zone-5 on a five-year and sixteen-year scale before and after 2000, respectively. These results demonstrated the superiority of principal components in homogeneous drought zones in exploring teleconnections. Due to the heterogeneity of droughts, even droughts within the same geographical location may be dominated by different atmospheric-oceanic indices. At the same time, it should be noted that the homogeneous drought zones were insufficient in exploring wildfire characteristics.

3.4 Summary

Overall, this chapter established the teleconnections between atmospheric-oceanic indices and homogeneous drought zones across Japan. The results of this chapter contributed to a better understanding of the homogeneity of spatial and temporal characteristics of droughts across Japan. Focusing on atmospheric-oceanic indices provides a valid and promising reference for predicting drought due to changing climatic, atmospheric, and oceanic conditions. The findings are also valuable for drought management and drought prevention.

Chapter 4 Quantifying the Contributions of Atmospheric-Oceanic Indices on Global Burned Area Homogenous Zones

This chapter was published in Scientific Reports in January 2022: Ke Shi and Yoshiya Touge. "Characterization of global wildfire burned area spatiotemporal patterns and underlying climatic causes." Scientific Reports 12.1 (2022a): 1-17.

4.1 Introduction

Wildfires are an important component of the ecological processes of the Earth's natural systems and range in scale from local to global. However, wildfire risk has increased significantly in recent years due to higher temperatures, more rain-free days, and more wildfire-affected areas (Vitolo et al., 2020). Historical estimates of annual global wildfire burned area range from 394×10^6 to 519×10^6 ha from 2001 to 2018, with an average of 463×10^6 ha (Lizundia-Loiola et al., 2020). There were 79,000 wildfire events in August 2019 globally, compared to 16,000 wildfire events in the same period last year (Fernández et al., 2016). In addition, catastrophic wildfires in recent years have been found to be on a marked increase globally. As an illustration, severe wildfires swept through California in consecutive years of 2017 and 2018 (Zhongming et al., 2019). The 2020 wildfire in the western United States was considered the most destructive wildfire in the country, a wildfire that killed thousands of people from smoke and damaged or destroyed over 10,000 structures (Higuera et al., 2021). Driven by extremely high temperatures, both Alaska and Siberia experienced widespread fires in 2019 (Zhongming et al., 2019). Temperate broadleaf forest fires accompanied by large burned areas (5.8×10^6 ha) were recorded in Australia from September 2019 to January 2020 (Boer et al., 2020), which were the most widespread wildfires ever recorded in the temperate broadleaf forest in Australia (Nolan et al., 2020).

"Climate variability is often the dominant factor affecting large wildfires." was stated by Intergovernmental Panel on Climate Change (IPCC, 2014). In addition, wildfire disturbance was identified by the Global Climatic Observing System (Secretariat, 2006) as an "important climate variable", and it was emphasized that long-term time series data were required to quantify the relationships between climate and wildfire. For example, the synchronization of wildfire weather conditions in far-off areas due to teleconnection processes driven by atmospheric-oceanic indices was how the atmosphere's globalizing influence manifests itself (Page et al., 2008). The ENSO-wildfire dynamic in Southeast Asia is one of the most well-known teleconnection processes (Murphy, 2006). In tropical woods (from 5.5°S to 5.5°N), there were significant associations between wildfires and the ENSO index (Murphy, 2006). Balzter et al. (2005) discovered the influence of the AO pattern on inter-annual wildfire variability in Central Siberia. The burnt region in Central Siberia may be essentially replicated using a linear combination of the Arctic Oscillation index and the summertime temperature (Balzter et al., 2005). The recent shift to the positive phase of the Atlantic Multidecadal Oscillation (AMO) provided evidence of higher wildfire frequencies in Colorado in the United States (Schoennagel et al., 2007). Years of combined positive AMO, negative ENSO, and Pacific Decadal Oscillation (PDO) phases represent "triple whammies" that significantly increased the occurrence of drought-induced wildfires in western Colorado (Schoennagel et al., 2007). However, it turns out that wildfires with greater intensity and the larger burned area are on the rise in the southwestern United States, which is more relevant than increased wildfire frequency (Singleton et al., 2019), underscoring our worry about burned areas.

Overall, the variation in wildfire behavior and severity at different temporal and geographical scales may be influenced by climatic variability (Liu et al., 2010). Therefore, many studies have concentrated on the connection between local wildfires, weather, and climate. The association between burned areas and hydro-meteorological elements, such as high temperatures and intermediate annual rainfall, was investigated (Aldersley et al., 2011). Similarly, the relationships between the worldwide burned area and vegetation production, precipitation, and crucial factors were explored based on the generalized additive model (Hantson et al., 2015). These studies, however, largely concentrated on relationship analysis between burned area and gridpoint-specific hydro-meteorological elements. In their worldwide wildfire research, atmospheric-oceanic indices like AMO and ENSO were not taken into account in more detail. As a result, the links between atmospheric-oceanic indices and wildfires are still not completely understood. It might even be expected to find teleconnections between wildfires in different regions, meaning that the same atmospheric-oceanic index affects wildfires in multiple regions.

In recent years, researchers have been drawn to the teleconnections between hydro-meteorological elements in various locations and atmospheric-oceanic indices. For example, 15 regional hazards (e.g., storms in Australia, rainfall in China, and rainfall in the USA) share links through ENSO (Steptoe et al., 2018). Research of this nature might improve knowledge of concurrent global hazards. Wavelet coherence was applied to evaluate the multivariate link between the streamflow of sixteen major rivers worldwide and meteorological factors/atmospheric-oceanic indices, which offered a reference for medium- to long-range hydrological predictions (Su et al., 2019). Nguyen et al. (2021) also investigated the combined impacts of ENSO and PDO on worldwide droughts and discovered that when ENSO and PDO were in phase, the Amazon, India, Central China, Indonesia, and eastern Australia were the places where drought tended to worsen and spread. The possible links in regional climates might be investigated using this teleconnection study between atmospheric-oceanic indices and hydro-meteorological elements. But the links between worldwide wildfire and the atmospheric-oceanic indices are still poorly understood. The first worldwide evaluation of cross-regional climatic effects and spatiotemporal wildfire variability was made by Page et al. (2008). But this study was limited in that they only examined wildfire activity and chose ENSO as the primary global climatic cause for study. The burned area, which reflects the level of wildfire severity, is another important criterion for gauging wildfires (Keeley, 2009). Burned area is often used to assess global wildfire traits, which have been connected to ancient records (Bowman et al., 2009) and are used to estimate carbon fluxes from the biosphere to the atmosphere (Van der Werf et al., 2010). But since many global climatic variables often impact wildfires at once (Aldersley et al., 2011), adding as many atmospheric-oceanic indices as possible will help us better understand how climate affects wildfires.

Research gaps in prior research have not been addressed by exploring the spatiotemporally homogenous zones of globally burned areas. Therefore, a thorough investigation of the patterns of burned areas worldwide will aid in our understanding of wildfires. This chapter's primary objective was to examine the teleconnections between burned areas and atmospheric-oceanic indices. First, the spatiotemporally homogenous zones of burned areas around the globe were identified using the distinct empirical orthogonal function (DEOF). Then, the cross-wavelet transform and wavelet coherence were utilized to evaluate the links between the main patterns of burned areas and numerous worldwide atmospheric-oceanic indices. Then, by identifying common regions and common atmospheric-oceanic indices for different wildfire patterns, the relationship between specific regions and important atmospheric-oceanic indices can be discussed in detail.

4.2 Results

4.2.1 Spatial and temporal patterns of wildfire

The monthly *logBAA* time series at 1° resolution was utilized by DEOF computation. The top eight DEOFs accounted for 30.0% of the overall variation. The explained variance did not reach high levels for two key reasons. The first reason is that in the global teleconnection analysis, the competitive relationship between local correlation and long-distance teleconnection makes it difficult to find the dominant principal component. For instance, in identifying the global homogeneous drought zones, the explained variance of the first two principal components was only 6.7% and 5.1%, respectively (Dai et al., 2004). Another reason is that wildfires are not only affected by weather or climate but also by human activities, so wildfires are highly heterogeneous and different from traditional hydro-meteorological elements. Similarly, in the identification of homogeneous zones of global wildfire activity, the explained variance of the first nine principal components was only 40% (Page et al., 2008). The first eight DEOFs, which account for 30% of the total explained variance, were actually consistent with the anticipated outcomes since the factors that contributed to the burned area are more complex than the wildfire activity. As this research focuses on wildfire anomalies, it should be highlighted that the wildfire anomalies in areas prone to wildfires (like the United States) had less influence.

The spatial patterns of DEOF1~DEOF8 are presented in Figure 4.1, and Figure 4.2 depicts the time series aspect of DPCs. And the DPCs were normalized to a range of -1 to 1 to display the time series more clearly. Each DEOF pattern's logBAA time series projection was known as a DPC. The burned area in the positive loading zone was bigger than the multi-year monthly average when the DPCs value was positive. In contrast, the burned area in the negative loading zone was less than the multi-year monthly average.

Different DEOFs illustrated various atypical features of burned areas. The 20% of the greatest (smallest) DEOF values were deemed to be positive (negative) loading values. For instance, the geographical distribution of DEOF2 showed negative loadings in several areas of Russia and Ukraine. At the same time, the high positive loadings were mostly concentrated in northern Kazakhstan. The two concentrated areas of negative and positive loading had opposite characteristics of burned areas.

DPCs can be used for the time function to determine the precise moment the aberrant wildfire event happened. There was a substantial lowering trend in DPC1, indicating that the burned area was diminishing in the portion of Russia and the north of Kazakhstan, where strong positive loadings are concentrated. This trend of burned area reduction in Kazakhstan has also been verified in other studies (Xu et al., 2021a). In contrast, the burned area for DPC7 has increased in recent years, showing that the burned area in eastern Brazil was expanding, which was also identified by Forkel et al. (2019). August 2002 had a large and atypically high value in DPC1. Correspondingly, in 2002, Kazakhstan had the most devastating wildfire, with a maximum burned area of 4.6×10^6 ha (Xu et al., 2021a). With DPC5, an exceptionally high value was seen in 2010 and 2012, and a strong positive loading was identified in Brazil. Schmidt et al. (2020) also uncovered these two enormous wildfires in Brazil that occurred barely two years apart.

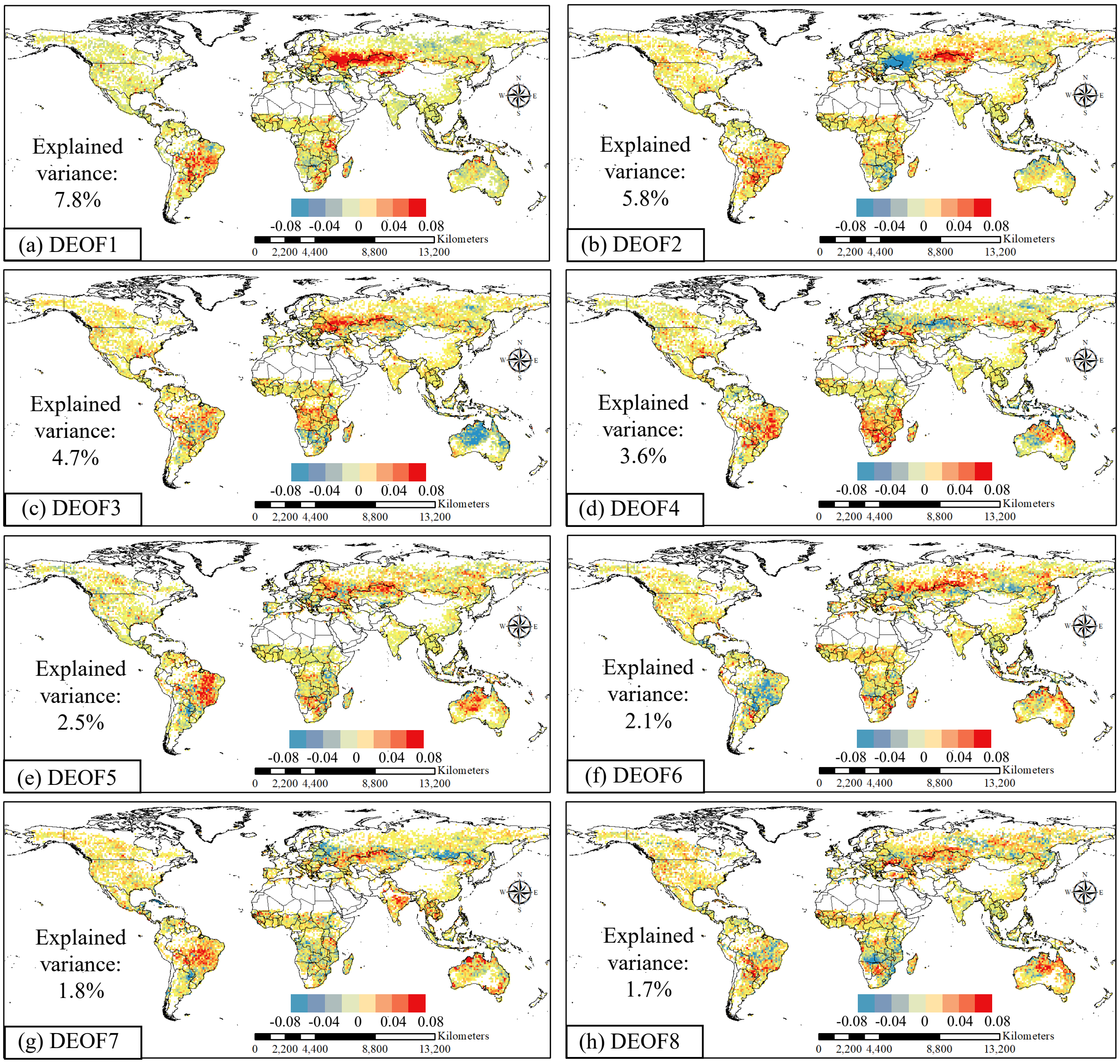

Figure 4.1 DEOF1~8 for the spatial distribution of log*BAA*.

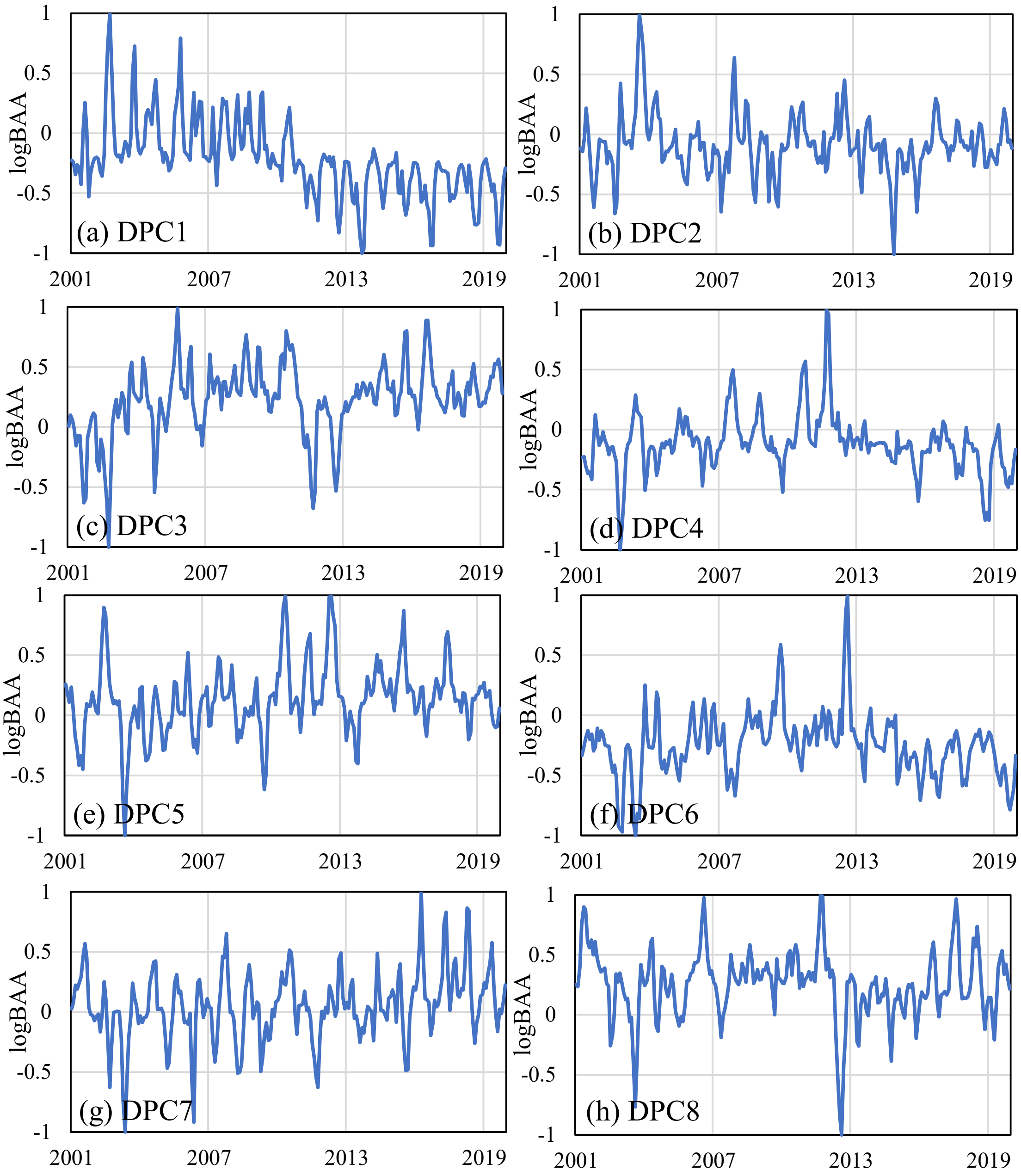

Figure 4.2 DPC1~8 time series of log*BAA* (DPCs are the projection of log*BAA* time series in each DEOF pattern).

Figure 4.3 depicts the precise temporal periodicity of DPC1~8 as determined by CWT. The black contour represents a 95% confidence level against red noise, whereas the COI, where edge effects may distort the image, is shown as a softer and paler tone. These findings indicated that none of the DPCs had a dominating long-term periodicity. Except for DPC1 and DPC4, all DPCs exhibited dominant but intermittent roughly yearly (8~16 month) periodicities relative to inter-annual ones. For instance, DPC7 had two yearly periodic bands from 2003 to 2009 and

2016 to 2018. The periodic bands of DPC2 tended to be concentrated on the inter-annual scale, while those of DPC4 tended to be concentrated on the multiyear scale.

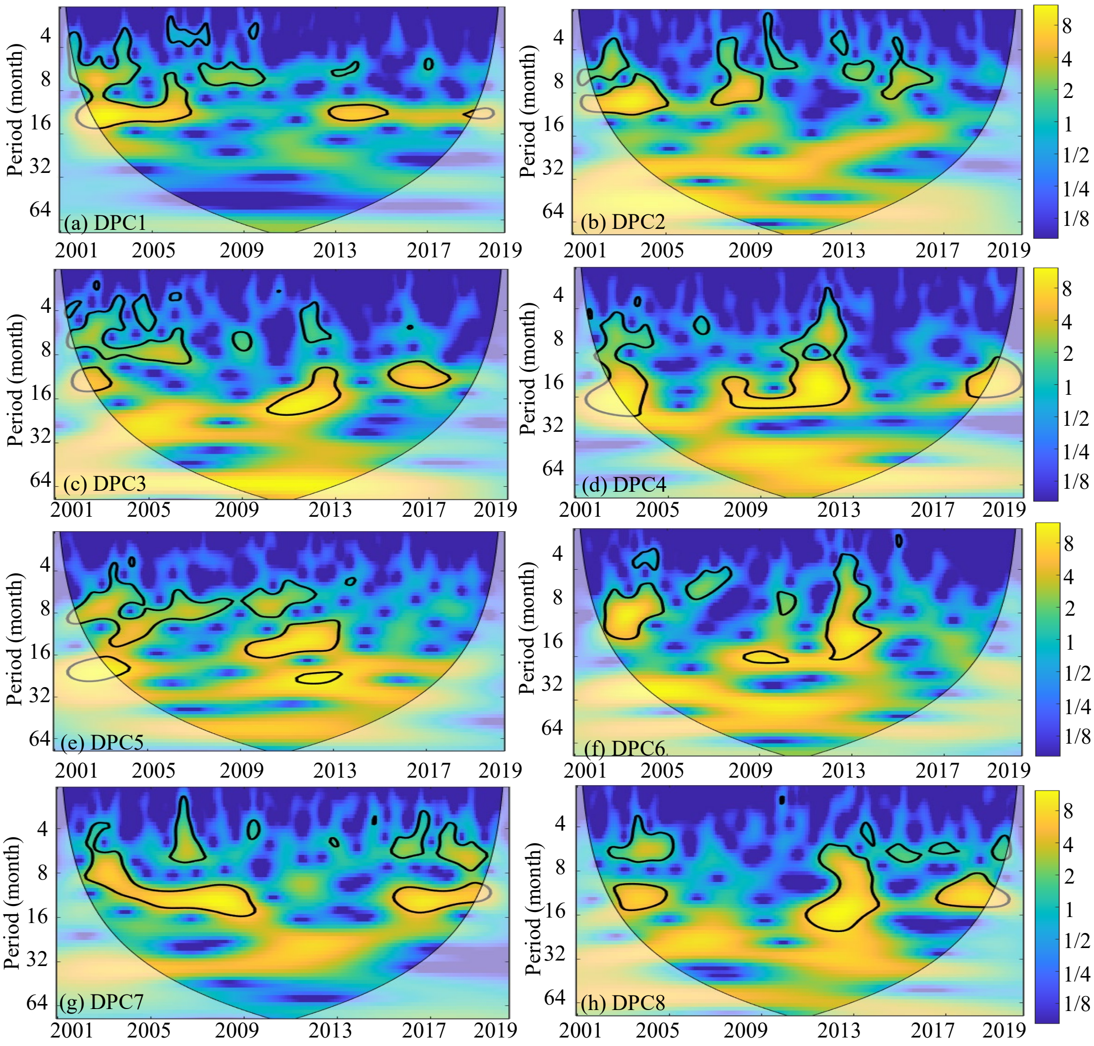

Figure 4.3 WPS of the DPC time series (Periodicity of time series). The black contour designates the 95% confidence level against red noise, and the COI, where edge effects might distort the picture, is shown as a lighter, paler shade.

4.2.2 Teleconnection between atmospheric-oceanic indices and DEOFs

Table 4.1 summarizes the impacts of atmospheric-oceanic indices on DPC1~8. For each DEOF pattern, the atmospheric-oceanic indices with the biggest PASC are shown in italics, and the top three PASCs are highlighted in bold. According to the PASC, distinct atmospheric-oceanic indices contributed differently to wildfire patterns. The maximum PASC for atmospheric-oceanic indices throughout DPC1~8 varied from 11.3% to 21.0%, with an average of 16.0%. PNA and EA/WR exhibited the greatest ranges of effect among these atmospheric-oceanic indices on DPC1~8. Concurrently, the AAO and DMI were the global climate factors that had no discernible impact on any DEOF1~8 patterns.

Table 4.1 PASC (%) for the wavelet transform coherence between DPCs and atmospheric-oceanic indices. Italic indicates the most significant atmospheric-oceanic indices, and bold indicates the first three most significant atmospheric-oceanic indices.

	DPC1	DPC2	DPC3	DPC4	DPC5	DPC6	DPC7	DPC8
TSA	9.5%	3.5%	10.4%	14.5%	1.3%	**6.4%**	3.3%	7.0%
POL	11.5%	3.7%	3.6%	5.5%	3.8%	***15.0%***	**11.4%**	1.5%
WP	6.5%	7.9%	12.4%	8.0%	4.7%	4.5%	8.1%	12.0%
PDO	4.8%	8.4%	12.3%	**20.6%**	6.5%	5.2%	8.4%	4.1%
ONI	4.6%	8.4%	12.2%	17.3%	4.6%	**6.9%**	5.8%	6.6%
AMO	***20.4%***	4.9%	5.9%	10.0%	6.8%	4.7%	**10.1%**	6.8%
DMI	3.6%	3.8%	9.4%	5.9%	2.6%	4.1%	5.0%	4.7%
AO	3.3%	4.0%	7.3%	4.8%	***11.3%***	5.5%	5.2%	**13.7%**
NAO	4.8%	3.6%	11.2%	9.7%	**10.6%**	5.7%	8.9%	3.6%
PNA	7.8%	**12.5%**	**15.0%**	***21.0%***	3.5%	5.2%	4.7%	7.6%
AAO	13.5%	7.4%	10.1%	6.2%	5.7%	3.3%	5.2%	7.0%
EA	5.6%	**14.5%**	4.4%	11.9%	4.3%	3.8%	3.9%	7.1%
EA/WR	4.9%	10.0%	8.3%	6.8%	**8.8%**	4.0%	***12.7%***	***14.7%***
TNA	**13.8%**	3.5%	**12.8%**	10.6%	4.7%	5.7%	6.2%	9.3%
MEI	5.4%	5.9%	***17.0%***	**18.1%**	2.8%	5.4%	4.5%	4.7%

	DPC1	DPC2	DPC3	DPC4	DPC5	DPC6	DPC7	DPC8
EP/NP	**17.9%**	***16.0%***	8.3%	14.8%	7.0%	6.1%	4.1%	**9.8%**

Figure 4.4 depicts the zone delineated by the three atmospheric-oceanic indices that have the greatest effect on DEOF1~8. Different DEOF patterns regularly occurred in various places. DEOF1~3 discovered hotspot-1 (near Ukraine and Kazakhstan). Among these indices, AMP, EP/NP, and PNA were the biggest influencing factors for hotspot-1. There were three potential combinations of global climatic factors impacting hotspot-2 (Australia) for DEOF3, DEOF5, and DEOF8: MEI-DEOF3, AO-DEOF5, and EA/WR-DEOF8. The atmospheric-oceanic indices that impact hotspot 3 (Brazil) have grown quite diversified, with ten separate atmospheric-oceanic indices identified as having an effect. In hotspot 3 of DEOF4~7, which was affected by ten atmospheric-oceanic indices, PNA, AO, POL, and EA/WR were the predominant atmospheric-oceanic indices.

The time periodicity of sixteen g atmospheric-oceanic indices is shown in Figure 4.5. The ONI and MEI, which represent the influence of ENSO in different ways, have substantial multiyear periodicity. The intra-annual periodicity is the AMO's primary periodic band. However, it is challenging to identify the dominating periodicity among the thirteen remaining g atmospheric-oceanic indices. Figures 4.6 and 4.7 indicate the coherence coefficient between DPCs and the top three atmospheric-oceanic indices with phase delays shown by black arrows. Among DPC1~8, DPC6 had the lowest coherence with atmospheric-oceanic indices (the average PASC of the top three atmospheric-oceanic indices s was only 9.5%). On the other hand, DPC4 had 19.1% of the top three average PASC, showing significant coherence with atmospheric-oceanic indices.

Atmospheric-oceanic indices had strong wavelet coherence for DPC1 and DPC4 at more than four-year scales (48~64 months) over the whole study period. In addition, strong wavelet coherence was found in EA-DPC2, EP/NP-DPC2, POL-DPC6, and WP-DPC8. Similarly, PNA-DPC2, PNA-DPC3, MEI-DPC3, TSA-DPC6, and AMO-DPC7 exhibited strong wavelet coherence at about two-year scales (16~32 months) with atmospheric-oceanic indices. This two-year wavelet coherence persisted longest between MEI and DPC3, from 2001 to 2018, but the coherence between TSA and DPC6 did not emerge until 2010.

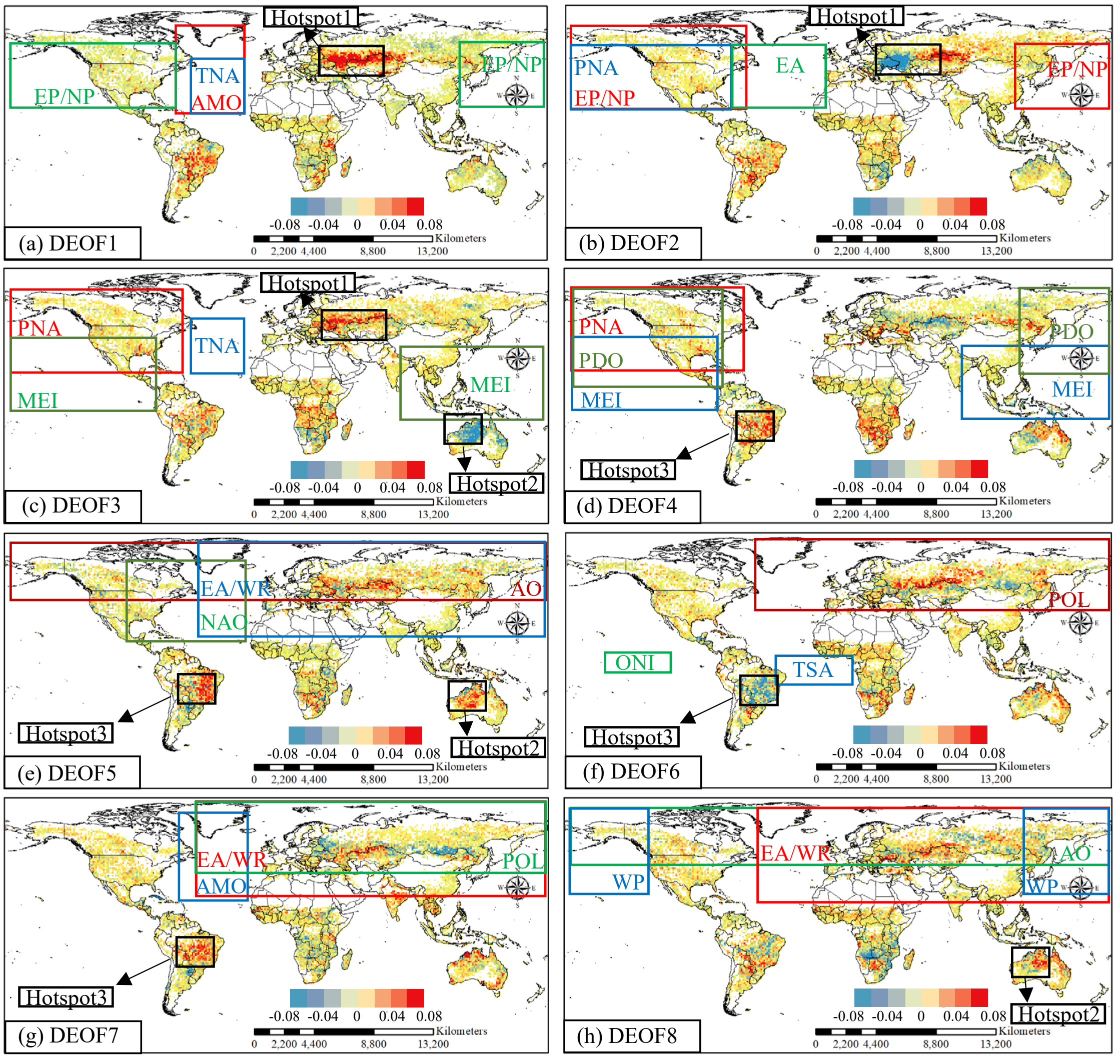

Figure 4.4 The location distribution of the top three atmospheric-oceanic indices with the strongest influence on DEOF patterns. The red, blue, and green rectangles indicate the strongest, second-strongest, and third-strongest atmospheric-oceanic indices on the DEOFs, respectively. The black circle indicates the common region in different patterns. Hotspot 1: around Ukraine and Kazakhstan; Hotspot 2: Australia; Hotspot 3: Brazil.

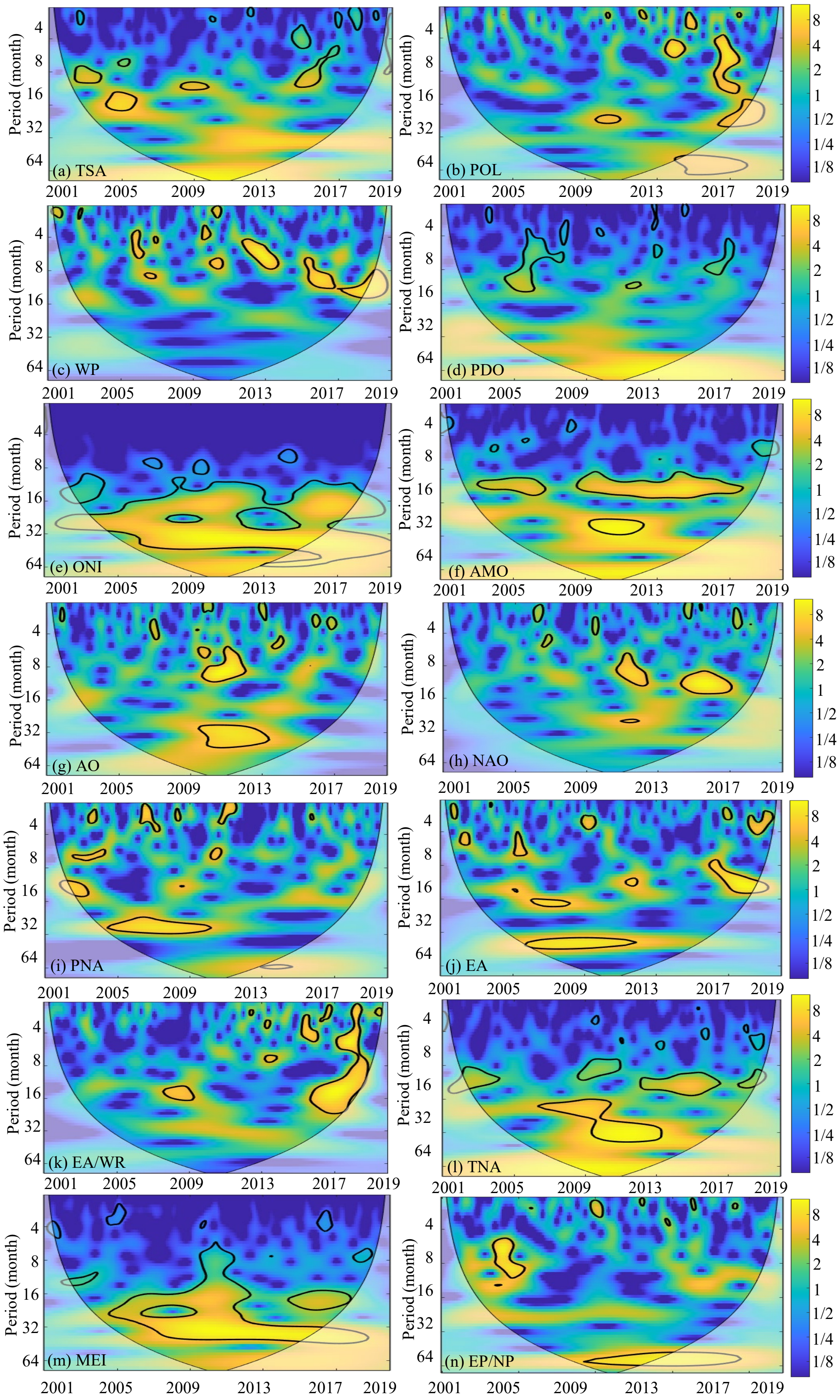
Period (month)
4
8
16
32
64
2001
2005
2009
2013
2017
2019
8
4
2
1
1/2
1/4
1/8
(a) TSA
(b) POL
(c) WP
(d) PDO
(e) ONI
(f) AMO
(g) AO
(h) NAO
(i) PNA
(j) EA
(k) EA/WR
(l) TNA
(m) MEI
(n) EP/NP

Figure 4.5 WPS of the large-scale climatic single time series (periodicity of time series). The black contour designates the 95% confidence level against red noise, and the COI, where edge effects might distort the picture, is shown as a lighter, paler shade. (DMI and AAO, which have no significant impact on any DEOFs, are removed).

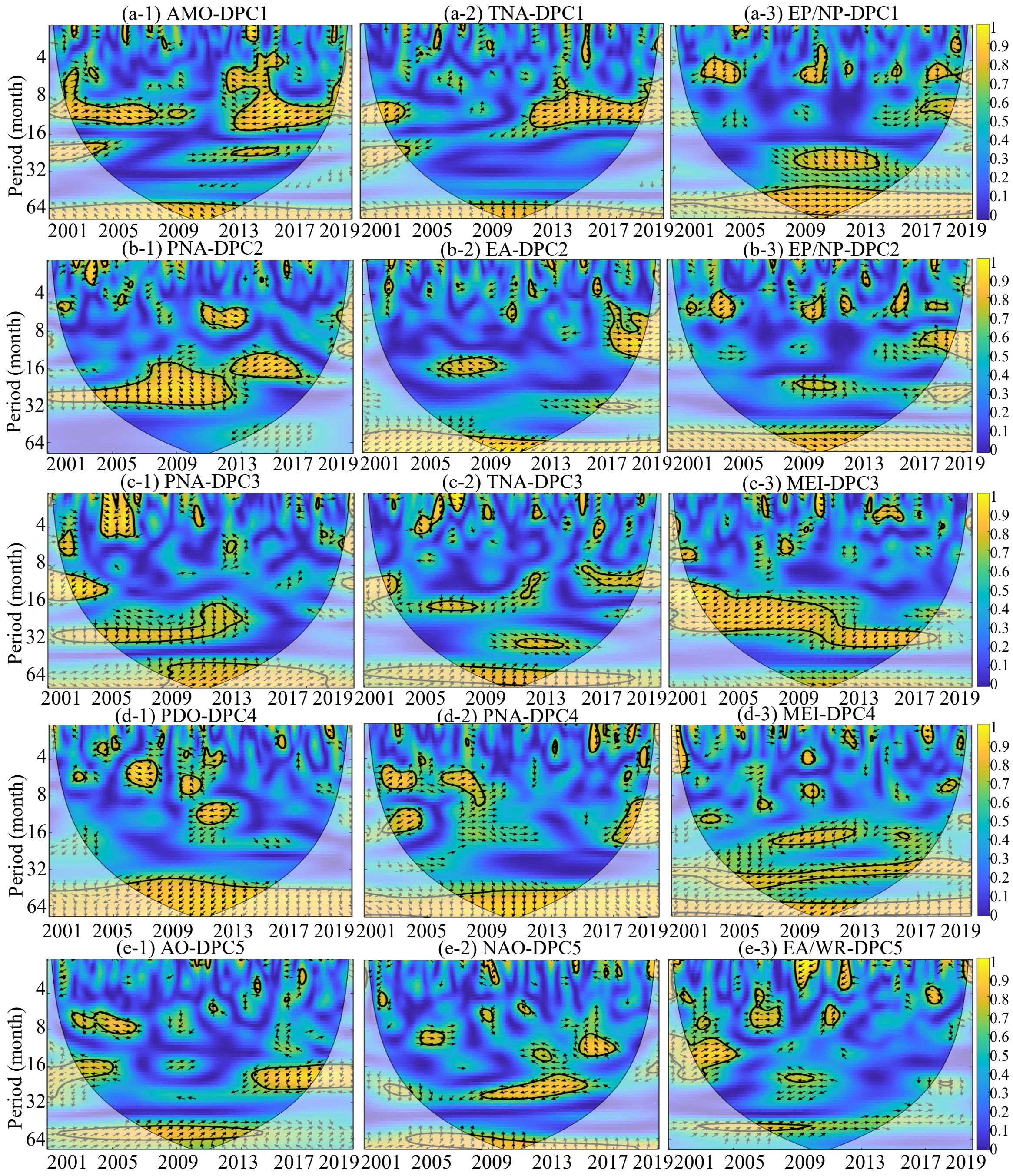

Figure 4.6 Squared wavelet coherence between the atmospheric-oceanic indices and the temporal patterns of DPC1~5 (coherence coefficient between the atmospheric-oceanic indices and DPCs). The black contour designates the 95% confidence level against red noise, and the COI, where edge effects might distort the picture, is shown as a lighter, paler shade. In

addition, the phase lags are illustrated by black arrows. The y-axis represents the coherence period, and the color represents the level of the coherence coefficient.

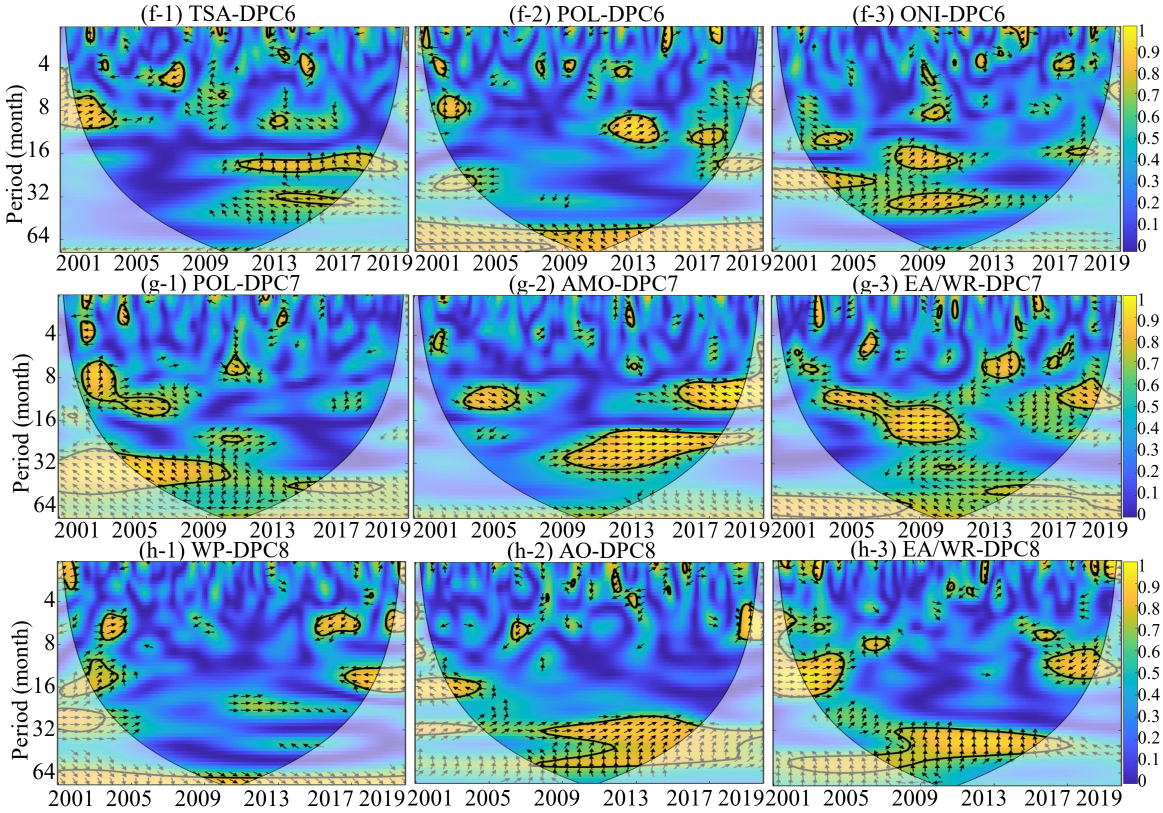

Figure 4.7 Squared wavelet coherence between the atmospheric-oceanic indices and the temporal patterns of DPC6~8 (coherence coefficient between the atmospheric-oceanic indices and DPCs). The black contour designates the 95% confidence level against red noise, and the COI, where edge effects might distort the picture, is shown as a lighter, paler shade. In addition, the phase lags are illustrated by black arrows. The y-axis represents the coherence period, and the color represents the level of the coherence coefficient.

The global coherence coefficients are shown in Figure 4.8 and provide an assessment of the averaged coherence between the monthly DPCs and the top three atmospheric-oceanic indices across various periods. It is feasible to assess the relative coherence relevance of the atmospheric-oceanic index in each burned area pattern under all-time scales by displaying the top three atmospheric-oceanic indices together. Only DPC1 demonstrated strong coherence coefficients with global climate factors on an annual and multiyear scale. High global coherence coefficients for DPC3 were observed at timescales of more than four years and around two years. These findings suggested that certain global climatic factors may significantly impact both long and short periods. Other DPCs, on the other hand, only demonstrated strong coherence coefficients on time scales greater than 32 months. Particularly, several atmospheric-oceanic indices, such as PNA-DPC2 and ONI-DPC6, could not achieve high global coherence coefficients on all time scales, suggesting that these atmospheric-oceanic indices have very limited effects on these DEOF patterns.

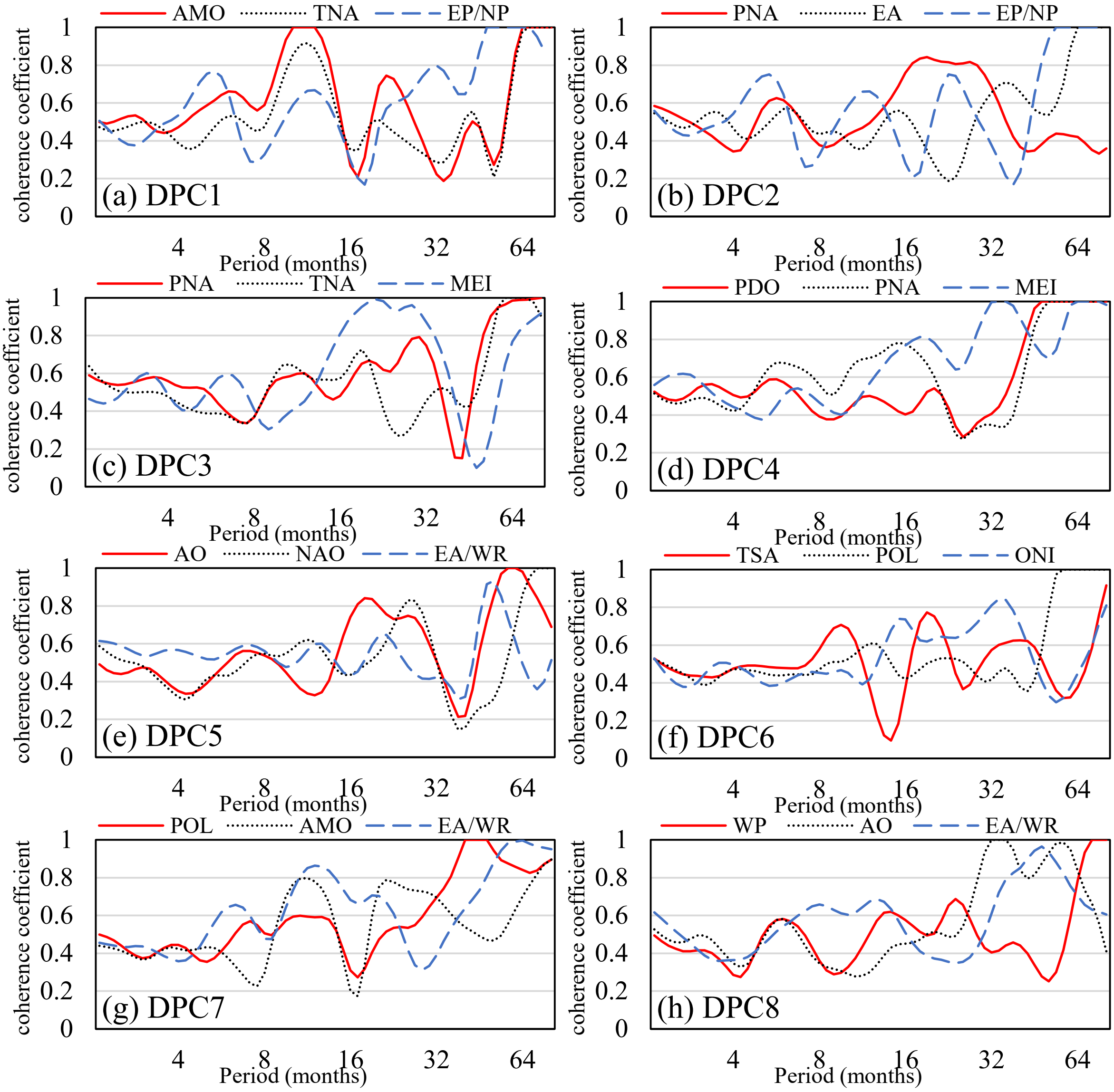

Figure 4.8 The global coherence coefficient between atmospheric-oceanic indices and the temporal patterns of DPC1~8.

Figure 4.9 summarizes the combinations of the top three atmospheric-oceanic indices that explain global burned area pattern variations. From Figure 4.9(a), the interactive effect of AMO-TNA on DPC1 at 8~16 months and the interactive effect of AMO-TNA-EP/NP on DPC1 at 64 months can be identified. Nevertheless, for DPC9 (Figure 4.9(h)), only WP showed significant coherence at 64 months, and the interaction effect of WP-AO-EA/WR on DPC1 became insignificant at 64 months. Consequently, when atmospheric-oceanic indices show the same periodicity or have significant impacts on DPCs at the same period frequency, the interactive effect of atmospheric-oceanic indices will strengthen this influence relationship on DPCs. Conversely, when the interaction between atmospheric-oceanic indices is insignificant, multifactor coherence will reduce the impact of atmospheric-oceanic indices on DPCs.

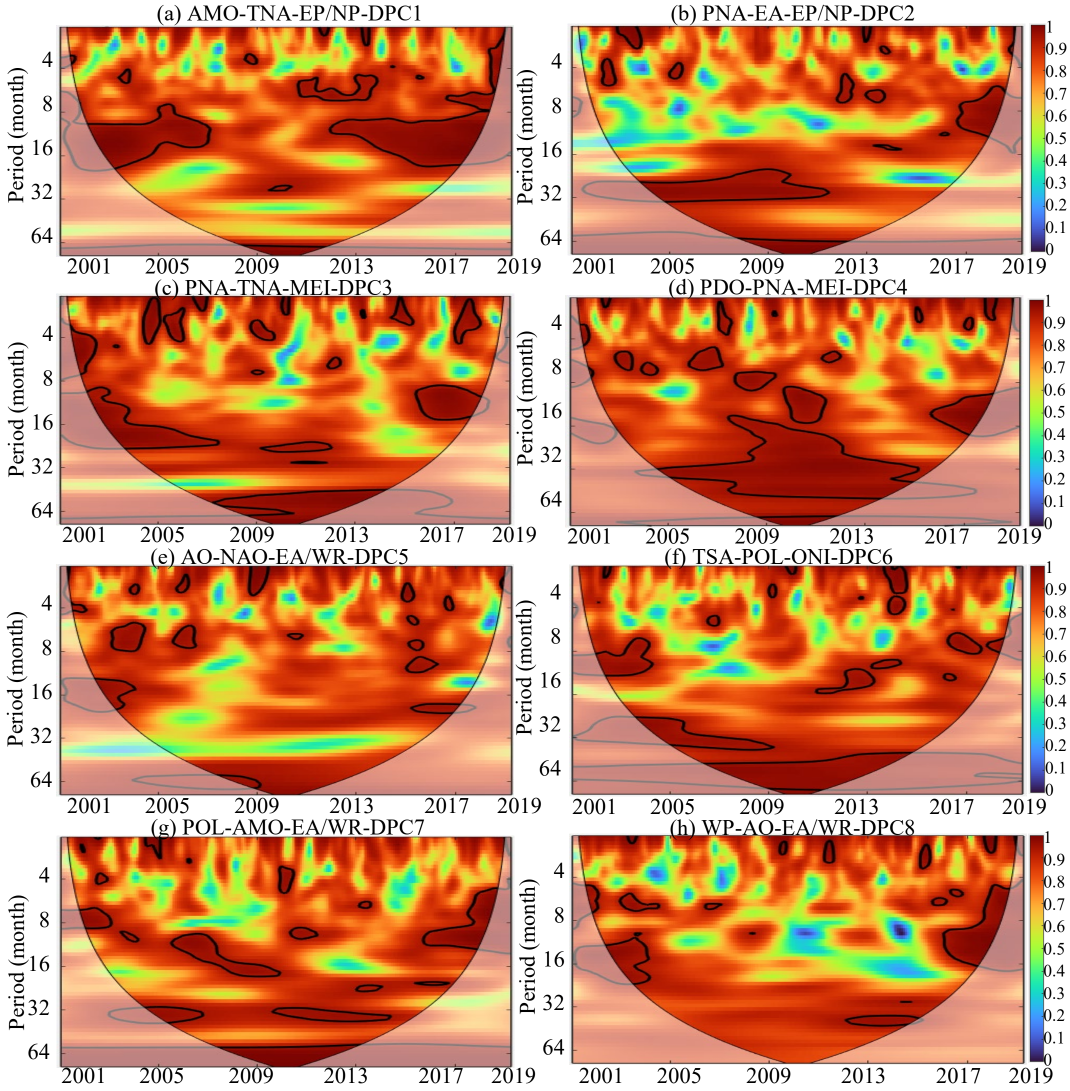

Figure 4.9 Three-factor multiple wavelet coherence between the top three atmospheric-oceanic indices and the temporal patterns of DPC1~8. The black contour designates the 95% confidence level against red noise, and the COI, where edge effects might distort the picture, is shown as a lighter, paler shade. The y-axis represents the coherence period, and the color represents the level of the coherence coefficient.

4.3 Discussion

Overall, our teleconnection research has shown how atmospheric-oceanic indices influence worldwide burned area patterns, therefore providing a means for predicting burned areas. In terms of worldwide patterns of burned area, heterogeneity is quite apparent. These hotspots, such as the regions around Ukraine and Kazakhstan, Australia, and Brazil, regularly emerge in various worldwide burned area patterns. Similarly, the regions around Ukraine and Kazakhstan, as well as a portion of Australia, were identified as hotspots for the simultaneous occurrence of wildfires and heatwaves (Ridder et al., 2020). In addition, most of the locations mapped by Sungmin et al. (2020) for the largest monthly burned area percentage from 2001 to 2018 were similar to the hotspots observed in our research. Even while there was not a substantial extensive burned area in the Ukrainian region, there were significant burned area anomalies.

The most significant combinations of hotspots and atmospheric-oceanic indices were AMO-EP/NP-PNA with the pattern around Ukraine and Kazakhstan, ENSO-AO-EA/WR with the pattern in Australia, and PNA-AO-POL-EA/WR with the pattern in Brazil, in terms of relationships between wildfire and atmospheric-oceanic indices. For instance, Figure 4.10 depicts the land cover of hotspot-1 (Ukraine and Kazakhstan). It can be observed that the Ukrainian area consists mostly of agriculture interspersed with various kinds of woodland. In addition, after the dissolution of the Soviet Union (Alcantara et al., 2013), the amount of abandoned agriculture in Ukraine has continued to rise. These abandoned croplands were particularly susceptible to wildfires due to the fast vegetation growth and fuel accumulation (Zambon et al., 2019). It should be emphasized, however, that the 1° resolution utilized in our wildfire pattern makes it easy for agriculture, abandoned cropland, and woodland to show on the same grid. For this reason, log transformation and analysis of burned area anomalies will minimize the human effect on agricultural burning and concentrate on uncontrolled fires in abandoned cropland and forest regions.

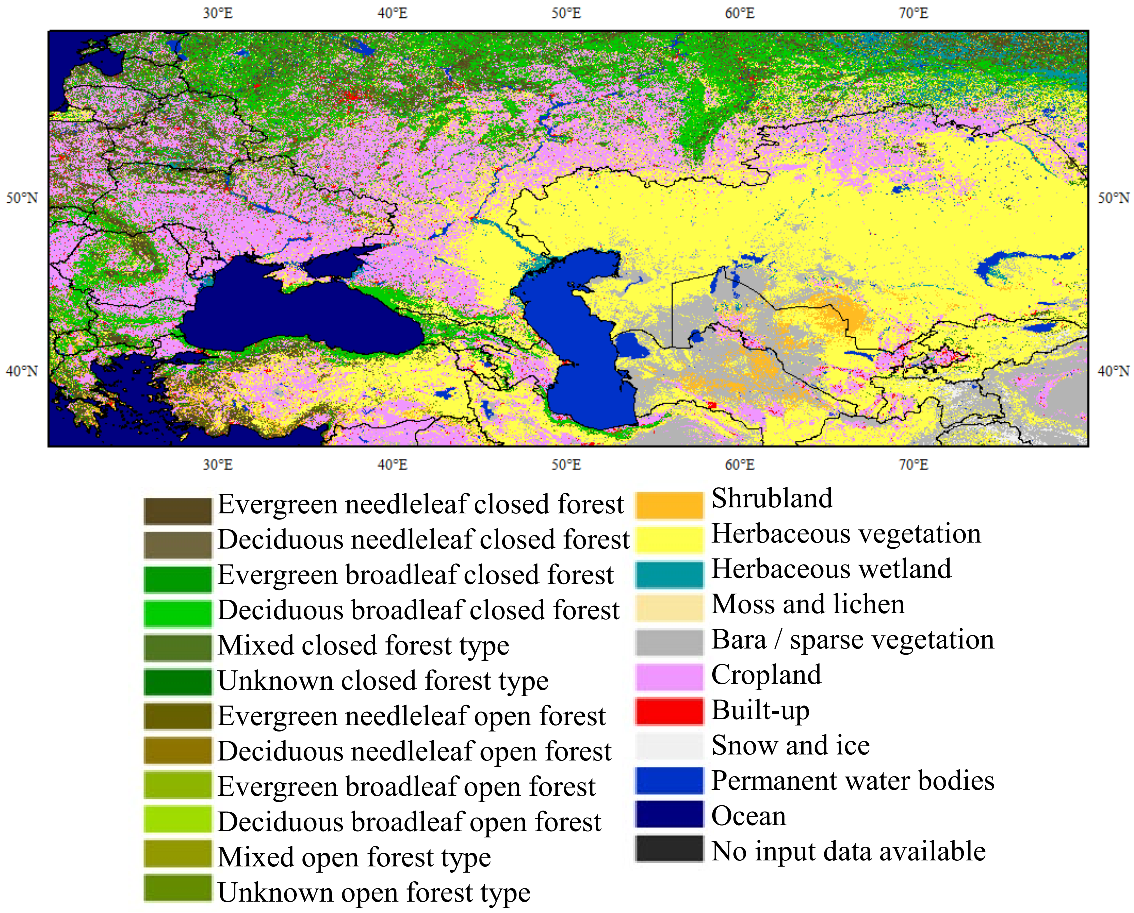

Figure 4.10 Land cover map of hotspot-1 (around Ukraine and Kazakhstan).

After a warm winter caused by AMO, a considerably greater sea level pressure and geopotential height in the summer of Eurasia will be noted for the coupling of AMO with the pattern surrounding Ukraine and Kazakhstan (Gao et al., 2021). The high sea level pressure associated with descending atmospheric motion can result in the possibility of favoring fewer clouds and precipitation, more incoming solar energy, and an increase in the pace of warming (Betts, 1973; Gao et al., 2021). The findings of the broad time scale coherence between AMO and wildfires may be questionable over longer periods owing to the availability of global wildfires, which is a limitation of our research. AMO itself really has a well-known periodicity characteristic of more than 60 years (Ionita et al., 2013; Schlesinger et al., 1994). On a decades scale, there was a considerable consistency between the AMO and European temperatures (Buchhorn et al., 2020). Larger-scale coherence between the AMO and wildfire is more likely to be found as the time series of wildfire data becomes longer.

A significant correlation between ENSO and burned areas was discovered in northern Australia (Harris et al., 2008). But as shown in Figure 4.11, unlike forest wildfires in southeastern Australia (Attiwill et al., 2013), wildfires in grasslands are more common in northern Australia (Rossiter et al., 2003). In northern Australia, a lot of grassland serves as fuel for wildfires. And there is a well-known cycle of grass and wildfires (Prior et al., 2011). Wildfires damaged the vegetation, but rain enabled new flora to reemerge where it had been burned away. The significance of precipitation for the cycle of grass and wildfires in northern Australia is obvious. Given the apparent link between ENSO events and precipitation in northern Australia (Harris et al., 2008), ENSO events presumably influenced precipitation in northern Australia, which tended to influence wildfire anomalies.

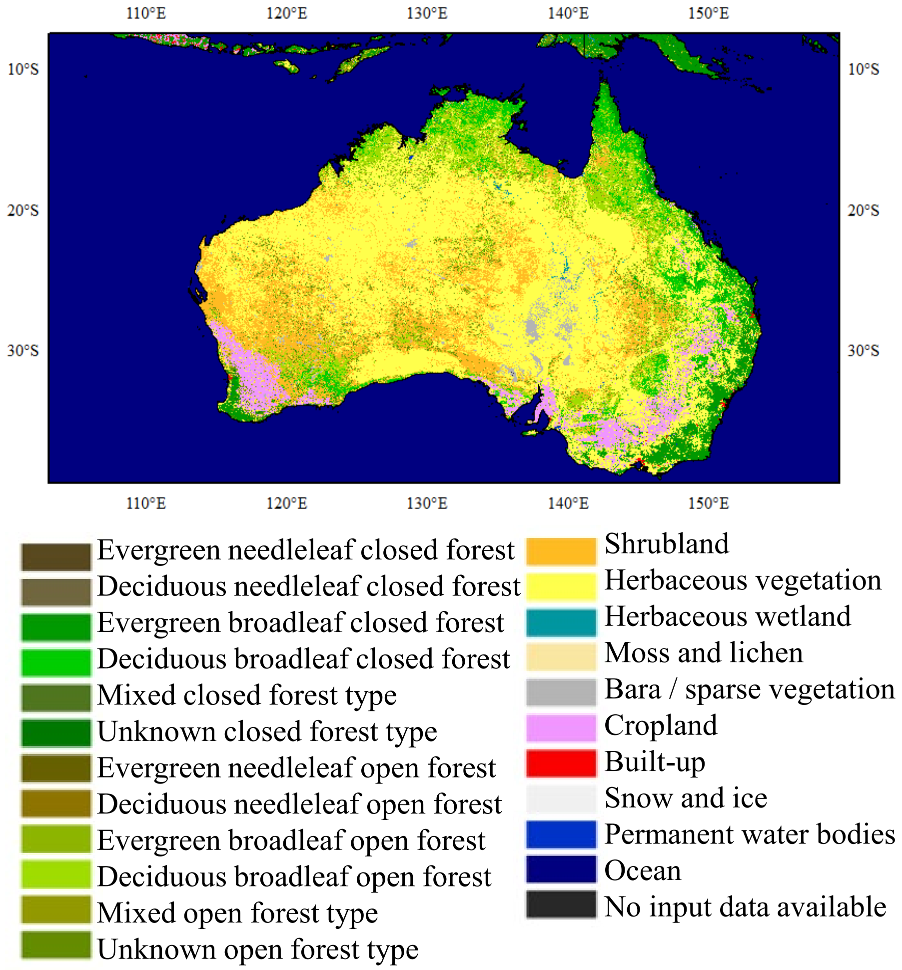

Figure 4.11 Land cover map of hotspot-2 (Australia).

Figure 4.12 depicts the vegetation types in hotspot-3. Broadleaf forests, shrubland, and herbaceous vegetation predominate, with farmland making up a tiny portion of the vegetation types. The mixed-vegetation regions of Mato Grosso, Mato Grosso do Su, Tocantins, and Goiás in central Brazil had more anomalous burned areas than the vast tropical rain forests in northern Brazil. The biggest wildfire outbreaks occur in illegal deforestation regions, particularly in Mato Grosso (Rossi et al., 2020). However, the climate has a greater direct influence on Brazilian wildfires than human activity because favorable weather conditions are a precondition for human-induced wildfires (Silvestrini et al., 2011).

Regarding the PNA-Brazil, equatorial central and eastern Pacific sea surface temperature anomalies were inversely linked with precipitation over Northeast Brazil from March to May (Uvo et al., 1998). Pacific sea surface temperature anomalies primarily have two effects on Northeast Brazil's precipitation: one is a direct process by which the location of the Atlantic Intertropical Convergence Zone is influenced by anomalous Walker circulation (Giannini et al., 2001; Uvo et al., 1998); another way is by a covert process using an air bridge resembling the PNA pattern, which causes anomalies in tropical North Atlantic sea surface temperatures and shifts the location of the Atlantic Intertropical Convergence Zone (Nobre et al., 1996). Heavy precipitation and cumulus clouds are often associated with the Atlantic Intertropical Convergence Zone. (Schneider et al., 2014). In other words, PNA has an impact on precipitation anomalies, which in turn has an impact on the wildfire danger of hotspot-3.

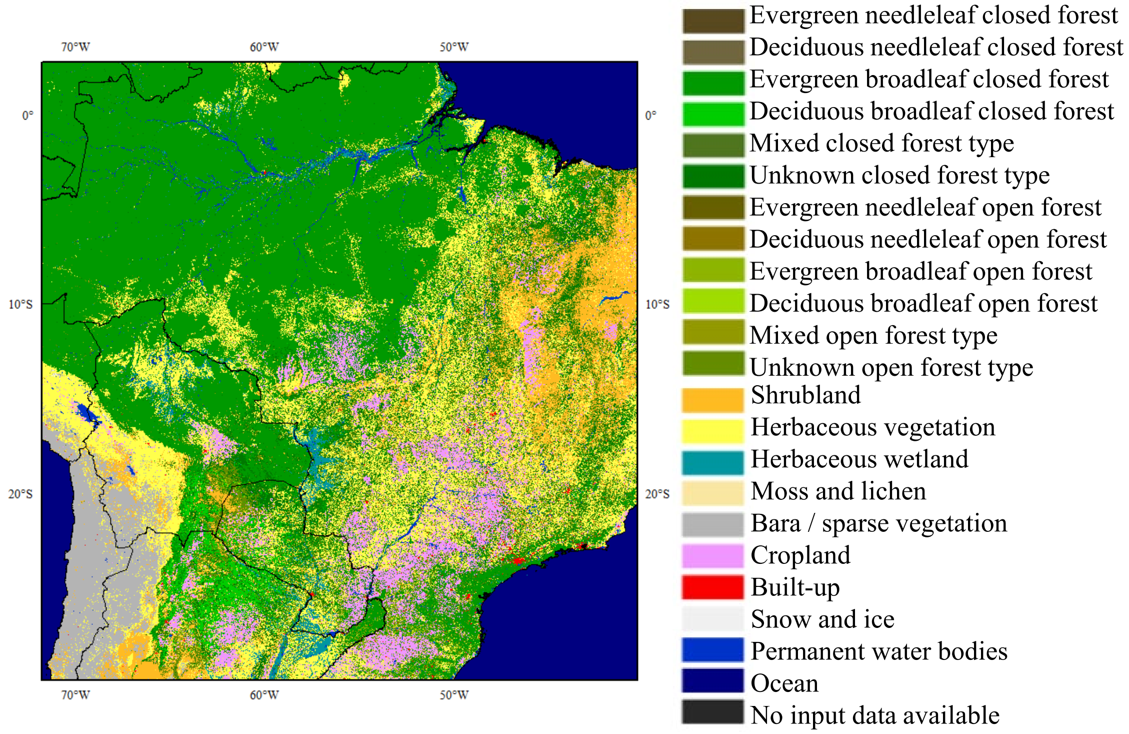

Figure 4.12 Land cover map of hotspot-3 (Brazil).

4.4 Summary

This chapter demonstrated for the first time the teleconnection between atmospheric-oceanic indices and burned area patterns, investigating the physical mechanism behind their teleconnection from a global viewpoint. Under the combined effect of the Atlantic Multidecadal Oscillation (AMO) and a rise in abandoned agriculture, the hotspot-1 (around Ukraine and Kazakhstan) has shown anomalies of burned areas. The burnt area of hotspot-2 (Australia) varies due to the inter-annual volatility of ENSO. In hotspot 3 (Brazil), hydro-meteorological conditions are still a prerequisite for human-caused wildfires. These findings contribute to a greater comprehension of the spatiotemporal aspects of the global burned area. The results will also be useful for wildfire management, wildfire prevention, and the ecological climatology of global wildfires.

Chapter 5 A New Approach to Describing the Wildfire Extremes Illustrated by the Example of the Contiguous United States

This chapter was under review in the International Journal of Wildland Fire: Ke Shi, and Yoshiya Touge. "Probabilistic Assessment of Burned Area and Wildfire Activity Considering the Wildfire Bivariate Statistical Characteristics in the Continental United States".

5.1 Introduction

Wildfires constitute a critical ecological process in the natural Earth system associated with regional and global biogeochemical cycles, human activities, and vegetation structure (Bowman et al., 2009). Also, wildfire, as a major agent of soil erosion and land degradation, has been suggested as the most significant factor of geomorphological change (Shakesby, 2011). The post-fire effect on vegetation cover, physical properties of soil, and biological activity changes with the characteristics of wildfire (Efthimiou et al., 2020). Therefore, before discussing the post-fire effect, a comprehensive perspective is essential to elucidate what kind of wildfire has a higher severity or risk, especially in the United States, which hosts 823 million acres of forest- and woodland areas (Brashaw et al., 2021). Over just four years, from 2017 to 2020, nearly 200 lives were lost, and more than 45,000 structures were destroyed in California wildfires (Brashaw et al., 2021). In particular, wildfires with large burned areas have increased in the western United States in recent years (Dennison et al., 2014; Zhang et al., 2020). Subjectively, more wildfire activities could lead to more severe wildfires and larger burned areas. However, the reduction in wildfire activities (number of wildfires) driven by policy and wildfire management has resulted in changes in the vegetation structure and an increase in fuel accumulation in the western United States (Hurteau et al., 2014). As a consequence, wildfire suppression and the subsequent increase in fuel loads have coincided with warmer and drier wildfire seasons, causing high-severity wildfire events yielding large burned areas (Dennison et al., 2014; Fulé et al., 2003; Holden et al., 2018; Steel et al., 2015) . These two seemingly contradictory situations are attributed to the unique relationship structure between the wildfire activity and burned area, posing challenges for assessing the wildfire characteristics comprehensively.

In particular, to describe the relationship among wildfire statistics in detail, this study first provides a concept map of wildfire bivariate statistical characteristics, as shown in Figure 5.1. Three lines control the wildfire bivariate statistical characteristics—the wildfire increase vector (WIV), wildfire extent vector (WEV), and wildfire extreme line (WEL). Assuming that every wildfire event is immediately detected and controlled, even if each wildfire event is associated with a statistically minimum burned area, the burned area moves linearly upward along the WIV with increasing wildfire activity. Notably, the wildfire activity and burned area attain a positive correlation near the WIV. For example, a strong positive correlation between wildfire activity and the burned area was demonstrated in parts of the western United States (Cattau et al., 2020), Portugal (Moreira et al., 2010), Australia (Adams, 2013), and Africa (Ramo et al., 2021). In contrast, lower-frequency wildfire activities near the WEL could lead to a larger burned area because lower-frequency wildfire activities could increase fuel load accumulation and wildfire risk. For example, forests in Arizona (Fulé et al., 2003), California, Nevada (Miller et al., 2009), and the southwestern United States face low-frequency wildfires yielding large burned areas (Hurteau et al., 2014). Additionally, with increasing wildfire activity, the length of the WEV gradually decreases. Given a single wildfire event, the burned area achieves the largest range of WSL variation. Under the influence of different meteorological conditions and human activities, wildfires can be extinguished before spreading or become mega-wildfires.

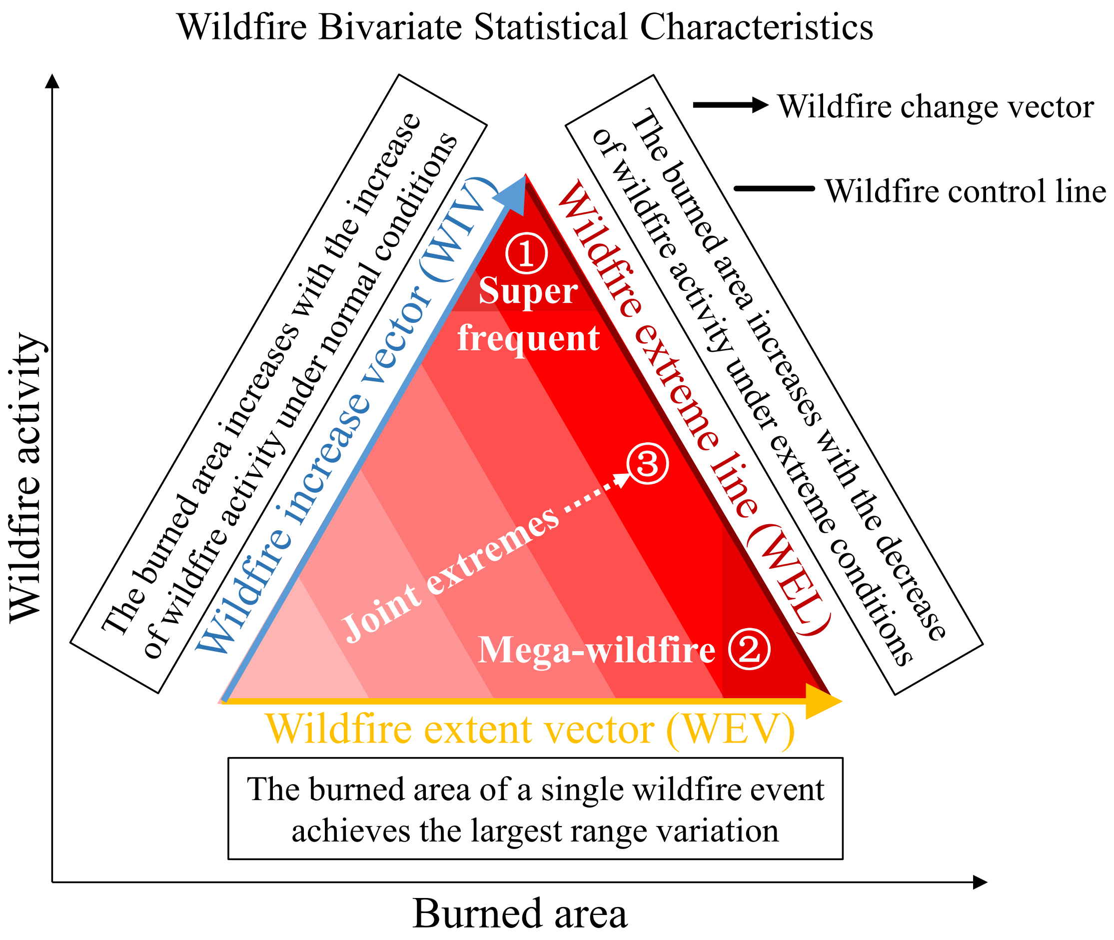

Figure 5.1 Concept map of wildfire bivariate statistical characteristics.

The above unique wildfire bivariate statistical characteristics interacting with the nexus of wildfires, weather, soil, vegetation, and human activities pose challenges in explaining the impact of wildfires and assessing the wildfire risk (Black et al., 2016; Goodrick et al., 2017; Martin, 2016; Neary, 2019). In general wildfire risk analysis, a wildfire has often been characterized by its severity, intensity, and soil burn severity from a single wildfire event (Keeley, 2009). Simultaneously, wildfires can also be characterized by wildfire activity (Mozny et al., 2020) and burned areas (Jiang et al., 2020; Wu et al., 2021) at annual and monthly scales. For example, the relationship between the return period (RP) of wildfire activities and the mean rainfall, vegetation type, and effects of grazing herbivores was analyzed (O'Connor et al., 2011). Their results clarified that the RP of wildfire activities decreased with increasing mean annual rainfall in a semiarid African savanna (O'Connor et al., 2011). A wildfire risk map was also proposed by determining the wildfire RP under different burned area thresholds (Oliveira et al., 2012). Nevertheless, current research has often only focused on univariate wildfire characteristics in risk analysis, which is inadequate to describe wildfires' multivariate phenomenon probabilistic properties accurately. Moreover, it is difficult to evaluate the wildfire risk in which year or month is higher from a comprehensive perspective. Accordingly, this study aims to perform a wildfire risk assessment considering the wildfire bivariate statistical characteristics.

For disaster analysis, research on the derivation of bi- and multivariate joint distributions of hydro-meteorological elements has been extensively carried out in statistical hydrology and statistical climatology. The copula theory is the most widely adopted method to derive joint distributions (Sklar, 1959). Copulas are mathematical functions that build a multivariate joint distribution considering the dependence structure among variables (Nelsen, 2003, 2007), regardless of their univariate distributions (Genest et al., 2007). For example, Zheng et al. (2015) proposed a method to assess the coastal flooding risk by constructing the joint probability distribution of extreme precipitation and storm tides. Yang et al. (2018) constructed a nonlinear multivariate drought index through the 3-dimensional theoretical joint cumulative probability considering three drought indices (meteorological drought, hydrological drought, and agricultural drought) in the Wei River Basin, China. The joint return period of the drought duration and severity was also analyzed based on the Bayesian framework in California, United States (Kwon et al., 2016). Li et al. (2015) applied the copula theory and determined the behavior of precipitation extremes considering the co-occurrence of extremely high and low precipitation under historical and future scenarios. Unfortunately, due to the unique wildfire bivariate statistical characteristics, the relationship between wildfire variables is more complicated than that between traditional hydro-meteorological elements. The application of a similar copula approach to wildfire characteristics remains inadequate. It will only consider joint wildfire events and may overlook single mega-wildfire events (as indicated by zone 2 in Figure 5.1) (an extraordinary wildfire devastating a large area (Westerling et al., 2006; Williams, 2013)) and super frequent wildfires (as shown by zone 1 in Figure 5.1). This occurs because the copula approach considers wildfire events as joint extremes only when the burned area and wildfire activity are both notable (as revealed by zone 3 in Figure 5.1). Notably, mega-wildfires are unprecedentedly destructive. One mega-wildfire, the 2017 Thomas Fire in California, burned approximately 114 thousand ha and directly threatened approximately 262,407 people with the potential for fire damage in or near cities (Kress, 2020). Similar disasters are not regarded as high-risk disasters in joint frequency analysis through the copula approach because of the limited number of wildfire activities. Therefore, single wildfire characteristics and the direct application of copula theory are both insufficient to reveal the complicated wildfire bivariate statistical characteristics, and the wildfire risk cannot be accurately assessed. To overcome this issue, another objective of this study is to construct a probability distribution of the wildfire priority (WP) to comprehensively measure the wildfire risk through the weighted average of the univariate and joint probabilities of wildfire statistics.

Accordingly, this chapter simultaneously focuses on the univariate extreme probability distribution of wildfire characteristics and copula-based bivariate probability distribution considering the wildfire activity and burned area. First, we determine the univariate distribution of these two target wildfire characteristics. Correspondingly, zones 1 and 2, as shown in Figure 5.1, are identified as priority events in terms of the wildfire activity and burned area, respectively. Second, we calculate the joint probability of the wildfire activity and burned area according to a copula-based joint distribution. In particular, zone 3 is considered a joint priority event. Then, the weighted average method is applied to balance the copula-based bivariate and univariate probability distributions to calculate the WP probability. If the same weight is assigned to zones 1, 2, and 3 in WP analysis, these three situations are comprehensively considered. If zone 3 is assigned a higher weight in WP analysis, mega-wildfires can be better considered, which agrees with the definition of severe disasters. In this manner, a comprehensive method for wildfire risk assessment is proposed. Finally, this WP analysis approach can explore the spatiotemporal variability and trends of wildfire risk. Since the contiguous United States is experiencing increasingly extreme wildfires, this region is selected as the study area.

5.2 Results

5.2.1 Overall wildfire conditions in the contiguous United States

To better understand the spatiotemporal characteristics of wildfire statistics in the contiguous United States, the total monthly burned area and monthly wildfire activities in the United States are first obtained, as shown in Figure 5.2. There occurs an increasing trend of the burned area. The two most notable wildfire months both occurred after 2010. Especially in August 2018, the burned area in the United States reached as large as 4.18 billion m^2 within a month. Conversely, wildfire activity exhibits a decreasing trend. Notably, the wildfire activity in August 2018 and July 2015 was much lower than that in March 2006, at 13.86 thousand events.

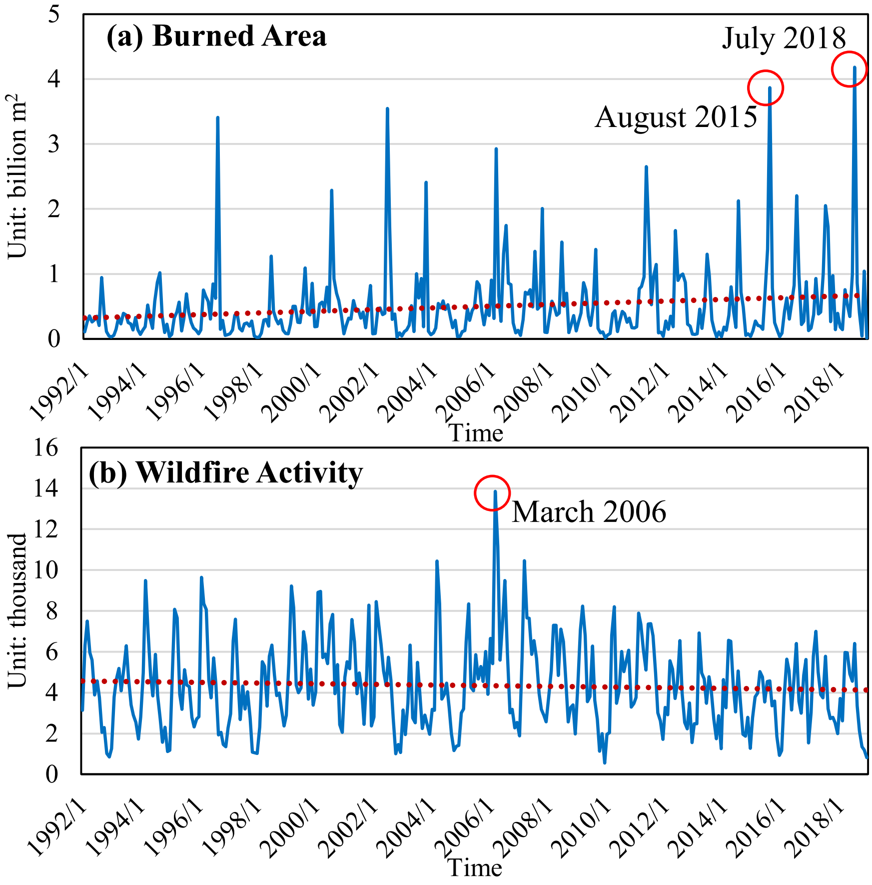

Figure 5.2 Time series of spatial total wildfire statistics for the United States.

Then, Figure 5.3 shows the total burned area and monthly wildfire activities in each grid cell to indicate the spatial distribution of wildfire statistics. Grid cells with large burned areas are mainly distributed in California, and some grid cells are scattered in Oklahoma and the junction of Kentucky and West Virginia. California, Oklahoma, Mississippi, and Georgia contain high wildfire activity grid cells. California hosts many grid cells with high wildfire activity, indicating frequent wildfire events. The obtained spatial distribution of wildfire statistics clarifies that high-frequency wildfire events and large burned areas are not completely consistent. For example, although Georgia hosts grid cells with high-frequency wildfire activity, grid cells with large burned areas rarely occur.

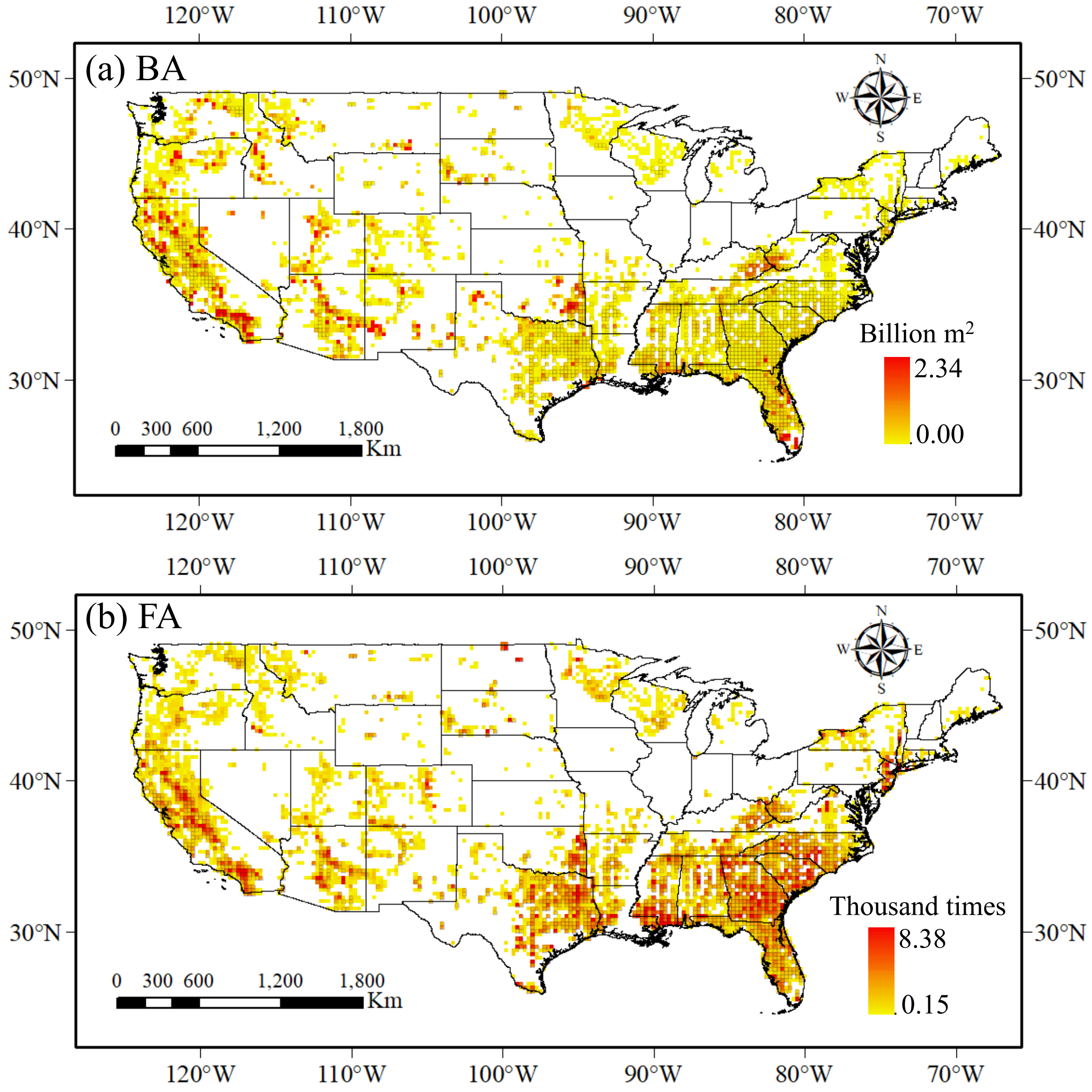

Figure 5.3 Temporal total wildfire statistics for the United States. The bordered grid cells are considered in frequency analysis. (a) burned area. (b) wildfire activity.

5.2.2 Selected univariate probability distributions

The first step for wildfire risk assessment is determining the optimal marginal distribution functions of monthly wildfire statistics (LFA and LBA) in wildfire bivariate statistical characteristics. Firstly, the distributions of wildfire statistics are shown in Figure 5.4. It can be seen that there is a right-skewed characteristic of the distribution of LBA, that is: mode value <median value <mean value. The distribution functions without a right-skewed structure (like the normal distribution) are not suitable for fitting the LBA in most instances. However, when the distribution is close to the minimum value, there is a finite positive slope in the LFA distribution. For such a structure, the three-parameter Weibull distribution can generally fit well. And the follow-up results indeed confirmed the previous conjecture.

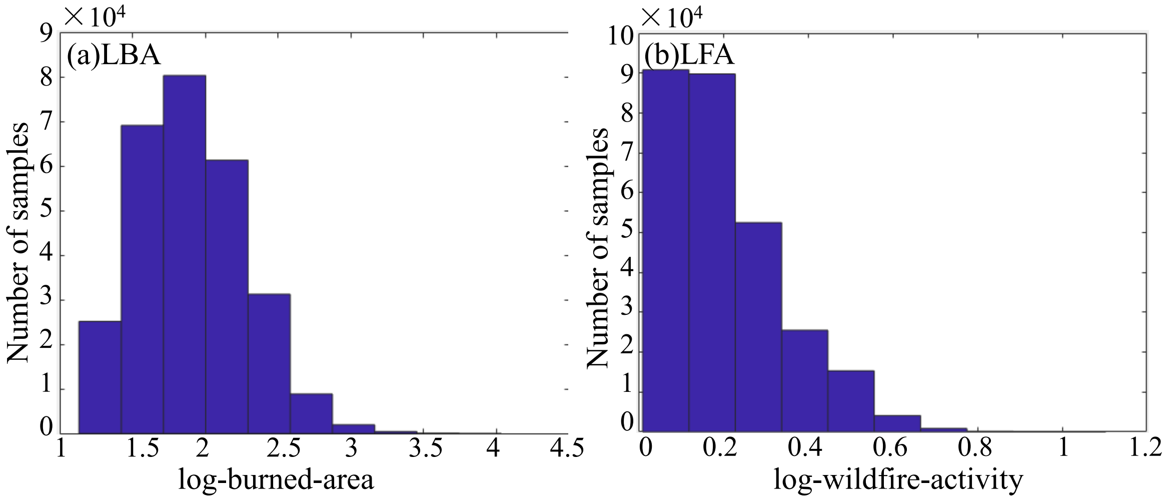

Figure 5.4 Distribution of wildfire statistics: (a) log-burned-area and (b) log-wildfire-activity

Seven marginal distribution functions were employed to fit monthly LFA and LBA values based on the L-moments approach. Afterward, according to the RMSE and PPCC, the optimal goodness of fit of six marginal distribution functions was calculated by comparing the theoretical cumulative probabilities of the LFA and LBA statistics. In contrast to traditional frequency analysis of hydro-meteorological elements, there was significant regionality in the statistical characteristics of wildfires under the influence of local climate conditions. Accordingly, this study did not choose the same marginal distribution function to fit the entire study area but determined the best distribution function for each grid cell. Grid cells with the largest monthly burned area and highest wildfire activity in the continental United States were chosen as an example to explain the determination process of the optimal marginal distribution functions.

The smallest RMSE and largest PPCC values represent the best goodness-of-fit of the selected marginal distribution function. For example, given sample 2 (as indicated in Table 5.1), the values of the two evaluation indices of the Weibull (WEI) distribution are RMSE=0.0954 and PPCC=0.9844. Therefore, a WEI distribution with α =1.5452, β = 3.4592, and γ =3.5551 is the most appropriate marginal distribution function to fit the monthly LBA values in sample 2. Similarly, a generalized extreme-value (GEV) distribution with α=4.3182, β=0.9755, and γ=0.2863 is the most appropriate marginal distribution function to fit the monthly LFA values in sample 2.

Table 5.1 Goodness-of-fit criterion results of the marginal distribution functions and parameters of sample 2.

Type	Function	Parameters			Goodness-of-fit indices	
		α	β	γ	RMSE	PPCC
LBA	GEV	4.3182	0.9755	0.2863	0.0956	0.9841
	GUM	4.2007	0.7961	/	0.1623	0.9479
	GLO	4.6614	0.5518	0.0014	0.1245	0.9649
	NOR	4.6602	0.9780	/	0.1073	0.9806
	WEI	1.5452	3.4592	3.5551	0.0954	0.9844
	P-III	4.6602	0.9780	-0.0085	0.1072	0.9806
	EXP	3.5566	1.1036	/	0.2568	0.8838
LFA	GEV	1.0869	0.7035	0.2641	0.1358	0.9677
	GUM	1.0084	0.5809	/	0.1405	0.9620

Type	Function	Parameters			Goodness-of-fit indices	
		α	β	γ	RMSE	PPCC
	GLO	1.3364	0.4026	-0.0110	0.1835	0.9181
	NOR	1.3437	0.7137	/	0.1703	0.9416
	WEI	-0.7775	2.3650	3.2927	0.1689	0.9517
	P-III	1.3437	0.7138	0.0678	0.1735	0.9493
	EXP	0.5384	0.8053	/	0.2863	0.8257

Analogously, the spatial distribution of the selected univariate probability distributions of the monthly LBA and LFA statistics is shown in Figure 5.5. About the monthly LBA, the WEI distribution is the most applicable to the entire grid of the United States, reaching 57.7%, followed by the GEV distribution with 25.6%. Notably, the grid cells under the GEV distribution are mainly concentrated in the central and eastern parts of the United States. The optimal marginal distributions for 9.2% and 5.6% of all grid cells are the Pearson type III (P-III) and generalized logistic (GLO) distributions, respectively. The other four distributions (exponential (EXP), Gumbel (extreme-value type I) (GUM), and normal (NOR) only apply to 1.9% of the total grid. For monthly LFA, the WEI distribution occupies a dominant position, accounting for 83.5% of all grid cells. In contrast to LBA, the second best distribution of LFA is the P-III distribution, accounting for 8.3% of all cells. The GEV, GLO, and EXP distributions accounted for 3.8%, 3.4%, and 1.0%, respectively. These distribution optimization results illustrate that the NOR and GUM distributions are completely unsuitable for monthly LFA.

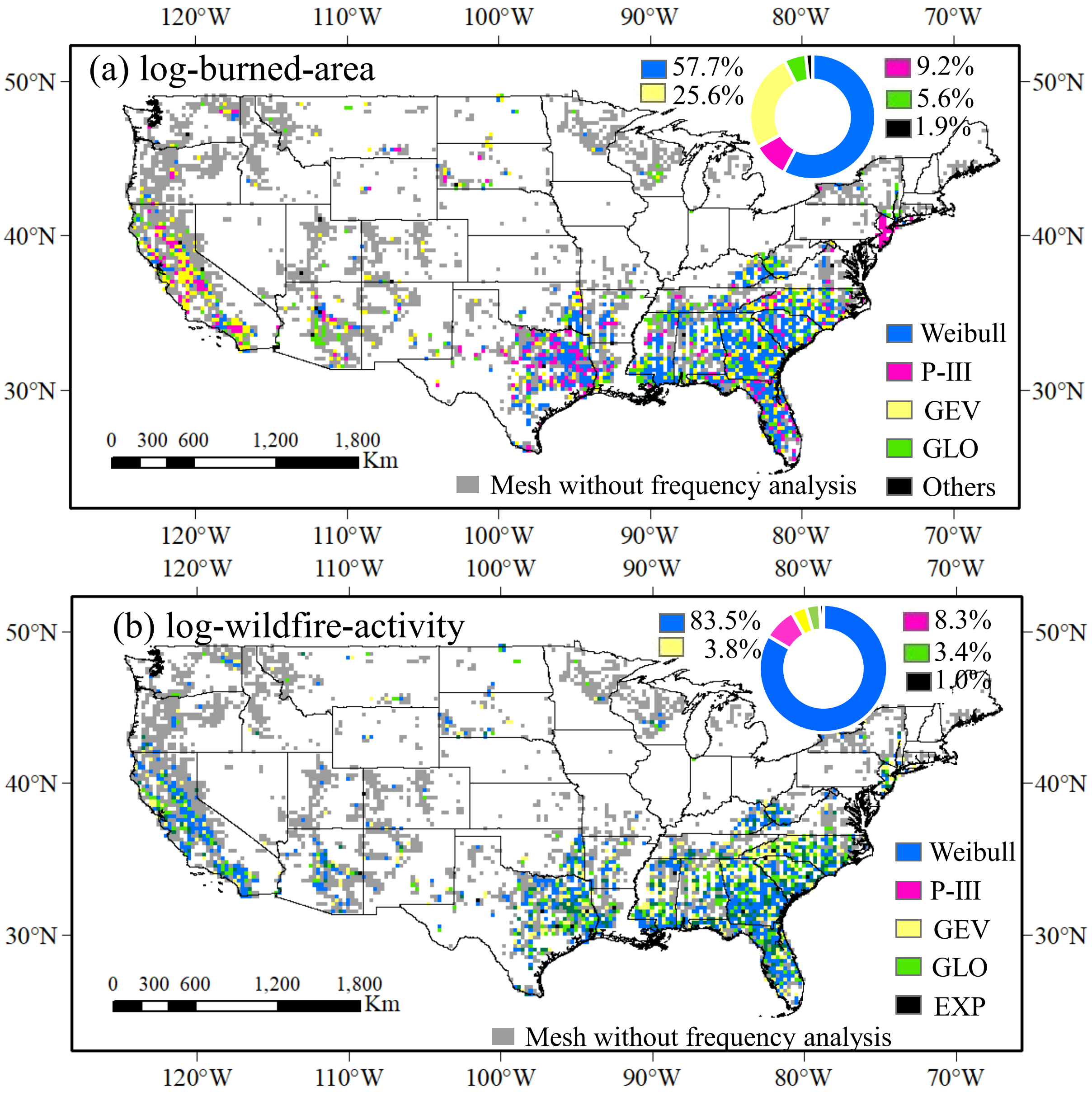

Figure 5.5 Spatial distribution optimal univariate probability distribution function. In particular, regarding LFA, only five distributions pass the optimization step.

5.2.3 Differences in choosing the various copula functions

The choice of the joint function can affect the final WP probability and the calculation of the RP. Therefore, it is necessary to evaluate whether the selection of the GUM function conforms to the underlying physical mechanism between LBA and LFA. The joint probability of Joint for sample 2 based on the different copulas is shown in Figure 5.6. Through optimization, the GUM function is considered the most suitable copula for sample 2. The isoline indicates the joint probability, and the different colors indicate the joint density. Independent copulas are not applicable in this analysis, so they are not discussed. Among the other five copulas, the probability isoline of the GUM function attained the highest inclination. In contrast, the probability isoline of the AMH function attained the lowest inclination, indicating that the correlation between LFA and LBA increased from AMH to GUM. Additionally, the GAU and GUM functions revealed characteristics whereby the upper tail was higher than the lower tail, while the other three copulas revealed opposite characteristics. Notably, in the GAU and GUM functions, LBA was correlated with the upper tail of LFA, and the lower tail became increasingly independent, demonstrating that the minimum LFA imposed little influence on LBA. At the same time, the maximum LFA exerted a significant influence on LBA. Frequent wildfire activities can lead to large burned areas, and their correlation can further increase. On the other hand, when fire activities do not frequently occur, fuel can more notably accumulate, which increases the possibility of large-scale wildfires. Under these circumstances, the correlation between wildfire activity and burned areas can weaken.

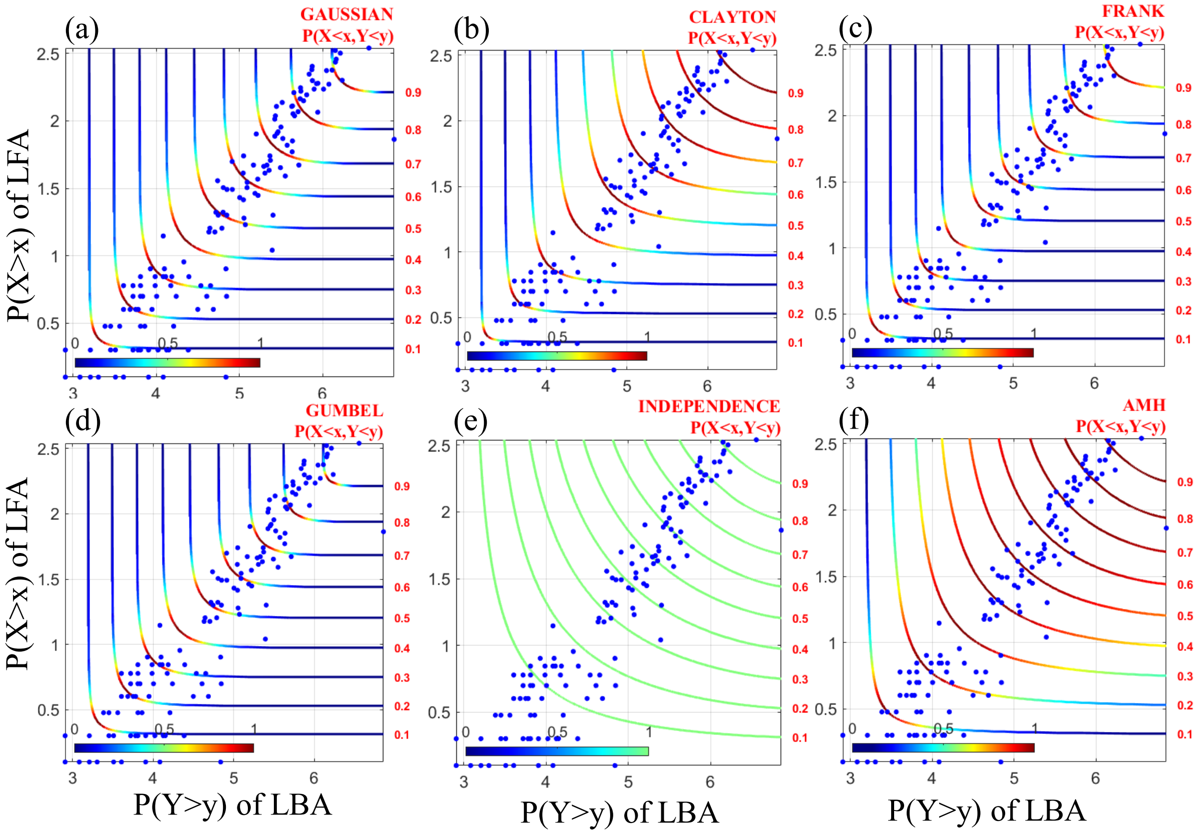

Figure 5.6 Joint probability based on the different copulas: choosing sample 2 as an example.

5.2.4 Selected joint probability distributions

After determining the optimal marginal distribution functions of the LBA and LFA data in each grid cell, six bivariate copulas were employed to fit joint distributions of these LBA and LFA data based on the Bayesian and MCMC approaches. Subsequently, according to the RMSE, AIC, and BIC, the optimal goodness-of-fit of these six bivariate copulas was calculated by comparing the theoretical joint cumulative probability between the LBA and LFA data. Similarly, the parameters of the bivariate copulas and goodness-of-fit of samples 1 and 2 are chosen as examples.

Small RMSE, AIC, and BIC values indicate the best goodness-of-fit of the selected bivariate copulas. Concerning sample 2 (as indicated in Table 5.2), the GUM distribution resulting in the smallest values of these indices, i.e., RMSE=0.1342, AIC=-1402, and BIC=-1399, was considered the most appropriate bivariate copula. The corresponding parameter is θ=4.1939.

Table 5.2 Goodness-of-fit criterion results of the joint distribution functions and parameters of sample 2.

Function	Parameter	The goodness of fit indices		
	θ	AIC	BIC	RMSE
GAU	0.9149	-1344	-1341	0.1619
CLA	3.2326	-1236	-1233	0.2298
FRA	16.5556	-1359	-1356	0.1544
GUM	4.1939	-1402	-1399	0.1342
IND	/	-608	-608	1.7508
AMH	0.9999	-757	-754	1.0745

In addition, the spatial distribution of the selected bivariate copulas of the monthly LBA and LFA is shown in Figure 5.7. The applicability of the Gaussian (GAU) function is the highest among the six alternative copulas, reaching 43.1%. The second most applicable copula is the Frank (FRA) function, reaching 22.5%, followed by the Clayton (CLA) function with 17.0%. Additionally, the GUM and Ali-Mikhail-Haq (AMH) functions account for 16.4% and 1.0%, respectively. As expected, the independent function is unsuitable in all grid cells, reflecting the correlation between LFA and LBA.

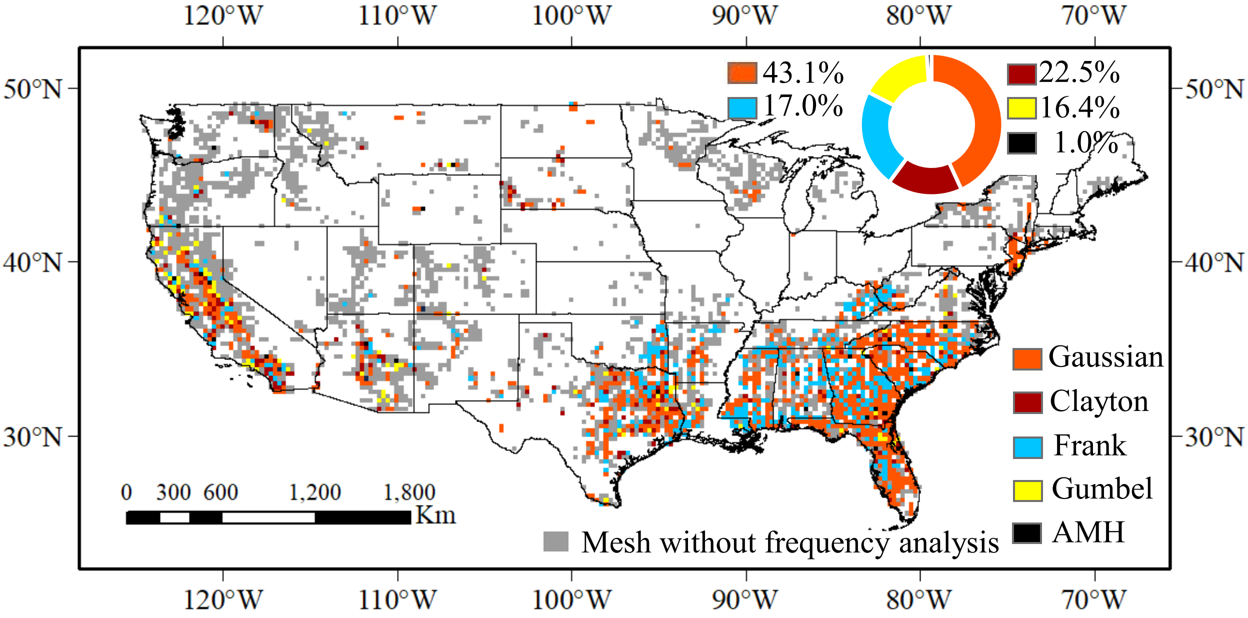

Figure 5.7 Spatial distribution optimal bivariate joint probability distribution function.

5.2.5 Spatiotemporal characteristics of the wildfire statistics

Figure 5.8 shows the relationship between LBA and LFA, and the color of the different points corresponds to the RP of these variables. The points in Figure 10 include all grid cells participating in frequency analysis, and the RP is calculated for each grid. First, the relationship between LBA and LFA reveals that there exists an approximately triangular boundary. Then, based on the RP, large RP values of LBA are mainly concentrated in the center-right and bottom-right of the triangle. Regarding the RP of LBA, the upper part of the triangle is the concentration area of large values. The RP of the LBA of super frequent wildfires is generally smaller than that of mega-wildfires. Because frequent wildfire activities make it difficult for fuel to accumulate, thus preventing the formation of a larger burned area. However, once the fuel is fully accumulated, even a single ignition event may cause a mega-wildfire.

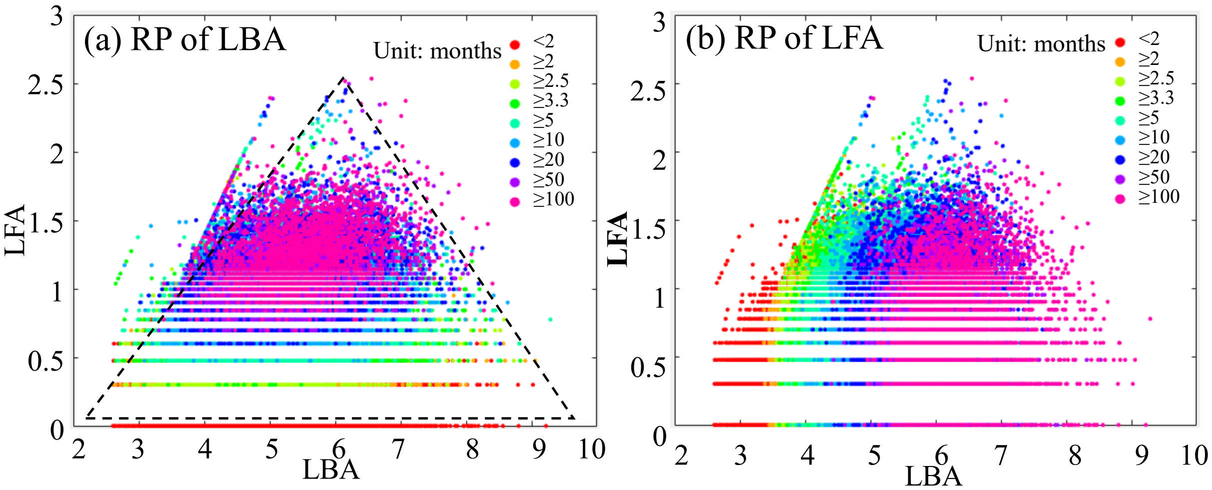

Figure 5.8 Relationship between the monthly LFA and LBA in the United States and the corresponding return period of the different variables. RP: return period (unit: months).

The optimal parameter C for WP is determined based on the selected univariate and bivariate joint probability distributions, as shown in Figure 5.9. The value of the large parameter C means that more weight is given to the mega-wildfire. But when the value of C exceeds 0.77, the objective function begins to decrease. In other words, the too-large parameter C will ignore most super frequent wildfires and further affect the ability of WP to assess wildfire risks.

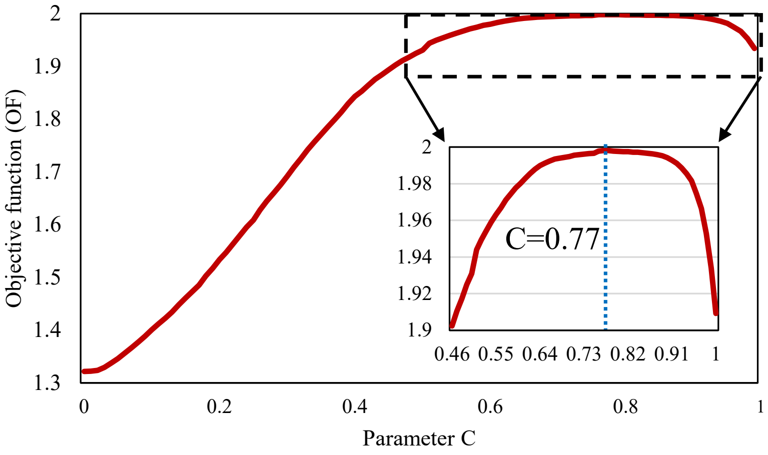

Figure 5.9 Optimal curve of parameter C. When the parameter C =0.77, the objective function has the optimal value.

To compare the wildfire assessment ability of the optimal WP in detail, Figure 5.10 shows the difference between Joint, WP-1(Control group: $\alpha=1/3$, $\beta=1/3$, and $\gamma=1/3$) and WP-2 (Optimal group: $\alpha=1/3$, $\beta=77/150$, and $\gamma=23/150$) in describing the wildfire risk through the probability and RP. Additionally, this study selected four representative samples to evaluate the advantages and disadvantages of these three different methods. Figure 5.10 demonstrates that the probability more sensitively measures the difference in extreme events (super frequent wildfires and mega-wildfires), while the RP is more sensitive to joint wildfire events. In other words, the probability can suitably represent the difference between Joint, WP-1, and WP-2 given the considered samples, while the RP is suitable for disaster risk trend analysis. Therefore, the $P(x>X, y>Y)$ of representative samples are listed in Table 5.3. Sample 1 represents super frequent wildfires resulting in a normal burned area. Ten wildfire events occurred within a month in the grid of sample 1 in February 2000. The corresponding $P(x>X, y>Y)$ values of WP-1 and WP-2 are 40.70% and 23.10%, respectively. WP-1 indicates that the priority of super frequent wildfires is higher than WP-2, but both perform better than Joint. Given sample 2, which exhibits both a burned area and wildfire activity associated with a large RP value in April 1998, there is a minor difference in the performance of the RP between WP-1 and WP-2, reaching more than 99% of $P(x>X, y>Y)$. The advantage of focusing on mega-wildfires is more significant in WP-2 when considering sample 3. Sample 3 contains the largest mega-wildfire in California history from 1992-2018, the Mendocino Complex Fire (Jia et al., 2020; Tentoglou et al., 2021). The total burned area due to the Mendocino Complex Fire reached almost 460 thousand acres, destroying over 280 businesses and homes (Yaloveha et al., 2019). The probability of such a mega-wildfire considering Joint and WP-1 is still lower than 50%, indicating that these two methods are insufficient in assessing mega-wildfires. In contrast, the probability of WP-2 is 67.26%, which is significantly higher than Joint and WP-1. Sample 4 attains a $P(x>X, y>Y)$ value of 99.04% for the burned area and a $P(x>X, y>Y)$ value of 90.06% for the wildfire activity. The burned area of sample 4 in April 1995 reached 34 thousand acres, which was the second-largest fire in the history of this sample. The performance of WP-2 is also better than WP-1, reaching a probability of 94.59%. Overall, both WP-1 and WP-2 perform better than Joint in assessing wildfire conditions. In particular, the advantage of WP-

2 is that mega-wildfires are assigned a higher priority.

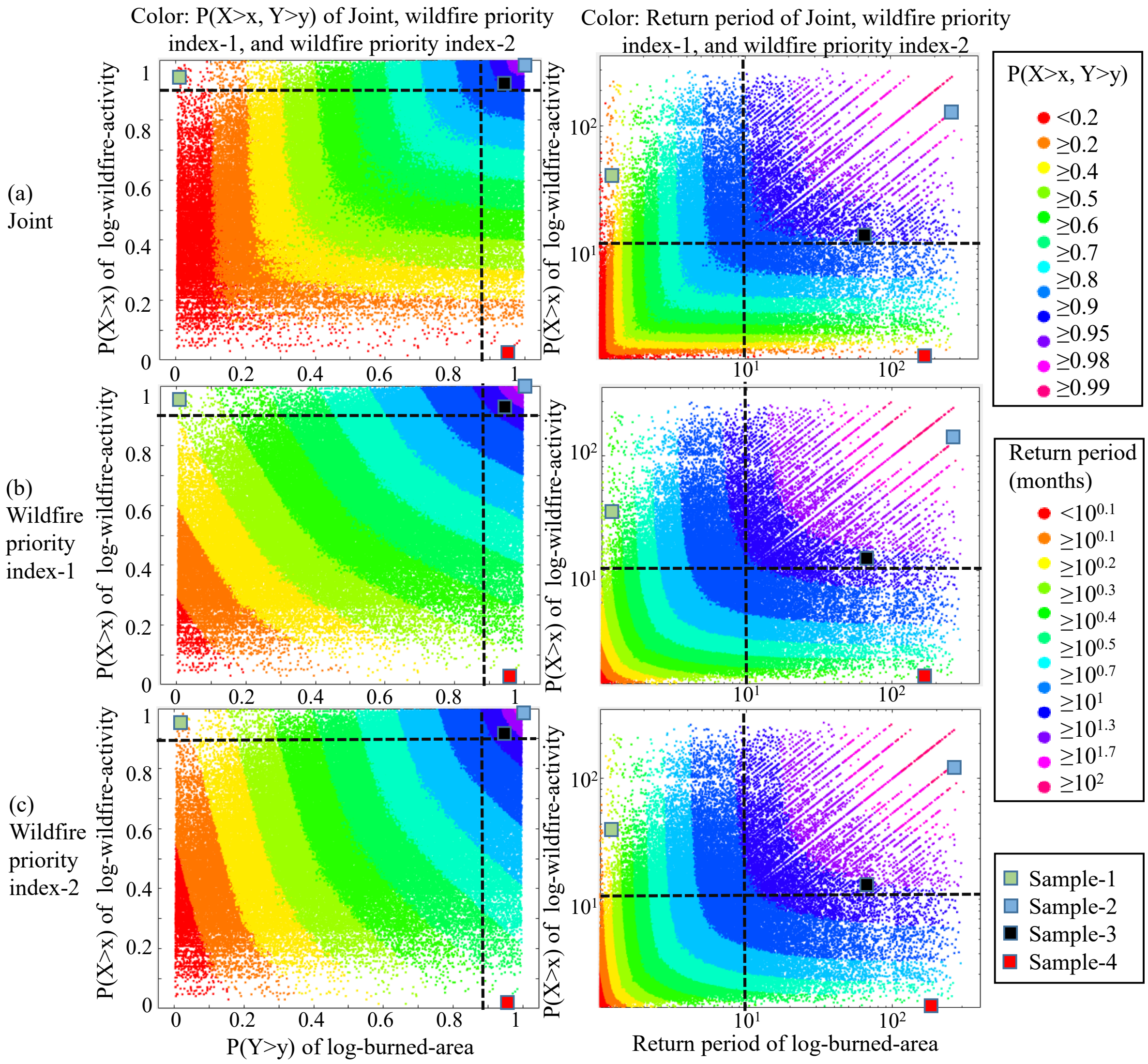

Figure 5.10 Comparison of the probability and return period between Joint, WP1, and WP2. WP1 is the control group: α=1/3, β=1/3, and γ=1/3. WP2 is the optimal group: α=1/3, β=77/150, and γ=23/150.

Table 5.3 P(x>X, y>Y) and return period of the four representative samples. The locations of the four sample points are shown in Figure 2.1.

	P of LBA	P of LFA	P of Joint	P of WP-1	P of WP-2	Date
Sample 1	1.39%	99.17%	21.55%	40.70%	23.10%	February 2000
Sample 2	99.03%	99.68%	98.72%	99.14%	99.03%	April 1998

	P of LBA	P of LFA	P of Joint	P of WP-1	P of WP-2	Date
Sample 3	99.56%	0.44%	48.25%	49.42%	67.26%	July 2018
Sample 4	99.04%	90.06%	89.81%	92.97%	94.59%	April 1995

Analogously, WP-2 is considered to assess the wildfire conditions in the United States comprehensively. According to the RP trends of WP-2, future wildfire risk changes can also be determined. In particular, the RP trends of WP-2 are shown in Figure 5.11. The results indicated that the RP of LBA exhibits a significant increasing trend in California, Texas, Kentucky, and Arkansas. Moreover, most of the southeastern United States exhibits significant decreasing trends. Overall, the RP of LBA significantly increased and decreased in 15.9% and 34.9% of all grid cells, respectively.

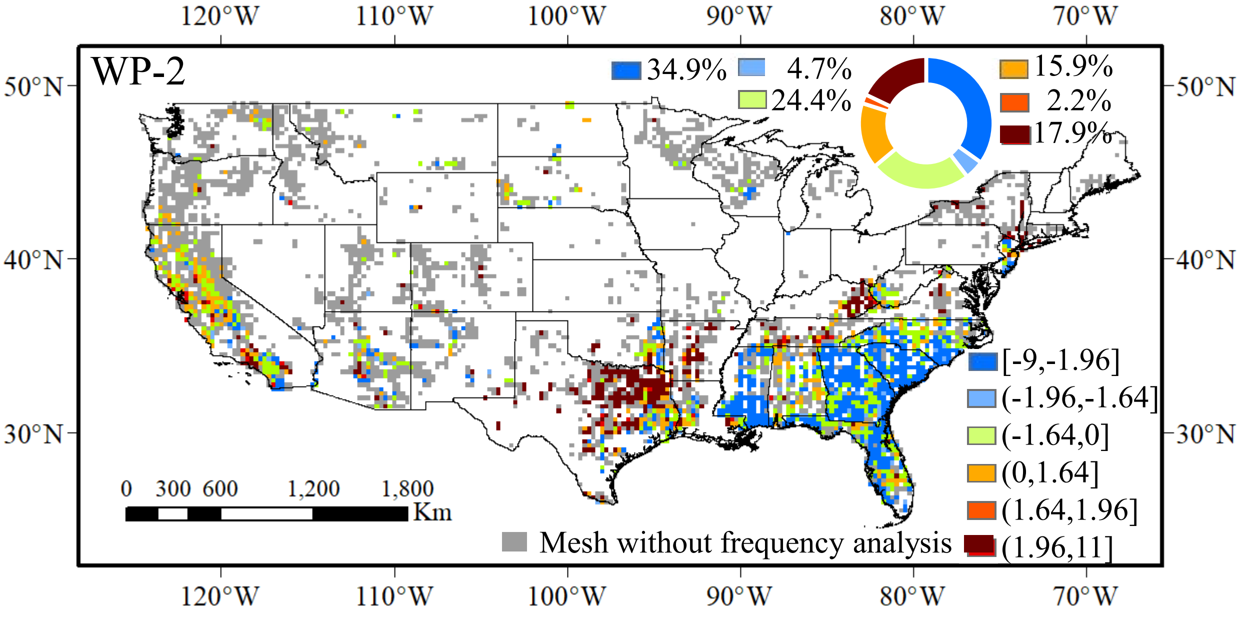

Figure 5.11 Return period trends of wildfire priority index-2 (WP-2).

5.3 Discussion

This study called for attention to the wildfire bivariate statistical characteristics and proposed a comprehensive framework for wildfire risk assessment based on these statistical characteristics. In this framework, different risk conditions in mega-wildfire events, joint extremes, and super frequent wildfires can be assessed, which is an important prerequisite for wildfire management and post-fire effect analysis. In particular, this study established the joint probability of wildfire statistics considering the wildfire activity and burned area in the United States from 1992-2018 for the first time. Marginal distributions of the wildfire activity and burned area were determined, and corresponding joint distributions were constructed. The final distribution function was optimized according to the goodness of fit. The RP and RP trends of wildfire statistics were calculated, and the possible physical mechanism determining the choice of copulas was examined.

There remain a few limitations in describing the bivariate characteristics of wildfire. Wildfire statistics do not yield long-term continuous time series similar to other traditional hydro-meteorological data. It is also common that no wildfire occurs for several months in a high-rainfall year. Even though grid cells with fewer than 100 valid data points were removed in this study, the data length remains an unavoidable source of uncertainty in frequency analysis. The generation of longer data series or reconstruction of wildfire events through paleoclimate research can provide more reliable data for wildfire frequency analysis.

5.4 Summary

Based on the results, the major conclusions are as follows:

(1) The statistical structure of the burned area is more variable than that of the wildfire activity. Different probability distributions are suitable for various regions. Among the seven univariate probability distribution functions, the WEI distribution is the most applicable to the burned areas in the United States, followed by the GEV distribution. Regarding wildfire activity, the WEI distribution occupies a dominant position, accounting for more than 80% of all grid cells. The second-best distribution of wildfire activity is the P-III distribution. Additionally, the optimal copulas are determined in each grid cell. The weighted probability of WP-2 can better reflect the triangular relationship between the wildfire activity and burned area instead of ignoring single mega-wildfire events and frequent wildfire events yielding normal burned areas.

(2) Based on the example obtained from sample 2, the GUM function can better reflect the underlying physical mechanism between the wildfire activity and burned area. In the GUM

function, the minimum wildfire activity imposes little influence on the burned area, while the maximum wildfire activity significantly influences the burned area. Notably, the correlation between the burned area and wildfire activity increases with increasing wildfire activity, which the GUM function can distinguish.

(3) WP-1 and WP-2 perform better than Joint in describing the joint RP of wildfires. In particular, WP-2 defines more mega-wildfires as a high priority. On this basis, through trend analysis of the RP of WP-2, there occurs an increasing trend in California, Texas, Kentucky, and Arkansas. Moreover, most southeastern United States exhibits significantly decreasing trends in wildfire risk.

Overall, the framework of wildfire frequency analysis proposed in this study can provide a reference to understand the spatiotemporal characteristics of wildfire statistics better. In addition, this new wildfire risk assessment approach will also facilitate considering post-fire effects.

Chapter 6 Quantifying the Contributions of Hydro-Meteorological Elements on Different Wildfire Types Illustrated by the Example of the Contiguous United States

This chapter was under review in Agricultural and Forest Meteorology: Ke Shi, Yoshiya Touge, and So Kazama. "Hydrometeorology-Wildfire Relationship Analysis Based on a Wildfire Bivariate Probabilistic Framework in Different Ecoregions of the Continental United States."

6.1 Introduction

Wildfire is a vegetation disturbance of our earth system associated with interactions between climate/weather, fuel, and human activity (Flannigan et al., 2009; Kennedy et al., 2021). The burned area and wildfire activity (number of wildfires) trends vary by region globally (Riaño et al., 2007), with some regions experiencing increasing trends and others experiencing decreasing trends (Earl et al., 2018; Ellis et al., 2022; Forkel et al., 2019; Jones et al., 2022). This spatiotemporal heterogeneity of wildfires leads to unique triangular structures in wildfire statistics, as shown in Figure 6.1. Additionally, when considering extreme wildfires (wildfire extreme zone as shown in Figure 6.1), five different types of wildfires can be seen in the wildfire statistics relationship. Among them, the most extensive attention is given to mega-wildfires, such as the 2014 California mega-wildfire in the United States (Coen et al., 2018), the 2017 mega-wildfire in Chile (Pliscoff et al., 2020) and the 2019/2020 mega-wildfire in Victoria, Australia (Geary et al., 2022). This kind of wildfire has non-negligible negative social, economic, and environmental effects due to its large amount of burned area (Jones et al., 2021; Le Breton et al., 2022; Shen et al., 2022). On the other hand, studying super frequent wildfires in different regions, such as Portugal (Moreira et al., 2010), Australia (Clarke et al., 2019), and the United States (Cattau et al., 2020), is also a hot topic in wildfire science. A related issue associated with super frequent wildfires is that they may result in alien species expansion

(Syphard et al., 2009). For example, biodiversity in California is threatened by shrubbery conversion to alien annual grasses under the influence of super frequent wildfires (Keeley et al., 2005). However, the discussion of the other three types of wildfires has thus far been very limited. Without the ability to characterize different types of wildfires using wildfire bivariate statistical characteristics and only roughly characterizing super frequent wildfires and mega-wildfires, it is impossible to determine how wildfires can transition from a wildfire type-1 (WT1) to a wildfire type-5 (WT5) under the influence of weather conditions and human activity. Thus, only by systematically understanding the relationship and causes of different types of wildfires using wildfire bivariate statistical characteristics can we implement more targeted wildfire prevention plans, thereby increasing the resilience of vegetation and reducing the losses caused by wildfires.

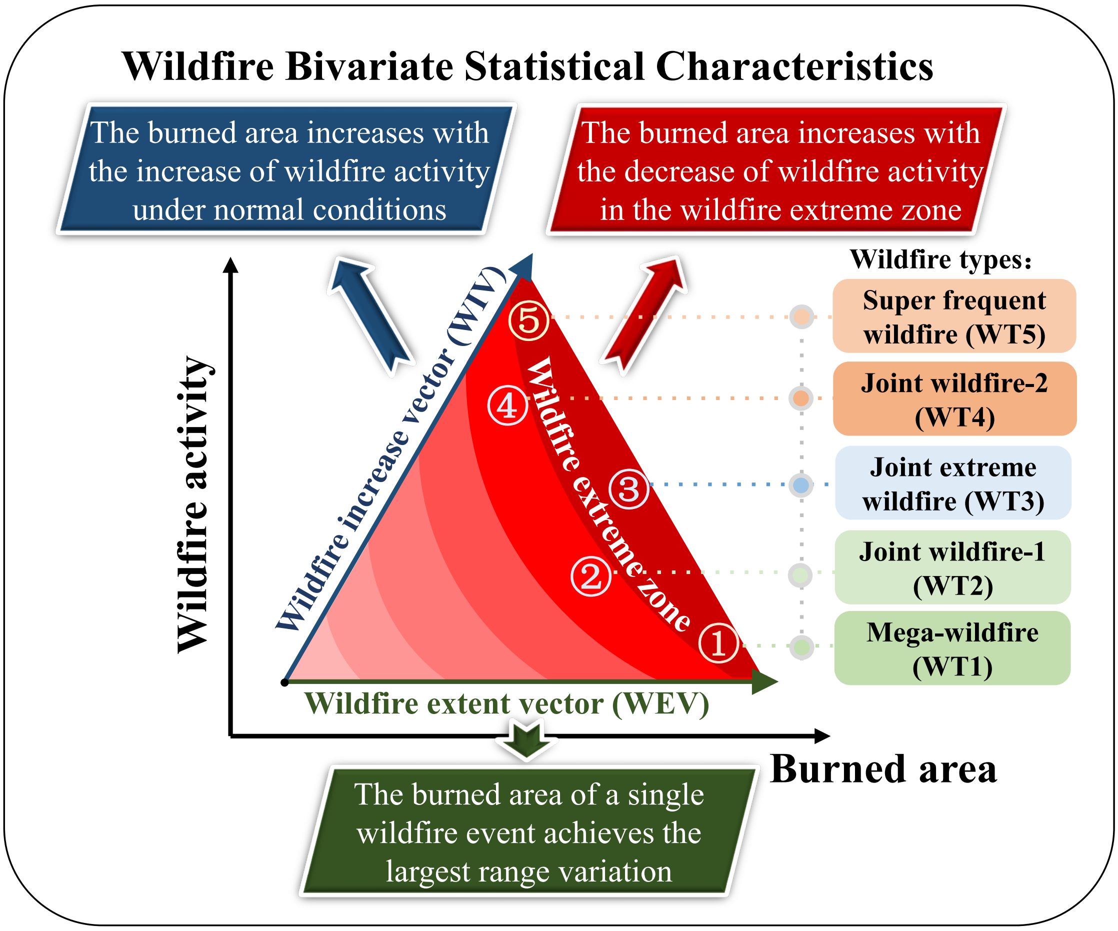

Figure 6.1 Conceptual diagram of the wildfire statistics relationship and the locations of five typical wildfire types.

Existing studies have extensively explored the relationship between hydro-meteorological elements and burned areas or wildfire activity from a univariate perspective. Antecedent hydro-meteorological conditions, such as reduced precipitation, high temperature, and drought events, influence these wildfire events through the preconditioning of fuels (Littell et al., 2016). In contrast, wind speed is a key factor affecting the spread of wildfire after the wildfire has begun (Andrews et al., 2013; Özbayoğlu et al., 2012). Specifically, long-term trends in the burned area and wildfire activity are more significantly affected by precipitation than short-term trends (Andela et al., 2017; Flannigan et al., 2016; Wei et al., 2020). High temperatures can increase evaporation, resulting in drier fuels and water loss in forest flora, thus increasing wildfire activity (Mansoor et al., 2022). The largest wildfire-burned area was associated with high-temperature events (Aldersley et al., 2011; Cardil et al., 2015; Wang et al., 2021). Wind speed can only play a secondary role in wildfire activity (de Dios et al., 2022) but is more sensitive to the burned area (Shabbir et al., 2020). Wildfire activity is limited to extreme, wind-driven wildfires. However, once a wildfire occurs, the severity of the wind will affect the ultimate size of the wildfire event (Keeley et al., 2017). To date, several different types of drought indices, such as the Standardized Precipitation-Evapotranspiration index (SPEI) (Cardil et al., 2019; Rodrigues et al., 2021), Palmer Drought Severity Index (PDSI) (Collins et al., 2006; Flatley et al., 2011) and surface soil moisture (SSM) (Bartsch et al., 2009; Dadap et al., 2019), have been used in the discussion of the relationship between drought and wildfire. The regional depletion of soil (e.g., PDSI and SSM) and atmospheric (e.g., SPI) moisture can lead to a low moisture content in duff (both fibrous and humic horizons) and surface fuels. It can ultimately result in a higher potential for widespread wildfires (Littell et al., 2016). Drought affects the likelihood of ignition at multiple time scales, affecting fuel moisture and propagation on shorter time scales and affecting fuel availability by controlling ecosystem characteristics and productivity on longer time scales (Loehman et al., 2014). Considering wildfire activity and burned area separately, the relationship between hydro-meteorological elements and wildfire activity or burned area is well documented. In contrast, the relationship between meteorological variables and wildfire bivariate statistical characteristics is still emerging. In particular, the effect of meteorological conditions on the simultaneous occurrence of extreme burned areas and extreme wildfire activity, i.e., wildfire type-2 (WT2), -3 (WT3), and-4 (WT4), has not been explored. Also, it is difficult to fairly compare burned areas and wildfire activity in previous studies because of their large magnitude differences. Using a probabilistic framework makes it possible to compare WT1 and WT5 at the same extreme level.

In the continental United States, since 2000, an average of 70,072 wildfires have occurred each year, burning over 2.8 million ha annually (Hoover et al., 2021). Moreover, wildfires in the United States are becoming increasingly frequent, leading to greater environmental degradation, property damage, and economic loss (Dennison et al., 2014). Wildfires in the United States are projected to cost nearly \$1.8 billion annually in wildfire suppression by 2025 (USFS, 2015). The United States experienced not only multiple mega-wildfire events (Buckland, 2019), such as the 2002 Biscuit wildfire (Harma et al., 2003), the 2013 Rim wildfire (Povak et al., 2020), the 2007 Zaca wildfire (Keeley et al., 2009) , and the 2014 King wildfire (Coen et al., 2018) but also super frequent wildfire events (Cattau et al., 2020). Additionally, considering geology, landforms, soils, vegetation, climate, land use, wildlife, and hydrology, the continental United States can be divided into different ecoregions (Omernik et al., 2014), and wildfires in different ecoregions show spatial heterogeneity. For example, the average burned area in the western United States was more extensive than in the eastern United States (Nagy et al., 2018). Additionally, wildfire activity showed a decreasing trend in Mediterranean California but an increasing trend in the Rocky Mountains (Dennison et al., 2014). Wildfire characteristics can show temporal heterogeneity under the current anthropogenic climate change, even in the same regions. As the climate becomes warmer and drier, the shift in vegetation from mesic forest and cold forest to dry forest and then to shrubland/grassland becomes possible, corresponding to an increasing trend of wildfire activity at first, followed by a decreasing trend (Parks et al., 2018). The wide variety of wildfires and spatiotemporal heterogeneity of wildfire characteristics make the United States a suitable study area for examining the hydrometeorology-wildfire relationship.

Chapter 5 documented wildfire bivariate statistical characteristics based on extensive wildfire data in the continental United States. From a bivariate perspective, we expanded on this research by examining the potential relationships between hydro-meteorological elements and wildfires. In addition, most studies of hydrometeorology in relation to wildfires have examined the relationship between seasonal or annual hydro-meteorological elements and wildfire variables (wildfire activity and burned area) to measure and link patterns of the key drivers of wildfires (Higuera et al., 2021; Holden et al., 2018; van Wagtendonk et al., 2020). Nevertheless, the relationship between hydrometeorology and wildfire should be examined on at least a monthly scale to prevent extreme weather conditions from being overlooked due to averaging. Here, we analyzed hydrometeorology-wildfire relationships for 324 months of wildfire data from 1992 to 2018 to assess how these relationships persist across different ecoregions of the continental United States. Specifically, the bivariate probability of wildfire was first calculated from the univariate and bivariate probability distributions. Next, the five different types of wildfires were classified according to their probability threshold. Then, the probability of hydro-meteorological elements corresponding to the different wildfire types was calculated to discuss the relationship between hydrometeorology and wildfire. Based on our hydrometeorology-wildfire relationship results, we additionally performed a cluster analysis to obtain new wildfire clusters with similar wildfire characteristics and hydro-meteorological impacts on the wildfire. Finally, the trends of each hydro-meteorological element within the new wildfire clusters were analyzed. In particular, we addressed the following key issues in hydrometeorology-wildfire relationships: (1) the dominant hydro-meteorological elements of the five types of wildfires, (2) the possible intrinsic relationship between the five types of wildfires, and (3) the significant changes in hydro-meteorological elements that need to be noted in the new, different wildfire clusters.

6.2 Results

6.2.1 Performance capabilities with different probabilities

To assess the hydrometeorology-wildfire relationship, it is first necessary to determine how to classify the five wildfire types. This paper selected marginal probabilities and joint probabilities combined with marginal probabilities as control groups to compare the differences in assessing the hydrometeorology-wildfire relationship under different probability calculation methods. For the probability thresholds of the control group, the burned area was the dominant element in WT1 and WT2. Thus, the required probability of the burned area exceeded 0.99. In addition, in WT1, which also ensured less wildfire activity, the probability of wildfire activity was set to less than 0.3. The reason for not choosing a threshold of 0.2 or 0.1 here was that there were no WT1 fires in the entire study area. For WT2, wildfire activity near the 0.5 probability was selected, i.e., fire activity probabilities between 0.45 and 0.55. The same approach was used for WT4 and WT5. WT3 indicates that both the burned area and wildfire activity reached extremes, so the probability threshold for both was 0.99. For the experimental group, the univariate probabilities were selected according to the same principles as the control group. WT3 indicated the extreme condition for the joint probability and thus had a joint probability threshold of 0.99. The threshold range was adjusted several times for WT1, WT2, WT4, and WT5. The three experimental groups achieved the most similarity to the control group when the final probability thresholds were within the range in Table 6.1.

Based on the probability threshold in Table 6.1, Figure 6.2 shows the comparison results for the experimental and control groups, with different colors indicating the median probability of weather values. WP2 was most similar to the control group, especially in WT1 and WT2, where the burned area was the dominant element. WP2 performed significantly better than WP1 and the joint, especially when measuring the relationship between the hydro-meteorological elements and WT1, which was also consistent with the findings in chapter 5. For WT3, there was no significant difference between the three experimental groups. Additionally, WP1 and WP2 also outperformed the joint for WT4. In conclusion, by comparing the probabilities calculated under the different methods, WP2 outperformed the other two methods. Therefore, WP2 was used to classify the wildfire types in all subsequent analyses.

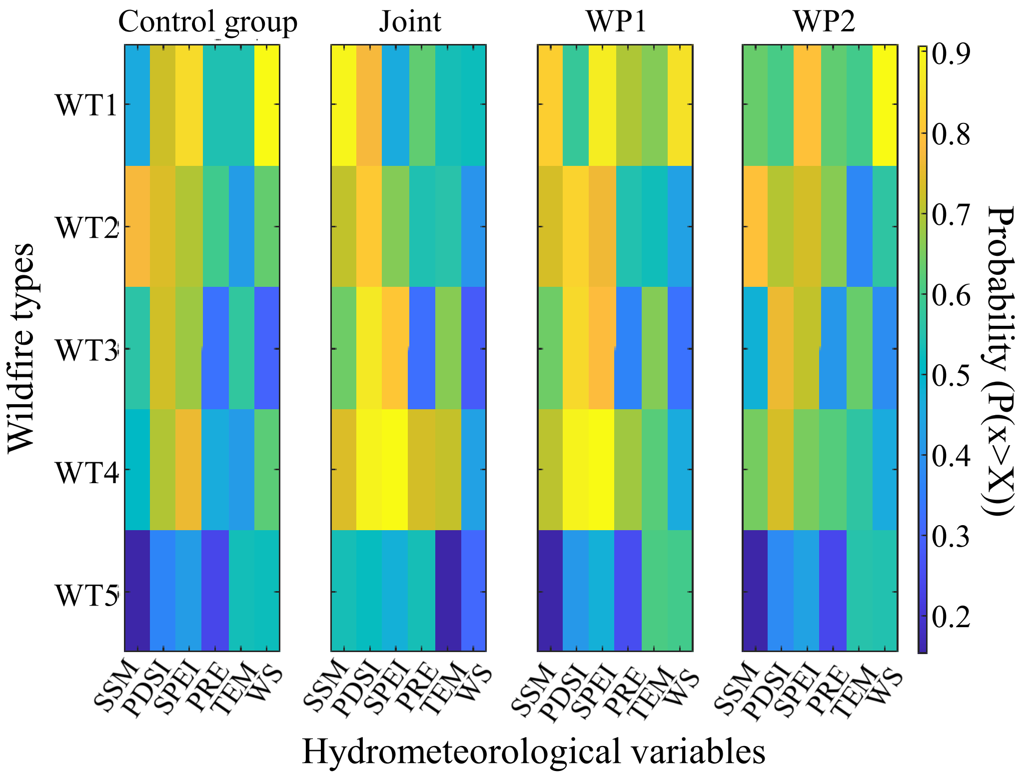

Figure 6.2 Comparison of the performance of the Joint, WP1, and WP2 methods in assessing the impact of weather elements using the wildfire bivariate statistical characteristics framework.

Table 6.1 Probability thresholds for wildfire classification.

Types	Control Group	Joint	WP1	WP2
WT1 (mega-wildfire)	$P_{BA}>0.99$ $P_{FA}<0.30$	$P_{BA}>0.99$ $0.7<P_{Joint,WP1,\ WP2}<0.8$		
WT2 (joint wildfire-1)	$P_{BA}>0.99$ $0.45<P_{FA}<0.55$	$P_{BA}>0.99$ $0.8< P_{Joint,WP1,\ WP2}<0.9$		
WT3 (joint extremes)	$P_{BA}>0.99$ $P_{FA}>0.99$	$P_{Joint,WP1,\ WP2}>0.99$		
WT4 (joint wildfire-2)	$0.45<P_{BA}<0.55$ $P_{FA}>0.99$	$P_{FA}>0.99$ $0.8< P_{Joint,WP1,\ WP2}<0.9$		
WT5	$P_{FA}>0.99$	$P_{FA}>0.99$		

Types	Control Group	Joint	WP1	WP2
(super frequent wildfires)	$P_{BA}<0.30$	$0.7< P_{Joint,WP1, WP2}<0.8$		

6.2.2 Overall wildfire conditions in the United States

Based on the classification method of WP2, the seasonal distribution of the five wildfire types is shown in Figure 6.3. WT1 and WT5 showed significant seasonality. WT1 was mainly concentrated in summer, while WT5 corresponded to spring. For WT2 and WT4, the wildfire was dominant in autumn. However, WT3 could be distributed in any season. In fact, in the United States, especially in the eastern United States, there is much wildfire activity (especially human-caused wildfires) in the spring (Balch et al., 2017; Nagy et al., 2018). On the other hand, of the 43 notable mega-wildfires in the United States (Buckland, 2019), 33 wildfires occurred in the summer, and July accounted for 42.2% of the summer mega-wildfires.

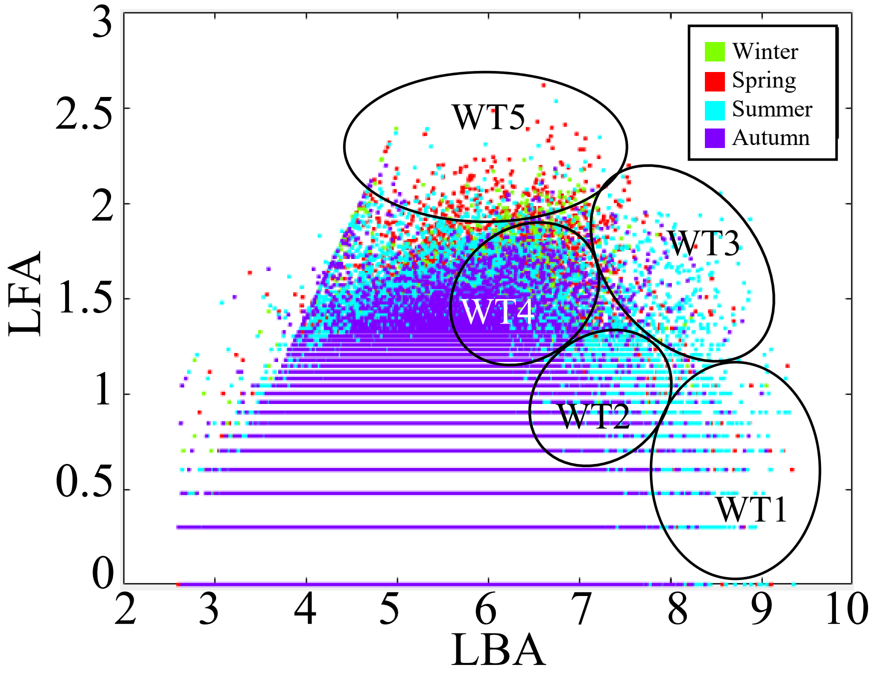

Figure 6.3 Seasonal distribution of wildfires in the continental United States.

To further understand the hydrometeorology-wildfire relationship in the United States, the probabilities of the hydro-meteorological elements under different wildfire types are tabulated in Figure 6.4. A higher probability indicated drier (less precipitation and lower SPEI, PDSI, or

SSM values), hotter weather, and stronger wind speeds. No single hydro-meteorological element had a significantly higher probability than the others in WT1 and WT2. However, this does not suggest that there is no relationship between hydro-meteorological elements WT1 or WT2. Because wildfires are often subject to a combination of meteorological elements in locations dominated by large burned areas. Three significant high-probability variables could be identified for the other three wildfire types. Specifically, WT3 was dominated by SPEI, PRE, and TEM; SSM, SPEI, and PRE dominated WT4; and SSM, PRE, and TEM dominated WT5. Compared to a regular wet and rainy spring, a warm and dry spring dominated by a high probability of SSM, PRE, and TEM created natural conditions for frequent wildfire activity, i.e., WT5.

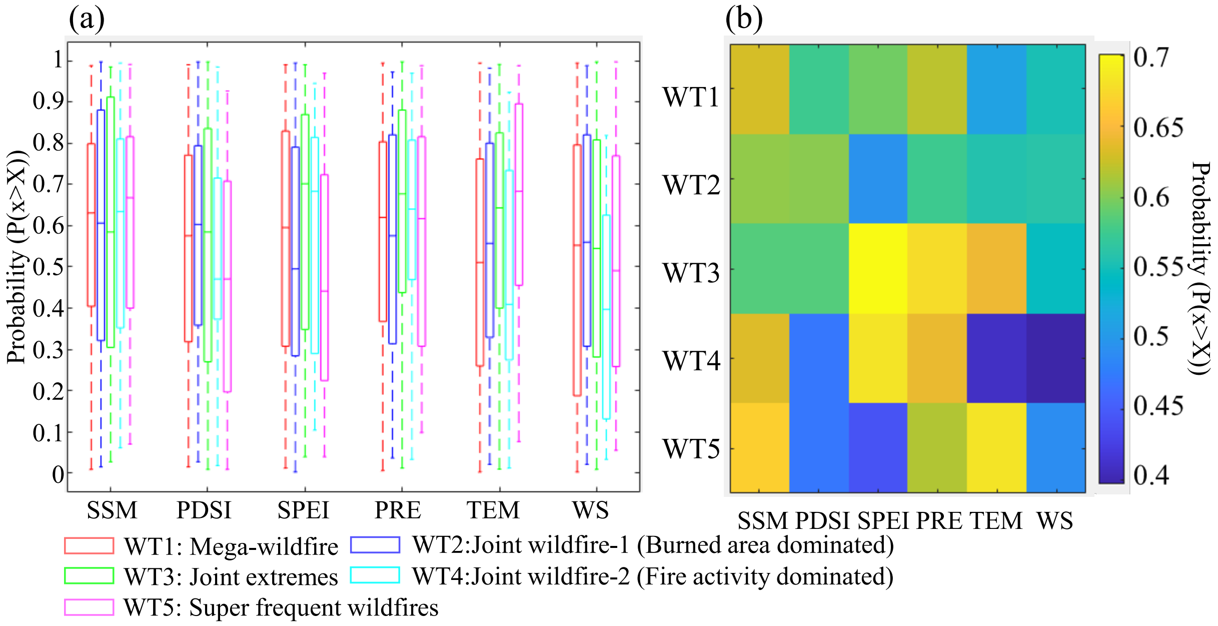

Figure 6.4 Average probability (P(x>X)) of meteorological values under the five fire types in the continental United States: (a) Overall conditions; and (b) Median value.

6.2.3 Hydrometeorology-wildfire relationship in different ecoregions

Hydro-meteorological conditions and vegetation characteristics vary among ecoregions in the United States. Therefore, to fully understand their complex relationship, Figures 6.5~6.7 show the hydro-meteorological and wildfire relationships within each zone during different seasons. These seventeen ecoregions can be divided into three major categories based on their distributions of wildfire types: ecoregions containing five wildfire types, ecoregions containing four wildfire types in addition to super frequent fires, and ecoregions with only three or fewer wildfire types.

Six ecoregions, the Western Sierra Madre Piedmont and Warm Deserts, Western Cordillera, Southeastern Plains, Ozark Ouachita-Appalachian Forests, Mississippi Alluvial, and Southeastern Coastal Plains, and West-Central Semi-Arid Prairies, had all wildfire types. Specifically, the WT5 in Western Sierra Madre Piedmont and Warm Deserts were concentrated in the summer months of 1992~1999, and high temperatures were their main causal factor. Moreover, extreme wildfires in this ecoregion showed a decreasing trend, with no occurrence of WT1 or WT5 from 2010 to 2018. In the Ozark Ouachita-Appalachian Forests and West-Central Semi-Arid Prairies, a strong wind speed provided conditions for spreading mega-wildfires, i.e., WT5. In contrast, for WT3, these two ecoregions differed, with WT3 in the Ozark Ouachita-Appalachian Forests being dominated by PDSI. In comparison, WT3 in the West-Central Semi-Arid Prairies was consistent with the dominant factors of mega-wildfire, both PRE and WS. WT2 in Southeastern Plains presented high-probability values of hydro-meteorological elements. The extremely low precipitation and drought index value (especially SPEI) led to conditions that were suitable for WT2. The most notable combination in the Mississippi Alluvial and Southeastern Coastal Plains was PRE-WT1. Additionally, the Western Cordillera was dominated by extremely high temperatures for both WT4 and WT5 (dominated by wildfire activity). This region significantly increased extreme wildfire events, especially during 2010~2018, with WT2 and WT4 occurring in all seasons.

(1)Cold deserts (2)Mediterranean California

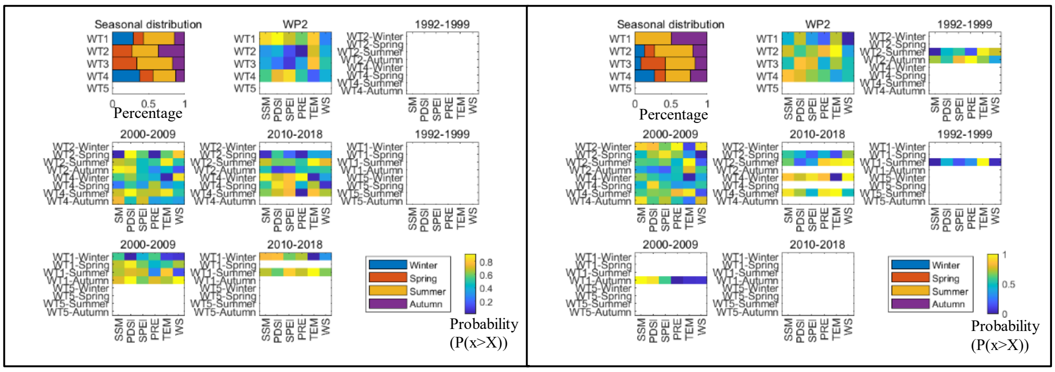

(3)Mixed wood Shield (4)Marine West Coast Forest

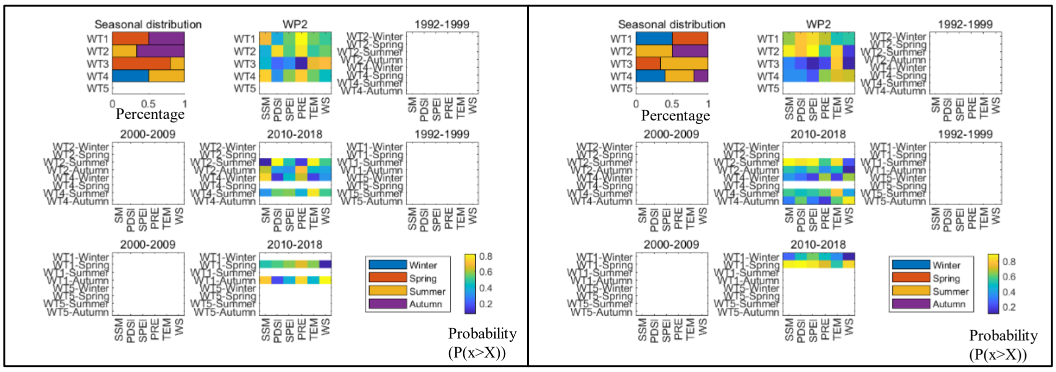

(5)Mixed wood Plains (6)Temperate Prairies

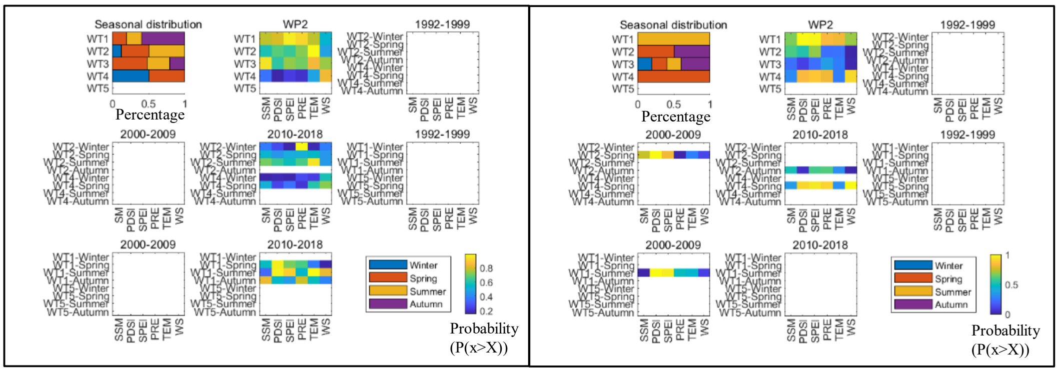

(7)South-Central Semi-Arid Prairies

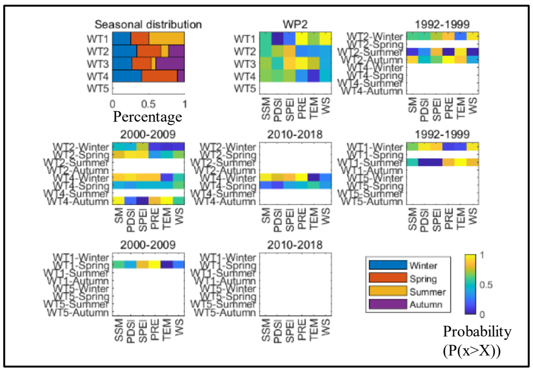

Figure 6.5 Median probability (P(x>X)) of meteorological factors in ecological regions 1-7 in different seasons and years.

There were seven ecoregions without super frequent wildfires (WT5), namely Cold deserts, Mediterranean California, Mixed wood Shield, Marine West Coast Forest, Mixed wood Plains, Temperate Prairies, and South-Central Semi-Arid Prairies. For WT1, the high probability of hydro-meteorological elements was in the Cold deserts, Mixed wood Shield, Temperate Prairies, and South-Central Semi-Arid Prairies. The specific combinations were PDSI-SSM-WT1 in the Cold deserts, PRE-WT1 in the Mixed wood Shield, PDSI-SPEI-WT1 in the Temperate Prairies, and PRE-WS-WT1 in the South-Central Semi-Arid Prairies. On the other hand, the dominant hydro-meteorological elements in the other three regions were reflected in WT2, such as TEM-WT2 in Mediterranean California, SSM-SPEI-WT2 in the Marine West Coast Forest, and TEM-WT2 in the Mixed wood Plains. Additionally, WT1, WT2, and WT4 in the Mixed wood Shield, Marine West Coast Forest, and Mixed wood Plains curred only in the period from 2010~2018.

Among the four other ecoregions (the Upper Gila Mountains, Atlantic Highlands, Central Plains, and Texas-Louisiana Coastal Plain and Tamaulipas-Texas Semiarid Plain), joint extremes existed only in the Central Plains. The vegetation cover of the Central Plains is mainly grassland, and wildfire activity and burned area have a strong correlation, with a high probability of wildfire activity and burned area often occurring simultaneously. The dominant combinations of hydrometeorological-wildfire relationships in the other three ecoregions were WT1 with PDSI in the Upper Gila Mountains, WT1 with WS in the Atlantic Highlands, and WT2 with TEM in the Texas-Louisiana Coastal Plain and Tamaulipas-Texas Semiarid Plain.

(1)Western Sierra Madre Piedmont and Warm Deserts

(2)Western Cordillera

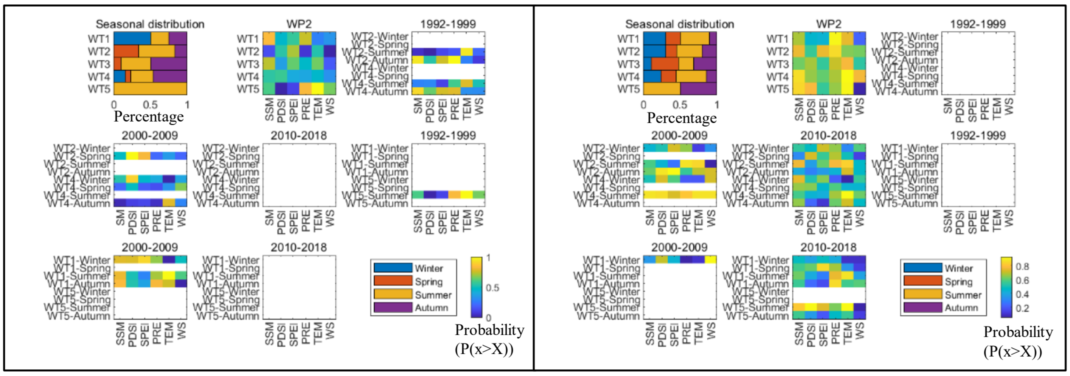

(3)Southeastern Plains

(4)Ozark Ouachita-Appalachian Forests

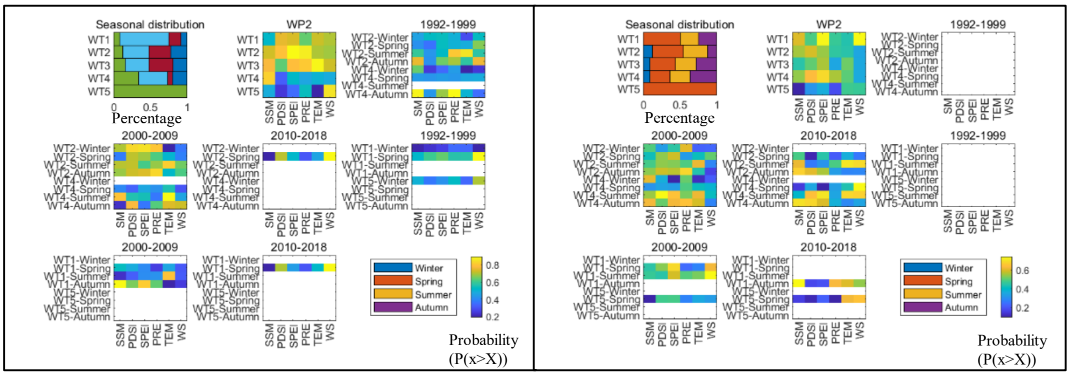

(5)Mississippi Alluvial and Southeastern Coastal Plains

(6)West-Central Semi-Arid Prairie

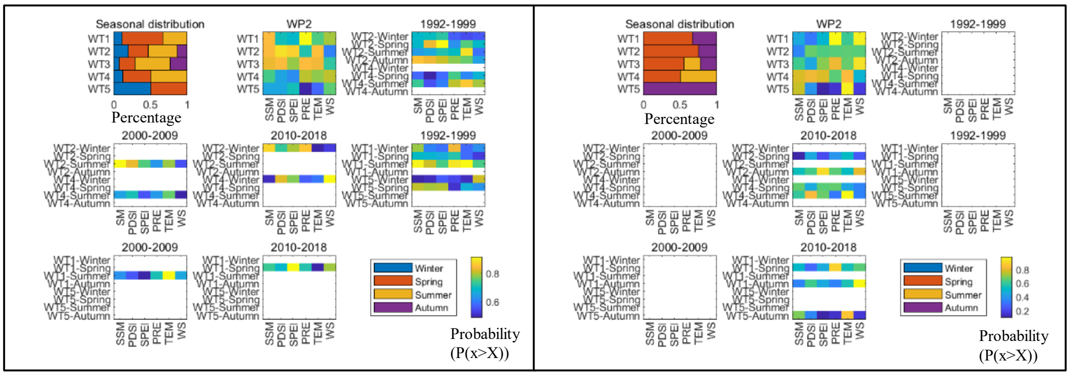

Figure 6.6 Median probability (P(x>X)) of meteorological factors in ecological regions 8-13 in different seasons and years.

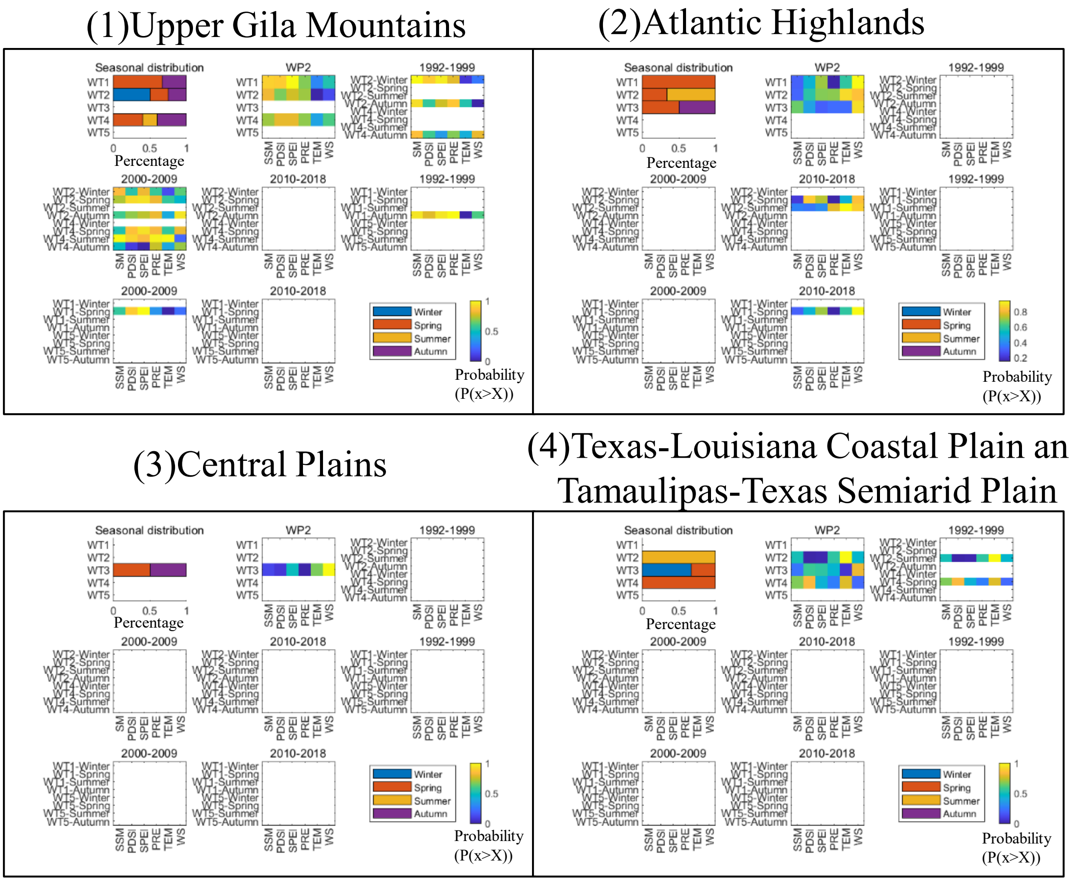
(1)Upper Gila Mountains
(2)Atlantic Highlands
(3)Central Plains
(4)Texas-Louisiana Coastal Plain and Tamaulipas-Texas Semiarid Plain

Figure 6.7 Median probability (P(x>X)) of meteorological factors in ecological regions 14-17 in different seasons and years.

In addition, we focused on the seasonal variation in wildfires. For example, in Mediterranean California and the Ozark Ouachita-Appalachian Forests, the season of large wildfires shifted from spring and summer to autumn, and low soil moisture content was dominant in autumn. In other words, the impact of extreme autumn drought on mega-fires increased. Furthermore, both WT2 and WT4 in Mediterranean California had the same second dominant factor, i.e., wind, but WT4 could change to WT2 when the first dominant factor changed from PRE to TEM. A similar situation was found in the Ozark Ouachita-Appalachian Forests, where WT2 could also change to WT4 when the dominant factor changed from PDSI combined with SPEI to PDSI combined with SSM. This result revealed that similar factors influence joint wildfires and that changes in meteorological elements at different times can cause joint wildfires to transition between WT2 and WT4.

6.2.4 Spatial clustering of wildfire bivariate characteristics

The hydrometeorology-wildfire relationships within the 17 ecoregions presented too much information. To further extract valid information and thus provide guidance for wildfire prevention, the median hydro-meteorological probability values under each wildfire type were used as input (missing fire types were input as 0) to obtain four new clusters, as shown in Figure 6.8. This cluster partitioning divided the original classification of ecoregions that considered only vegetation and climatic characteristics. Considering the relationship between hydrometeorology and wildfire through classification is more instructive for wildfire research. For example, cluster 2 contained two ecoregions, the Central Plains and the Texas-Louisiana Coastal Plain and Tamaulipas-Texas Semiarid Plain. Unlike other plain types, the wildfire activity and burned area within these two ecoregions had a strong correlation, and WT1 and WT5 were completely absent from these two ecoregions.

As shown in Figure 6.9, among the four clusters, only cluster 3 had all wildfire types, and cluster 2 had only three types of wildfires: WT2, WT3, and WT4. The most significant combination of all the combinations of wildfire type and hydro-meteorological elements in both cluster 1 and cluster 2 was WT2-TEM. In cluster 3, the dominant roles of the SPEI and PDSI for WT2 prevailed. The dominant role of the SPEI and PDS in cluster 4 was reflected in WT1.

Additionally, we analyzed the trend of the hydro-meteorological elements in all the clusters and extracted the top two elements with the highest probability. From Figure 6.10, it can be seen that drought showed an intensifying trend among the hydro-meteorological elements in cluster 1. Cluster 4 was similar to cluster 1 and also has increased drought concerns. The hydro-meteorological elements in cluster 2 showed no significant change trend. Multiple extreme hydro-meteorological elements (stronger winds, drier weather, higher temperatures) intensified simultaneously in cluster 3.

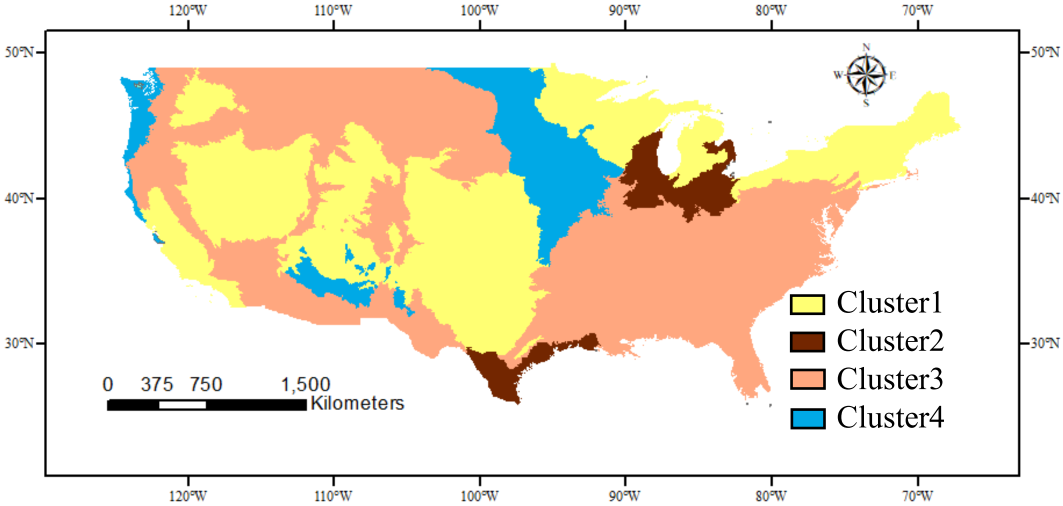

Figure 6.8 Clustering zones of ecoregions based on the probability of meteorological factors.

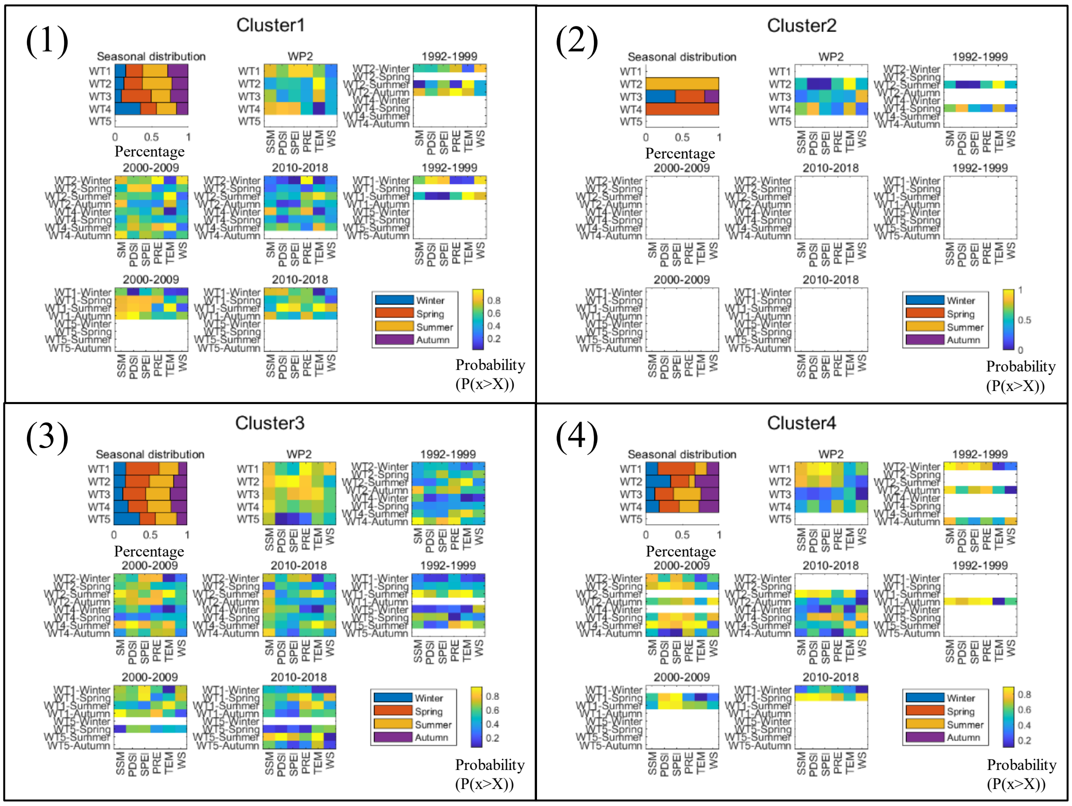

Figure 6.9 Probability of meteorological factors in the clustering zones.

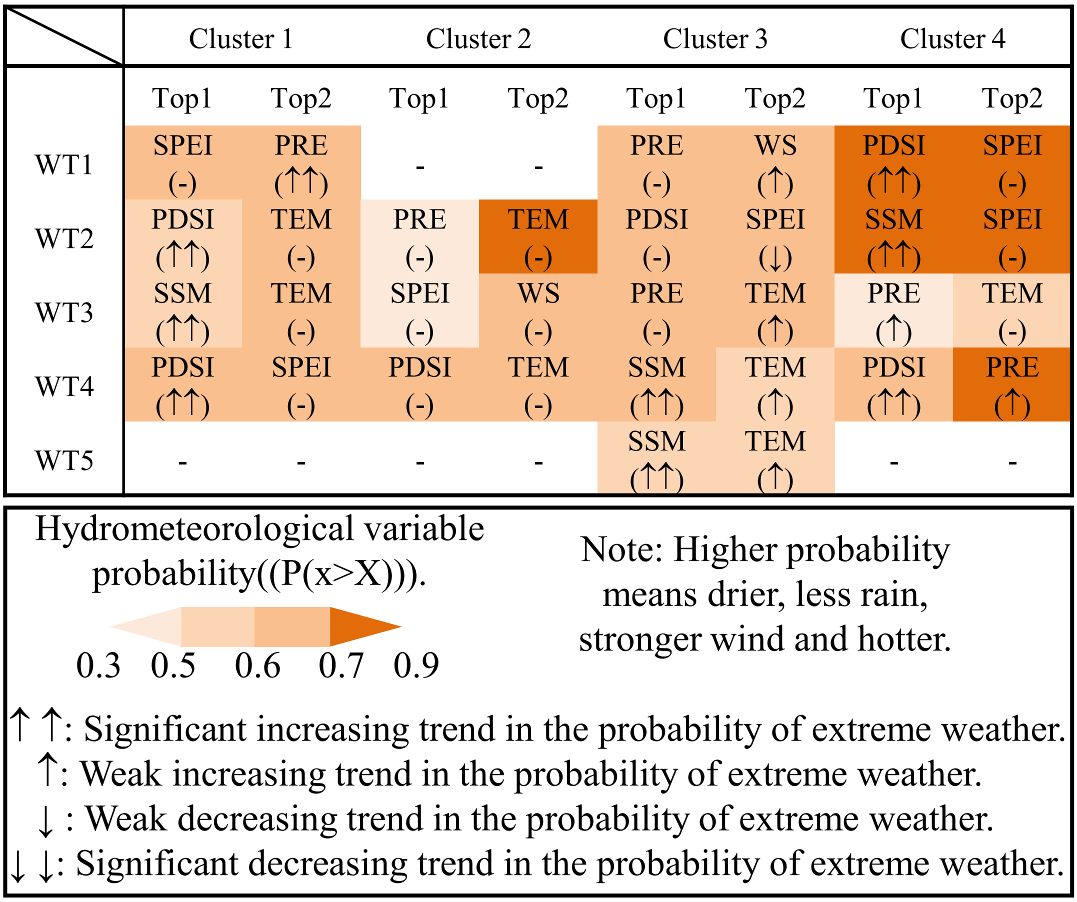

	Cluster 1		Cluster 2		Cluster 3		Cluster 4	
	Top1	Top2	Top1	Top2	Top1	Top2	Top1	Top2
WT1	SPEI (-)	PRE (↑↑)	-	-	PRE (-)	WS (↑)	PDSI (↑↑)	SPEI (-)
WT2	PDSI (↑↑)	TEM (-)	PRE (-)	TEM (-)	PDSI (-)	SPEI (↓)	SSM (↑↑)	SPEI (-)
WT3	SSM (↑↑)	TEM (-)	SPEI (-)	WS (-)	PRE (-)	TEM (↑)	PRE (↑)	TEM (-)
WT4	PDSI (↑↑)	SPEI (-)	PDSI (-)	TEM (-)	SSM (↑↑)	TEM (↑)	PDSI (↑↑)	PRE (↑)
WT5	-	-	-	-	SSM (↑↑)	TEM (↑)	-	-

Hydrometeorological variable probability((P(x>X))).

Note: Higher probability means drier, less rain, stronger wind and hotter.

↑↑: Significant increasing trend in the probability of extreme weather.

↑: Weak increasing trend in the probability of extreme weather.

↓ : Weak decreasing trend in the probability of extreme weather.

↓↓: Significant decreasing trend in the probability of extreme weather.

Figure 6.10 The top two dominant meteorological factors in the clustering zones.

6.3 Discussion

Even though our study focused only on bivariate statistical characteristics of wildfire, it also provided a new way of thinking about other compound hazards in the face of climate change. Research on compound hazards such as compound droughts and hot extremes (Hao et al., 2018) and compound wildfires and COVID-19 (Navarro et al., 2021) has surfaced recently. By applying the analytical framework of compound hazards in this chapter, understanding other types of compound hazards can also be improved.

There are still some limitations in characterizing the wildfire bivariate characteristics. Wildfire statistics do not produce long-term continuous time series similar to other traditional time series. It is not uncommon for wildfires to be absent for several months in rainy years. Data length is an unavoidable source of uncertainty in frequency analysis.

6.4 Summary

Unlike previous studies that considered burned area and wildfire activity separately in their wildfire regime classifications (Brewer et al., 2005; Malamud et al., 2005; Trucchia et al., 2022), we present the first wildfire type classification based on the wildfire bivariate statistical characteristics. On this basis, the influence of hydro-meteorological elements on different wildfire types was examined from 1992 to 2018. The major conclusions were as follows:

(1) In this paper, wildfires were classified into five types using the bivariate statistical characteristics of wildfire: WT1 (mega-wildfire), WT2 (joint wildfire-1), WT3 (joint extremes), WT4 (joint wildfire-2), and WT5 (super frequent wildfires). In the continental United States, WT1 and WT2 were affected by multiple weather elements, and their causes were more complicated, while WT5 was mainly affected by soil moisture, precipitation, and temperature.

(2) The influence of hydro-meteorological elements on different wildfire types was discussed in 17 ecoregions. The most dominant combinations of hydro-meteorological elements and wildfire types in the 17 ecoregions were: PDSI-WT1 in the Cold deserts, TEM-WT2 in Mediterranean California, TEM-WT5 in the Western Sierra Madre Piedmont and Warm Deserts, SPEI-WT1 in the Upper Gila Mountains, PRE-WT1 in the Mixed wood Shield, WIND-WT1 in the Atlantic Highlands, PRE-WT1 in the Western Cordillera, SPEI-WT2 in the Marine West Coast Forest, TEM-WT2 in the Mixed wood Plains, WS-WT3 in the Central Plains, SPEI-WT2 in the Southeastern Plains, WS-WT1 in the Ozark Ouachita-Appalachian Forests, PRE-WT1 in the Mississippi Alluvial and Southeastern Coastal Plains, PDSI-WT1 in the Temperate Prairies, TEM-WT5 in the West-Central Semi-Arid Prairies, SPEI-WT2 in the South-Central Semi-Arid Prairies, and TEM-WT2 in the Texas-Louisiana Coastal Plain and Tamaulipas-Texas Semiarid Plain. Changes in hydro-meteorological elements in different periods could also lead to mutual conversion between WT2 and WT4.

(3) In the four new clusters, intensifying droughts are a concern in clusters 1 and 4, while there are multiple concerns in cluster 3, namely, stronger winds, higher temperatures, and more drought.

Chapter 7 Simulating Global Wildfire Bivariate Characteristics through Hydrometeorology-Wildfire Relationship

This chapter is scheduled for submission to Agricultural and Forest Meteorology: Ke Shi and Yoshiya Touge. "Simulating global wildfire bivariate characteristics through hydrometeorology-wildfire relationship"

7.1 Introduction

Wildfires are natural factors around the globe that affect human communities and the ecosystems on which we depend (Moritz et al., 2014). The occurrence and spread of wildfires are influenced by many aspects, including human activities, atmospheric-oceanic indices, and hydro-meteorological elements. Under the complex influence of various factors, wildfire has the characteristics of many types, including super frequent wildfires, mega-wildfires (wildfires with a particularly large burned area) (Linley et al., 2022), etc. Also, the loss caused by wildfire varies according to the type of wildfire. On the one hand, wildfires were part of the world well before humans evolved and helped the environment. As an ecosystem service, wildfires can maintain diversity and genetic variability, contributing to creating a range of natural products for human consumption (Pausas et al., 2019). On the other hand, extreme wildfires, such as mega-wildfires, can cause huge damage. Extreme wildfires can destroy buildings and houses, burn forests, and even claim lives (Linley et al., 2022). For example, in 2003, the mega-wildfire was directly responsible for the loss of 21 lives and an estimated total burned area of 450,000 ha in Portugal, double the largest fire previously recorded in Portugal (Tedim et al., 2013; Trigo et al., 2006). However, in the existing wildfire forecast and early warning system, the target is often the univariate characteristics of wildfire (modeling wildfire activity and burned area separately), rather than bivariate characteristics of wildfire.

There has been much research into wildfire warning and forecasting based on the relationship between hydrometeorology and wildfire, for example, the three well-known wildfire warning systems: Canadian Forest Service Fire Weather Index Rating System (Van Wagner, 1974; Van Wagner et al., 1987; Van Wagner et al., 1985), Australian McArthur Mark 5 Rating System (Cruz et al., 2015; Keetch et al., 1968; McArthur, 1967; Moore, 1986), and U.S. Forest Service National Fire-Danger Rating System (Mees et al., 1991; Schlobohm et al., 2002), which have been widely used around the world. Simultaneously, statistical or process-based physical models have also been applied to simulate wildfires using hydro-meteorological elements. The Glob-FIRM model, an empirical model, used fuel moisture as a threshold to determine whether a wildfire can occur or not (Thonicke et al., 2001). The dynamic simulations of autoregressive distributed lag (ARDL) models were also used to simulate burned areas through the relationship between temperature, relative humidity, precipitation, wind speed, sunlight, and wildfire (Shabbir et al., 2020). Like the LPJ-LMfire model (Pfeiffer et al., 2013), the SPread and InTensity of FIRE (SPITFIRE) model (Thonicke et al., 2010), and the HESFIRE (Human–Earth System FIRE) model (Page et al., 2015) , the process-based physical models determined the probability of wildfire occurrence and extinguishment based on hydro-meteorological elements and landscape fragmentation (human activities, topography, or past wildfire events). In other words, the models for simulating the final burned area and the occurrence wildfire have been extensively studied and discussed. But given the impact of wildfires, it is the extreme wildfires that deserve our attention rather than all wildfires. Just like floods, we don't have to worry about the runoff every moment in the river, but only need to focus on the flood process when heavy rain will hit, which is enough to provide guidance on reducing disaster damage. Accordingly, in early warning and forecasting of wildfires, we need to pay more attention to bivariate characteristics of wildfire to improve pertinence and efficiency.

For wildfire simulation, since wildfires are similar in frequency analysis to extreme floods and extreme droughts, the research on flood and drought forecasting can be transplanted to wildfire. Furthermore, with the rise of machine learning in recent years, more and more machine learning techniques have been applied to flood-related and drought-related research. Because machine learning techniques provide easier implementation, low computation cost, fast training, validation, testing, and evaluation, high performance compared to physical models, and relatively less complexity (Mosavi et al., 2018). Artificial Neural Networks (ANNs) are the most popular learning algorithms among all machine learning methods. They are known to be versatile and efficient in modeling complex processes with high fault tolerance and accurate approximations (Abbot et al., 2014). In particular, ANNs are proven to provide a reliable means of detecting the flood hazard in South Korea (Kim et al., 2000), the U.K. (Dawson et al., 2006), Sudan (Elsafi, 2014), and Japan (Arai et al., 2022). Similarly, as for drought forecasting, ANNs are used to predict the Streamflow Drought Index (SDI) for hydrological drought (Eroğluer et al., 2020), the Standard Precipitation Index (SPI) for meteorological drought (Achite et al., 2022), Soil Moisture Deficit Index (SMDI) for agricultural drought (Wambua, 2019), etc., and the modeling framework based on ANNs has wide applicability in drought forecasting. Nevertheless, we have not come across studies that utilize ANN methods for wildfire bivariate characteristics forecasting by linking hydro-meteorological elements and wildfires comprehensively. And the joint probability between different hydro-meteorological elements also has not been considered in the existing model.

Consequently, this chapter aims to fill these gaps by comprehensively analyzing hydrometeorology-wildfire relationships across the globe. In particular, the research objective of this chapter is to simulate wildfire bivariate characteristics in different regions at the global scale based on the hydrometeorology-wildfire relationship. First, this chapter uses the wildfire priority index proposed in chapter 5 to describe the wildfire bivariate characteristics. Second, the control effects of hydro-meteorological elements on wildfires were quantified through the correlation coefficient. Then, after identifying the dominant hydro-meteorological elements in different regions, ANNs were utilized for wildfire bivariate characteristics simulation. This study will provide a new understanding of global wildfire forecasting to reduce the losses to human communities and the ecosystems caused by wildfires in the future.

7.2 Results

7.2.1 Wildfire characteristics in sub-regions around the world

First, according to the AR5 (IPCC 5th Assessment Report) Reference Regions, the world is divided into 27 sub-regions (the sub-regions where no wildfires have occurred were removed). The 27 sub-regions are specifically Alaska/N.W. Canada (ALA), Central America/Mexico (CAM), Central Europe (CEU), Central North America (CNA), East Asia (EAS), South Europe/Mediterranean (MED), North Australia (NAU), North Europe (NEU), Sahara (SAH), Southeast Asia (SEA), South Asia (SAS), Tibetan Plateau (TIB), West Asia (WAS), West Coast South America (WSA), Amazon (AMZ), Central Asia (CAS), Small Islands Regions Caribbean (CAR), Canada/Greenland/Iceland (CGI), East Africa (EAF). East North America (ENA), North Asia (NAS), North-East Brazil (NEB), Southern Africa (SAF), South Australia/New Zealand (SAU), Southeastern South America (SSA), West Africa (WAF), and West North America (WNA).

To fully understand the wildfire characteristics of each sub-region, the average burned area per wildfire ($\frac{total\ burned\ area}{total\ wildfire\ activity}$) within each sub-region was plotted in Figure 7.1 (1). It is clear that the sub-regions with higher average burned area per wildfire were mainly concentrated in WNA, SAF, NAU, and CAS. Especially in NUA, almost every grid cell has experienced extensive wildfires. Figure 7.1 (2) shows the maximum burned area month and the most frequent wildfire activity month of each sub-region. This result illustrated temporal heterogeneity between burned areas and wildfire activity. For example, in the SAU, the largest burned area of this sub-region occurred in December 2019, while the most frequent wildfire activity occurred in April 2011. Among the 27 sub-regions, the largest burned area and the most frequent wildfire activities were consistent only in the five regions of TIB, CGI, CAR, CEU, and WAS. The largest burned area in the SEA, NAU, SAU, SAS, CNA, AMZ, NEB, SAH, WAF, and SAF was later than the most frequent wildfires, which means that the wildfire characteristics in these regions tended to become larger rather than more frequent. At the same time, the wildfires became more frequent in the remaining eleven regions (ALA, NEU, WNA, ENA, WSA, SSA, NAS, MED, EAF, CAS, and EAS). Because the burned area and wildfire activity were not highly correlated, the wildfire bivariate characteristics must be comprehensively considered in wildfire forecasting.

Figure 7.2 further shows the log-processed statistical characteristics of the total burned area and total wildfire activity within each sub-region. The month with the most frequent wildfire activity occurred in SAF, while WAF had the highest median of wildfire activity and burned area worldwide.

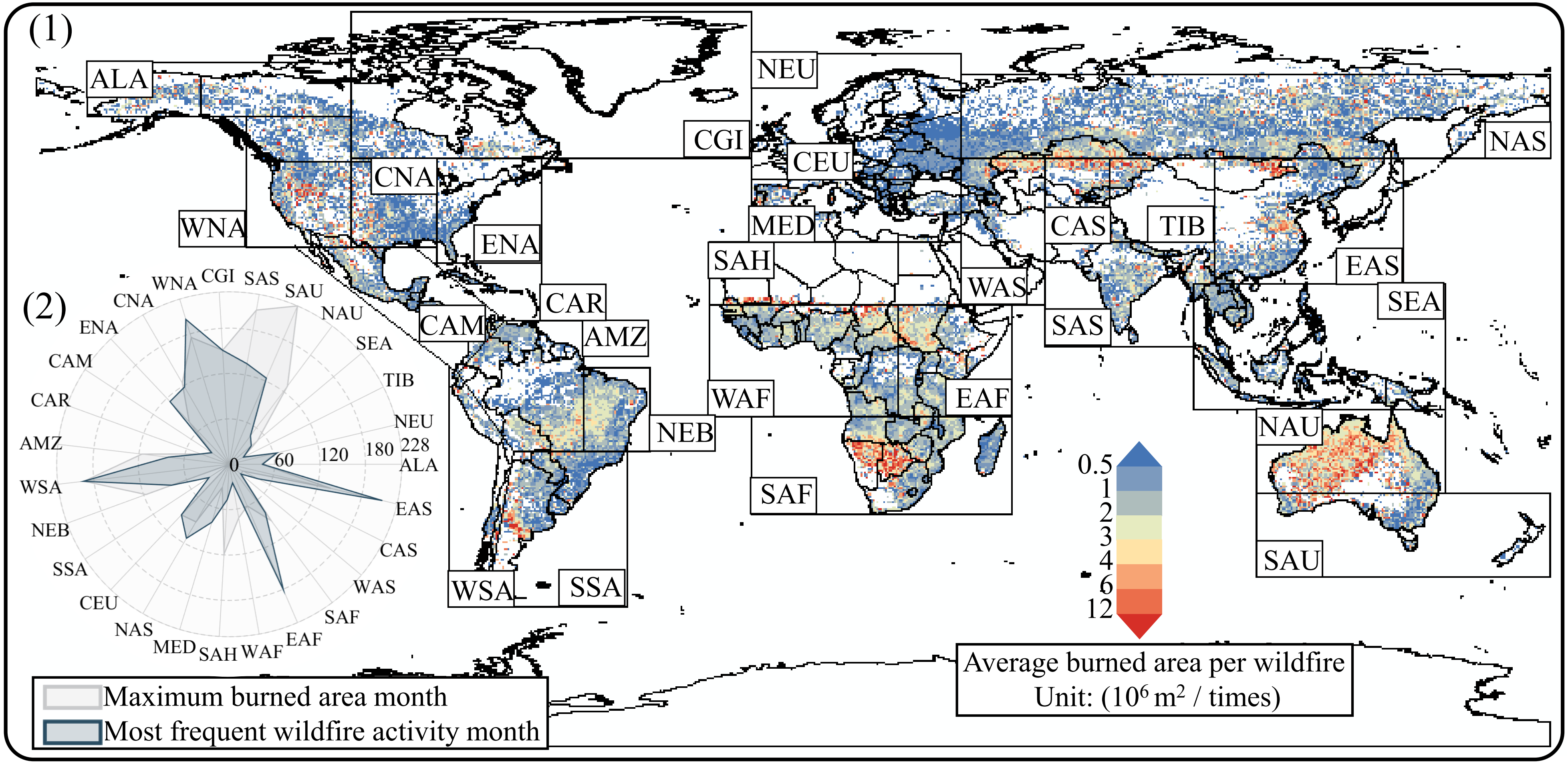

Figure 7.1 Global wildfire characteristics. Figure 7.1(1) shows the average burned area per wildfire event. Figure (2) shows the largest burned area and the most frequent wildfire activity month in each sub-region. Where 1 to 228 indicates the specific number of months in the study period, e.g., 1 indicates January 2001, while 228 indicates December 2019.

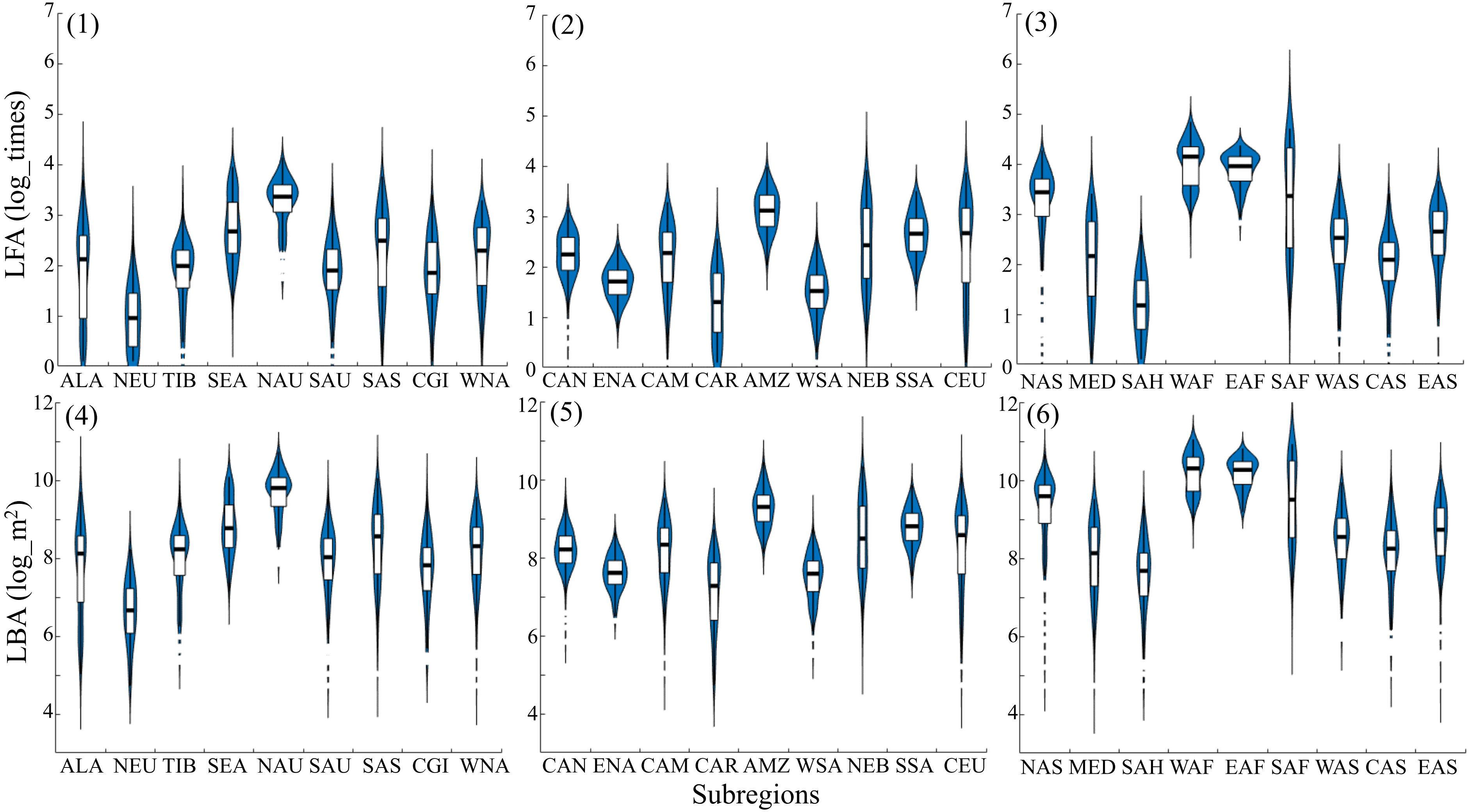

Figure 7.2 Violin chart for the log burned area and log wildfire activity.

7.2.2 Wildfire bivariate characteristics simulation in sub-regions around the world

The wildfire priority index proposed in chapter 5 was first applied globally to consider the wildfire bivariate characteristics in wildfire forecasting. Then, to choose the appropriate predictor as much as possible in wildfire forecasting for preventing overfitting, the correlation coefficients of each hydro-meteorological element and wildfire priority index were calculated, as shown in Figure 7.3. Not only single hydro-meteorological elements such as precipitation (PRE) and surface soil moisture (SSM) were considered, but the joint probabilities of hydro-meteorological elements were also used as an alternative predictor for wildfire. Each sub-region is located in different climatic zones and covered by different vegetation types. Therefore, the hydro-meteorological elements that dominate the wildfire bivariate characteristics varied by sub-regions. In particular, in ALA, the relationship between the wildfire priority index with temperature (TEM), TEM + PRE, and TEM + SSM showed the strongest correlation, all above 0.8. Combinations with correlation coefficients greater than 0.8 for the first three dominant variables also included NEB and SAF. Especially in SAF, the correlation coefficient between SSM and the wildfire priority index was as high as 0.94. In addition, the correlation coefficients of the first three dominant hydro-meteorological elements of SAS and MED were all higher than 0.7. And SSM and SSM-based joint probability significantly affected the wildfire characteristics of these two sub-regions. In the SEA, CGI, CAM, and NAS sub-regions, the correlation coefficients of the first three dominant elements can only reach above 0.6. Also, the most significant elements affecting these four regions were SSM, TEM, SSM, and TEM, respectively. In TIB, NAU, SAU, WNA, SSA, SAH, WAF, EAF, WAS, and CAS, the correlation coefficients of the first three leading factors varied widely, ranging from 0.40 to 0.87. And the dominant combinations were TEM-TIB, PRE+SSM-SAU, TEM-WNA, SSM-SSA, PRE-SAH, TEM+PRE-WAF, TEM+PRE-EAF, TEM-WAS, and TEM-CAS. However, the relationship between hydro-meteorological elements and wildfire characteristics was insignificant in the NEU, CNA, WSA, CEU, and EAS sub-regions. Especially in EAS, the highest correlation coefficient was only 0.20.

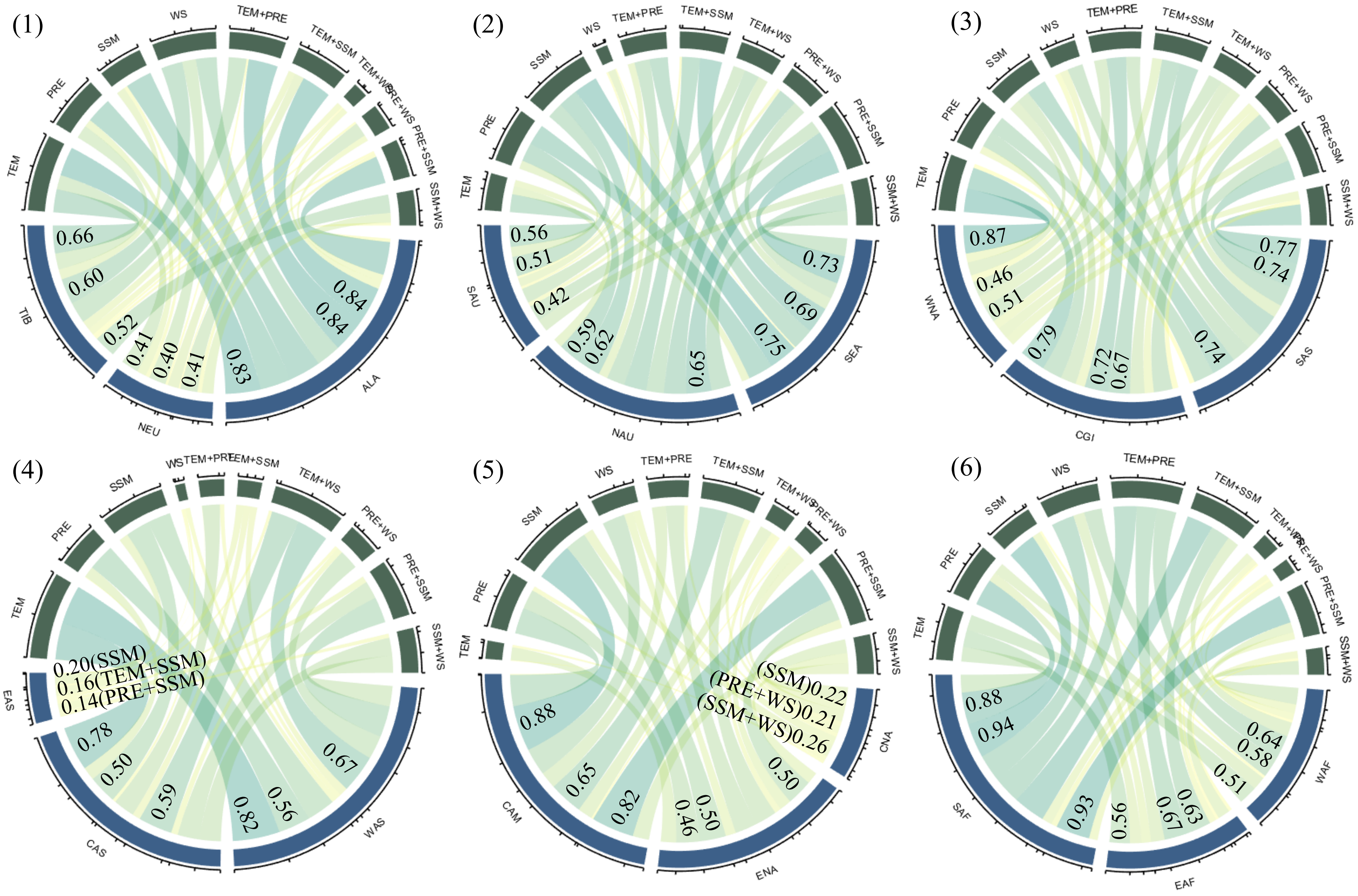
(1)
TEM
PRE
SSM
WS
TEM+PRE
TEM+SSM
TEM+WS
PRE+WS
PRE+SSM
SSM+WS
TIB
NEU
ALA
0.66
0.60
0.52
0.41
0.40
0.41
0.83
0.84
0.84
(2)
TEM
PRE
SSM
WS
TEM+PRE
TEM+SSM
TEM+WS
PRE+WS
PRE+SSM
SSM+WS
SAU
NAU
SEA
0.56
0.51
0.42
0.59
0.62
0.65
0.75
0.69
0.73
(3)
TEM
PRE
SSM
WS
TEM+PRE
TEM+SSM
TEM+WS
PRE+WS
PRE+SSM
SSM+WS
WNA
CGI
SAS
0.87
0.46
0.51
0.79
0.72
0.67
0.74
0.77
0.74
(4)
TEM
PRE
SSM
WS
TEM+PRE
TEM+SSM
TEM+WS
PRE+WS
PRE+SSM
SSM+WS
EAS
CAS
WAS
0.20(SSM)
0.16(TEM+SSM)
0.14(PRE+SSM)
0.78
0.50
0.59
0.82
0.56
0.67
(5)
TEM
PRE
SSM
WS
TEM+PRE
TEM+SSM
TEM+WS
PRE+WS
PRE+SSM
SSM+WS
CAM
ENA
CNA
0.88
0.65
0.82
0.46
0.50
0.50
(SSM)0.22
(PRE+WS)0.21
(SSM+WS)0.26
(6)
TEM
PRE
SSM
WS
TEM+PRE
TEM+SSM
TEM+WS
PRE+WS
PRE+SSM
SSM+WS
SAF
EAF
WAF
0.88
0.94
0.93
0.56
0.67
0.63
0.51
0.58
0.64

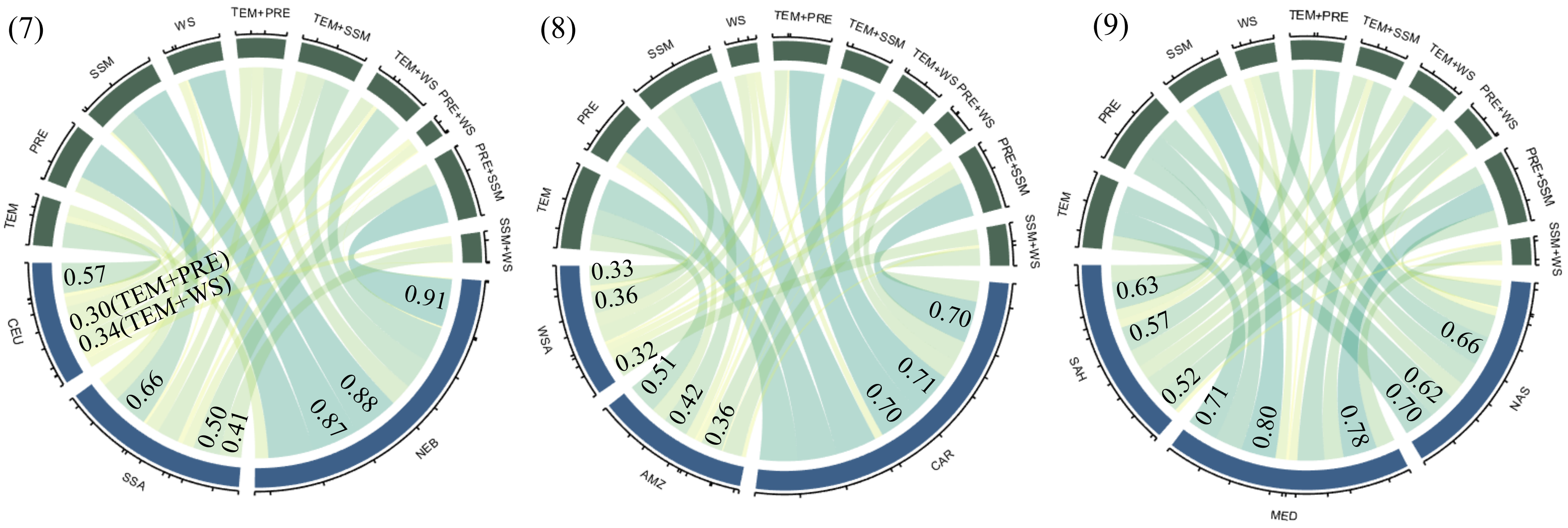

Figure 7.3 Chord diagram for the correlation coefficient between the hydro-meteorological elements and wildfire priority index. This figure mainly shows the comparison between the correlation coefficients in the same region. The thicker line means the stronger correlation. The correlation coefficient values of the top three hydro-meteorological elements that dominate each region are also marked in the figure.

After quantifying the relationship between the hydro-meteorological elements and the wildfire priority index in each sub-region, this chapter selected the first three dominant hydro-meteorological elements as predictors to simulate the wildfire priority index based on Back Propagation Neural Network (BPNN). BPNN is one of the most widely used Artificial Neural Networks. The performance of the BPNN simulations for each sub-region is shown in Figure 7.4. Even with only three predictors, the accuracy of the model achieved good performance. The R^2 of the overall data in 16 sub-regions has reached over 0.80. The R^2 of the test data of 12 regions has also reached over 0.80. And all the data R^2 in the five sub-regions of CAM, MED, NEB, WAF, and SAF even reached 0.90 or more. The model performed best in the SAF region, with R^2 of 0.95 and 0.94 for all data and test data, respectively. However, the R^2 of all data was only 0.41 in the CNA sub-region, and the simulation performance in this sub-region was poor. Similar poor model performance was also found in the ENA region, with 0.50 R^2 of all data.

To further explore the reasons for the differences in simulation performance, Figure 7.5 selects four representative regions: ALA with the 0.89 R^2 of all data, NEU with the 0.66 R^2 of all data, CNA with the worst simulation performance, and SAF with the best simulation performance. Firstly, the wildfire bivariate characteristics in this sub-region showed significant cyclicality for the SAF sub-region. Secondly, the correlation between meteorological elements and wildfire characteristics was very strong. The correlation coefficients for the three predictors were above 0.85, with 0.94, 0.93, and 0.88, respectively. Similarly, the ALA sub-region also had similar characteristics with significant cyclicality and high correlation coefficients. The cyclicality was weaker for the wildfire bivariate time series in the NEU and CNA sub-regions. The highest correlation coefficient in NEU was only 0.41, while the highest value in the CNA was only 0.26. The weak correlation between hydro-meteorological elements and the wildfire priority index led to the low accuracy of BPNN model simulations. However, it could be seen from the NEU and CNA sub-regions that even though there was a lack of ability to simulate specific wildfire priority index values in these sub-regions accurately, the trends in the simulated time series were largely consistent with the observed time series. The three predictors selected in this chapter to simulate the wildfire bivariate characteristics still achieved some breakthroughs. The BPNN model achieved good results in most areas regarding accuracy values and time series trends. Even in some areas where accuracy was lacking, a good ability to follow time series could also guide wildfire prevention and management.

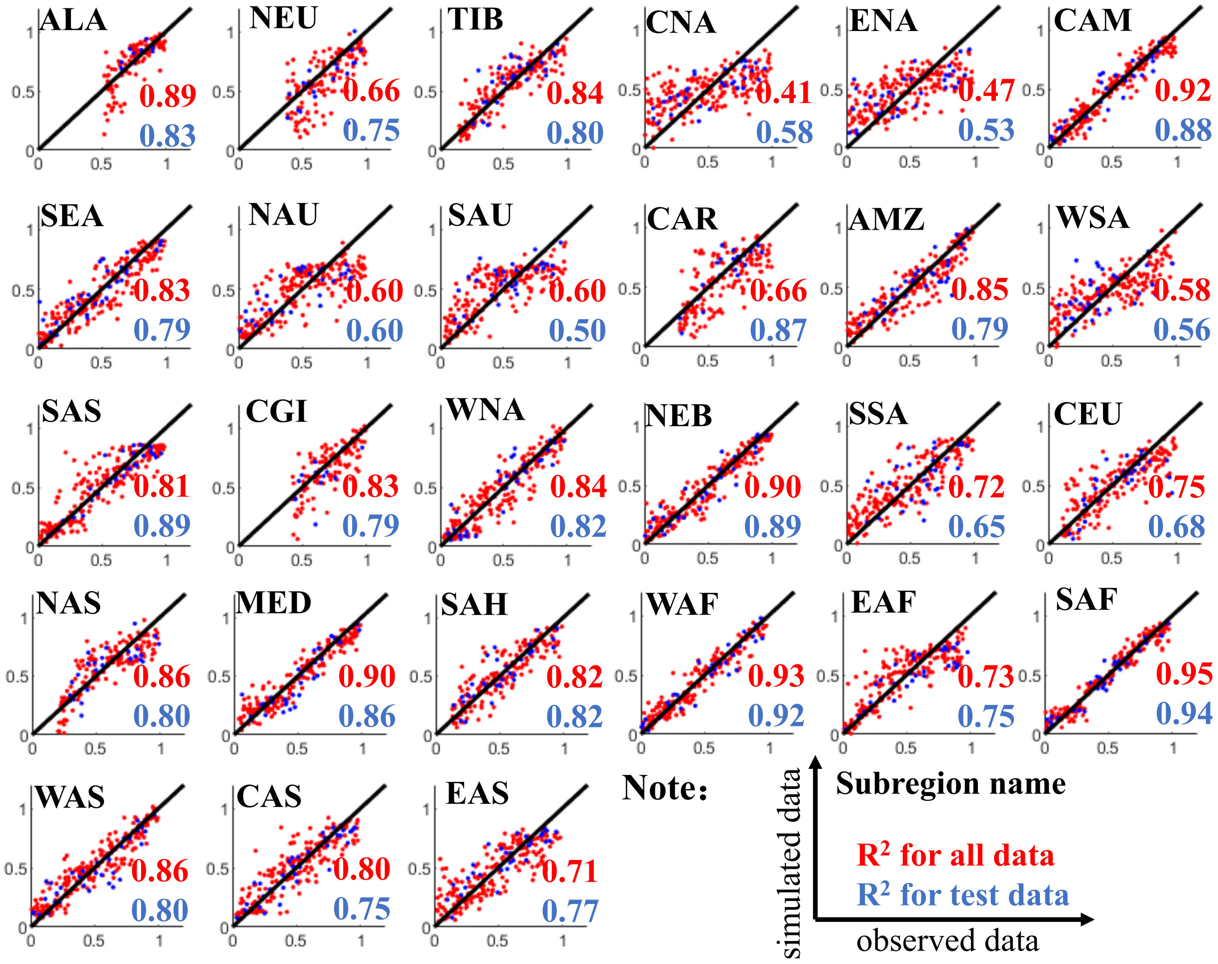

Figure 7.4 The performance of wildfire priority index based on BPNN simulation in different sub-regions.

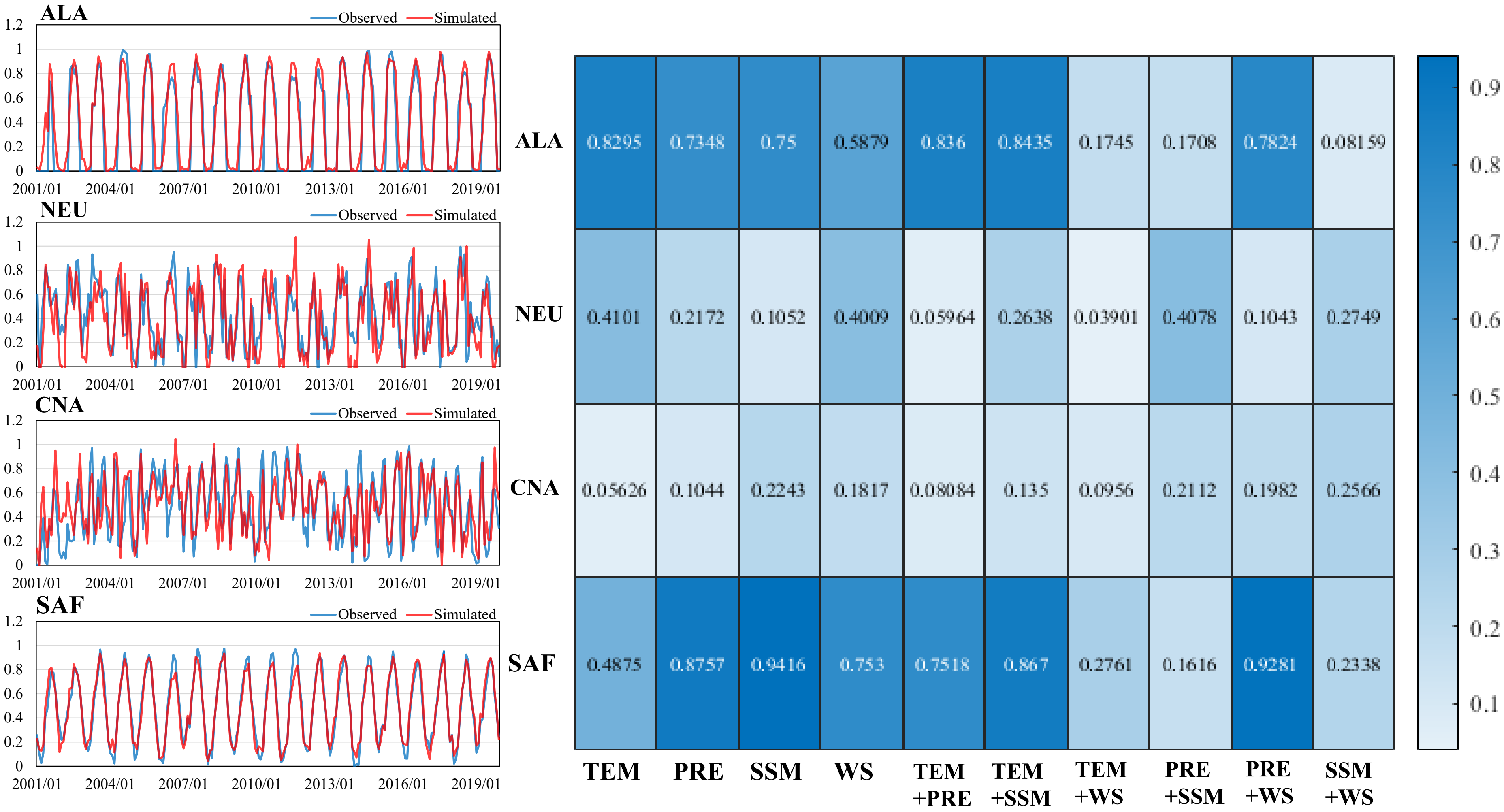

	TEM	PRE	SSM	WS	TEM +PRE	TEM +SSM	TEM +WS	PRE +SSM	PRE +WS	SSM +WS
ALA	0.8295	0.7348	0.75	0.5879	0.836	0.8435	0.1745	0.1708	0.7824	0.08159
NEU	0.4101	0.2172	0.1052	0.4009	0.05964	0.2638	0.03901	0.4078	0.1043	0.2749
CNA	0.05626	0.1044	0.2243	0.1817	0.08084	0.135	0.0956	0.2112	0.1982	0.2566
SAF	0.4875	0.8757	0.9416	0.753	0.7518	0.867	0.2761	0.1616	0.9281	0.2338

Figure 7.5 Observed and simulated time series for four representative sub-regions. And the correlation coefficient plots in these four sub-regions.

7.3 Discussion

This study called for attention to the wildfire bivariate characteristics simulation and proposed a wildfire simulation framework based on the hydrometeorology-wildfire relationship. In particular, this study first analyzed the wildfire characteristics from 2001~2019 of 27 sub-regions worldwide. Then, the relationship between hydro-meteorological elements and wildfire bivariate characteristics (described by the wildfire priority index proposed in chapter 5) in different sub-regions was quantified by Pearson correlation coefficients. Finally, the first three dominant hydro-meteorological elements in each sub-region were selected as predictors, and the BPNN model simulated the wildfire bivariate characteristics.

However, for the modeling of wildfire bivariate characteristics in this Chapter, only historical hydro-meteorological data was used for wildfire simulation without further predicting future wildfire bivariate characteristics under the current climate change. In future work, inputting hydro-meteorological data is an important direction to carry out the long-term prediction and trend analysis of wildfire bivariate characteristics.

7.4 Summary

Based on the results, the major conclusions are as follows:

(1) Among the 27 sub-regions, the largest burned area and the most frequent wildfire activities were consistent only in the five sub-regions. In the SEA, NAU, SAU, SAS, CNA, AMZ, NEB, SAH, WAF, and SAF, wildfire characteristics in these regions tended to become larger. In contrast, wildfires became more frequent in the sub-regions of ALA, NEU, WNA, ENA, WSA, SSA, NAS, MED, EAF, CAS, and EAS. Also, the month with the most frequent wildfire activity occurred in SAF, while WAF had the highest median of wildfire activity and burned area worldwide.

(2) In the wildfire bivariate characteristics simulation results of the BPNN model, there were five sub-regions where the model achieved high simulation accuracy, with the R^2 reaching more than 0.90. In addition, eleven sub-regions also achieved good simulation results, and their

R^2 was between 0.8 and 0.9. Only two sub-regions had poor simulation accuracy with R^2 below 0.5.

(3) On the one hand, when the observed time series had significant periodicity and a high correlation occurred between the hydro-meteorological elements and wildfire bivariate characteristics, the model accuracy of BPNN would be very high. For example, the R^2 in the ALA and SAF sub-regions were as high as 0.89 and 0.95, respectively. On the other hand, when the correlation between hydrometeorology and wildfire was weak, BPNN was insufficient to simulate time series accurately. Still, its ability to follow the original observation time series was not inferior

Overall, the framework of wildfire bivariate characteristic simulation proposed in this study can provide a reference for future wildfire management and wildfire prevention in various global sub-regions.

Chapter 8 Conclusions and Recommendations

8.1 Conclusions

This research attempted to analyze how atmospheric-oceanic indices and hydro-meteorological elements affected the spatiotemporal distribution characteristics of wildfires. On the one hand, first illustrated by the example of Japan, the teleconnections between atmospheric-oceanic indices and the drought (soil moisture) homogeneous zones were identified, and the wildfire statistics were compared with the drought (soil moisture) homogeneous zones. Then, looking at the global, the teleconnections between atmospheric-oceanic indices and the global wildfire (burned area) homogeneous zones were discussed. On the other hand, illustrated by the example of the continental United States, a probability-based index was developed to evaluate the bivariate characteristics s of wildfire comprehensively. On this basis, the control effects of hydro-meteorological elements on different types of wildfires were quantified. Finally, the dominant hydro-meteorological elements for each wildfire type were identified in different global climate reference regions. In particular, the conclusions are generalized as follows:

(1) Among these nine zones, zone 1 was dominated by extreme drought events. Zones 2 and 6 were typical representatives of spring droughts, whereas zone 7 was wet for most of the period. The Hokkaido region was divided into wetter zone 4 and drier zone 9. The topography distinguished zones-3, -5, and -8. The analyses also reveal almost all nine zones had a high level of homogeneity, with more than 60% explained variance. Also, these nine zones were dominated by different large-scale climate signals: the Arctic Oscillation had the strongest impact on zones 1, 7, and 8; the influence of the North Atlantic Oscillation on zones 3, 4, and 6 was significant; zones 2 and 9 were both dominated by the Pacific decadal oscillation; El Ni˜no–Southern Oscillation dominated zone 5. The results will be valuable for drought management and drought prevention.

(2) The most significant atmospheric-oceanic indices that strongly impacted each of the eight major wildfire patterns (the explained variance accounted for 30%) were identified. The

most significant combinations of hotspots and atmospheric-oceanic indices were the Atlantic multidecadal Oscillation-East Pacific/North Pacific Oscillation (EP/NP)-Pacific North American Pattern (PNA) with the pattern around Ukraine and Kazakhstan, El Niño/Southern Oscillation-Arctic Oscillation (AO)-East Atlantic/Western Russia Pattern (EA/WR) with the pattern in Australia, and PNA-AO-Polar/Eurasia Pattern-EA/WR with the pattern in Brazil. Overall, these results provided a reference for predicting wildfire and understanding wildfire homogeneity. Overall, this study established the teleconnection between atmospheric-oceanic indices and burned area patterns for the first time and explored the physical mechanism behind their teleconnection from a global perspective.

(3) The regional difference in the optimal marginal distribution of the burned area was more significant than the wildfire activity. The Weibull (WEI) distribution remained applicable to these two variables in most grid cells. Compared to the direct joint probability, the probability of WP was more sensitive in capturing extreme wildfire events. Also, the wildfire risk exhibited an increasing trend in California, Texas, Kentucky, and Arkansas, while most southeastern United States exhibited decreasing wildfire risk trends. Overall, this analysis can provide a reference to understand the spatiotemporal characteristics of wildfire statistics better and contribute to wildfire management.

(4) Through the probability of wildfire bivariate statistical characteristics, wildfires could be classified into five types in this paper: WT-1 (mega-wildfire), WT-2 (joint wildfire-1 (burned area dominated)), WT-3 (joint extremes), WT-4 (joint wildfire-2 (fire activity dominated)), and WT-5 (super frequent wildfires). The dominant hydro-meteorological elements under different wildfire types were discussed in 17 ecoregions of the United States. Also, in the four new cluster regions, intensifying droughts were a concern in clusters 1 and 4, while there were multiple concerns in cluster 3, namely, stronger winds, higher temperatures, and more drought. Overall, the hydrometeorology-wildfire relationship analysis based on the wildfire bivariate probabilistic framework proposed in this study provides new information on the causes of wildfires and other compound hazards.

(5) A global wildfire simulation framework was proposed based on the

hydrometeorology-wildfire relationship. Among the 27 sub-regions around the world, when the observed time series has significant periodicity and the hydro-meteorological elements and wildfire bivariate characteristics were significantly correlated, the model accuracy of BPNN would be very high. For example, the R^2 in the ALA and SAF sub-regions were as high as 0.89 and 0.95, respectively. On the other hand, when the correlation between hydrometeorology and wildfire was weak, BPNN was insufficient to simulate time series accurately. Still, its ability to follow the original observation time series was not inferior. Overall, the framework of wildfire bivariate characteristic simulation proposed in this study can provide a reference for future wildfire management and wildfire prevention in various global sub-regions.

8.2 Recommendations for future studies

Although this study has analyzed and discussed the effects of atmospheric-oceanic indices and hydro-meteorological elements on wildfire as fully as possible, there are still some limitations in this study. The following are specific limitations in this study and recommendations for future studies:

(1) For studies about return periods, only long data periods can ensure greater results robustness. However, the discussion on the wildfire return period in this dissertation is limited by the period length of the wildfire data, which is difficult to overcome. Therefore, in future research, the period can be increased through the reconstruction of ancient wildfires or wildfire simulation in future scenarios to further improve the robustness of the return period results.

(2) As the teleconnections between atmospheric-oceanic indices and the global wildfire (burned area) homogeneous zones, the limitations include the lack of validation of the physical mechanism between wildfires and atmospheric-oceanic indices. Furthermore, some regions were ignored in our identified global wildfire patterns. Although some studies described how atmospheric-oceanic indices affect wildfires in specific regions, due to the limited hotspots of global wildfire patterns, it is not easy to compare with some climate-wildfire relationships, such as ENSO-wildfire dynamics in Insular Southeast Asia (Murphy, 2006), AO-wildfire in Central Siberia (Balzter et al., 2005) and AMO+ENSO+PDO-wildfire in Colorado (Schoennagel et al., 2007). On the other hand, the advantage of teleconnection between global

wildfire patterns and atmospheric-oceanic indices lies in direct finding the widespread climatic influence from a global perspective, that is, the discovery of global wildfire homogeneity under the influence of the same atmospheric-oceanic indices. Therefore, how to further balance regional phenomena and global relevance should be addressed in future studies.

(3) There remain a few limitations in describing the bivariate characteristics of wildfire. Wildfire statistics do not yield long-term continuous time series similar to other traditional hydro-meteorological data. It is also common that no wildfire occurs for several months in a high-rainfall year. Even though grid cells with fewer than 100 valid data points were removed in this study, the data length remains an unavoidable source of uncertainty in frequency analysis. The generation of longer data series or reconstruction of wildfire events through paleoclimate research can provide more reliable data for wildfire frequency analysis.

(4) Neither the analysis of the impact of atmospheric-oceanic indices on wildfire nor the impact of hydro-meteorological elements on wildfire has considered human influences, such as wildfire management, wildfire suppression, wildfire prevention, and fuel treatments. Considering human influences on wildfire will be critical in future research. In wildfire forecasting, atmospheric-oceanic indices and hydro-meteorological elements and indicators such as GDP and population density need to be considered as predictor variables.

(5) The analysis in this dissertation is only aimed at wildfire statistics on a monthly scale. While the results are useful for analyzing wildfire trends and characteristics over the long-term time scales, they cannot achieve the forecasting and early warning of wildfire occurrence in the short-term time scales (hourly scale, daily scale, and weekly scale). However, the fine-scale physical process-based wildfire model has the characteristics of a too large amount of computation and is too complicated for long-term wildfire trend forecasting. Therefore, the future research direction is to couple the control effects of atmospheric-oceanic indices and hydro-meteorological elements on wildfire quantified in this dissertation with the fine-scale physical process-based wildfire model to achieve the purpose of variable-scale wildfire forecasting and early warning.

(6) For the modeling of wildfire bivariate characteristics in this dissertation, only historical

hydro-meteorological data was used for wildfire simulation without further predicting future wildfire bivariate characteristics under the current climate change. In future work, inputting hydro-meteorological data is an important direction to carry out the long-term prediction and trend analysis of wildfire bivariate characteristics. And by predicting future wildfires, the response of wildfires to climate change can be further discussed.

References

Abbot, J., & Marohasy, J. (2014). Input selection and optimisation for monthly rainfall forecasting in Queensland, Australia, using artificial neural networks. *Atmospheric Research, 138*, 166-178.

Abramowitz, M., & Stegun, I. A. (1964). Handbook of mathematical functions with formulas, graphs, and mathematical tables (Vol. 55): US Government printing office.

Achite, M., Banadkooki, F. B., Ehteram, M., Bouharira, A., Ahmed, A. N., & Elshafie, A. (2022). Exploring Bayesian model averaging with multiple ANNs for meteorological drought forecasts. *Stochastic Environmental Research and Risk Assessment*, 1-26.

Adams, M. A. (2013). Mega-fires, tipping points and ecosystem services: Managing forests and woodlands in an uncertain future. *Forest Ecology and Management, 294*, 250-261.

Aho, K., Derryberry, D., & Peterson, T. (2014). Model selection for ecologists: the worldviews of AIC and BIC. *Ecology, 95*(3), 631-636.

Aizen, E. M., Aizen, V. B., Melack, J. M., Nakamura, T., & Ohta, T. (2001). Precipitation and atmospheric circulation patterns at mid-latitudes of Asia. *International Journal of Climatology: A Journal of the Royal Meteorological Society, 21*(5), 535-556.

Akaike, H. (1974). A new look at the statistical model identification. *IEEE transactions on automatic control, 19*(6), 716-723.

Alcantara, C., Kuemmerle, T., Baumann, M., Bragina, E. V., Griffiths, P., Hostert, P., . . . Schierhorn, F. (2013). Mapping the extent of abandoned farmland in Central and Eastern Europe using MODIS time series satellite data. *Environmental Research Letters, 8*(3), 035035.

Aldersley, A., Murray, S. J., & Cornell, S. E. (2011). Global and regional analysis of climate and human drivers of wildfire. *Science of the Total Environment, 409*(18), 3472-3481.

Alencar, A., Nepstad, D., & Diaz, M. C. V. (2006). Forest understory fire in the Brazilian Amazon in ENSO and non-ENSO years: area burned and committed carbon emissions. *Earth Interactions, 10*(6), 1-17.

Allen, R. G., Pereira, L. S., Raes, D., & Smith, M. (1998). Crop evapotranspiration-Guidelines for computing crop water requirements-FAO Irrigation and drainage paper 56. *Fao, Rome, 300*(9), D05109.

Andela, N., Morton, D. C., Giglio, L., Chen, Y., van der Werf, G. R., Kasibhatla, P. S., . . . Kloster, S. (2017). A human-driven decline in global burned area. *Science, 356*(6345), 1356-1362.

Anderson, S. A. (2009). Future options for fire behaviour modelling and fire danger rating in New Zealand. *Proceedings of the Royal Society of Queensland, The, 115*, 119-128.

Andrews, P. L., Cruz, M. G., & Rothermel, R. C. (2013). Examination of the wind speed limit function in the Rothermel surface fire spread model. *International Journal of Wildland Fire, 22*(7), 959-969.

Andrieu, C., & Thoms, J. (2008). A tutorial on adaptive MCMC. *Statistics and computing, 18*(4), 343-373.

Arai, R., Toyoda, Y., & Kazama, S. (2022). Streamflow maps for run-of-river hydropower developments in Japan. *Journal of Hydrology, 607*, 127512.

Asong, Z. E., Wheater, H. S., Bonsal, B., Razavi, S., & Kurkute, S. (2018). Historical drought patterns over Canada and their teleconnections with large-scale climate signals. *Hydrology and Earth System Sciences, 22*(6), 3105-3124.

Attiwill, P. M., & Adams, M. A. (2013). Mega-fires, inquiries and politics in the eucalypt forests of Victoria, south-eastern Australia. *Forest Ecology and Management, 294*, 45-53.

Balch, J. K., Bradley, B. A., Abatzoglou, J. T., Nagy, R. C., Fusco, E. J., & Mahood, A. L. (2017). Human-started wildfires expand the fire niche across the United States. *Proceedings of the National Academy of Sciences, 114*(11), 2946-2951.

Baltacı, H., Akkoyunlu, B. O., & Tayanc, M. (2018). Relationships between teleconnection patterns and Turkish climatic extremes. *Theoretical and Applied Climatology, 134*(3), 1365-1386.

Balzter, H., Gerard, F. F., George, C. T., Rowland, C. S., Jupp, T. E., McCallum, I., . . . Onuchin, A. (2005). Impact of the Arctic Oscillation pattern on interannual forest fire variability in Central Siberia. *Geophysical Research Letters, 32*(14).

Bamston, A. G., Chelliah, M., & Goldenberg, S. B. (1997). Documentation of a highly ENSO-related SST region in the equatorial Pacific: Research note. *Atmosphere-ocean, 35*(3), 367-383.

Barnston, A. G., & Livezey, R. E. (1987). Classification, seasonality and persistence of low-frequency atmospheric circulation patterns. *Monthly weather review, 115*(6), 1083-1126.

Bartsch, A., Balzter, H., & George, C. (2009). The influence of regional surface soil moisture anomalies on forest fires in Siberia observed from satellites. *Environmental Research Letters, 4*(4), 045021.

Beguería, S., Vicente-Serrano, S. M., Reig, F., & Latorre, B. (2014). Standardized precipitation evapotranspiration index (SPEI) revisited: parameter fitting, evapotranspiration models, tools, datasets and drought monitoring. *International Journal of Climatology, 34*(10), 3001-3023.

Bell, G. D., & Janowiak, J. E. (1995). Atmospheric circulation associated with the Midwest floods of 1993. *Bulletin of the American Meteorological Society, 76*(5), 681-696.

Betts, A. (1973). Non-precipitating cumulus convection and its parameterization. *Quarterly Journal of the Royal Meteorological Society, 99*(419), 178-196.

Bistinas, I., Oom, D., Sá, A. C., Harrison, S. P., Prentice, I. C., & Pereira, J. M. (2013). Relationships between human population density and burned area at continental and global scales. *PLoS One, 8*(12), e81188.

Black, M. P., Mooney, S. D., & Haberle, S. G. (2016). The fire, human and climate nexus in the Sydney Basin, eastern Australia. *The Holocene, 17*(4), 469-480.

Blackmon, M. L., Lee, Y., Wallace, J. M., & Hsu, H.-H. (1984). Time variation of 500 mb height fluctuations with long, intermediate and short time scales as deduced from lag-correlation statistics. *Journal of Atmospheric Sciences, 41*(6), 981-991.

Boer, M. M., de Dios, V. R., & Bradstock, R. A. (2020). Unprecedented burn area of Australian mega forest fires. *Nature Climate Change, 10*(3), 171-172.

Borchers Arriagada, N., Palmer, A. J., Bowman, D. M., Morgan, G. G., Jalaludin, B. B., & Johnston, F. H. (2020). Unprecedented smoke-related health burden associated with the 2019–20 bushfires in eastern Australia. *Medical Journal of Australia, 213*(6), 282-283.

Bowman, D. M., Balch, J. K., Artaxo, P., Bond, W. J., Carlson, J. M., Cochrane, M. A., . . . Pyne, S. J. (2009). Fire in the Earth system. *Science, 324*(5926), 481-484.

Bradley, P. S., Fayyad, U., & Reina, C. (1998). Scaling EM (expectation-maximization) clustering to large databases. *Microsoft Research*, 0-25.

Brashaw, B., & Bergman, R. (2021). Wood as a renewable and sustainable resource.

Brewer, C. K., Winne, J. C., Redmond, R. L., Opitz, D. W., & Mangrich, M. V. (2005). Classifying and mapping wildfire severity. *Photogrammetric Engineering & Remote Sensing, 71*(11), 1311-1320.

Buchhorn, M., Lesiv, M., Tsendbazar, N.-E., Herold, M., Bertels, L., & Smets, B. (2020). Copernicus global land cover layers—collection 2. *Remote Sensing, 12*(6), 1044.

Buckland, M. K. (2019). What is a megafire? Defining the social and physical dimensions of extreme US wildfires (1988-2014). University of Colorado at Boulder

Calvert, E. (1934). Background for fire-weather warmings. *Eos, Transactions American Geophysical Union, 15*(1), 96-97.

Cardil, A., Eastaugh, C. S., & Molina, D. (2015). Extreme temperature conditions and wildland fires in Spain. *Theoretical and Applied Climatology, 122*(1), 219-228.

Cardil, A., Vega-García, C., Ascoli, D., Molina-Terrén, D., Silva, C., & Rodrigues, M. (2019). How does drought impact burned area in Mediterranean vegetation communities? *Science of the Total Environment, 693*, 133603.

Carvalho, A., Flannigan, M. D., Logan, K., Miranda, A. I., & Borrego, C. (2008). Fire activity in Portugal and its relationship to weather and the Canadian Fire Weather Index System. *International Journal of Wildland Fire, 17*(3), 328-338.

Cattau, M. E., Wessman, C., Mahood, A., & Balch, J. K. (2020). Anthropogenic and lightningstarted fires are becoming larger and more frequent over a longer season length in the USA. *Global Ecology and Biogeography, 29*(4), 668-681.

Champeaux, J. L., Masson, V., & Chauvin, F. (2005). ECOCLIMAP: a global database of land surface parameters at 1 km resolution. *Meteorological Applications: A journal of forecasting, practical applications, training techniques and modelling, 12*(1), 29-32.

Chuvieco, E., Pettinari, M., Lizundia-Loiola, J., Storm, T., Padilla Parellada, M., & Initiative, E. F. C. C. (2018). MODIS Fire_cci Burned Area Pixel Product, version 5.1. *Centre for Environmental Data Analysis: Didcot, UK.*

Clarke, H., Gibson, R., Cirulis, B., Bradstock, R. A., & Penman, T. D. (2019). Developing and testing models of the drivers of anthropogenic and lightning-caused wildfire ignitions in south-eastern Australia. *Journal of environmental management, 235*, 34-41.

Coen, J. L., Stavros, E. N., & Fites-Kaufman, J. A. (2018). Deconstructing the King megafire. *Ecological Applications, 28*(6), 1565-1580.

Collins, B. M., Omi, P. N., & Chapman, P. L. (2006). Regional relationships between climate and wildfire-burned area in the Interior West, USA. *Canadian Journal of Forest Research, 36*(3), 699-709.

Cook, B. I., Seager, R., & Smerdon, J. E. (2014). The worst North American drought year of the last millennium: 1934. *Geophysical Research Letters, 41*(20), 7298-7305.

Cruz, M. G., Gould, J. S., Alexander, M. E., Sullivan, A. L., McCaw, W. L., & Matthews, S. (2015). Empirical-based models for predicting head-fire rate of spread in Australian fuel types. *Australian Forestry, 78*(3), 118-158.

Dadap, N. C., Cobb, A. R., Hoyt, A. M., Harvey, C. F., & Konings, A. G. (2019). Satellite soil moisture observations predict burned area in Southeast Asian peatlands. *Environmental Research Letters, 14*(9), 094014.

Dai, A. (2011). Drought under global warming: a review. *Wiley Interdisciplinary Reviews: Climate Change, 2*(1), 45-65.

Dai, A., Trenberth, K. E., & Qian, T. (2004). A global dataset of Palmer Drought Severity Index for 1870–2002: Relationship with soil moisture and effects of surface warming. *Journal of Hydrometeorology, 5*(6), 1117-1130.

Dawson, C. W., Abrahart, R. J., Shamseldin, A. Y., & Wilby, R. L. (2006). Flood estimation at ungauged sites using artificial neural networks. *Journal of Hydrology, 319*(1-4), 391-409.

de Dios, V. R., Camprubí, À. C., Pérez-Zanón, N., Peña, J. C., Del Castillo, E. M., Rodrigues, M., . . . Boer, M. M. (2022). Convergence in critical fuel moisture and fire weather thresholds associated with fire activity in the pyroregions of Mediterranean Europe. *Science of the Total Environment, 806*, 151462.

Dempster, A. P., Laird, N. M., & Rubin, D. B. (1977). Maximum likelihood from incomplete data via the EM algorithm. *Journal of the Royal Statistical Society: Series B*

(Methodological), 39(1), 1-22.

Dennison, P. E., Brewer, S. C., Arnold, J. D., & Moritz, M. A. (2014). Large wildfire trends in the western United States, 1984-2011. *Geophysical Research Letters, 41*(8), 2928-2933.

Doerr, S. H., & Santín, C. (2016). Global trends in wildfire and its impacts: perceptions versus realities in a changing world. *Philosophical Transactions of the Royal Society B: Biological Sciences, 371*(1696), 20150345.

Dommenget, D. (2007). Evaluating EOF modes against a stochastic null hypothesis. *Climate dynamics, 28*(5), 517-531.

Duncan, A. P. (2014). The analysis and application of artificial neural networks for early warning systems in hydrology and the environment.

Earl, N., & Simmonds, I. (2018). Spatial and temporal variability and trends in 2001–2016 global fire activity. *Journal of Geophysical Research: Atmospheres, 123*(5), 2524-2536.

Edwards, B., Gray, M., & Hunter, B. (2019). The social and economic impacts of drought. *Australian Journal of Social Issues, 54*(1), 22-31.

Efthimiou, N., Psomiadis, E., & Panagos, P. (2020). Fire severity and soil erosion susceptibility mapping using multi-temporal Earth Observation data: The case of Mati fatal wildfire in Eastern Attica, Greece. *Catena, 187*, 104320.

Ellis, T. M., Bowman, D. M., Jain, P., Flannigan, M. D., & Williamson, G. J. (2022). Global increase in wildfire risk due to climate-driven declines in fuel moisture. *Global change biology, 28*(4), 1544-1559.

Elsafi, S. H. (2014). Artificial neural networks (ANNs) for flood forecasting at Dongola Station in the River Nile, Sudan. *Alexandria Engineering Journal, 53*(3), 655-662.

Enfield, D. B., Mestas-Nuñez, A. M., Mayer, D. A., & Cid-Serrano, L. (1999). How ubiquitous is the dipole relationship in tropical Atlantic sea surface temperatures? *Journal of Geophysical Research: Oceans, 104*(C4), 7841-7848.

Enfield, D. B., Mestas-Nuñez, A. M., & Trimble, P. J. (2001). The Atlantic multidecadal oscillation and its relation to rainfall and river flows in the continental US. *Geophysical Research Letters, 28*(10), 2077-2080.

Eroğluer, T. A., & Apaydin, H. (2020). Estimation of drought by streamflow drought index (SDI) and artificial neural networks (ANNs) in Ankara-Nallihan region. *Turkish Journal of Agriculture-Food Science and Technology, 8*(2), 348-357.

Fernández, J., Fernández, C., Féménias, P., & Peter, H. (2016). The Copernicus Sentinel-3 mission. Paper presented at the ILRS workshop.

Filliben, J. J. (1975). The probability plot correlation coefficient test for normality. *Technometrics, 17*(1), 111-117.

Flannigan, D., M., Krawchuk, M. A., de Groot, W. J., Wotton, B. M., & Gowman, L. M. (2009).

Implications of changing climate for global wildland fire. *International Journal of Wildland Fire, 18*(5), 483-507.

Flannigan, MD, Wotton, B., Marshall, G., De Groot, W., Johnston, J., . . . Cantin, A. (2016). Fuel moisture sensitivity to temperature and precipitation: climate change implications. *Climatic Change, 134*(1), 59-71.

Flannigan, M. D., Stocks, B. J., & Wotton, B. M. (2000). Climate change and forest fires. *Science of the Total Environment, 262*(3), 221-229.

Flatley, W. T., Lafon, C. W., & Grissino-Mayer, H. D. (2011). Climatic and topographic controls on patterns of fire in the southern and central Appalachian Mountains, USA. *Landscape Ecology, 26*(2), 195-209.

Forkel, M., Dorigo, W., Lasslop, G., Chuvieco, E., Hantson, S., Heil, A., . . . Harrison, S. P. (2019). Recent global and regional trends in burned area and their compensating environmental controls. *Environmental Research Communications, 1*(5), 051005.

Fox, D., Carrega, P., Ren, Y., Caillouet, P., Bouillon, C., & Robert, S. (2018). How wildfire risk is related to urban planning and Fire Weather Index in SE France (1990–2013). *Science of the Total Environment, 621*, 120-129.

Fraley, C., & Raftery, A. E. (2002). Model-based clustering, discriminant analysis, and density estimation. *Journal of the American statistical Association, 97*(458), 611-631.

Fraley, C., Raftery, A. E., Murphy, T. B., & Scrucca, L. (2012). mclust version 4 for R: normal mixture modeling for model-based clustering, classification, and density estimation.

Fujihara, Y., Tanaka, K., Watanabe, T., Nagano, T., & Kojiri, T. (2008). Assessing the impacts of climate change on the water resources of the Seyhan River Basin in Turkey: Use of dynamically downscaled data for hydrologic simulations. *Journal of Hydrology, 353*(1-2), 33-48.

Fulé, P. Z., Crouse, J. E., Heinlein, T. A., Moore, M. M., Covington, W. W., & Verkamp, G. (2003). Mixed-severity fire regime in a high-elevation forest of Grand Canyon, Arizona, USA. *Landscape Ecology, 18*(5), 465-486.

Gao, C., Zhao, F., Shi, C., Liu, K., Wu, X., Wu, G., . . . Shu, L. (2021). Previous Atlantic Multidecadal Oscillation (AMO) modulates the lightning-ignited fire regime in the boreal forest of Northeast China. *Environmental Research Letters, 16*(2), 024054.

Geary, W. L., Buchan, A., Allen, T., Attard, D., Bruce, M. J., Collins, L., . . . Loeffler, E. (2022). Responding to the biodiversity impacts of a megafire: A case study from south-eastern Australia's Black Summer. *Diversity and distributions, 28*(3), 463-478.

Genest, C., & Favre, A.-C. (2007). Everything you always wanted to know about copula modeling but were afraid to ask. *Journal of hydrologic engineering, 12*(4), 347-368.

Giannini, A., Chiang, J. C., Cane, M. A., Kushnir, Y., & Seager, R. (2001). The ENSO teleconnection to the tropical Atlantic Ocean: Contributions of the remote and local SSTs to rainfall variability in the tropical Americas. *Journal of Climate, 14*(24), 4530-4544.

Gong, D., & Wang, S. (1998). Antarctic oscillation: concept and applications. *Chinese Science Bulletin, 43*(9), 734-738.

Gong, D., & Wang, S. (1999). Definition of Antarctic oscillation index. *Geophysical Research Letters, 26*(4), 459-462.

Goodrick, S. L., Brown, T. J., & Jolly, W. M. (2017). Weather, fuels, fire behavior, plumes, and smoke-the nexus of fire meteorology. *Fire Management Today., 75*(1), 33-38.

Greenwood, J. A., Landwehr, J. M., Matalas, N. C., & Wallis, J. R. (1979). Probability weighted moments: definition and relation to parameters of several distributions expressable in inverse form. *Water Resources Research, 15*(5), 1049-1054.

Grinsted, A., Moore, J. C., & Jevrejeva, S. (2004). Application of the cross wavelet transform and wavelet coherence to geophysical time series. *Nonlinear processes in geophysics, 11*(5/6), 561-566.

Gu, X., Zhang, Q., Singh, V. P., & Shi, P. (2017). Non-stationarities in the occurrence rate of heavy precipitation across China and its relationship to climate teleconnection patterns. *International Journal of Climatology, 37*(11), 4186-4198.

Hadisuwito, A., & Hassan, F. (2021). A Comparative Study of Drought Factors in the Mcarthur Forest Fire Danger Index in Indonesian Forest. *Ecol. Environ. Conserv. Pap, 5*, 202-206.

Hagman, G., Beer, H., Bendz, M., & Wijkman, A. (1984). Prevention better than cure. Report on human and environmental disasters in the Third World. 2.

Hantson, S., Pueyo, S., & Chuvieco, E. (2015). Global fire size distribution is driven by human impact and climate. *Global Ecology and Biogeography, 24*(1), 77-86.

Hao, Z., Hao, F., Singh, V. P., & Zhang, X. (2018). Changes in the severity of compound drought and hot extremes over global land areas. *Environmental Research Letters, 13*(12), 124022.

Harma, K., & Morrison, P. (2003). Analysis of vegetation mortality and prior landscape condition, 2002 Biscuit Fire Complex. *Pacific Biodiversity Institute, Winthrop, WA*.

Harris, S., Tapper, N., Packham, D., Orlove, B., & Nicholls, N. (2008). The relationship between the monsoonal summer rain and dry-season fire activity of northern Australia. *International Journal of Wildland Fire, 17*(5), 674-684.

Hayes, M., Svoboda, M., Wall, N., & Widhalm, M. (2011). The Lincoln declaration on drought indices: universal meteorological drought index recommended. *Bulletin of the American Meteorological Society, 92*(4), 485-488.

He, S., Gao, Y., Li, F., Wang, H., & He, Y. (2017). Impact of Arctic Oscillation on the East Asian climate: A review. *Earth-Science Reviews, 164*, 48-62.

Herrera-Estrada, J. E., Satoh, Y., & Sheffield, J. (2017). Spatiotemporal dynamics of global drought. *Geophysical Research Letters, 44*(5), 2254-2263.

Hersbach, H., Bell, B., Berrisford, P., Biavati, G., Horányi, A., Muñoz Sabater, J., . . . Rozum, I. (2018). ERA5 hourly data on single levels from 1979 to present. *Copernicus climate change service (c3s) climate data store (cds), 10.*

Hersbach, H., Bell, B., Berrisford, P., Hirahara, S., Horányi, A., Muñoz-Sabater, J., . . . Schepers, D. (2020). The ERA5 global reanalysis. *Quarterly Journal of the Royal Meteorological Society, 146*(730), 1999-2049.

Hessl, A. E., McKenzie, D., & Schellhaas, R. (2004). Drought and Pacific Decadal Oscillation linked to fire occurrence in the inland Pacific Northwest. *Ecological Applications, 14*(2), 425-442.

Higuera, P. E., & Abatzoglou, J. T. (2021). Record-setting climate enabled the extraordinary 2020 fire season in the western United States. *Global change biology, 27*(1).

Hoffman, K. M., Gavin, D. G., & Starzomski, B. M. (2016). Seven hundred years of human-driven and climate-influenced fire activity in a British Columbia coastal temperate rainforest. *Royal Society open science, 3*(10), 160608.

Holden, Z. A., Swanson, A., Luce, C. H., Jolly, W. M., Maneta, M., Oyler, J. W., . . . Affleck, D. (2018). Decreasing fire season precipitation increased recent western US forest wildfire activity. *Proc Natl Acad Sci U S A, 115*(36), E8349-E8357.

Hoover, K., & Hanson, L. A. (2021). Wildfire statistics. *Congressional Research Service, 2.*

Hosking, J. R. (1990). L-moments: Analysis and estimation of distributions using linear combinations of order statistics. *Journal of the Royal Statistical Society: Series B (Methodological), 52*(1), 105-124.

Hu, W., & Si, B. C. (2016). Multiple wavelet coherence for untangling scale-specific and localized multivariate relationships in geosciences. *Hydrology and Earth System Sciences, 20*(8), 3183-3191.

Hu, Z. Z., Wu, R., Kinter III, J. L., & Yang, S. (2005). Connection of summer rainfall variations in South and East Asia: role of El Niño–southern oscillation. *International Journal of Climatology: A Journal of the Royal Meteorological Society, 25*(9), 1279-1289.

Huang, B., Thorne, P. W., Banzon, V. F., Boyer, T., Chepurin, G., Lawrimore, J. H., . . . Zhang, H.-M. (2017). Extended reconstructed sea surface temperature, version 5 (ERSSTv5): upgrades, validations, and intercomparisons. *Journal of Climate, 30*(20), 8179-8205.

Hurrell, J. W. (1995). Decadal trends in the North Atlantic Oscillation: Regional temperatures and precipitation. *Science, 269*(5224), 676-679.

Hurteau, M. D., Bradford, J. B., Fulé, P. Z., Taylor, A. H., & Martin, K. L. (2014). Climate change, fire management, and ecological services in the southwestern US. *Forest Ecology and Management, 327*, 280-289.

Ionita, M., Rimbu, N., Chelcea, S., & Patrut, S. (2013). Multidecadal variability of summer temperature over Romania and its relation with Atlantic Multidecadal Oscillation. *Theoretical and Applied Climatology, 113*(1), 305-315.

IPCC, A. (2014). IPCC Fifth Assessment Report—Synthesis Report. In: IPPC Rome, Italy.

Jackson, A. (1968). Drought Index Chart As a Fire Weather Forecast Tool. Paper presented at the Bulletin of the American Meteorological Society.

Jia, S., Kim, S. H., Nghiem, S. V., Doherty, P., & Kafatos, M. C. (2020). Patterns of population displacement during mega-fires in California detected using Facebook Disaster Maps. *Environmental Research Letters, 15*(7).

Jiang, Y., Zhou, L., & Raghavendra, A. (2020). Observed changes in fire patterns and possible drivers over Central Africa. *Environmental Research Letters, 15*(9).

Jianping, L., & Wang, J. X. (2003). A new North Atlantic Oscillation index and its variability. *Advances in Atmospheric Sciences, 20*(5), 661-676.

Jones, GM, Kramer, H., Berigan, W., Whitmore, S., Gutiérrez, R., & Peery, M. (2021). Megafire causes persistent loss of an old-forest species. *Animal Conservation, 24*(6), 925-936.

Jones, M.W., Abatzoglou, J. T., Veraverbeke, S., Andela, N., Lasslop, G., . . . van der Werf, G. R. (2022). Global and regional trends and drivers of fire under climate change. *Reviews of Geophysics*, e2020RG000726.

Kamiguchi, K., Arakawa, O., & Kitoh, A. (2011). Long-term changes in Japanese extreme precipitation analyzed with APHRO_JP_EX. *Glob Environ Res, 15*, 91-99.

Kamiguchi, K., Arakawa, O., Kitoh, A., Yatagai, A., Hamada, A., & Yasutomi, N. (2010). Development of APHRO_JP, the first Japanese high-resolution daily precipitation product for more than 100 years. *Hydrological Research Letters, 4*, 60-64.

Kansakar, S. R., Hannah, D. M., Gerrard, J., & Rees, G. (2004). Spatial pattern in the precipitation regime of Nepal. *International Journal of Climatology: A Journal of the Royal Meteorological Society, 24*(13), 1645-1659.

Kayaba, N., Yamada, T., Hayashi, S., Onogi, K., Kobayashi, S., Yoshimoto, K., . . . Yamashita, K. (2016). Dynamical regional downscaling using the JRA-55 reanalysis (DSJRA-55). *Sola, 12*, 1-5.

Keeley, J. E. (2009). Fire intensity, fire severity and burn severity: a brief review and suggested usage. *International Journal of Wildland Fire, 18*(1).

Keeley, J. E., Baer-Keeley, M., & Fotheringham, C. (2005). Alien plant dynamics following fire in Mediterranean-climate California shrublands. *Ecological Applications, 15*(6), 2109-2125.

Keeley, J. E., Safford, H., Fotheringham, C., Franklin, J., & Moritz, M. (2009). The 2007 southern California wildfires: lessons in complexity. *Journal of Forestry, 107*(6), 287-296.

Keeley, J. E., & Syphard, A. D. (2017). Different historical fire–climate patterns in California. *International Journal of Wildland Fire, 26*(4), 253-268.

Keeley, J. E., & Syphard, A. D. (2021). Large California wildfires: 2020 fires in historical context. *Fire Ecology, 17*(1), 1-11.

Keetch, J. J., & Byram, G. M. (1968). *A drought index for forest fire control* (Vol. 38): US Department of Agriculture, Forest Service, Southeastern Forest Experiment ….

Kendall, M. G. (1948). Rank correlation methods.

Kennedy, M. C., Bart, R. R., Tague, C. L., & Choate, J. S. (2021). Does hot and dry equal more wildfire? Contrasting short-and long-term climate effects on fire in the Sierra Nevada, CA. *Ecosphere, 12*(7), e03657.

Keyantash, J., & Dracup, J. A. (2002). The quantification of drought: an evaluation of drought indices. *Bulletin of the American Meteorological Society, 83*(8), 1167-1180.

Kim, D. H., Yoo, C., & Kim, T.-W. (2011). Application of spatial EOF and multivariate time series model for evaluating agricultural drought vulnerability in Korea. *Advances in Water Resources, 34*(3), 340-350.

Kim, S., & Lee, S. (2000). Forecasting of flood stage using neural networks in the Nakdong river, South Korea. In *Watershed Management and Operations Management 2000* (pp. 1-8).

Kirchmeier-Young, M., Gillett, N., Zwiers, F., Cannon, A., & Anslow, F. (2019). Attribution of the influence of human-induced climate change on an extreme fire season. *Earth's Future, 7*(1), 2-10.

Kitzberger, T., Swetnam, T. W., & Veblen, T. T. (2001). Inter-hemispheric synchrony of forest fires and the El Niño-Southern Oscillation. *Global Ecology and Biogeography, 10*(3), 315-326.

Kogan, F., & Guo, W. (2016). Early twenty-first-century droughts during the warmest climate. *Geomatics, Natural Hazards and Risk, 7*(1), 127-137.

Kotsuki, S., Takenaka, H., Tanaka, K., Higuchi, A., & Miyoshi, T. (2015). 1-km-resolution land surface analysis over Japan: Impact of satellite-derived solar radiation. *Hydrological Research Letters, 9*(1), 14-19.

Kotsuki, S., & Tanaka, K. (2013). Uncertainties of precipitation products and their impacts on runoff estimates through hydrological land surface simulation in Southeast Asia. *Hydrological Research Letters, 7*(4), 79-84.

Kraaij, T., Baard, J. A., Arndt, J., Vhengani, L., & Van Wilgen, B. W. (2018). An assessment of climate, weather, and fuel factors influencing a large, destructive wildfire in the Knysna region, South Africa. *Fire Ecology, 14*(2), 1-12.

Kress, D. (2020). Understanding the Geographic Impacts and Causation of the 2017 Thomas Fire Towards Improved Wildfire Mitigation Policy for WUI Communities. California State University, Northridge.

Kwon, H.-H., & Lall, U. (2016). A copula-based nonstationary frequency analysis for the 2012-2015 drought in California. *Water Resources Research, 52*(7), 5662-5675.

Le Breton, T. D., Lyons, M. B., Nolan, R. H., Penman, T., Williamson, G. J., & Ooi, M. K. (2022). Megafire-induced interval squeeze threatens vegetation at landscape scales. *Frontiers in Ecology and the Environment.*

Le Page, Y., Morton, D., Bond-Lamberty, B., Pereira, J., & Hurtt, G. (2015). HESFIRE: a global fire model to explore the role of anthropogenic and weather drivers. *Biogeosciences, 12*(3), 887-903.

Leblanc, M. J., Tregoning, P., Ramillien, G., Tweed, S. O., & Fakes, A. (2009). Basin-scale, integrated observations of the early 21st century multiyear drought in southeast Australia. *Water Resources Research, 45*(4).

Lee, M. H., Ho, C. H., Kim, J. H., & Song, H. J. (2012a). Low-frequency variability of tropical cyclone-induced heavy rainfall over East Asia associated with tropical and North Pacific sea surface temperatures. *Journal of Geophysical Research: Atmospheres, 117*(D12).

Lee, S.-M., Byun, H.-R., & Tanaka, H. L. (2012b). Spatiotemporal characteristics of drought occurrences over Japan. *Journal of Applied Meteorology and Climatology, 51*(6), 1087-1098.

Lei, Z., & Yang, Y.-b. (2019). Research on data mining algorithm for regional photovoltaic generation. Paper presented at the International Conference on Advanced Hybrid Information Processing.

Li, J., Zhang, Q., Chen, Y. D., & Singh, V. P. (2015). Future joint probability behaviors of precipitation extremes across China: Spatiotemporal patterns and implications for flood and drought hazards. *Global and Planetary Change, 124*, 107-122.

Liesowska, A. (2015). Fire rages on as death toll from two blazes reaches 33. *Availabe online: http://siberiantimes.com/ecology/casestudy/news.*

Linley, G. D., Jolly, C. J., Doherty, T. S., Geary, W. L., Armenteras, D., Belcher, C. M., . . . Giorgis, M. A. (2022). What do you mean,'megafire'? *Global Ecology and Biogeography.*

Littell, J. S., Peterson, D. L., Riley, K. L., Liu, Y., & Luce, C. H. (2016). A review of the relationships between drought and forest fire in the United States. *Global change biology, 22*(7), 2353-2369.

Liu, Y., Stanturf, J., & Goodrick, S. (2010). Trends in global wildfire potential in a changing climate. *Forest Ecology and Management, 259*(4), 685-697.

Lizundia-Loiola, J., Otón, G., Ramo, R., & Chuvieco, E. (2020). A spatio-temporal active-fire clustering approach for global burned area mapping at 250 m from MODIS data. *Remote*

Sensing of Environment, 236, 111493.

Loehman, R. A., Reinhardt, E., & Riley, K. L. (2014). Wildland fire emissions, carbon, and climate: Seeing the forest and the trees–A cross-scale assessment of wildfire and carbon dynamics in fire-prone, forested ecosystems. *Forest Ecology and Management, 317*, 9-19.

Lorenz, E. N. (1956). Empirical orthogonal functions and statistical weather prediction (Vol. 1): Massachusetts Institute of Technology, Department of Meteorology Cambridge.

Loveland, T. R., Reed, B. C., Brown, J. F., Ohlen, D. O., Zhu, Z., Yang, L., & Merchant, J. W. (2000). Development of a global land cover characteristics database and IGBP DISCover from 1 km AVHRR data. *International journal of remote sensing, 21*(6-7), 1303-1330.

Malamud, B. D., Millington, J. D., & Perry, G. L. (2005). Characterizing wildfire regimes in the United States. *Proceedings of the National Academy of Sciences, 102*(13), 4694-4699.

Mann, H. B. (1945). Nonparametric tests against trend. *Econometrica: Journal of the econometric society*, 245-259.

Mansoor, S., Farooq, I., Kachroo, M. M., Mahmoud, A. E. D., Fawzy, M., Popescu, S. M., . . . Ahmad, P. (2022). Elevation in wildfire frequencies with respect to the climate change. *Journal of environmental management, 301*, 113769.

Mantua, N. J., & Hare, S. R. (2002). The Pacific decadal oscillation. *Journal of oceanography, 58*(1), 35-44.

Mariani, M., Fletcher, M. S., Holz, A., & Nyman, P. (2016). ENSO controls interannual fire activity in southeast Australia. *Geophysical Research Letters, 43*(20), 10,891-810,900.

Martin, D. A. (2016). At the nexus of fire, water and society. *Philos Trans R Soc Lond B Biol Sci, 371*(1696).

McArthur, A. G. (1967). Fire behaviour in eucalypt forests.

McCabe, G. J., Palecki, M. A., & Betancourt, J. L. (2004). Pacific and Atlantic Ocean influences on multidecadal drought frequency in the United States. *Proceedings of the National Academy of Sciences, 101*(12), 4136-4141.

McCaffrey, S. (2004). Thinking of wildfire as a natural hazard. *Society and Natural Resources, 17*(6), 509-516.

McMahon, G., Gregonis, S. M., Waltman, S. W., Omernik, J. M., Thorson, T. D., Freeouf, J. A., . . . Keys, J. E. (2001). Developing a spatial framework of common ecological regions for the conterminous United States. *Environmental management, 28*(3), 293-316.

Meehl, G. A., Tebaldi, C., Teng, H., & Peterson, T. C. (2007). Current and future US weather extremes and El Niño. *Geophysical Research Letters, 34*(20).

Mees, R., & Chase, R. (1991). Relating burning index to wildfire workload over broad geographic areas. *International Journal of Wildland Fire, 1*(4), 235-238.

Miller, J. D., Safford, H., Crimmins, M., & Thode, A. E. (2009). Quantitative evidence for increasing forest fire severity in the Sierra Nevada and southern Cascade Mountains, California and Nevada, USA. *Ecosystems, 12*(1), 16-32.

Mishra, A. K., & Singh, V. P. (2010). A review of drought concepts. *Journal of Hydrology, 391*(1-2), 202-216.

Moore, P. F. (1986). Comparison of the Forest Fire Danger Meter Mk. 5 and the BEHAVE fire behavior prediction system in a dry eucalypt forest.

Moré, J. J. (1978). The Levenberg-Marquardt algorithm: implementation and theory. In *Numerical analysis* (pp. 105-116): Springer.

Moreira, F., Catry, F. X., Rego, F., & Bacao, F. (2010). Size-dependent pattern of wildfire ignitions in Portugal: when do ignitions turn into big fires? *Landscape Ecology, 25*(9), 1405-1417.

Moritz, M. A., Batllori, E., Bradstock, R. A., Gill, A. M., Handmer, J., Hessburg, P. F., . . . Schoennagel, T. (2014). Learning to coexist with wildfire. *Nature, 515*(7525), 58-66.

Mosavi, A., Ozturk, P., & Chau, K.-w. (2018). Flood prediction using machine learning models: Literature review. *Water, 10*(11), 1536.

Mozny, M., Trnka, M., & Brázdil, R. (2020). Climate change driven changes of vegetation fires in the Czech Republic. *Theoretical and Applied Climatology, 143*(1-2), 691-699.

Murphy, K. (2006). The ENSO-fire dynamic in insular Southeast Asia. *Climatic Change, 74*(4), 435-455.

Nagy, R. C., Fusco, E., Bradley, B., Abatzoglou, J. T., & Balch, J. (2018). Human-related ignitions increase the number of large wildfires across US ecoregions. *Fire, 1*(1), 4.

Navarro, K. M., Clark, K. A., Hardt, D. J., Reid, C. E., Lahm, P. W., Domitrovich, J. W., . . . Balmes, J. R. (2021). Wildland firefighter exposure to smoke and COVID-19: A new risk on the fire line. *Science of the Total Environment, 760*, 144296.

Neary, D. G. (2019). Forest Soil Disturbance: Implications of Factors Contributing to the Wildland Fire Nexus. *Soil Science Society of America Journal, 83*(S1).

Nelsen, R. B. (2003). Properties and applications of copulas: A brief survey. Paper presented at the Proceedings of the first brazilian conference on statistical modeling in insurance and finance.

Nelsen, R. B. (2007). An introduction to copulas: Springer Science & Business Media.

Newman, M., Alexander, M. A., Ault, T. R., Cobb, K. M., Deser, C., Di Lorenzo, E., . . . Nakamura, H. (2016). The Pacific decadal oscillation, revisited. *Journal of Climate, 29*(12), 4399-4427.

Nguyen, P. L., Min, S. K., & Kim, Y. H. (2021). Combined impacts of the El Niño-Southern Oscillation and Pacific Decadal Oscillation on global droughts assessed using the standardized precipitation evapotranspiration index. *International Journal of Climatology, 41*, E1645-E1662.

Nishi, A., & Kusaka, H. (2019). Effect of foehn wind on record-breaking high temperature event (41.1° C) at Kumagaya on 23 July 2018. *Sola*.

Nobre, P., & Shukla, J. (1996). Variations of sea surface temperature, wind stress, and rainfall over the tropical Atlantic and South America. *Journal of Climate, 9*(10), 2464-2479.

Nolan, R. H., Boer, M. M., Collins, L., Resco de Dios, V., Clarke, H. G., Jenkins, M., . . . Bradstock, R. A. (2020). Causes and consequences of eastern Australia's 2019-20 season of mega-fires. *Global change biology*.

O'Connor, T. G., Mulqueeny, C. M., & Goodman, P. S. (2011). Determinants of spatial variation in fire return period in a semiarid African savanna. *International Journal of Wildland Fire, 20*(4).

Okada, T. (2016). Integrated water resources management and drought risk management in Japan. *Water Policy, 18*(S2), 70-88.

Oliveira, S. L. J., Pereira, J. M. C., & Carreiras, J. M. B. (2012). Fire frequency analysis in Portugal (1975 - 2005), using Landsat-based burnt area maps. *International Journal of Wildland Fire, 21*(1).

Omar, A. H., Won, J. G., Winker, D. M., Yoon, S. C., Dubovik, O., & McCormick, M. P. (2005). Development of global aerosol models using cluster analysis of Aerosol Robotic Network (AERONET) measurements. *Journal of Geophysical Research: Atmospheres, 110*(D10).

Omernik, J. M. (1987). Ecoregions of the conterminous United States. *Annals of the Association of American geographers, 77*(1), 118-125.

Omernik, J. M. (2004). Perspectives on the nature and definition of ecological regions. *Environmental management, 34*(1), S27-S38.

Omernik, J. M., & Griffith, G. E. (2014). Ecoregions of the conterminous United States: evolution of a hierarchical spatial framework. *Environmental management, 54*(6), 1249-1266.

Özbayoğlu, A. M., & Bozer, R. (2012). Estimation of the burned area in forest fires using computational intelligence techniques. *Procedia Computer Science, 12*, 282-287.

Page, Y. L., Pereira, J., Trigo, R., Camara, C. d., Oom, D., & Mota, B. (2008). Global fire activity patterns (1996–2006) and climatic influence: an analysis using the World Fire Atlas. *Atmospheric Chemistry and Physics, 8*(7), 1911-1924.

Palmer, W. C. (1965). Meteorological drought (Vol. 30): US Department of Commerce, Weather Bureau.

Park, S., Kang, D., Yoo, C., Im, J., & Lee, M.-I. (2020). Recent ENSO influence on East African drought during rainy seasons through the synergistic use of satellite and reanalysis data. *ISPRS Journal of Photogrammetry and Remote Sensing, 162*, 17-26.

Parks, S. A., Holsinger, L. M., Miller, C., & Parisien, M. A. (2018). Analog-based fire regime and vegetation shifts in mountainous regions of the western US. *Ecography, 41*(6), 910-921.

Partal, T., & Küçük, M. (2006). Long-term trend analysis using discrete wavelet components of annual precipitations measurements in Marmara region (Turkey). *Physics and Chemistry of the Earth, Parts A/B/C, 31*(18), 1189-1200.

Pausas, J. G., & Keeley, J. E. (2019). Wildfires as an ecosystem service. *Frontiers in Ecology and the Environment, 17*(5), 289-295.

Pfeiffer, M., Spessa, A., & Kaplan, J. O. (2013). A model for global biomass burning in preindustrial time: LPJ-LMfire (v1. 0). *Geoscientific Model Development, 6*(3), 643-685.

Pliscoff, P., Folchi, M., Aliste, E., Cea, D., & Simonetti, J. A. (2020). Chile mega-fire 2017: An analysis of social representation of forest plantation territory. *Applied geography, 119*, 102226.

Povak, N. A., Kane, V. R., Collins, B. M., Lydersen, J. M., & Kane, J. T. (2020). Multi-scaled drivers of severity patterns vary across land ownerships for the 2013 Rim Fire, California. *Landscape Ecology, 35*(2), 293-318.

Prior, L. D., McCaw, W. L., Grierson, P. F., Murphy, B. P., & Bowman, D. M. (2011). Population structures of the widespread Australian conifer Callitris columellaris are a bio-indicator of continental environmental change. *Forest Ecology and Management, 262*(2), 252-262.

Ramo, R., Roteta, E., Bistinas, I., Van Wees, D., Bastarrika, A., Chuvieco, E., & Van der Werf, G. R. (2021). African burned area and fire carbon emissions are strongly impacted by small fires undetected by coarse resolution satellite data. *Proceedings of the National Academy of Sciences, 118*(9).

Riaño, D., Moreno Ruiz, J., Isidoro, D., & Ustin, S. (2007). Global spatial patterns and temporal trends of burned area between 1981 and 2000 using NOAA-NASA Pathfinder. *Global change biology, 13*(1), 40-50.

Richardson, H. W. (1919). The Northeastern Minnesota Forest Fires of October 12, 1918. *Geographical Review, 7*(4), 220-232.

Ridder, N. N., Pitman, A. J., Westra, S., Ukkola, A., Do, H. X., Bador, M., . . . Zscheischler, J. (2020). Global hotspots for the occurrence of compound events. *Nature communications, 11*(1), 1-10.

Rodrigues, M., Gelabert, P. J., Ameztegui, A., Coll, L., & Vega-García, C. (2021). Has COVID-19 halted winter-spring wildfires in the Mediterranean? Insights for wildfire science under a pandemic context. *Science of the Total Environment, 765*, 142793.

Rossi, F. S., & Santos, G. A. d. A. (2020). Fire dynamics in Mato Grosso state, Brazil: The relative roles of gross primary productivity. *Big Earth Data, 4*(1), 23-44.

Rossiter, N. A., Setterfield, S. A., Douglas, M. M., & Hutley, L. B. (2003). Testing the grass-fire cycle: alien grass invasion in the tropical savannas of northern Australia. *Diversity and distributions, 9*(3), 169-176.

Sadegh, M., Ragno, E., & AghaKouchak, A. (2017). Multivariate Copula Analysis Toolbox (MvCAT): Describing dependence and underlying uncertainty using a Bayesian framework. *Water Resources Research, 53*(6), 5166-5183.

Saji, N., Goswami, B. N., Vinayachandran, P., & Yamagata, T. (1999). A dipole mode in the tropical Indian Ocean. *Nature, 401*(6751), 360-363.

Schlesinger, M. E., & Ramankutty, N. (1994). Low-frequency oscillation. *Nature, 372*(6506), 508-509.

Schlobohm, P., & Brain, J. (2002). Gaining an understanding of the national fire danger rating system. *National Wildfire Coordinating Group, PMS, 932*.

Schmidt, I. B., & Eloy, L. (2020). Fire regime in the Brazilian Savanna: Recent changes, policy and management. *Flora, 268*, 151613.

Schneider, T., Bischoff, T., & Haug, G. H. (2014). Migrations and dynamics of the intertropical convergence zone. *Nature, 513*(7516), 45-53.

Schoenberg, F. P., Chang, C.-H., Keeley, J. E., Pompa, J., Woods, J., & Xu, H. (2007). A critical assessment of the burning index in Los Angeles County, California. *International Journal of Wildland Fire, 16*(4), 473-483.

Schoennagel, T., Veblen, T. T., Kulakowski, D., & Holz, A. (2007). Multidecadal climate variability and climate interactions affect subalpine fire occurrence, western Colorado (USA). *Ecology, 88*(11), 2891-2902.

Schoennagel, T., Veblen, T. T., Romme, W. H., Sibold, J. S., & Cook, E. R. (2005). ENSO and PDO variability affect drought-induced fire occurrence in Rocky Mountain subalpine forests. *Ecological Applications, 15*(6), 2000-2014.

Schwarz, G. (1978). Estimating the dimension of a model. *The annals of statistics*, 461-464.

Scrucca, L., Fop, M., Murphy, T. B., & Raftery, A. E. (2016). mclust 5: clustering, classification and density estimation using Gaussian finite mixture models. *The R journal, 8*(1), 289.

Secretariat, G. (2006). Systematic Observation Requirements for Satellite-based Products for Climate. *GCOS Implementation Plan*.

Shabbar, A., Skinner, W., & Flannigan, M. D. (2011). Prediction of seasonal forest fire severity in Canada from large-scale climate patterns. *Journal of Applied Meteorology and Climatology, 50*(4), 785-799.

Shabbir, A. H., Zhang, J., Johnston, J. D., Sarkodie, S. A., Lutz, J. A., & Liu, X. (2020). Predicting the influence of climate on grassland area burned in Xilingol, China with dynamic simulations of autoregressive distributed lag models. *PLoS One, 15*(4), e0229894.

Shakesby, R. (2011). Post-wildfire soil erosion in the Mediterranean: review and future research directions. *Earth-Science Reviews, 105*(3-4), 71-100.

Shen, L., Zhao, C., Yang, X., Yang, Y., & Zhou, P. (2022). Observed slump of sea land breeze in Brisbane under the effect of aerosols from remote transport during 2019 Australian mega fire events. *Atmospheric Chemistry and Physics, 22*(1), 419-439.

Shi, K., & Touge, Y. (2022a). Characterization of global wildfire burned area spatiotemporal patterns and underlying climatic causes. *Scientific reports, 12*(1), 1-17.

Shi, K., Touge, Y., & Kazama, S. (2022b). Defining Homogeneous Drought Zones Based on Soil Moisture across Japan and Teleconnections with Large-Scale Climate Signals. *Journal of Applied Meteorology and Climatology, 61*(1), 43-60.

Short, K. C. (2021). Spatial wildfire occurrence data for the United States, 1992-2018 [FPA_FOD_20210617].

Sibold, J. S., & Veblen, T. T. (2006). Relationships of subalpine forest fires in the Colorado Front Range with interannual and multidecadal-scale climatic variation. *Journal of biogeography, 33*(5), 833-842.

Silvestrini, R. A., Soares-Filho, B. S., Nepstad, D., Coe, M., Rodrigues, H., & Assunção, R. (2011). Simulating fire regimes in the Amazon in response to climate change and deforestation. *Ecological Applications, 21*(5), 1573-1590.

Singleton, M. P., Thode, A. E., Meador, A. J. S., & Iniguez, J. M. (2019). Increasing trends in high-severity fire in the southwestern USA from 1984 to 2015. *Forest Ecology and Management, 433*, 709-719.

Sklar, M. (1959). Fonctions de repartition an dimensions et leurs marges. *Publ. inst. statist. univ. Paris, 8*, 229-231.

Stedinger, J. R. (1993). Frequency analysis of extreme events. *in Handbook of Hydrology.*

Steel, Z. L., Safford, H. D., & Viers, J. H. (2015). The fire frequency-severity relationship and the legacy of fire suppression in California forests. *Ecosphere, 6*(1).

Stephens, S. L., Skinner, C. N., & Gill, S. J. (2003). Dendrochronology-based fire history of Jeffrey pine-mixed conifer forests in the Sierra San Pedro Martir, Mexico. *Canadian Journal of Forest Research, 33*(6), 1090-1101.

Steptoe, H., Jones, S., & Fox, H. (2018). Correlations between extreme atmospheric hazards and global teleconnections: implications for multihazard resilience. *Reviews of Geophysics, 56*(1), 50-78.

Su, L., Miao, C., Duan, Q., Lei, X., & Li, H. (2019). Multiple-wavelet coherence of world's large rivers with meteorological factors and ocean signals. *Journal of Geophysical*

Research: Atmospheres, 124(9), 4932-4954.

Sungmin, O., Hou, X., & Orth, R. (2020). Observational evidence of wildfire-promoting soil moisture anomalies. *Scientific reports, 10*(1), 1-8.

Supriya, L. (2017). Ecosystems could once bounce back from wildfires. now they're being wiped out for good. *Science. Available at: https://www.sciencemag.org/news/2017/12/ecosystems-could-once-bounce-back-wildfires-now-they-re-being-wiped-out-good#:~: text= Wildfires% 20are% 20a% 20natural% 20part, the% 20reproduction% 20of% 20some% 20plants (accessed 19 February 2021).*

Swetnam, T. W., & Betancourt, J. L. (1990). Fire-southern oscillation relations in the southwestern United States. *Science, 249*(4972), 1017-1020.

Syphard, A. D., & Keeley, J. E. (2020). Mapping fire regime ecoregions in California. *International Journal of Wildland Fire, 29*(7), 595-601.

Syphard, A. D., Radeloff, V. C., Hawbaker, T. J., & Stewart, S. I. (2009). Conservation threats due to human-caused increases in fire frequency in Mediterranean-climate ecosystems. *Conservation Biology, 23*(3), 758-769.

Tabbussum, R., & Dar, A. Q. (2020). Comparative analysis of neural network training algorithms for the flood forecast modelling of an alluvial Himalayan river. *Journal of Flood Risk Management, 13*(4), e12656.

Tanaka, K. (2004). Development of the new land surface scheme SiBUC commonly applicable to basin water management and numerical weather prediction model. Graduate School of Engineering, Kyoto University, 289.

Tedim, F., Remelgado, R., Borges, C., Carvalho, S., & Martins, J. (2013). Exploring the occurrence of mega-fires in Portugal. *Forest Ecology and Management, 294*, 86-96.

Tehrany, M. S., Jones, S., & Shabani, F. (2019). Identifying the essential flood conditioning factors for flood prone area mapping using machine learning techniques. *Catena, 175*, 174-192.

Tentoglou, T., Burmistrova, J., & Hestir, E. (2021). Burn Severity and Albedo Analysis Concerning the Mendocino Complex Fire. Paper presented at the 2021 IEEE International Geoscience and Remote Sensing Symposium IGARSS.

Thompson, D. W., & Wallace, J. M. (1998). The Arctic Oscillation signature in the wintertime geopotential height and temperature fields. *Geophysical Research Letters, 25*(9), 1297-1300.

Thonicke, K., Spessa, A., Prentice, I., Harrison, S. P., Dong, L., & Carmona-Moreno, C. (2010). The influence of vegetation, fire spread and fire behaviour on biomass burning and trace gas emissions: results from a process-based model. *Biogeosciences, 7*(6), 1991-2011.

Thonicke, K., Venevsky, S., Sitch, S., & Cramer, W. (2001). The role of fire disturbance for global vegetation dynamics: coupling fire into a Dynamic Global Vegetation Model.

Global Ecology and Biogeography, 10(6), 661-677.

Tian, X., McRae, D. J., Jin, J., Shu, L., Zhao, F., & Wang, M. (2011). Wildfires and the Canadian Forest Fire Weather Index system for the Daxing'anling region of China. *International Journal of Wildland Fire, 20*(8), 963-973.

Torrence, C., & Compo, G. P. (1998). A practical guide to wavelet analysis. *Bulletin of the American Meteorological Society, 79*(1), 61-78.

Torrence, C., & Webster, P. J. (1999). Interdecadal changes in the ENSO–monsoon system. *Journal of Climate, 12*(8), 2679-2690.

Trigo, R. M., Pereira, J. M., Pereira, M. G., Mota, B., Calado, T. J., Dacamara, C. C., & Santo, F. E. (2006). Atmospheric conditions associated with the exceptional fire season of 2003 in Portugal. *International Journal of Climatology: A Journal of the Royal Meteorological Society, 26*(13), 1741-1757.

Trucchia, A., Meschi, G., Fiorucci, P., Gollini, A., & Negro, D. (2022). Defining Wildfire Susceptibility Maps in Italy for Understanding Seasonal Wildfire Regimes at the National Level. *Fire, 5*(1), 30.

Urrutia-Jalabert, R., González, M. E., González-Reyes, Á., Lara, A., & Garreaud, R. (2018). Climate variability and forest fires in central and south-central Chile. *Ecosphere, 9*(4), e02171.

USFS. (2015). The Rising Cost of Fire Operations: Effects on the Forest Service's Non-Fire Work. In: United States Department Agriculture Forest Service Washington, DC, USA.

Uvo, C. B., Repelli, C. A., Zebiak, S. E., & Kushnir, Y. (1998). The relationships between tropical Pacific and Atlantic SST and northeast Brazil monthly precipitation. *Journal of Climate, 11*(4), 551-562.

Van der Werf, G. R., Randerson, J. T., Giglio, L., Collatz, G., Mu, M., Kasibhatla, P. S., . . . van Leeuwen, T. T. (2010). Global fire emissions and the contribution of deforestation, savanna, forest, agricultural, and peat fires (1997–2009). *Atmospheric Chemistry and Physics, 10*(23), 11707-11735.

Van Wagner, C. (1974). Structure of the Canadian forest fire weather index (Vol. 1333): Environment Canada, Forestry Service Ontario.

Van Wagner, C., & Forest, P. (1987). Development and structure of the canadian forest fireweather index system. Paper presented at the Can. For. Serv., Forestry Tech. Rep.

Van Wagner, C., & Pickett, T. (1985). Equations and FORTRAN program for the Canadian forest fire weather index system (Vol. 33).

van Wagtendonk, J. W., Moore, P. E., Yee, J. L., & Lutz, J. A. (2020). The distribution of woody species in relation to climate and fire in Yosemite National Park, California, USA. *Fire Ecology, 16*(1), 1-23.

Vicente-Serrano, S. M., Beguería, S., & López-Moreno, J. I. (2010). A multiscalar drought index sensitive to global warming: the standardized precipitation evapotranspiration index. *Journal of climate, 23*(7), 1696-1718.

Vitolo, C., Di Giuseppe, F., Barnard, C., Coughlan, R., San-Miguel-Ayanz, J., Libertá, G., & Krzeminski, B. (2020). ERA5-based global meteorological wildfire danger maps. *Scientific data, 7*(1), 1-11.

Wallace, J. M., & Gutzler, D. S. (1981). Teleconnections in the geopotential height field during the Northern Hemisphere winter. *Monthly weather review, 109*(4), 784-812.

Wambua, R. M. (2019). Spatio-temporal characterization of Agricultural Drought using Soil Moisture Deficit Index (SMDI) in the Upper Tana River basin, Kenya. *International Journal of Engineering Research andAdvanced Technolog, 5*(2), 93-106.

Wang, Xiaoxiao, Di, Z., Li, M., & Yao, Y. (2021). Satellite-Derived Variation in Burned Area in China from 2001 to 2018 and Its Response to Climatic Factors. *Remote Sensing, 13*(7), 1287.

Wang, W., Zhu, Y., Xu, R., & Liu, J. (2015). Drought severity change in China during 1961–2012 indicated by SPI and SPEI. *Natural Hazards, 75*(3), 2437-2451.

Wei, F., Wang, S., Fu, B., Brandt, M., Pan, N., Wang, C., & Fensholt, R. (2020). Nonlinear dynamics of fires in Africa over recent decades controlled by precipitation. *Global change biology, 26*(8), 4495-4505.

Westerling, A. L., Hidalgo, H. G., Cayan, D. R., & Swetnam, T. W. (2006). Warming and earlier spring increase western U.S. forest wildfire activity. *Science, 313*(5789), 940-943.

Wilhite, D. A., Svoboda, M. D., & Hayes, M. J. (2007). Understanding the complex impacts of drought: A key to enhancing drought mitigation and preparedness. *Water resources management, 21*(5), 763-774.

Williams, J. (2013). Exploring the onset of high-impact mega-fires through a forest land management prism. *Forest Ecology and Management, 294*, 4-10.

Wolter, K., & Timlin, M. S. (1993). *Monitoring ENSO in COADS with a seasonally adjusted principal.* Paper presented at the Proc. of the 17th Climate Diagnostics Workshop, Norman, OK, NOAA/NMC/CAC, NSSL, Oklahoma Clim. Survey, CIMMS and the School of Meteor., Univ. of Oklahoma.

Wolter, K., & Timlin, M. S. (1998). Measuring the strength of ENSO events: How does 1997/98 rank? *Weather, 53*(9), 315-324.

Wolter, K., & Timlin, M. S. (2011). El Niño/Southern Oscillation behaviour since 1871 as diagnosed in an extended multivariate ENSO index (MEI. ext). *International Journal of Climatology, 31*(7), 1074-1087.

Wu, C., Venevsky, S., Sitch, S., Mercado, L. M., Huntingford, C., & Staver, A. C. (2021). Historical and future global burned area with changing climate and human demography.

One Earth, 4(4), 517-530.

Xu, Y., Lin, Z., & Wu, C. (2021). Spatiotemporal Variation of the Burned Area and Its Relationship with Climatic Factors in Central Kazakhstan. *Remote Sensing, 13*(2), 313.

Yaloveha, V., Hlavcheva, D., Podorozhniak, A., & Kuchuk, H. (2019). Fire hazard research of forest areas based on the use of convolutional and capsule neural networks. Paper presented at the 2019 IEEE 2nd Ukraine Conference on Electrical and Computer Engineering (UKRCON).

Yamak, Ç. (2006). Investigation over a national meteorological fire danger approach for Turkey with geographic information systems. Middle East Technical University,

Yang, J., Chang, J., Wang, Y., Li, Y., Hu, H., Chen, Y., . . . Yao, J. (2018). Comprehensive drought characteristics analysis based on a nonlinear multivariate drought index. *Journal of Hydrology, 557*, 651-667.

Yatagai, A., Kamiguchi, K., Arakawa, O., Hamada, A., Yasutomi, N., & Kitoh, A. (2012). APHRODITE: Constructing a long-term daily gridded precipitation dataset for Asia based on a dense network of rain gauges. *Bulletin of the American Meteorological Society, 93*(9), 1401-1415.

Yue, S., & Wang, C. Y. (2002). Applicability of prewhitening to eliminate the influence of serial correlation on the Mann-Kendall test. *Water Resources Research, 38*(6), 4-1-4-7.

Zambon, I., Cerdà, A., Cudlin, P., Serra, P., Pili, S., & Salvati, L. (2019). Road network and the spatial distribution of wildfires in the Valencian community (1993–2015). *Agriculture, 9*(5), 100.

Zhai, J., Su, B., Krysanova, V., Vetter, T., Gao, C., & Jiang, T. (2010). Spatial variation and trends in PDSI and SPI indices and their relation to streamflow in 10 large regions of China. *Journal of Climate, 23*(3), 649-663.

Zhang, L., Lau, W., Tao, W., & Li, Z. (2020). Large Wildfires in the Western United States Exacerbated by Tropospheric Drying Linked to a Multi-Decadal Trend in the Expansion of the Hadley Circulation. *Geophysical Research Letters, 47*(16).

Zheng, F., Leonard, M., & Westra, S. (2015). Efficient joint probability analysis of flood risk. *Journal of Hydroinformatics, 17*(4), 584-597.

Zhongming, Z., Linong, L., Wangqiang, Z., & Wei, L. (2019). Satellite Data Record Shows Climate Change's Impact on Fires.

Publications and Conferences

Peer-reviewed journals

10. **Shi, K.**, & Touge, Y. (2023). Identifying the shift in global wildfire weather conditions over the past four decades: an analysis based on change-points and long-term trends. Geoscience Letters, 10(1), 1-16. **(Corresponds to Chapter 1)**

9. **Shi, K.**, & Touge, Y. (2022). Characterization of global wildfire burned area spatiotemporal patterns and underlying climatic causes. *Scientific reports*, *12*(1), 1-17. **(Corresponds to Chapter 4)**

8. **Shi, K.**, Touge, Y., & Kazama, S. (2022). Defining Homogeneous Drought Zones Based on Soil Moisture across Japan and Teleconnections with Large-Scale Climate Signals. *Journal of Applied Meteorology and Climatology*, *61*(1), 43-60. **(Corresponds to Chapter 3)**

7. Touge, Y., **Shi, K.,** Huang, Q., & Sun, C. (2022). 栃木県足利市における 2021 年西宮林野火災の被災状況と延焼形態に関する調査報告. 自然災害科学, 41(2), 97-106.

6. Hendrawan, V. S. A., Kim, W., Touge, Y., **Ke, S.**, & Komori, D. (2022). A global-scale relationship between crop yield anomaly and multiscalar drought index based on multiple precipitation data. *Environmental Research Letters*, *17*(1), 014037.

5. Chai, Y., Touge, Y., **Shi, K**., & Kazama, S. (2020). Evaluating potential flood mitigation effect of paddy field dam for Typhoon No. 19 in 2019 in the Naruse River basin. *Journal of Japan Society of Civil Engineers, Ser. B1 (Hydraulic Engineering)*, *76*(1), 295-303.

4. Ye, L., **Shi, K.**, Zhang, H., Xin, Z., Hu, J., & Zhang, C. (2019). Spatio-temporal analysis of drought indicated by SPEI over northeastern China. *Water*, *11*(5), 908.

3. Ye, L., **Shi, K.**, Xin, Z., Wang, C., & Zhang, C. (2019). Compound droughts and heat waves in China. *Sustainability*, *11*(12), 3270.

2. Xin, Z., **Shi, K.**, Wu, C., Wang, L., & Ye, L. (2019). Applicability of hydrological models for flash flood simulation in small catchments of hilly area in China. *Open Geosciences*, *11*(1), 1168-1181.

1. Ji, R., Ye, L., Wu, J., Guo, L., **Shi, K.**, & Zhang, C. (2019). Research on the Derivation of Empirical Formula for the Peak Flow of Unit Hydrograph of Small Watershed in Mountainous Area. *China Rural Water and Hydropower,* 5, 1007-2284. (In Chinese)

Presentations in international conference

4. **JpGU Meeting 2022**, **Shi, K.**, and Touge, Y., 2022, May. Comprehensive Wildfire Characteristics Analysis Based on the Bivariate Copulas in the United States (Oral)

3. **AOGS 2022**, **Shi, K.**, and Touge, Y., 2022, August. Spatiotemporal Variability and Frequency Analysis of Copula Based Wildfire Activity and Burned Area in the United States (Oral)

2. **AGU Fall Meeting 2021, Shi, K.**, Touge, Y. and Kazama, S., 2021, December. Construction of Drought Regimes by Spatiotemporal Characteristics of Drought and Quantifying the Climatic Causes. In AGU Fall Meeting 2021. AGU. (Poster)

1. **AGU Fall Meeting 2020, Shi, K.**, Touge, Y. and Kazama, S., 2020, December. Evaluating Spatiotemporal Patterns of Drought in Japan from 1960 to 2018. In AGU Fall Meeting Abstracts (Vol. 2020, pp. H172-0008). (Poster)